

RE-280

CORRELATION OF MECHANICAL AND  
THERMAL PROPERTIES OF  
EXTRATERRESTRIAL MATERIALS

January 1967

*Grumman*

**RESEARCH DEPARTMENT**

FACILITY FORM 602

**N67-25958**  
(ACCESSION NUMBER)

**193**  
(PAGES)

**CV-83895**  
(NASA CR OR TMX OR AD NUMBER)

(THRU)  
**1**  
(CODE)

**30**  
(CATEGORY)

**GRUMMAN AIRCRAFT ENGINEERING CORPORATION**  
**BETHPAGE NEW YORK**

Grumman Research Department Report RE-280

CORRELATION OF MECHANICAL AND THERMAL PROPERTIES  
OF EXTRATERRESTRIAL MATERIALS

by

J. D. Halajian

J. Reichman

and

L. L. Karafiath

Geo-Astrophysics Section

Final Report on Contract NAS 8-20084

January 1967

Approved by: *Charles E. Mack, Jr.*  
Charles E. Mack, Jr.  
Director of Research

## A NOTE TO THE READER

In view of the length and interdisciplinary nature of this report, most readers will find the following guideline useful. Readers who are more interested in the results than the analyses may safely skip Phases I, II, and IV, and the Appendix, and limit their reading to the Summary, Phase III, and the Conclusions, a total of 12 pages, 2 of which deal with the interpretation of Surveyor 1 data.

"Phenomena-oriented" readers, who have a special interest in problems of heat transfer or soil and rock mechanics, will find Phase I of particular interest. We call their attention to our analyses of the thermal conductivity and bearing strength of porous media in Phases IA and IB, respectively. Readers who are familiar with the analysis of thermal emission of the lunar surface can find our treatment of this problem in Phase II. Phase IV deals with recommended programs in lunar thermophysics including analyses, experiments and direct lunar observations.

### ACKNOWLEDGMENT

We are very grateful to Mr. S. Winston of the Thermodynamics Department for his general assistance in preparing this report, to Mr. H. J. Behm of Advanced Systems for his extensive but largely unrewarding search of the literature for data on the mechanical properties of natural porous rocks, and to Mr. R. Basener, who was assigned to the Research Department during the past summer and is now continuing his studies at Manhattan College, for his valuable contribution in programming the mathematical thermal model of the lunar surface for IBM 7094.

## FOREWORD

This is the Final Report on the "Correlation of Mechanical and Thermal Properties of Extraterrestrial Materials" for the National Aeronautics and Space Administration, George C. Marshall Spaceflight Center, Huntsville, Alabama, under Contract NAS 8-20084 to the Grumman Aircraft Engineering Corporation, Bethpage, New York.

The contract authorized an 18-month analytical study (including a 6-month extension) to establish whether a correlation exists between the thermal emission of extraterrestrial surfaces and their mechanical properties. The study was conducted under the cognizance of the Research Projects Laboratory, with Mr. J. K. Harrison serving as Technical Representative.

## SUMMARY

Mechanical and thermal properties that are correlated in this report are the bearing strength and midnight temperatures of the lunar surface. The study is made in four phases. In Phase I, expressions are derived for the bearing strength and effective thermal conductivity (in vacuo) of porous media, including fluff, soils, and porous rocks. In Phase II, the heat conduction of the lunar surface during a lunation is solved for a wide range of porosity, degree of consolidation, and particle or pore size. In Phase III, these properties are used as a link to correlate bearing strength and midnight temperatures. In Phase IV, an experimental program is formulated to substantiate and complement the theoretical studies.

It is found that there is a definite trend of increasing bearing strength with increasing lunar nighttime temperatures. Most recent lunar nighttime observations show cold and hot spots which, according to this study, correlate with fluff and porous rocks, respectively. Average thermal and optical properties of the lunar surface suggest an underdense, relatively hard, partially consolidated material that can be approximated by cinders or semiwelded tuffs. Surveyor 1 appears to have landed on such an area. Some of the ambiguities in the correlation may best be resolved by laboratory measurements of the thermal conductivity and bearing strength of porous media; however, such data are scarce. Extending the analysis in this report to microwave frequencies would also help. Urgently needed are new and better infrared emission data on the dark side of the moon.

A graphic summary of the results of this study is shown in Fig. 53.

TABLE OF CONTENTS

<u>Item</u>	<u>Page</u>
Introduction .....	1
Method of Investigation .....	2
Phase I: Thermal and Mechanical Properties of Porous Media in Vacuo .....	6
Phase IA: Thermal Properties .....	7
Problem Areas .....	7
Effective Thermal Conductivity of Particulate Media .....	8
Solid Conductive Component .....	8
Radiative Component .....	14
Total Thermal Conductivity of Powders in a Vacuum .....	17
Comparison with Experimental Data .....	19
Effective Thermal Conductivity of Vesicular Media .....	21
Solid Conductive Component .....	21
Radiative Component .....	22
Total Thermal Conductivity .....	22
Comparison with Experimental Data .....	26
Evaluation of Theoretical Models .....	27
Phase IB: Mechanical Properties .....	45
Definition of Models and Terms .....	45
Problem Areas .....	45

<u>Item</u>	<u>Page</u>
Bearing Strength of Particulate Models .....	47
The "Fluff" Model .....	47
The "Cannonball" Model .....	65
Bearing Strength of Vesicular Model .....	73
Literature Review on Vesicular Rocks .....	73
Stresses in Porous Media .....	76
Mechanical Properties of Manufactured Porous Materials .....	78
Empirical Strength-Porosity Relationship of Vesicular Media .....	82
Phase II: Thermophysical Analysis of the Lunar Surface .....	110
Purpose .....	110
Background .....	110
Thermal Properties .....	111
Emissivity .....	111
Albedo or Reflectivity .....	112
Thermal Conductivity .....	113
Specific Heat .....	114
Mathematical Model .....	114
Case Studies of the Lunar Surface for Lunation Cooling .....	118
Effects of Latitude and Roughness on Lunation Temperatures .....	119



<u>Item</u>	<u>Page</u>
Importance of Lunar Nighttime Temperature Data .....	120
Available Lunar Nighttime Temperature Data .....	121
Nighttime Temperatures for Two-Layer Models .....	122
Nighttime Temperatures for a Homogeneous Model as Functions of $\gamma$ and Emissivity .....	125
Nighttime Temperatures for a Particulate Model with Temperature Dependent Thermal Conductivity .....	126
Nighttime Temperatures for a Vesicular Model .....	130
 Phase III: Correlation of Thermal and Mechanical Properties of the Lunar Surface .....	 146
Redefinition of Some Terms .....	146
Bearing Strength of Porous Media .....	147
Midnight Temperatures of Particulate and Vesicular Lunar Surfaces .....	148
Correlation of Lunar Midnight Temperature and Bearing Strength .....	149
Grain or Pore Size Effects in Correlating $T_m$ and $f$ .....	150
Effects of Porosity and Degree of Consolidation in Correlating $T_m$ and $f$ .....	150
Thermal and Mechanical Properties of Surveyor 1 Landing Site .....	152
 Phase IV: Recommended Programs in Lunar Thermophysics .....	 159
Theoretical Analyses .....	159
Laboratory Experiments .....	160

<u>Item</u>	<u>Page</u>
Group I Experiments (To Improve the Analytical Correlation) .....	160
Group II Experiments (To Study Roughness, Directionality, and Heterogeneity Effects on Remote Sensing of Thermal Emission) .....	163
Earth-Based Observations .....	164
Conclusions .....	167
Recommendations .....	170
References .....	171

## LIST OF ILLUSTRATIONS

<u>Figure</u>		<u>Page</u>
1	Particulate Model of Radiative Conduction Component .....	29
2	Suspended Particle Model of Radiative Conduction Component .....	29
3	Radiative Conductivity versus Porosity .....	30
4	Radiative Conductivity versus Porosity for Different Particle Sizes and Temperatures .....	31
5	Effective Thermal Conductivity in Vacuo of Basalt Powder versus Porosity for Different Particle Sizes and Temperatures .....	32
6	Effective Theoretical Thermal Conductivity in Vacuo of Basalt Powder versus Particle Size at 60 and 80 Percent Porosity and	
	a) 250°K .....	33
	b) 100°K .....	34
7	Total Theoretical Thermal Conductivity in Vacuo of Basalt Powder versus Temperature at Different Particle Sizes and	
	a) 60 Percent Porosity .....	35
	b) 80 Percent Porosity .....	36
8	$\gamma$ versus Temperature for a Temperature- Dependent Model at 70 Percent Porosity .....	37
9	Spectrum of Vesicular Thermal Models .....	38
10	Thermal Conductivity of Porous Rocks	
	a) Series Model .....	39
	b) Loeb and Parallel Models .....	40
	c) Maxwell Model .....	41
	d) Modified Maxwell Model .....	42
	e) Russell Model .....	43
11	Comparison of Loeb Model with Experimental Data on Thermal Conductivity of Porous Rocks .....	44

<u>Figure</u>	<u>Page</u>
12 Major Postulated Lunar Surface Model .....	85
13 Modes of Failure in Particulate Media .....	86
14 Failure Patterns in Fluff Model (2 Sheets) .....	87
15 Settlement Curves in Particulate Media .....	89
16 Postulated Failure Mode in Semi-Infinite Fluffy Medium .....	90
17 Compaction in Fluffy Soil .....	91
18 Interface Between Undisturbed and Compacted Fluffs .....	91
19 Relationship Between Coordination Number $m$ and Porosity $p$ .....	92
20 Relationship Between Initial Porosity $p_0$ and Bearing Capacity Factors	
a) Shear Component $N_s$ .....	93
b) Compaction Component $N_c$ .....	94
21 Bearing Strength of Fluff versus Porosity .....	95
22 Best-Fit Theoretical Function of Fluff Bearing Strength with Available Experimental Data .....	96
23 Drop Test in Fluff .....	97
24 Soil Adhesion in Ultra High Vacuum .....	98
25 Soil Bearing Strength Under Varying Gravity Fields .....	99
26 Theoretical $S_g N_\rho$ Values .....	100
27 Empirical Correlation of Frictional Angle and Porosity .....	101
28 Best-Fit of Theoretical Functions of Bearing Strength of "Cannonball" Model with Experimental Data .....	102

<u>Figure</u>	<u>Page</u>
29 Bearing Strength of Particulate Media versus Porosity .....	103
30 Systematic Arrangement of Spherical Holes in Vesicular Media .....	104
31 Stress Distribution in Vesicular Media .....	105
32 Reported Strength-Porosity Data on Vesicular Media and Best-Fit Curve for Porous Rocks .....	106
33 Strength-Porosity Relationship for Cellular Concrete .....	107
34 Comparison of Proposed Strength-Porosity Relationships .....	108
35 Strength-Porosity Relationship in the High Porosity Range .....	109
36 Lunation Temperature Data Taken From Sinton .....	131
37 Eclipse Temperature Data Taken From Pettit .....	132
38 IBM 7094 Calculated Lunation Temperatures for Various Values of $\gamma = (k\rho c)^{-1/2}$ .....	133
39 Calculated Lunation Temperatures for Various Values of $\gamma$ from Krotikov and Shchuko .....	134
40 Effect of Latitude on Lunation Temperatures .....	135
41 Lunation Temperatures of Moon for Two-Layer Model .....	136
42 Lunar Midnight Temperatures versus Upper Layer Thickness for Lower Layer $\gamma_1 = 250$ and Upper Layer $\gamma_0$ as Shown .....	137
43 Lunar Midnight Temperatures versus Upper Layer Thickness for Lower Layer $\gamma_1 = 20$ and Upper Layer $\gamma_0$ as Shown .....	138

<u>Figure</u>	<u>Page</u>
44 $\gamma_0$ versus Thickness of Upper Layer for Midnight Temperature of 110°K Lower Layer $\gamma_1$ as Shown .....	139
45 Lunar Midnight Temperature versus $\gamma$ and at Various Emissivities .....	140
46 Family of Lunation Curves at Various Porosities and Particles Sizes .....	141
47 Lunar Midnight Temperature versus Particle Size at Various Porosities .....	142
48 Midnight Temperatures versus Porosity at Various Particle Sizes .....	143
49 $\gamma$ versus Porosity for a Vesicular Model .....	144
50 Lunar Midnight Temperature versus Porosity for a Vesicular Model .....	145
51 Summary, Strength-Porosity Relationship of Porous Media .....	154
52 Summary, Lunar Midnight Temperatures versus Porosity .....	155
53 Correlation of Lunar Midnight Temperature and Bearing Strength .....	156
54 Schematic Cross Sections of Porous Rocks at $T_m = 148^\circ\text{K}$ and $f = 140$ psi .....	157
55 Flow Chart of Key Equations and Figures Leading to the Correlation .....	158
56 Hawaiian Volcanic Cinders .....	166

LIST OF TABLES

<u>Table</u>		<u>Page</u>
I	Purpose and Relationship of Phases in this Report .....	4
II	Material Properties of Basalt .....	17
III	Surface Energy Between Two Contacting Spheres .....	61
IV	Stress Concentration Factors Around Openings .....	77
V	Physical Properties of Rocks .....	84
VI	Cases Studied for Lunation Cooling .....	118

## INTRODUCTION

This report gives a detailed account of all work performed under NASA Contract No. NAS 8-20084. It includes most of the material submitted in three previous progress reports (Refs. 1, 2, and 3) and represents the final report on the "Correlation of Mechanical and Thermal Properties of Extraterrestrial Materials."

The primary purpose of this work is to examine whether a correlation exists between the measurable thermal emission of a remote body, such as the moon, and the mechanical properties of the energy emitting material. To be more specific, because thermal conductivity and bearing strength are both porosity dependent properties, an attempt is made to determine whether inferences can be made about the strength of porous media likely to be found on the moon from lunation and eclipse temperature measurements.

Studies of this nature help to interpret present and future lunar measurements and laboratory experiments in terms of the "engineering properties" of the lunar surface. This particular study is limited to thermal emission at infrared wavelength only. To be more meaningful, it should be complemented by investigations of other portions of the lunar data measured at shorter and longer wavelengths. These investigations, however, are beyond the scope of this report.

A major cause of disagreement among the interpreters of the lunar thermal data can be traced to the following sources: inadequacy of, and uncertainties in, lunar temperature measurements; questionable assumptions made to analyze these data; limited theoretical knowledge of the laws of heat flow and mechanical behavior of postulated lunar materials; and finally, the scarcity of reliable thermophysical data on such materials. In view of this situation, this study is performed in the following four phases:

- I Theoretical analysis of the thermal conductivity and bearing strength of poorly conducting materials likely to exist on the moon (these materials include soils and porous rocks).
- II A critical reevaluation of the thermal behavior of the lunar surface during a lunation, and solution of heat conduction of the lunar surface assumed to be covered with materials analyzed in Phase I.



III Correlation of the thermal and mechanical properties of the lunar surface.

IV Formulation of a program of lunar observation and laboratory experiments to verify or complement the studies in Phases I, II, and III.

Each phase or major topic in this report is followed by its own illustrations and may be read independently of the others. In view of the variety and length of the problems dealt with, the following section is devoted to "Method of Investigation," where we identify the various problem areas, indicate how they are related to one another, where they phase into the study, and what they contribute to the correlation we are seeking.

## METHOD OF INVESTIGATION

This report does not begin with a direct analysis of the thermal emission of the moon, because such an analysis would not reveal much about the nature of the lunar surface other than suggest that the outermost layer of the moon, down to a depth of about a decimeter, is porous or in an "underdense" state of packing. Knowledge of the thermal and mechanical behavior of porous media under high vacuum and low gravity conditions is necessary to establish at least the boundaries within which various combinations of porosity, grain size, and degree of consolidation are consistent with the lunar thermal data. Consequently, Phase I of this report begins with a theoretical study of thermal conductivity and bearing strength of porous materials such as soils and vesicular rocks. Particular emphasis is given to those aspects of thermal and mechanical behavior of porous media that are poorly understood, namely, the relative contributions of the conductive and radiative components of heat transfer in soils and porous rocks in a vacuum, and the mode of failure of highly porous "fluffy" powders and porous rocks.

The purpose of the following phases in this report and their relationship to one another are outlined in Table I. The expressions of thermal conductivity derived in Phase IA are used in the solution of the heat conduction equation of the lunar surface in Phase II. A computer program was developed for this purpose. This program was checked first against existing solutions worked out by Jaeger and Krotikov (Refs. 4 and 5). It was then expanded to include a number of effects related to the correlation of thermal and mechanical properties. As it stands now, the program is sufficiently broad and flexible to handle more complicated, inhomogeneous models without major changes.

In view of present uncertainties in the available lunar data, we have not tried to develop "best fit" models that match a given set of lunar data; instead, we have emphasized the study of the thermal behavior of various hypothetical and mostly homogeneous lunar thermal models under given inputs or boundary conditions. The "data-matching" approach is considered premature because the lunar data that could be matched are poorly defined in terms of location and resolution. The "model-behavior" approach as used throughout Phase II is believed to be more meaningful at this time. When high resolution emission data are obtained for distinct areas of the moon, then data-matching may be attempted in the light of the

TABLE I

Purpose and Relationship of Phases in this Report

Phase	Purpose	Remark
IA IB	Derive $k$ vs. $p$ relationship Derive $f$ vs. $p$ relationship	}for soils and }porous rocks
II	Derive $T_m$ vs. $p$ relationship	
III	Correlate $f$ and $T_m$	as derived in IB and II
IV	Formulate Experimental Program	to verify and/or comple- ment theoretical findings

Note:  $k$  = Thermal Conductivity  
 $f$  = Bearing Strength  
 $p$  = Porosity  
 $T_m$  = Lunar Midnight Temperature

known behavior of hypothetical models. We are currently developing similar techniques in studying the photometric and polarimetric properties of the lunar surface (Refs. 6 and 7).

The analysis of the nighttime temperatures of the lunar surface, as a function of material and geometric properties, could be cited as examples of "model-behavior" studies in Phase II. Generally, these studies reveal what new lunar data are needed to fill a specific gap in our knowledge, and how the new observations should be made in terms of wavelength, resolution, lunar phase, and location on the moon.

More emphasis is given to the study of the thermal behavior of the lunar surface during a lunation than during an eclipse, mainly because surface temperatures during a longer cooling transient are a better index of the thermal conductivity, hence, bearing strength of the cooling material. Also, eclipse temperatures are more difficult to interpret because of spurious effects explained in Phase II. In view of the greater relevance of nighttime temperatures to the mechanical properties, several case studies of the lunation regime are made, including "particulate" and "vesicular" models of the lunar surface. In the case of the particulate model, a more elaborate temperature dependent solution is sought.

Essentially, the case studies in Phase II are solved to give the lunar midnight temperature of a postulated model for a wide range of physical parameters, such as porosity and particle size. The bearing strength of the postulated model is investigated in Phase IB as a function of the same parameters. In Phase III the common parameters are used as a link to correlate lunar midnight temperature with bearing strength.

Because of the inherent complexity of particulate and vesicular materials, the thermal and mechanical models analyzed in Phase I have been considerably idealized. Nevertheless, it is felt that a theoretical analysis is useful, since it could indicate whether a correlation is at all possible, and if it is, whether it could reveal those factors that commonly affect the thermal and mechanical behavior of postulated lunar materials. Knowledge of these factors is essential to determine: 1) what experiments to perform, 2) what properties to measure, and 3) how to interpret and convert the results into semiempirical rules. These guidelines are used in formulating the experimental program discussed in Phase IV.

A flow chart of the first three phases and of key figures and equations leading to the final correlation is shown in Fig. 55.

PHASE I: THERMAL AND MECHANICAL PROPERTIES OF  
POROUS MEDIA IN VACUO

This phase represents the major portion of the work performed under the contract. It is divided into two parts dealing, respectively, with thermal and mechanical properties. The main purpose is to derive analytical or empirical expressions for both the effective thermal conductivity and bearing strength of porous materials likely to exist on the moon. For purposes of analysis, these materials are idealized into "particulate" and "vesicular" models representing, respectively, soils and porous rocks. Both models are defined in terms of their porosity, grain or pore size, interparticle contact area and other properties that are thermally and mechanically relevant. In Phase IA the solid and radiative components of thermal conductivity are formulated separately and combined. The combined formulae for each physical model are used in the solution of the heat balance equation of the lunar surface in Phase II. In Phase IB the bearing strength of these physical models are analyzed. The final objective of Phase IB is to prepare curves of bearing strength versus porosity for both the particulate and vesicular models. These curves will be correlated later in Phase III with lunar midnight temperature versus porosity curves that are derived in Phase II.

## PHASE IA: THERMAL PROPERTIES

### PROBLEM AREAS

The cooling curves of the moon analyzed in Phase II suggest that the surface is a good insulator. All insulating materials are porous, but not necessarily in a "suspended" or cohesionless state. There are several difficulties that hamper the interpretation of the lunar thermal data beyond the assertion that the lunar surface material is porous or in an "underdense" state of packing. One difficulty, which this study will attempt to alleviate, is that the unknown geometrical, mechanical, and thermal properties of the lunar surface are interdependent variables whose relationships have not been well explored, particularly under vacuum conditions. This difficulty is further complicated by the fact that there could be one or two mechanisms of heat transfer in porous media in vacuo, such as surface-to-surface radiation through the voids and/or solid conduction through points of interparticle contact. The radiative mechanism has little or no bearing on the manner in which the particles touch one another, and hence no bearing on the mechanical strength of the material. Furthermore, the fact that contribution of radiative heat transfer to the total conduction is more appreciable in vacuo than in air (this would tend to favor a "soft" lunar model) draws greater attention to this mechanism of heat transfer than it has been given to date. Conduction through the solid phase depends upon, among other things, the area of particle contact as well as the nature of interparticle strength (solid bridges or molecular or electrostatic forces of attraction). The relative contribution of the radiative and conductive components of heat transfer in vacuo is very poorly understood and experimentally documented. Likewise, the need to express conductivity through the solid phase in terms of interparticle contact conditions is not without theoretical difficulty particularly under "adsorption-free" interface conditions.

The limitation of theory in predicting thermal conductivity is more apparent in the "vesicular" model, which we arbitrarily define as a porous material, in which the solid phase is fully continuous or consolidated. Micropores or microcracks commonly occur in such materials, thereby significantly reducing thermal conductivity without appreciably altering porosity. Theoretically, one could estimate the relative contribution of the radiative and solid components of heat conduction, where the latter is only an upper limit. Since the solid component is usually predominant in "vesicular" materials, experiments are necessary to complement theory.

Another analytical difficulty is in interpreting the lunar thermal inertia constant, due to the lack of reliable observational data on the individual values of the interdependent variables named previously, i.e., the porosity of the lunar material and the thermal conductivity  $k_0$  of this material at zero percent porosity. In the past, assumptions made on one of these properties to solve for the other have inevitably led to conflicting estimates of the internal consistency of the lunar surface material. Until more reliable observational data become available, we plan to postulate preliminary values of these variables as long as these values are consistent with other aspects of the available lunar data measured at shorter and longer wavelength. For instance, "data-matching" investigations at Grumman of the lunar photometric data suggest a porosity for the lunar surface of the order of 70 to 80 percent (Ref. 6). Likewise, estimates of  $k_0$  can be based on data in the literature by using the chemical composition of the lunar surface as inferred from radiometric and radar observations (Ref. 8).

## EFFECTIVE THERMAL CONDUCTIVITY OF PARTICULATE MEDIA

### Solid Conductive Component

#### Literature Review

There are a large number of expressions given in the literature to predict the thermal conductivity of powders. Good reviews of many of the expressions are given by Godbee and Ziegler (Ref. 9); Everest, Glaser, and Wechsler (Ref. 10); and Gorring and Churchill (Ref. 11). The latter authors report the only expression that is applicable to the solid conduction component of powders as derived by Riemann (Ref. 12),

$$\bar{K} = \frac{K_s}{\frac{R}{r} + \frac{1}{\pi} \ln \frac{2R}{r}},$$

where  $K_s$  is the conductivity of the solid at zero percent porosity and  $r$  and  $R$  are the radii of the contact area and spherical particle, respectively. Unfortunately, we have not been able to find in the cited references the actual derivation of this equation, or examine the assumptions made by Riemann regarding the porosity of the particle system, the direction of heat flow, the geometry of contacting surfaces, etc.

The other reported equations cannot be used in lunar studies because they deal with the thermal conductivity of powders under conditions where gas conduction is significant. Under these conditions, the relatively small conduction of heat that takes place through the particle contact areas can be justifiably neglected. The resulting expressions that take into account combined gas and solid heat transfer and radiation have been reasonably successful in predicting the experimental results (Ref. 11).

In a vacuum, however, there are two mechanisms that contribute to heat transport through powdered materials: solid conduction and radiation. Solid conduction takes place both through the particles and between the particles across the contact areas. The relatively small contact areas between the particles in comparison to the particle size introduce a large thermal resistance that considerably reduces the effective thermal conductivity of the material. Because of the significance of contact area, an expression for the effective conductivity should necessarily include the area or a parameter relating to it. Unfortunately, the area of contact between real surfaces is a very sensitive function of the degree of roughness, hardness, and the applied pressure. For example, soft, rough particles should have larger areas of contact than smooth, hard spheres. Despite the rather complex dependence of specific geometry on contact area, the fact that an averaging process occurs for a system of many particles gives some confidence to the belief that a relatively simple model may be useful in predicting the solid conduction component of the thermal conductivity.

In order to gain a more fundamental understanding of the mechanisms involved, a review of the literature dealing with contact resistance theory was made. Existing methods for predicting thermal contact resistance depend upon a knowledge of the topography of the contacting areas. Fenech and Rohsenow (Ref. 13) use three parameters to describe the contacting surface. These parameters must be determined from recordings of surface profiles. Their theory has been applied to metallic surfaces in contact, for which they have obtained good agreement with experimental data. Clausing and Chao (Ref. 14) describe the contacting areas in terms of macroscopic and microscopic contact regions. The microscopic contacts depend on surface roughness and the macroscopic contact area depends on applied load and radii of curvature as given by Hertz's equation for elastic deformation. The results of their work indicate that the macroscopic constriction effect dominates the thermal contact resistance of many surfaces. It also was shown that film resistances were of small importance unless they were unusually thick. Kragelsky and Demkin (Ref. 15) consider both waviness and



roughness, and deduce a formula to calculate the real contact area as a function of load, geometry of the surfaces, and properties of the material. A significant conclusion of their study is that the number of contact spots increases much more significantly with applied load than do the individual areas of contacting spots. In order to use the equations it is necessary to experimentally determine topographical parameters.

To apply the work that has been done on contact resistance between rough surfaces to powders, it would be necessary to perform microscopic studies of the roughness features of individual particles. The points of a particle at which it makes contact with another particle are not known; hence, it appears necessary to use statistical methods to correlate the frequency of contact as a function of the nature of surface irregularity. Dallavalle (Ref. 16), in his book on fine particle technology, devotes an entire chapter to shape and size distribution of particles; however, the shape factors he discusses are of a very simple form and are not adequate for characterizing heat transport. From this limited investigation of contact resistance between real surfaces, it appears that it would be extremely difficult to formulate meaningful expressions to predict the thermal conductivity of powders under the most favorable conditions, i.e., when most of the geometrical and material properties are known.

The model, which is developed here to determine the effective thermal conductivity of powders, involves the naive but extremely simplifying assumption of smooth spheres. The same assumption is used in Phase IB to derive an expression for the bearing strength of fluff. The accuracy resulting from such an assumption can be estimated only by comparing predicted results from the equations with experimental data. Regardless of whether the estimated accuracy is as good as one would desire, there is additional justification for using the idealized models to describe the thermal conductivity of powders. It makes it convenient to investigate the use of lunar temperature measurements to estimate the model parameters and relate them to mechanical properties. If the results obtained with the idealized model lead to some correlation, we may have greater incentive to investigate experimentally the thermal characteristic of particulate systems under vacuum conditions.

### Mathematical Model

In this section we derive an equation that predicts the thermal conductivity of powders, and we compare it with the available experimental data.

In the theory of electrical contacts (Ref. 17), when two plane surfaces make contact forming a disk of radius (r), the total constriction resistance ( $\Omega_c$ ) is given by

$$\Omega_c = \frac{1}{2rK_s}, \quad (1)$$

where  $K_s$  is the material conductivity. This equation can be derived by solving Laplace's equation for two semi-infinite media making contact in a circular area. The equation can be applied to contacting bodies of finite size if the contact area is small in comparison to the body cross-sectional area. To calculate thermal conductivity from the above equation, we assume that for contacting spheres of radius (R) the resistance to heat flow is only due to constriction resistance. The thermal conductivity is then calculated by

$$K = \frac{L}{\Omega_c A},$$

where (L) is the distance between contacts and (A) is the cross-sectional area of the unit cell occupied by a sphere in a cubic lattice. Substituting  $4R^2$  for A,  $2R$  for L, and Eq. (1) for  $\Omega_c$ , we obtain for the conductivity

$$K = \frac{r}{R} K_s. \quad (2)$$

To evaluate the  $r/R$  ratio, we use the expressions derived by Hertz for the radius of contact  $r$ , between two elastic spheres,

$$r = \left( \frac{3}{4} \frac{F(1 - \nu^2)R}{E} \right)^{\frac{1}{3}}, \quad (3)$$

where  $F$  is the compression force, and  $\nu$  and  $E$  are Poisson's ratio and Young's modulus, respectively. If the compressive force is due to the weight of  $n$  spheres above the contact, then

$$F = n\rho \frac{4}{3} \pi R^3 g, \quad (4)$$

where  $g$  is the gravitational constant and  $\rho$  is the density of the material.

Substituting Eq. (4) into Eq. (3), we obtain

$$\frac{r}{R} = \left( \frac{\pi \rho g (1 - \nu^2) R}{E} \right)^{\frac{1}{3}} n^{\frac{1}{3}} . \quad (5)$$

By expressing the ratio in terms of the depth  $z$ , where  $z = 2Rn$ , we obtain

$$\frac{r}{R} = \left( \frac{\pi \rho g (1 - \nu^2)}{2E} \right)^{\frac{1}{3}} z^{\frac{1}{3}} .$$

The above equation indicates that the contact area, and hence thermal conductivity, increases with depth beneath the surface. Another initially surprising result is that the thermal conductivity at a given depth is independent of particle size. The decrease in conductivity due to the greater number of contact resistances per unit length for decreasing particle size is offset by the increased conductivity due to an increase in the ratio of contact radius to particle diameter. The dependence on the gravitational constant indicates that an identical bed of particles on the moon would exhibit a lower thermal conductivity than on earth.

Substituting Eq. (5) for the ratio  $(r/R)$  in Eq. (2), we obtain

$$K(n) = K_s \left( \frac{\pi \rho g (1 - \nu^2) R}{E} \right)^{\frac{1}{3}} n^{\frac{1}{3}}$$

or

$$K(n) = K_s \alpha n^{\frac{1}{3}} ,$$

where  $n$  is the number of spheres supported in the column above the contact, and  $\alpha$  is a material constant as given by the term in parentheses. The above equation gives the thermal conductivity as a function of number of particles. In order to determine the effective conductivity for a given thickness of the particle bed we must series sum the resistances of all particles in contact, or combine the conductivities as given by

$$\bar{K} = \frac{2Rn}{\sum_{n'=1}^n \frac{2R}{K_s \alpha (n')^{\frac{1}{3}}}}$$

Simplifying the above we obtain

$$\bar{K} = \frac{K_s \alpha n}{\sum_{n'=1}^n (n')^{-\frac{1}{3}}}$$

In order to evaluate numerically more readily the above equation, we replace the summation by an integration, and obtain the approximation

$$\bar{K} \approx \frac{K_s \alpha n}{\int_0^n (n')^{-\frac{1}{3}} dn'} \quad (6)$$

Integrating and simplifying the above equation yields

$$\bar{K} \approx \frac{2}{3} K_s \alpha n^{\frac{1}{3}}$$

By substituting the depth  $z = 2Rn$  in the above equation, we obtain the effective conductivity for a particle bed of thickness  $(z)$

$$\bar{K} \approx 0.528 \left( \frac{\pi \rho g (1 - v^2)}{E} \right)^{\frac{1}{3}} K_s z^{\frac{1}{3}} \quad (7)$$

The above derivation of the effective solid conductivity of a bed of particles is applicable for a cubic array of spheres that has a porosity of 48 percent. For more random packings, the porosity could be appreciably different. A more porous packing should make the effective solid conductivity lower than that given by Eq. (7). This can be viewed as due to two factors, the decreased

number of conduction paths per unit area normal to heat flow and the more tortuous conduction paths. To extend the range of validity of Eq. (7) to the more porous case, we assume that the effective conductivity varies linearly with porosity and approaches zero at 100 percent porosity. The equation resulting from this assumption is

$$\bar{K} = (1 - p)K_s \left( \frac{\pi \rho g (1 - v^2)}{E} \right)^{\frac{1}{3}} z^{\frac{1}{3}} . \quad (8)$$

### Radiative Component

Because the solid conductivity for powdered materials in a vacuum is quite small, the relative contribution of radiation to heat transport may be quite significant even at the modest temperature ranges (100°K-400°K) of interest to this study.

A general treatment of radiative transport in powders is extremely difficult because of the number and nature of the mechanisms involved. Processes of absorption, emission, scattering, and transmission of electromagnetic radiation are involved. These processes are characterized by parameters that are dependent upon the geometry and material properties of the medium. The dominant mechanisms of radiative transport may be significantly different for powders of differing physical properties. In addition, since radiation occurs over a range of wavelengths and the characterizing parameters are generally wavelength dependent, the dominant mechanisms of transport may significantly change with the temperature of the media. The utility of a generalized treatment would very much depend on a detailed knowledge of these parameters.

The highly speculative nature of the lunar surface material makes it unwarranted to consider the case of radiative transport to the degree of sophistication that has appeared in the recent literature (Ref. 18). Instead, two approximate methods will be considered for evaluating the radiative transport. The first can be considered an idealized discrete model where only radiation between surfaces is considered. Three such models are considered. The second approach is to homogenize the particulate medium and thus allow a formulation of the energy transport processes by differential equations. A discussion of the two methods follows.

## Discrete Model for Radiative Transport

Layered Slab Model — A powder medium is a rather complex arrangement of oddly shaped grains and interstices. To obtain a model that can be treated analytically, a rather drastic modification of this picture seems to be required. The first model that will be considered is one suggested by Wesselinck (Ref. 19). The lunar surface material is considered stratified into parallel slabs of uniform thickness as shown in Fig. 1.

In the Wesselinck model,  $s$  corresponds to the sum of the average size of grain and interstices. The temperature difference between the faces of a slab of solid material is considered negligible because of the relatively high conductivity. The rate of heat transfer between adjacent slabs is given by

$$q = \frac{\epsilon\sigma}{2 - \epsilon} (T_1^4 - T_2^4),$$

where the factor  $\epsilon/(2 - \epsilon)$  is obtained by considering multiple reflections between the slabs and using Kirchoff's law. For small distances between slabs, the above equation can be approximated by using a derivative:

$$q \approx \frac{\epsilon\sigma}{(2 - \epsilon)} \frac{\partial T^4}{\partial x} s = \frac{4\epsilon\sigma T^3}{2 - \epsilon} \frac{\partial T}{\partial x} s,$$

where  $\partial T/\partial x$  refers to the average gradient. The radiative conductivity is then

$$k_{\text{rad}} = \frac{4\epsilon\sigma T^3}{2 - \epsilon}.$$

To obtain an expression in terms of particle size and porosity we use the relation

$$(1 - p) = \frac{d}{s},$$

and obtain for the conductivity

$$k_{\text{rad}} = \frac{4\sigma\epsilon d T^3}{(2 - \epsilon)(1 - p)}. \quad (9)$$

Cubic Particle Model — Other models for radiative conductivity, with assumptions in the spirit of that used above, have been employed in other studies. Laubitz (Ref. 20) assumes the particles as cubes randomly scattered in cubical volumes but with the faces of two cubes remaining parallel. Based on this model he derives the following equation:

$$k_{\text{rad}} = \frac{4\sigma\epsilon dT^3}{1-p} \left[ 1 - (1-p)^{2/3} + (1-p)^{4/3} \right]. \quad (10)$$

Spherical Particle Model — Schotte (Ref. 21) obtains an equation for the radiative conductivity by considering radiation between the voids of packed spheres and radiation from the particle in series with conduction through the particle. The radiative conductivity is given by

$$k_{\text{rad}} = \frac{1-p}{\frac{1}{k_s} + \frac{1}{k_{ro}}} + pk_{ro}, \quad (11)$$

where  $k_{ro} = 4\sigma\epsilon dT^3$ , and  $k_s$  is the conductivity of the solid material.

The three expressions for the radiative conductivity have similar characteristics. They all display a linear variation of conductivity with particle size, a cubic dependence on temperature, and an increasing conductivity with increasing porosity. The major difference is the manner in which the conductivity varies with porosity. Figure 3 illustrates the dependence of radiative conductivity on porosity for the three equations. Equation (11) exhibits a linear variation of conductivity with porosity, the slope of the curve depending on the ratio of  $k_{ro}$  to the solid conductivity  $k_s$ . Equations (9) and (10) display asymptotic behavior at unit porosity. From physical considerations it is apparent that the radiative conductivity should become infinitely large as the porosity approaches unity and that it approaches zero as the porosity approaches zero. It is therefore concluded that Eqs. (9) and (10) give a more realistic picture of the physical situation at high porosities than Eq. (11). A plot of radiative conductivity versus porosity is shown in Fig. 4 for different particle sizes and temperatures.

## Total Thermal Conductivity of Powders in a Vacuum

To obtain the total thermal conductivity of powders in a vacuum, we must add the conductive and radiative components represented by Eqs. (8) and (9), respectively. Total thermal conductivity is then given by

$$k = \bar{K} + K_{\text{rad}} = (1 - p)K_s \left( \frac{\pi \rho g (1 - \nu^2)}{E} \right)^{\frac{1}{3}} z^{\frac{1}{3}} + \frac{4\sigma \epsilon d T^3}{(2 - \epsilon)(1 - p)} \cdot \quad (12)$$

The total thermal conductivity as determined by the above equation is a function of solid conductivity ( $K_s$ ), depth ( $z$ ), particle size ( $d$ ), porosity ( $p$ ), emissivity ( $\epsilon$ ), and temperature ( $T$ ). Other parameters that also affect thermal conductivity are Poisson's ratio ( $\nu$ ), modulus of elasticity ( $E$ ), density ( $\rho$ ), and the gravitational constant ( $g$ ).

In order to obtain numerical values of total thermal conductivity, the material properties of basalt were assumed as given in Table II. Plots of total thermal conductivity as a function of the various parameters are given in Figs. 5, 6, and 7.

TABLE II

### Material Properties of Basalt

<u>Property</u>	<u>Symbol</u>	<u>Value</u>
Density	$\rho$	2.9 gms/cm <sup>3</sup>
Poisson's Ratio	$\nu$	0.04
Modulus of Elasticity	$E$	$3.5 \times 10^{12}$ dynes/cm <sup>2</sup>
Thermal Conductivity	$K_s$	0.0045 cal/cm <sup>2</sup> °K sec/cm
Specific Heat	$c$	0.21 cal/gm °K
Emissivity	$\epsilon$	1.0



In Fig. 5a, where the effect of porosity on thermal conductivity at  $100^{\circ}\text{K}$  is shown, we notice that for a particle size of  $10\mu$ , the thermal conductivity decreases with porosity. For this small a particle, the radiative contribution is negligible at  $100^{\circ}\text{K}$ ; hence, only the conductivity due to solid conduction is present. As indicated by Eq. (8), the solid conduction component is independent of particle size. This is a direct consequence of the approximation of replacing the summation by an integration to obtain Eq. (5). The integral expression was compared with the summation, and they were found to agree with an accuracy error less 10 percent for more than 10 particles in series. We can therefore regard the thermal conductivity curve for  $10\mu$  at  $100^{\circ}\text{K}$  as being the lower limit of thermal conductivities of powdered basalt for the model derived and the conditions described (i.e., 1 cm depth and in a lunar gravitational field). Figure 5b shows a similar variation of thermal conductivity with porosity at  $250^{\circ}\text{K}$ . The values of conductivity are higher than in the previous curve because of the greater contribution of radiation at the elevated temperature. Figure 5c, which shows the thermal conductivity variation with porosity at  $400^{\circ}\text{K}$ , displays a minimum in the curve for the  $10\mu$  particle size occurring at a porosity of about 72 percent. The minimum is a consequence of the total conductivity being the sum of two components, the solid conductivity (which is a decreasing function of porosity) and the radiative conductivity (which increases with porosity).

Figures 6a and 6b show the variation of thermal conductivity with particle sizes at temperatures of  $100^{\circ}\text{K}$  and  $250^{\circ}\text{K}$ . At the low temperature of  $100^{\circ}\text{K}$ , the variation of thermal conductivity with particle size is quite small for particle sizes less than  $400\mu$ . This is due to the relatively small radiative contribution to the total conductivity at this low temperature. As the radiative contribution becomes more significant with increasing particle size, the thermal conductivity of the 80 percent porosity basalt powder becomes greater than the 60 percent porosity material. At  $250^{\circ}\text{K}$  the thermal conductivity is quite sensitive to particle size. At this temperature the 60 percent and 80 percent porosity powders have the same thermal conductivities for  $50\mu$  particles, however, at  $100^{\circ}\text{K}$  these powders have the same thermal conductivities for  $700\mu$  particles.

Figures 7a and 7b show the variation of thermal conductivity with temperature for different particle sizes and porosities of 60 percent and 80 percent. The variation of conductivity with temperature becomes much more significant for the larger particles because of the increased importance of the radiative contribution. Higher porosity materials show a more significant increase in conductivity with temperature, due to the increased importance of radiation.

### Comparison with Experimental Data

To compare our analytical model predictions of thermal conductivity with experimental data, it is necessary that these data be obtained in terms of relevant parameters on which the analytical expressions are based. Unfortunately, the available data reported in the literature (Refs. 25 through 30) do not meet this condition; the results of Bernett et al. (Ref. 26) are perhaps the most amenable for comparison.

There are two serious difficulties in using the Bernett data. Our model requires knowledge of the contact pressure between particles in order to calculate the contact area. The measurements of conductivity, however, were made by measuring heat flow and temperatures in a horizontal plane in which the force between the particles is determined by forces exerted by the containing walls. Differential thermal expansions between the basalt powder and the container could cause the interparticle force to vary as the test temperatures varied. Regardless of whether the force varied with experimental conditions, the determination of the interparticle force cannot be readily made. If, however, the measurements were made in a vertical plane with a free upper surface, the known gravitational force would be used to determine contact area.

Another difficulty arises in comparing the temperature dependence of the experimental data with our model predictions. A transient technique was used by Bernett et al. to determine the thermal diffusivity from which the thermal conductivity was calculated. The computational method they used to determine diffusivity from transient temperature measurements assumed a temperature-independent thermal conductivity, whereas our analytical expressions are based on a temperature dependent model. The thermal conductivity determined by their method would represent a sort of effective value over the range of temperatures of the experiment. A method of reducing the test data in order to determine more effectively the temperature dependence of thermal conductivity is presented in Ref. 111.

The data of Bernett et al. (Ref. 26) allow some conclusions to be made in a qualitative manner concerning the effects of parameters on thermal conductivity. The significant conclusions reached by the investigators were:

- a) decreasing the temperature resulted in a decrease in thermal conductivity;
- b) an increase in thermal conductivity resulted when the porosity of the test sample was decreased;
- c) the composition of the crushed material has only a minor effect on its thermal conductivity.

Conclusions a) and b) are in agreement with our model, and conclusion c) is based on the results for only two different rock materials.

The range of values of the measured thermal conductivities was from 4 to  $12 \times 10^{-6}$  cal/cm °K sec. This is in the range of values that are calculated from our model for the particle sizes (3-300 $\mu$ ) and temperatures (200-400°K) that were used.

## EFFECTIVE THERMAL CONDUCTIVITY OF VESICULAR MEDIA

In this section we describe the methods of predicting the thermal conductivity of vesicular materials, and apply them to calculating the conductivity of porous rock as a function of porosity. Comparison of the results between the available models and experimental results are made.

A vesicular solid can be considered basically as a two phase material consisting of a solid phase and a void or gas phase. It is likely that vesicular material close to the lunar surface would be outgassed either because of the continuity of the void phase or the diffusion of gas through the solid material over very long periods of time. We will assume therefore that the gas concentration in the void phase is not sufficient to contribute significantly to the transport of heat through the material. The two principal modes of heat conduction would then be solid conduction and radiation across the pores.

### Solid Conductive Component

The solid thermal conductivity of a rock will depend upon many factors, among these are its mineral composition, crystal size, shape and orientation and degree of consolidation or continuity. The term "degree of consolidation" refers to the freedom of the solid phase from microcracks and fractures. Although these cracks may be quite small and contribute negligibly to the over-all porosity, they could appreciably affect the thermal conductivity as will be shown later.

A summary of data on the thermal conductivity of solid rocks is given by Wechsler and Glaser (Ref. 29). As noted by these authors, the variation of data for any particular rock type is of the same order of magnitude as the variation between rock types. Whether the variations are due to differences in rock samples or differences incurred by experimental method cannot be assessed due to lack of sufficient information. A thermal conductivity range of from 2 to  $9 \times 10^{-3}$  cal/cm-°K-sec for rock types of lunar interest is shown. For all numerical calculations, an average thermal conductivity of  $5 \times 10^{-3}$  cal/cm-°K-sec is assumed. The uncertainty in rock composition could therefore affect the calculated values of thermal conductivity by a factor of two in either direction if the solid conduction is highly dominant in determining the total conductivity.

## Radiative Component

The effective thermal conductivity due to radiation across the pores will depend on the size and shape of the pore and its emissivity. Loeb (Ref. 31) derived expressions for the effective pore conductivity for various geometries by assuming unidimensional heat flow only. His equation is

$$k_p = 4\nu\ell\epsilon\sigma T^3,$$

where

$\ell$  = largest dimension of pore in the direction of heat flow,

$\nu = 2/3$  for spherical pores,

$\nu = \pi/4$  for cylindrical pores, and

$\nu = 1$  for laminar pores and cylindrical pores, with axis parallel to heat flow direction.

The above equation was numerically evaluated for pore sizes up to 1 cm and temperatures up to 400°K. The maximum value of pore conductivity at the extremes of the considered pore size and temperature was  $3.5 \times 10^{-4}$  cal/cm-°K-sec. The ratio of solid to pore conductivity, which plays a large role in the models that will next be discussed, has a minimum value of about 14, and becomes quite large for more realistic values of temperature and pore size.

## Total Thermal Conductivity

Three general approaches can be used to determine the conductivity of a two phase material. The first method is to use a highly idealized geometrical model and determine exactly the conductivity for that model; the second method is to assume a more complex geometrical model and reduce the problem to one of unidimensional conduction by assuming a zero or infinite sidewise conductivity. A third approach that has not been used for obtaining exact solutions for more complex models requires numerical methods that have the disadvantage of being highly specific to the model employed and difficult to generalize. The following sections discuss the various models that have been derived from these first two approaches, insofar as they apply to lunar surface studies. The results are based on the values of solid and pore conductivities given in the previous sections.

## Series Model

The series model can be visualized as applicable to a geometry in which layers of solid and void are arranged normal to the direction of heat flow as shown in Fig. 9. Although this model is physically unrealistic, it is useful for determining the lower limit of thermal conductivity for any two phase mixture. In addition, a porous material of random orientation and pore shape has a certain fraction of its configuration that can be well approximated by the series model. The thermal conductivity of the series model is derived from the weighted harmonic mean of the individual conductivities:

$$\frac{1}{k} = \frac{p}{k_p} + \frac{1-p}{k_s}$$

or

$$\frac{k}{k_s} = \frac{1}{1 + p \left( \frac{k_s}{k_p} - 1 \right)}$$

The latter equation is evaluated for different ratios of solid to porous conductivity as shown in Fig. 10a. As the ratio of conductivities become large, a small increase in porosity is sufficient to decrease substantially the total conductivity. Because the conductivity ratio can be of the order of 100 or greater for our case, it is apparent that if only a small fraction of the vesicular material obeys the series model, the total thermal conductivity can be substantially affected.

## Parallel Model

The parallel model consists of an arrangement of solid and void layers parallel to the direction of heat flow, as shown in Fig. 9. It represents the maximum conductivity that can be obtained for a two phase substance. The total conductivity is simply the weighted arithmetic mean of the individual conductivities

$$k = (1-p)k_s + pk_p$$

The above equation was evaluated for pore conductivities corresponding to the maximum pore size and temperature considered (1 cm and 400°K), and the lower limiting case of zero pore conductivity. As seen from the results shown in Fig. 10b, there is

very little difference between the limiting cases. This is due to the relatively small value of the maximum pore conductivity compared to the solid conductivity. A vesicular rock that obeys the parallel model would therefore not exhibit a strong temperature dependence. This is contrasted to the particulate model in which the thermal conductivities of both phases were of similar magnitudes. The Loeb model, discussed below, is also shown in Fig. 10b for comparison purposes.

#### Maxwell Model

Maxwell (Ref. 32) derived an equation for the conductivity of a random distribution of spheres in a continuous medium (see Fig. 9). The derivation did not take into account mutual interactions between spheres, hence it is strictly valid only for low porosities. A treatment by Runge (Ref. 33) allowed for interactions between equal sized spheres arranged in a cubic array. It was found, however, that for the largest porosity possible (52 percent) the difference between the two results is only 2 percent. We therefore consider the Maxwell equation to be valid even up to the maximum porosity. The Maxwell equation can be written as

$$\frac{k}{k_s} = \frac{1 - 2p \frac{\frac{k_s}{k_p} - 1}{2\frac{k_s}{k_p} + 1}}{1 + p \frac{\frac{k_s}{k_p} - 1}{2\frac{k_s}{k_p} + 1}}$$

This equation was evaluated for the upper and lower limits of the thermal conductivity ratio, and the results are shown in Fig. 10c. The results again show little difference for the extremes in pore thermal conductivity. Although the model is strictly applicable to porosities less than 52 percent, the calculations were extended to 100 percent porosity for purposes of comparison with other models. A "gray band," delineated by the upper and lower curves in Fig. 10b, is shown in Figs. 10c, d, and e in order to make a visual comparison of the models.

## Modified Maxwell Model

The modified Maxwell method refers to a random arrangement of spherical pores of two different pore sizes as shown in Fig. 9. The thermal conductivity of this model was calculated by using the Maxwell equation to determine the thermal conductivity of a porous matrix consisting of the small diameter pores. The calculated value of thermal conductivity was then used in the Maxwell equation; it replaced the solid conductivity term used to determine the conductivity of the two-pore size material. In this manner the porosity limit could be extended to greater values. Figure 10d shows the results of these calculations for small pore size porosities of 20 and 47 percent. These results do not differ significantly from the single pore size results, and therefore lend support to the extrapolation of the unmodified Maxwell model to the physically unrealistic porosity region.

## Russell Model

Russell (Ref. 34) derived an expression for the thermal conductivity of a porous material consisting of regularly spaced, cubic pores by assuming unidimensional heat flow. His equation is

$$\frac{k}{k_s} = \frac{p^{\frac{2}{3}} + \frac{k_s}{k_p} (1 - p^{\frac{2}{3}})}{p^{\frac{2}{3}} - p + \frac{k_s}{k_p} (1 - p^{\frac{2}{3}} + p)}$$

This equation can only be valid if the solid phase is continuous. The above equation was evaluated for the upper and lower limits of pore conductivity as shown in Fig. 10b. As in the Maxwell and Parallel models, there is little difference between the conductivities for the limits considered.

## Loeb Model

Loeb (Ref. 31) derived an equation for a random arrangement of pores. His equation was derived by assuming unidimensional heat flow:

$$\frac{k}{k_s} = (1 - P_c) + \frac{P_c}{1 + P_L \left( \frac{k_s}{k_p} - 1 \right)},$$



where

$P_C$  = area fraction of pores normal to heat flow, and

$P_L$  = length fraction of pores parallel to heat flow

If we assume that the pore distribution is isotropic, then  $P_L = p^{\frac{1}{3}}$  and  $P_C = p^{\frac{2}{3}}$ . Substituting the above in the Loeb equation results in

$$\frac{k}{k_s} = 1 - p^{\frac{2}{3}} + \frac{p^{\frac{2}{3}}}{1 + p^{\frac{1}{3}} \left( \frac{k_s}{k_p} - 1 \right)} .$$

This equation was evaluated for cubic pores, and the results are shown in Fig. 10b. The results are quite similar to that of the Russell model, Fig. 10e.

#### Other Models

There have been numerous other models that have been proposed to determine the thermal conductivities of heterogeneous materials. However, these models do not appear as useful for our study as those just described. Some of these models depend upon adjustable parameters that can best be determined by fits with experimental data (Ref. 35); others are only valid for limited ranges of porosity (Ref. 36). Reviews of other correlations are given in Refs. 11, 37, and 38.

#### Comparison with Experimental Data

The only data that were found in the literature on the thermal conductivity of vesicular rocks in a vacuum were those of Woodside and Messmer (Ref. 25) and Wechsler et al. (Ref. 29). These data are shown in Fig. 11 in terms of the relative conductivity (ratio of vesicular to solid conductivity). The Loeb model, which in the limiting case  $[(k_s/k_p \rightarrow \infty)]$  gave the lowest value of conductivity to the continuous solid phase models, is also shown. By inspection it is readily seen that the experimental values fall considerably below the predicted results based on a continuous solid phase.

This is not surprising when one considers that the solid phase of an igneous rock material may contain many discontinuities due to microcracks formed during cooling. Sedimentary rocks, such as sandstone, have discontinuities due to only partial consolidation. The degree of consolidation, or the extent of microcracks, can significantly affect the thermal conductivity, particularly under vacuum conditions where the ratio of solid to pore conductivity is large. These discontinuities can best be represented by the series model for thermal conductivity, as seen from Fig. 10a. The thermal conductivity of the series model is quite sensitive to the conductivity ratio and porosity. Because the pore conductivity is a function of the size and geometry of the pores as well as of temperature, it does not appear possible to predict the thermal conductivity of a vesicular material that has solid phase discontinuities without detailed knowledge of its structure.

There are more data available on the thermal conductivity of two phase materials other than rock. Francl and Kingery (Ref. 39) experimentally determined the thermal conductivity of prepared ceramic samples that had well defined systematic variation in pore size and shape. They found that for samples with up to 50 percent porosity, the data could be well represented by the theories of Loeb and Russell, with Loeb's model giving somewhat better results. Continuity of the solid phase was maintained, hence the agreement with test data is not surprising.

### Evaluation of Theoretical Models

The thermal analysis of various vesicular models has led to at least two conclusions that should be stressed because they will have a bearing on the succeeding phases of this report. These conclusions deal with the effects of both temperature and "solid-phase discontinuities" on the thermal conductivity of porous rocks. As will be seen, some of these effects simplify, while others could complicate, the correlation that is being sought.

Regarding the effects of temperature, it is found that the thermal conductivity of fully consolidated porous rocks, unlike that of powders, is nearly independent of temperature. As far as the moon is concerned, this fact implies that in Phase II it will not be necessary to seek an elaborate, temperature dependent solution for the heat conduction of the fully consolidated porous model. Consequently, it will be permissible to describe the lunation temperatures of a "vesicular moon" in terms of the parameter  $\gamma$ . In the case of a "particulate moon," where thermal conductivity is temperature dependent,  $\gamma$  is a meaningless quantity; it should be substituted by nighttime temperatures.  $\gamma$  can also be replaced by nighttime temperatures for a vesicular moon, but more as a convenience than as a necessity.

The second conclusion concerns the limitations of theory in predicting the thermal conductivity of vesicular materials as a function of porosity. It is found that such predictions are possible only if the solid phase is fully continuous and thermally effective. This conclusion is confirmed by theoretical and experimental findings. If the solid phase is partially continuous (due to microcracks, poor welding, etc., as is more often the case), an a priori prediction of thermal conductivity on the basis of porosity alone cannot be made. However, the correlation between thermal conductivity and bearing strength need not be seriously affected by this difficulty, because porosity in this case is an "operator" that may be of little importance after linking thermal conductivity with bearing strength. This concept is discussed in greater detail in Phase III in terms of the actual outcome of the correlation.

With the exception of the series model, all the models analyzed are in substantial agreement with one another, the Loeb model giving somewhat better results.

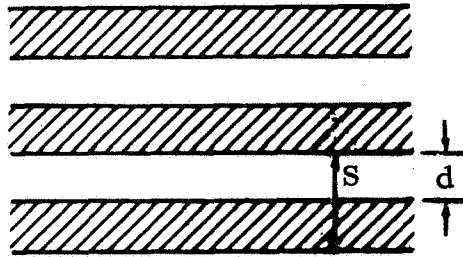


Fig. 1 Particulate Model of Radiative Conduction Component

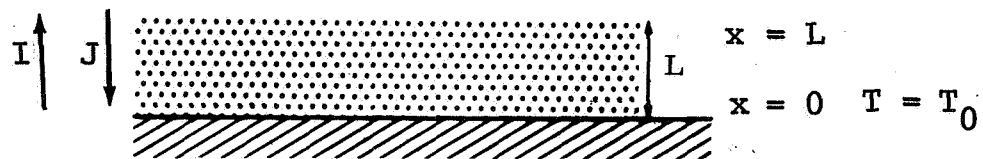


Fig. 2 Suspended Particle Model of Radiative Conduction Component

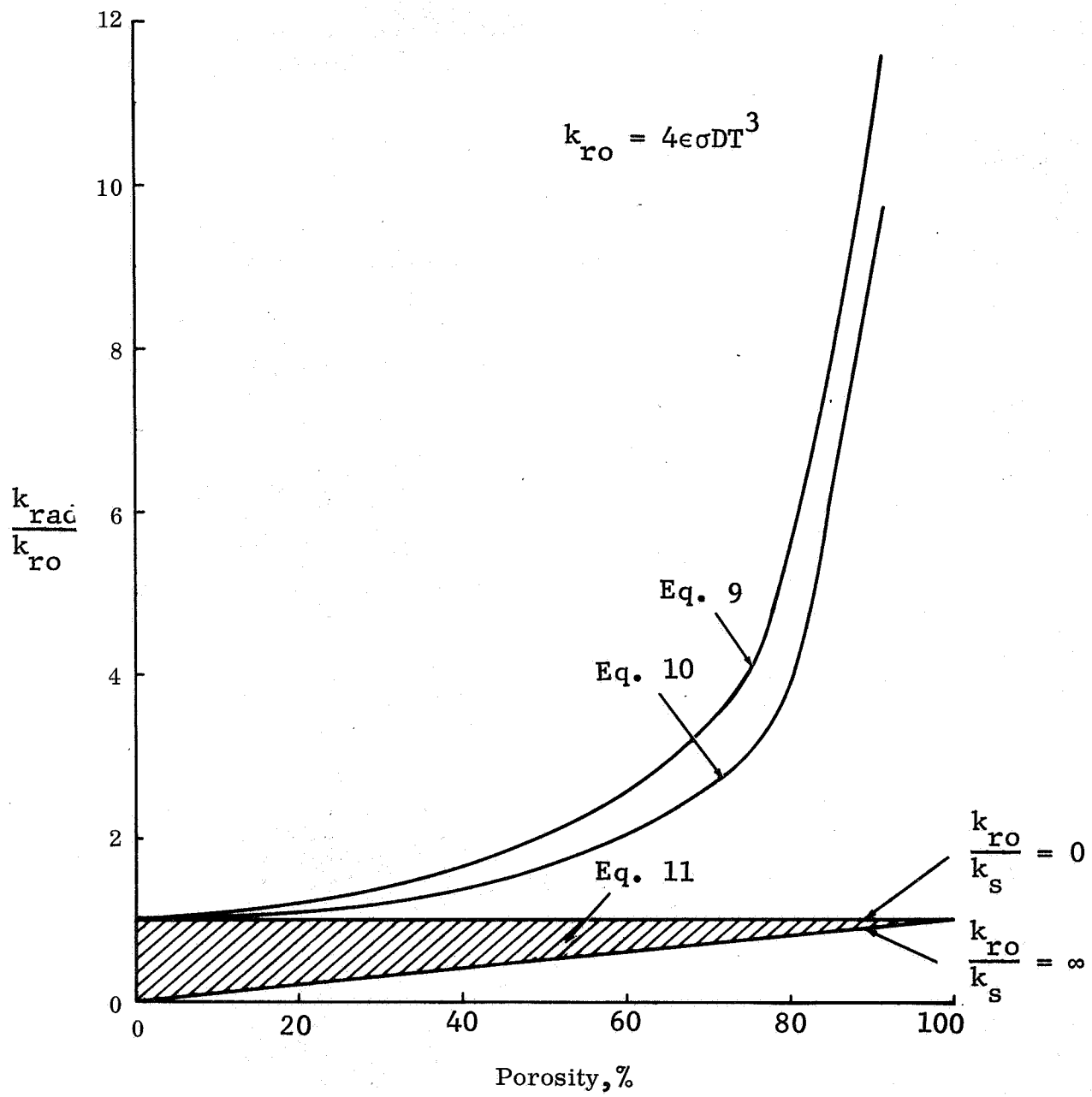


Fig. 3 Radiative Conductivity versus Porosity

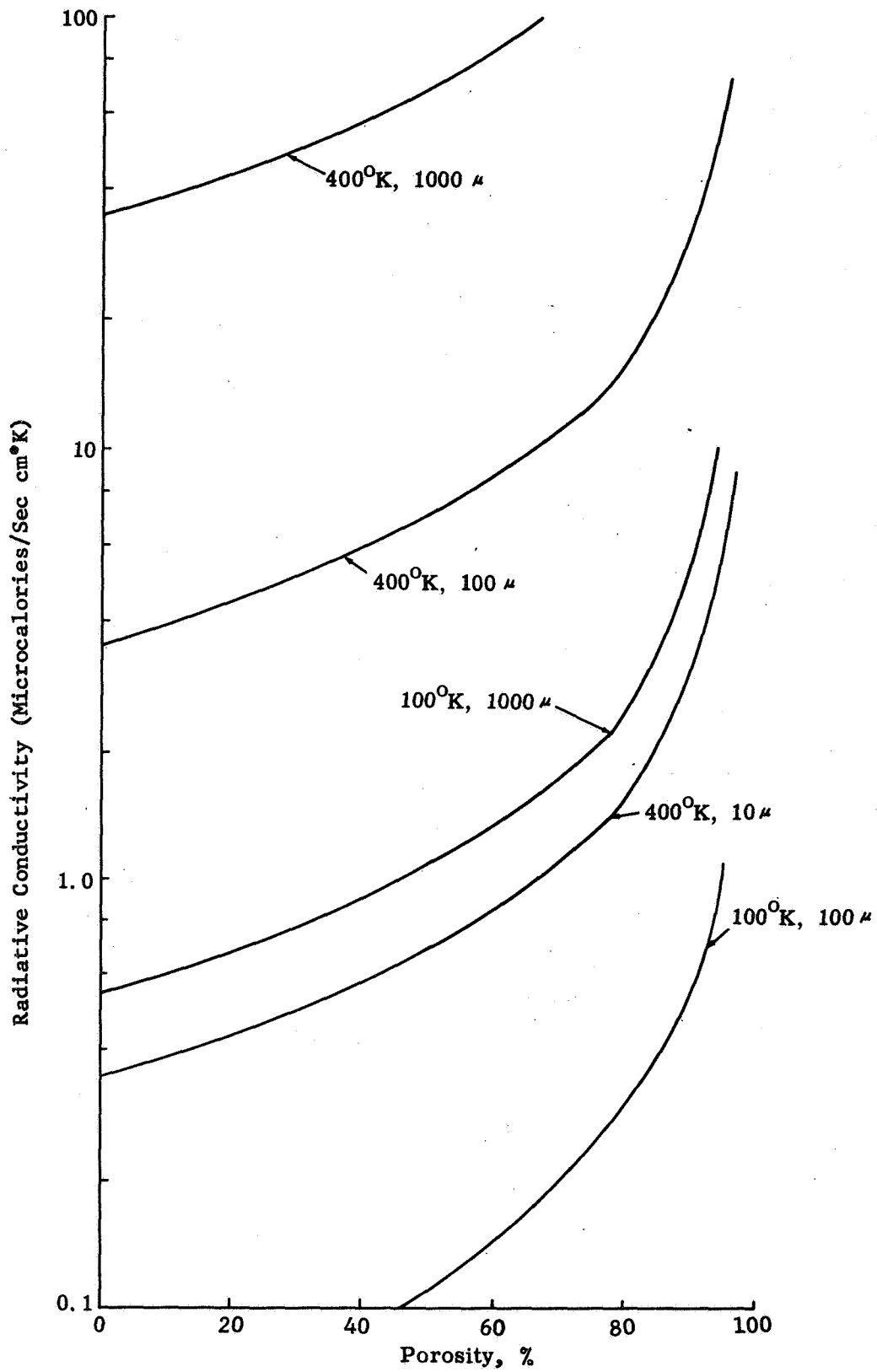
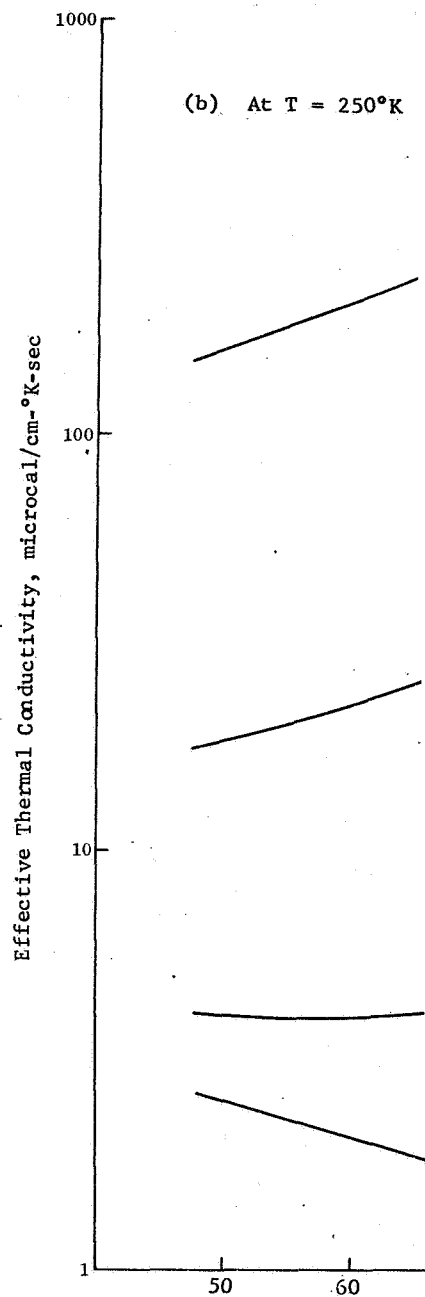
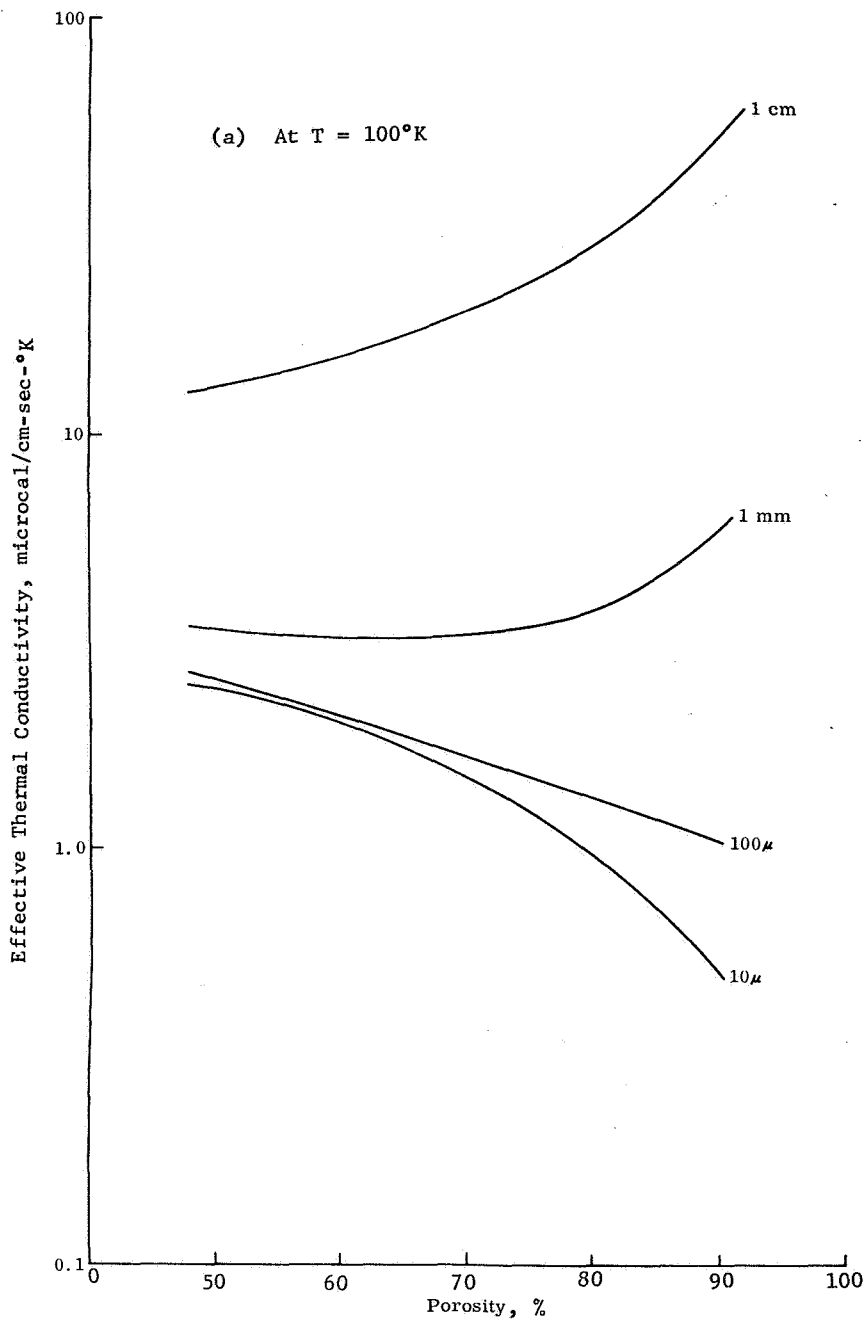


Fig. 4 Radiative Conductivity versus Porosity for Different Particle Sizes and Temperatures



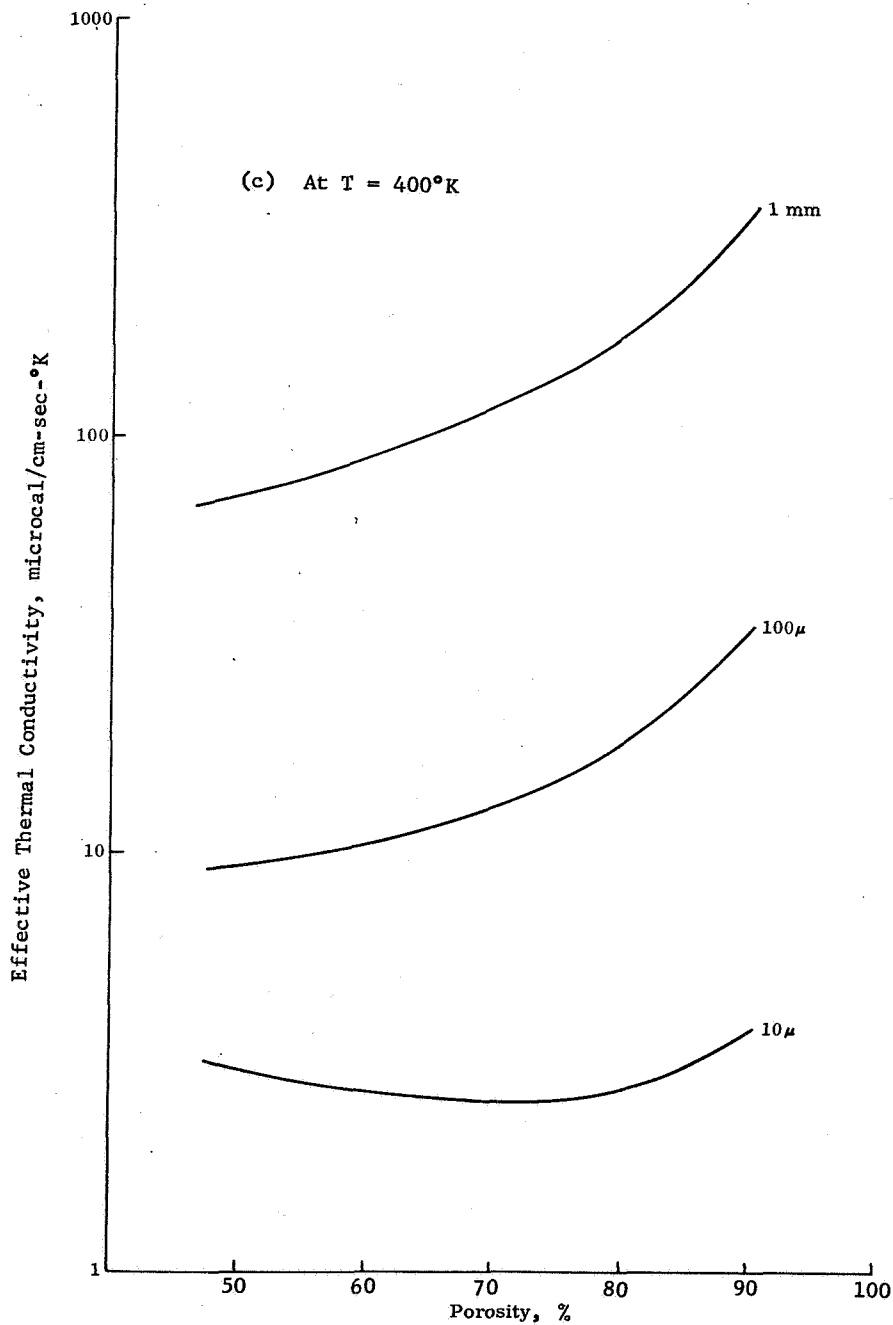
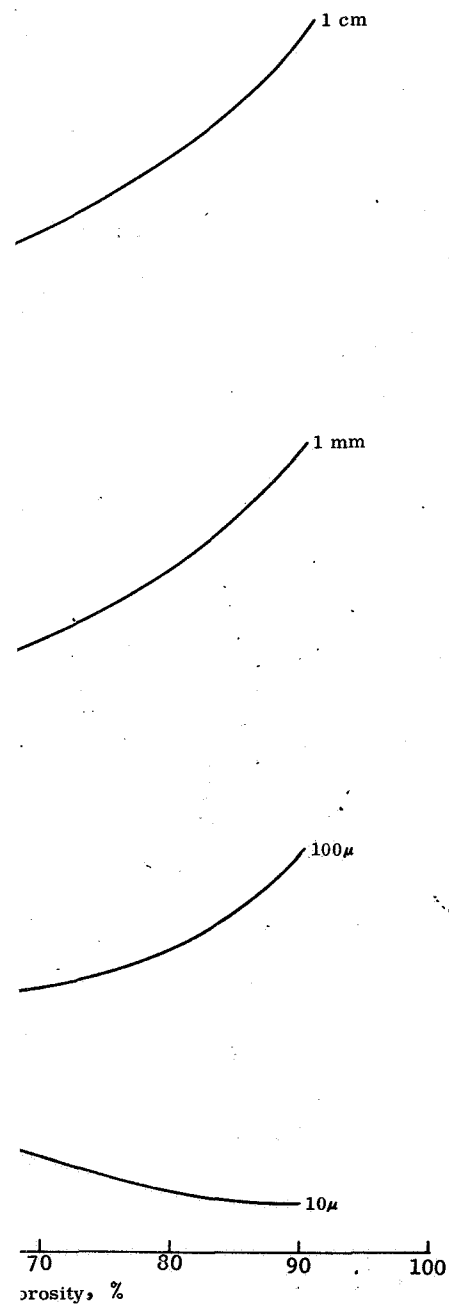


Fig. 5 Effective Thermal Conductivity in Vacuo of Basalt Powder versus Porosity for Different Particle Sizes and Temperatures Note: 1 cm Depth, Lunar Gravity Field



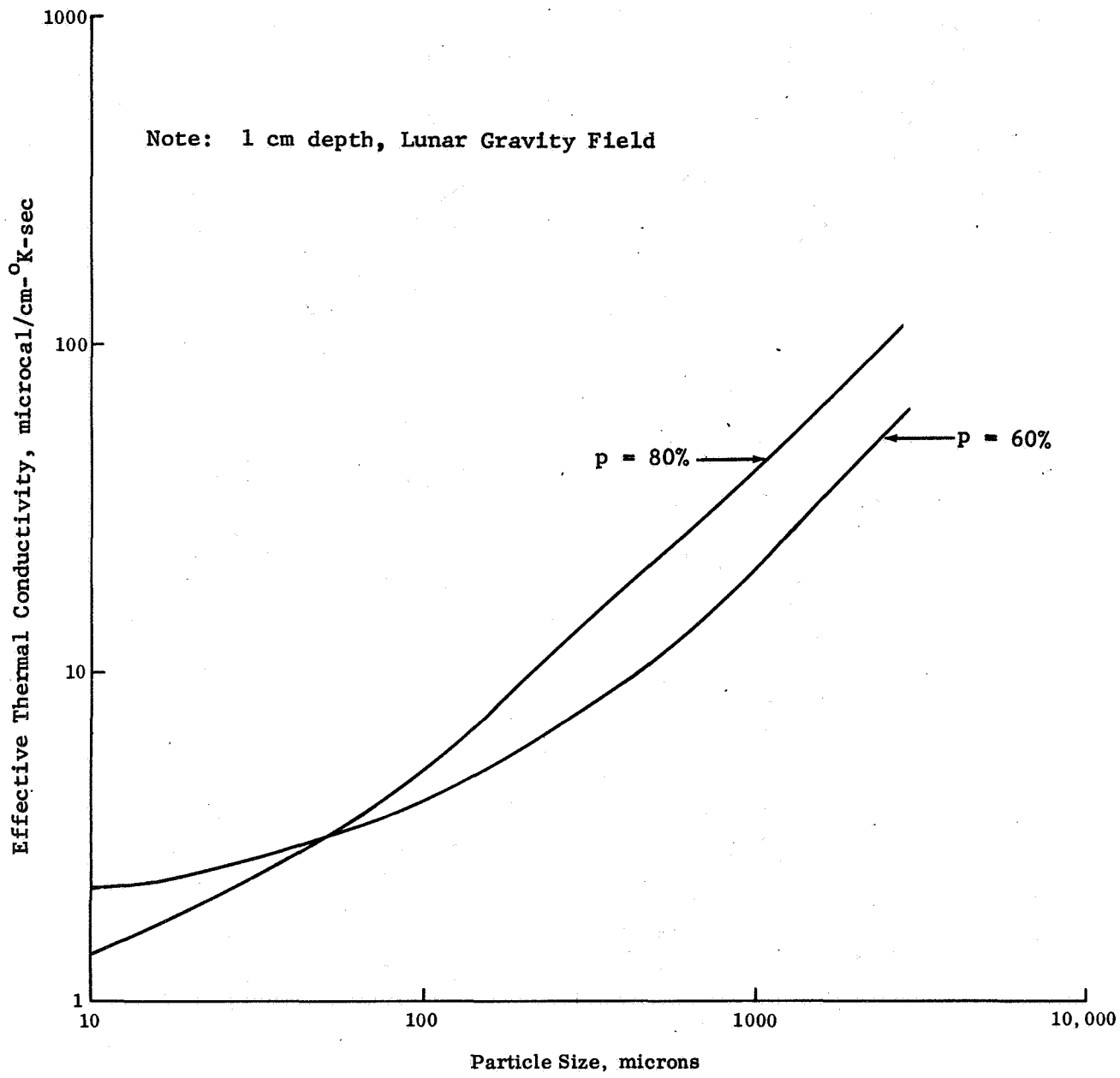
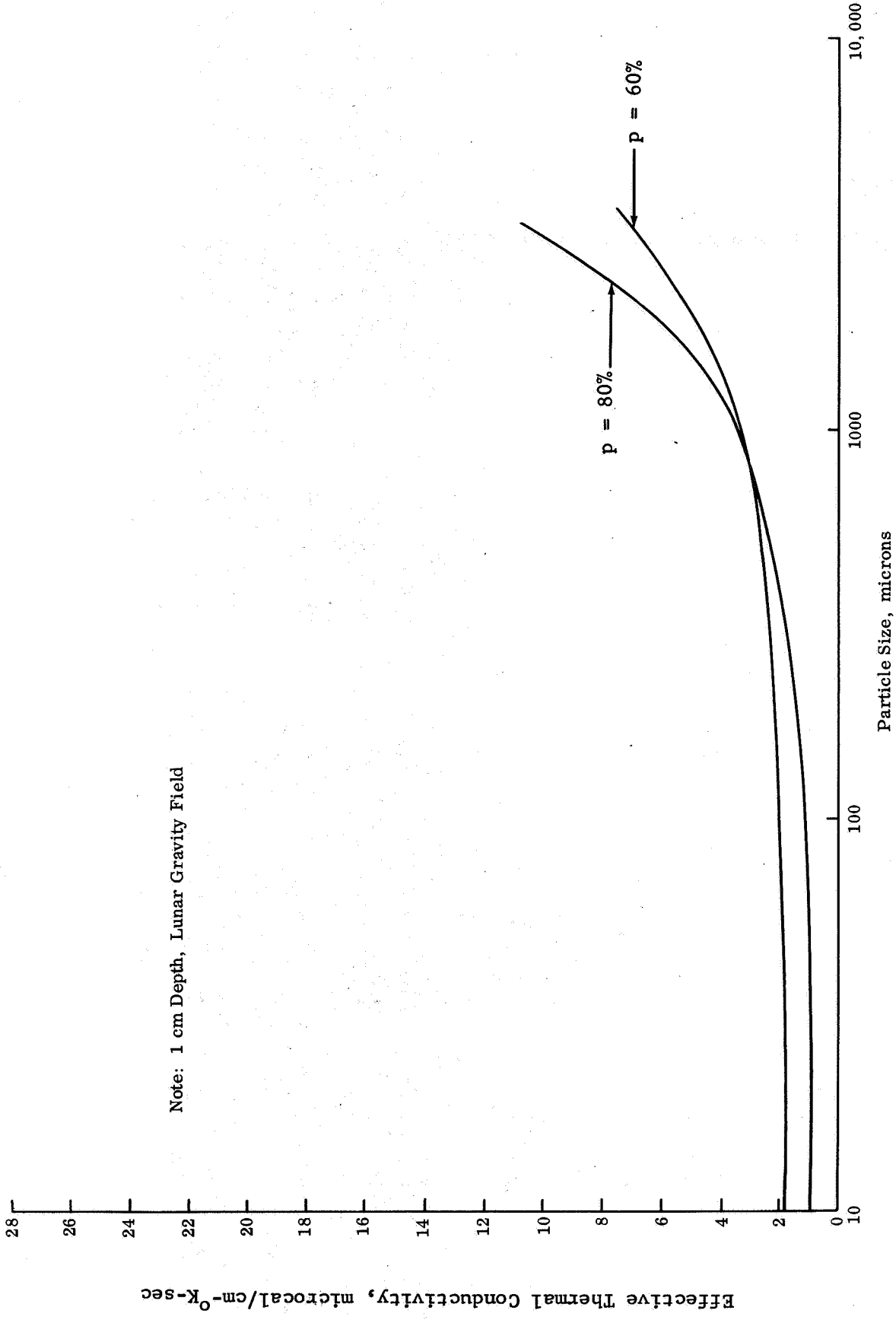


Fig. 6a Effective Theoretical Thermal Conductivity in Vacuo of Basalt Powder versus Particle Size at 60 and 80 Percent Porosity and 250°K



Note: 1 cm Depth, Lunar Gravity Field

Fig. 6b Effective Theoretical Thermal Conductivity in Vacuo of Basalt Powder versus Particle Size at 60 and 80 Percent Porosity and 100°K

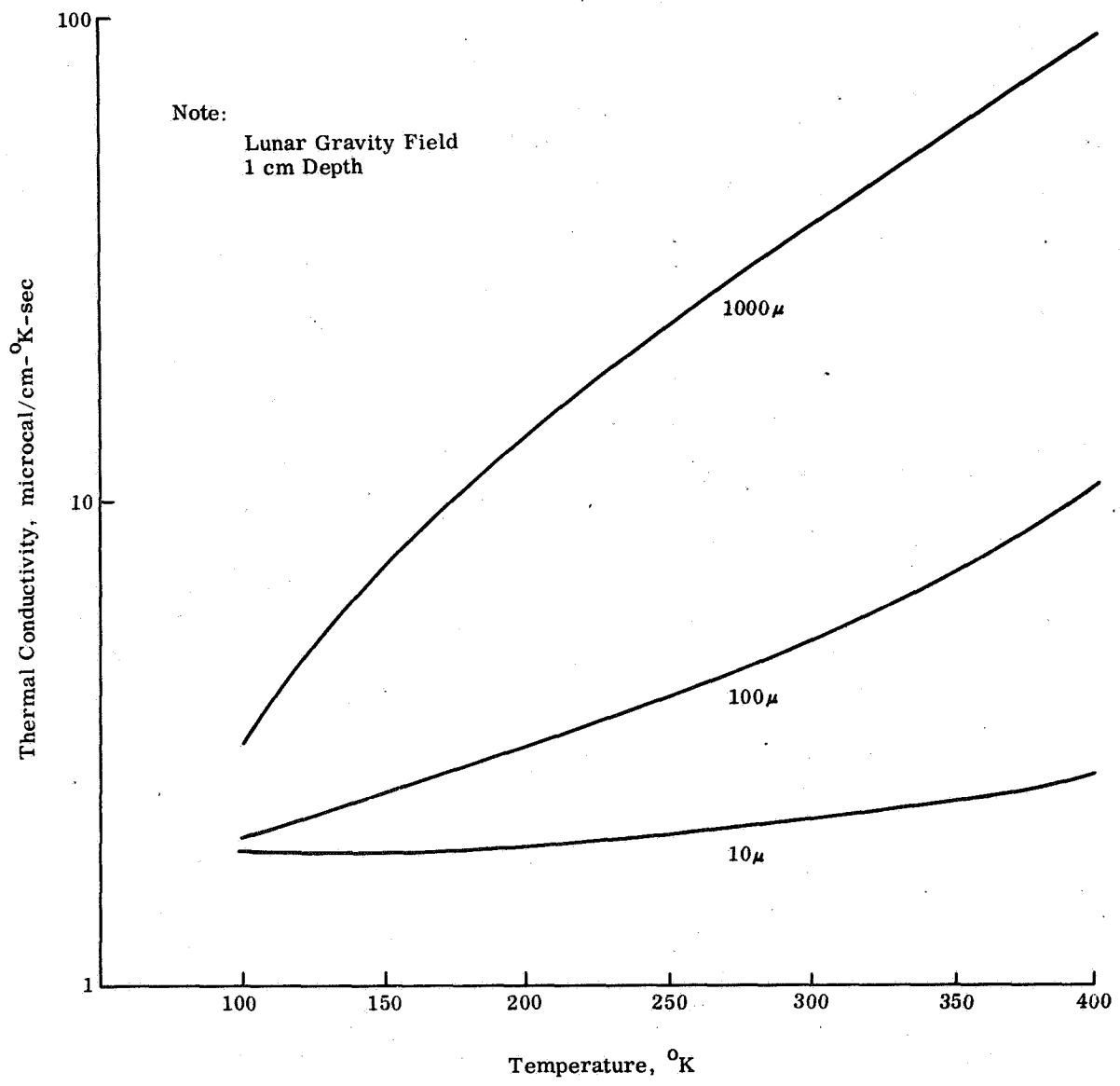


Fig. 7a Total Theoretical Thermal Conductivity in Vacuo of Basalt Powder versus Temperature at Different Particle Sizes and 60 Percent Porosity

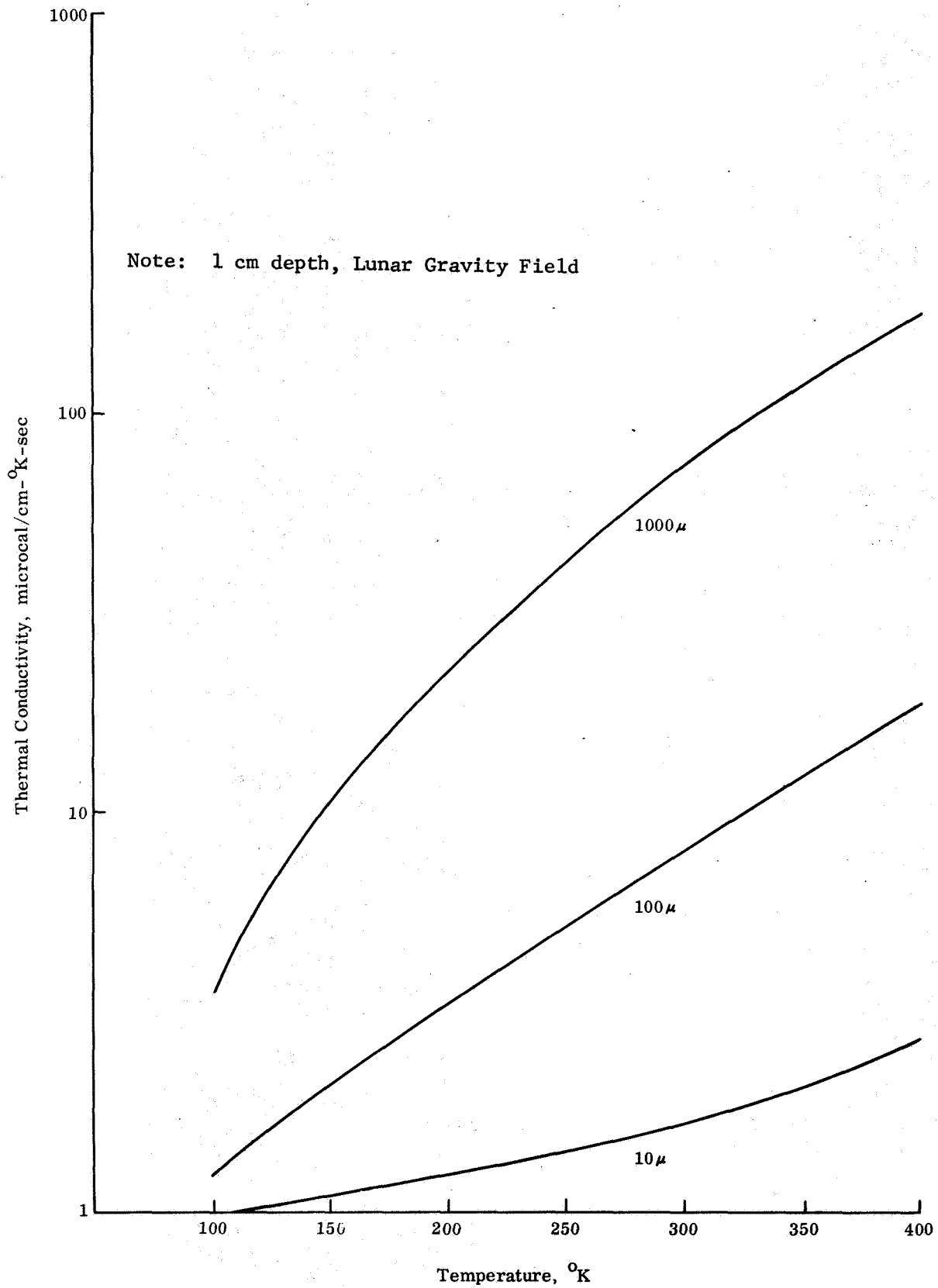


Fig. 7b Total Theoretical Thermal Conductivity in Vacuo of Basalt Powder versus Temperature at Different Particle Sizes and 80 Percent Porosity

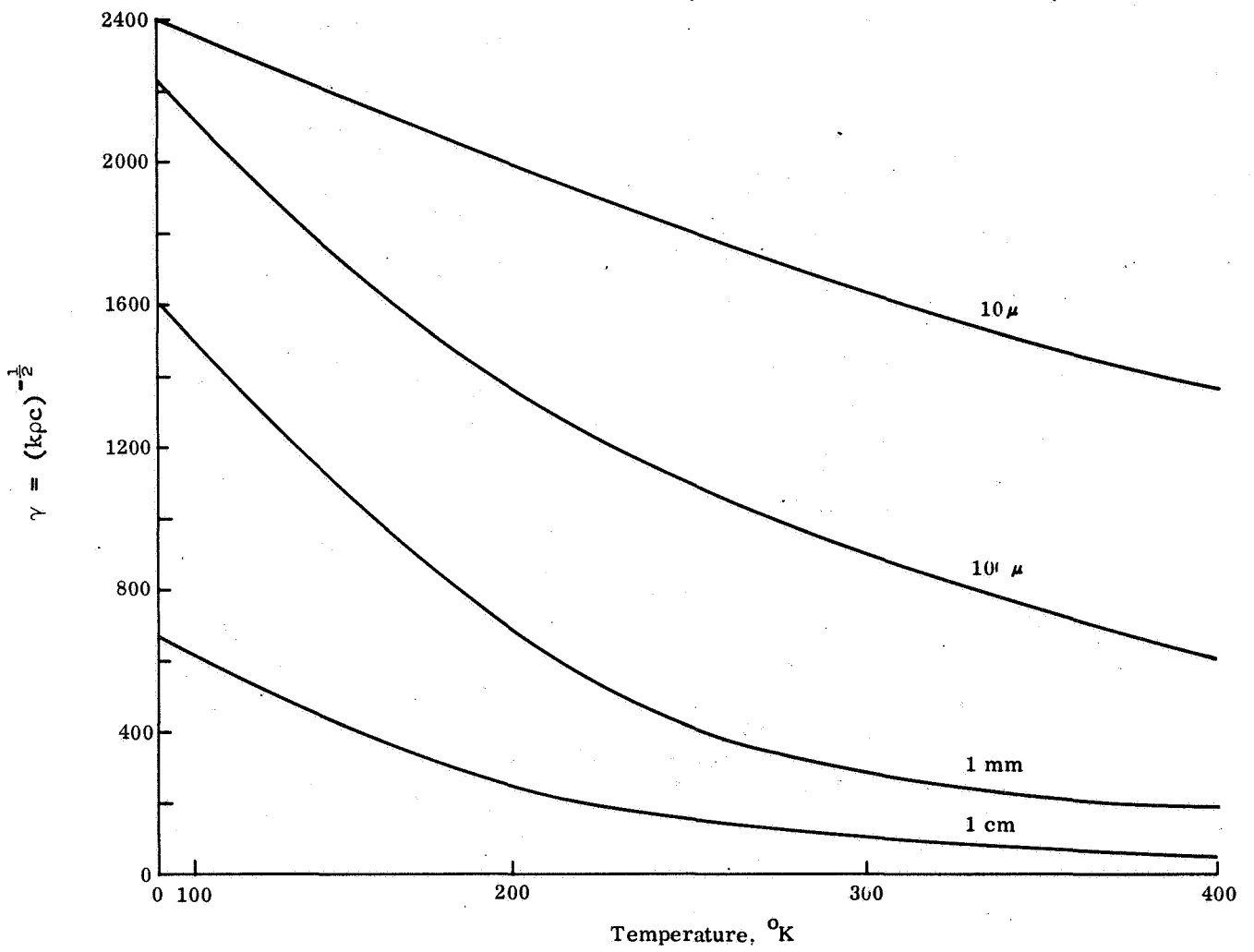
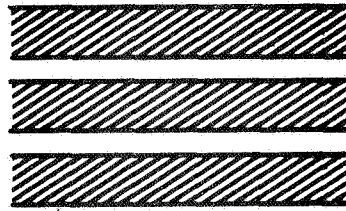
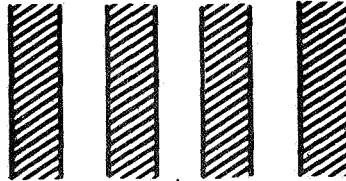


Fig. 8  $\gamma$  versus Temperature for a Temperature-Dependent Model at 70 Percent Porosity

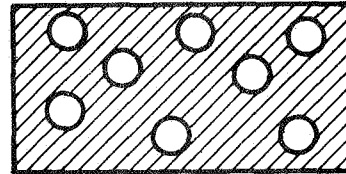
1. Layered Transverse Model  
(in series)



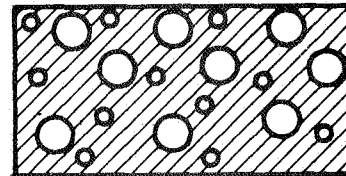
2. Layered Longitudinal Model  
(in parallel)



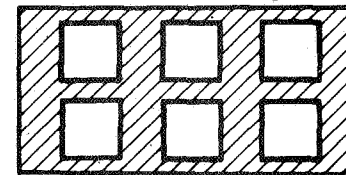
3. Maxwell Model  
(Random isolated uniform pores)



4. Modified Maxwell Model  
(Random isolated nonuniform pores)



5. Russell Model  
(cubic, ordered pores)



6. Loeb Model  
(cubic random pores)

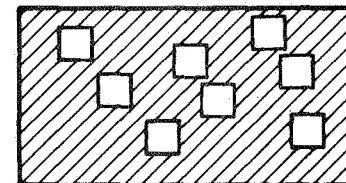


Fig. 9 Spectrum of Vesicular Thermal Models

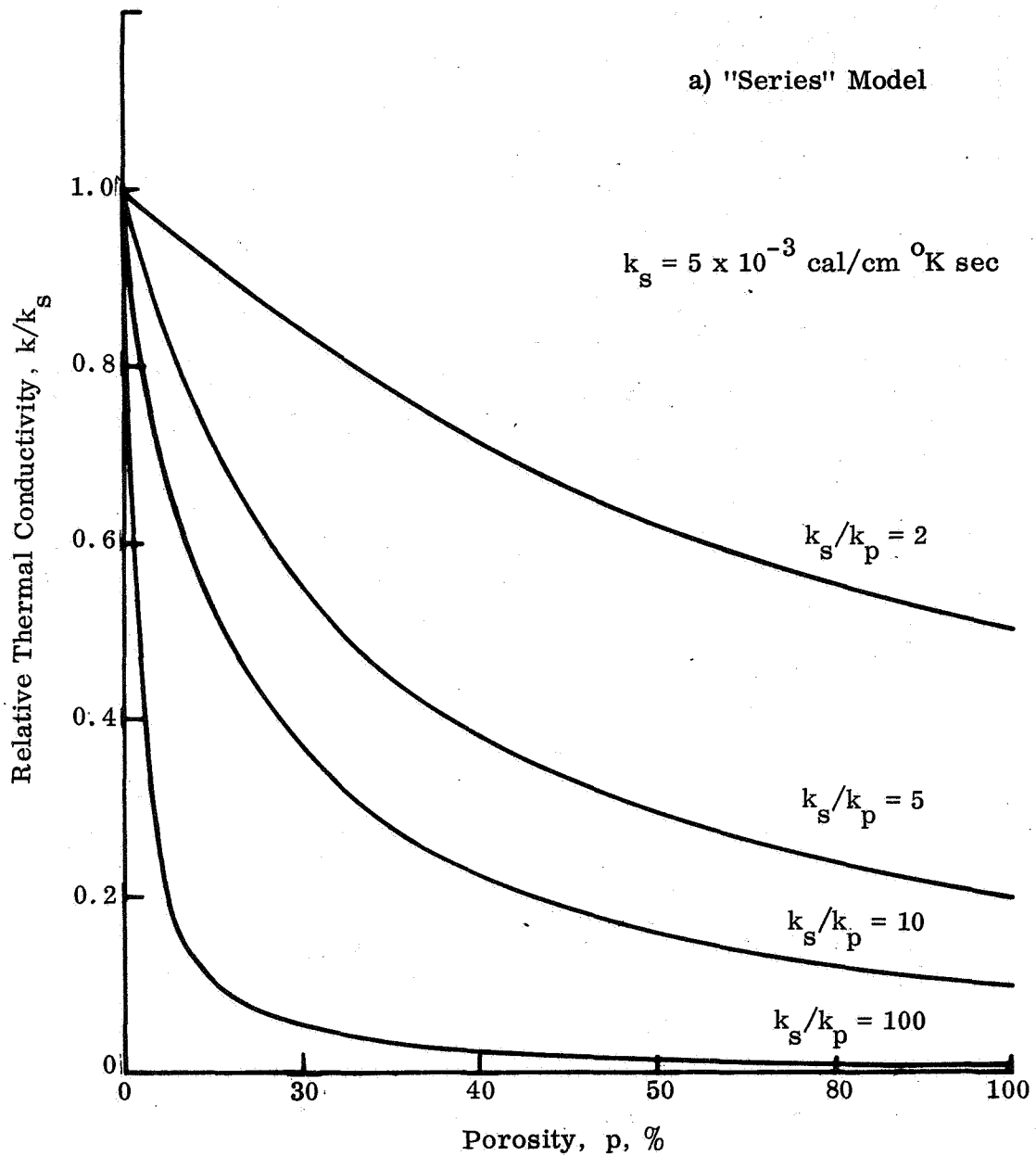


Fig. 10 Thermal Conductivity of Porous Rocks  
a) Series Model

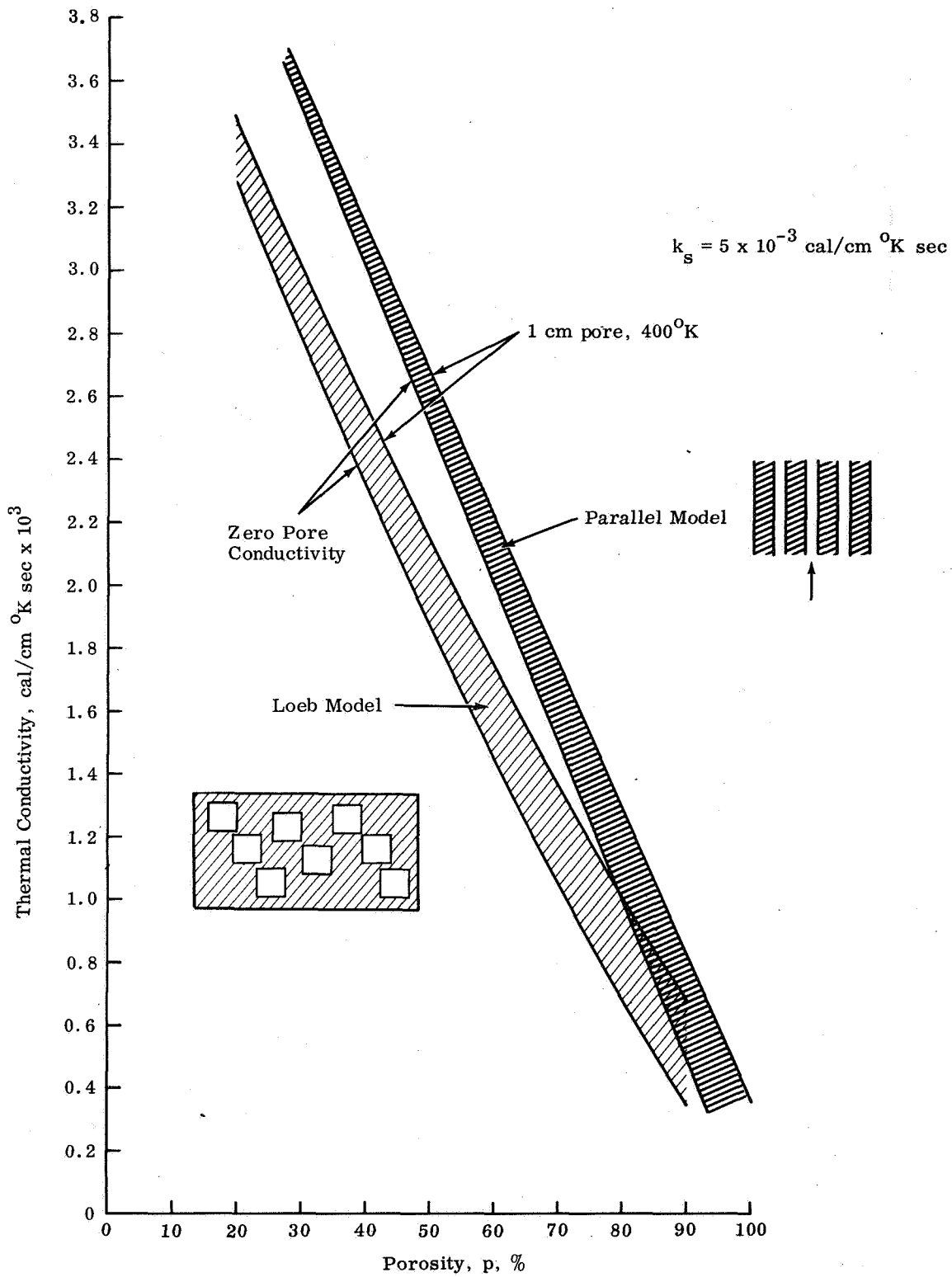


Fig. 10 Thermal Conductivity of Porous Rocks (Cont.)  
 b) Loeb and Parallel Models



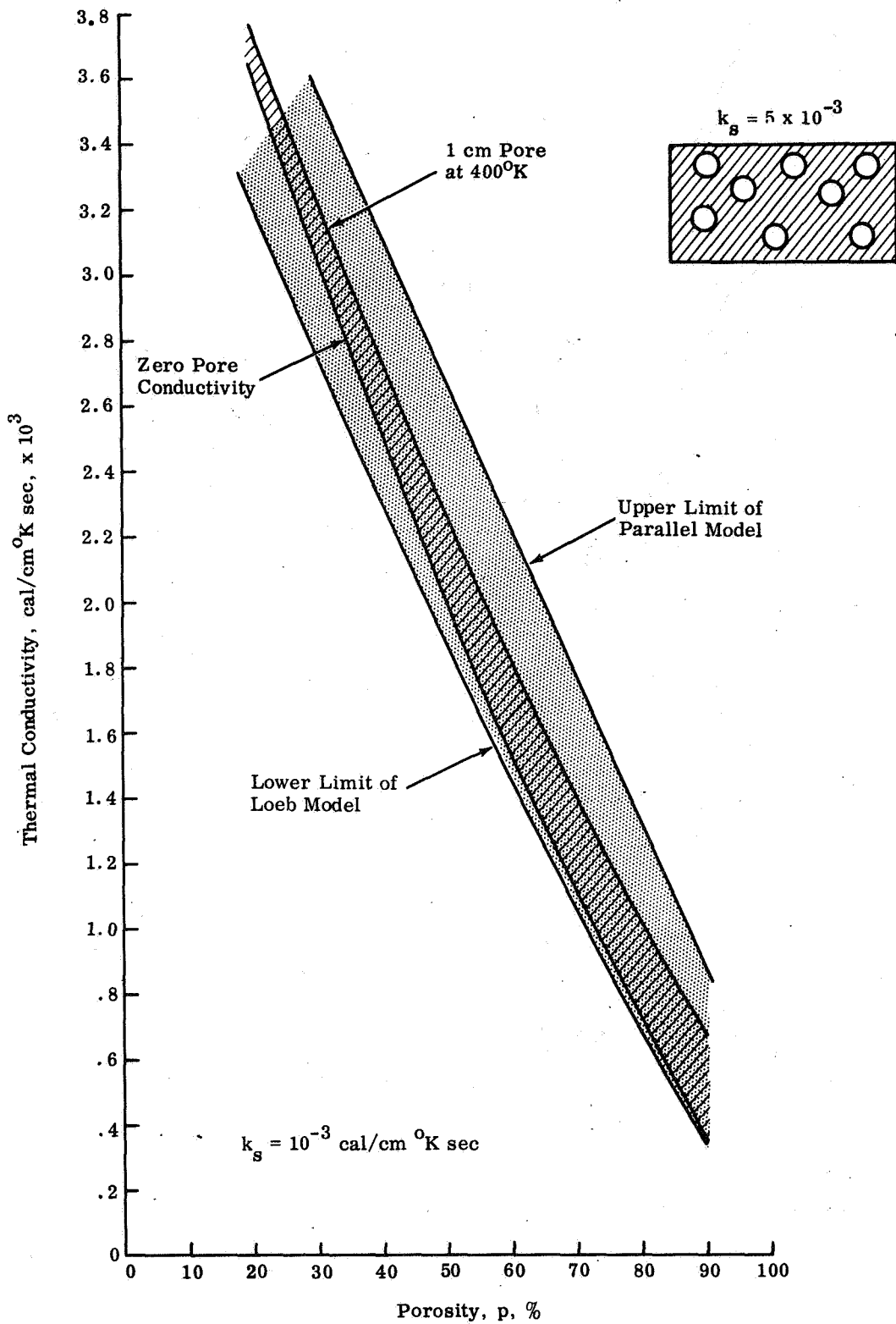


Fig. 10 Thermal Conductivity of Porous Rocks (Cont.)  
c) Maxwell Model

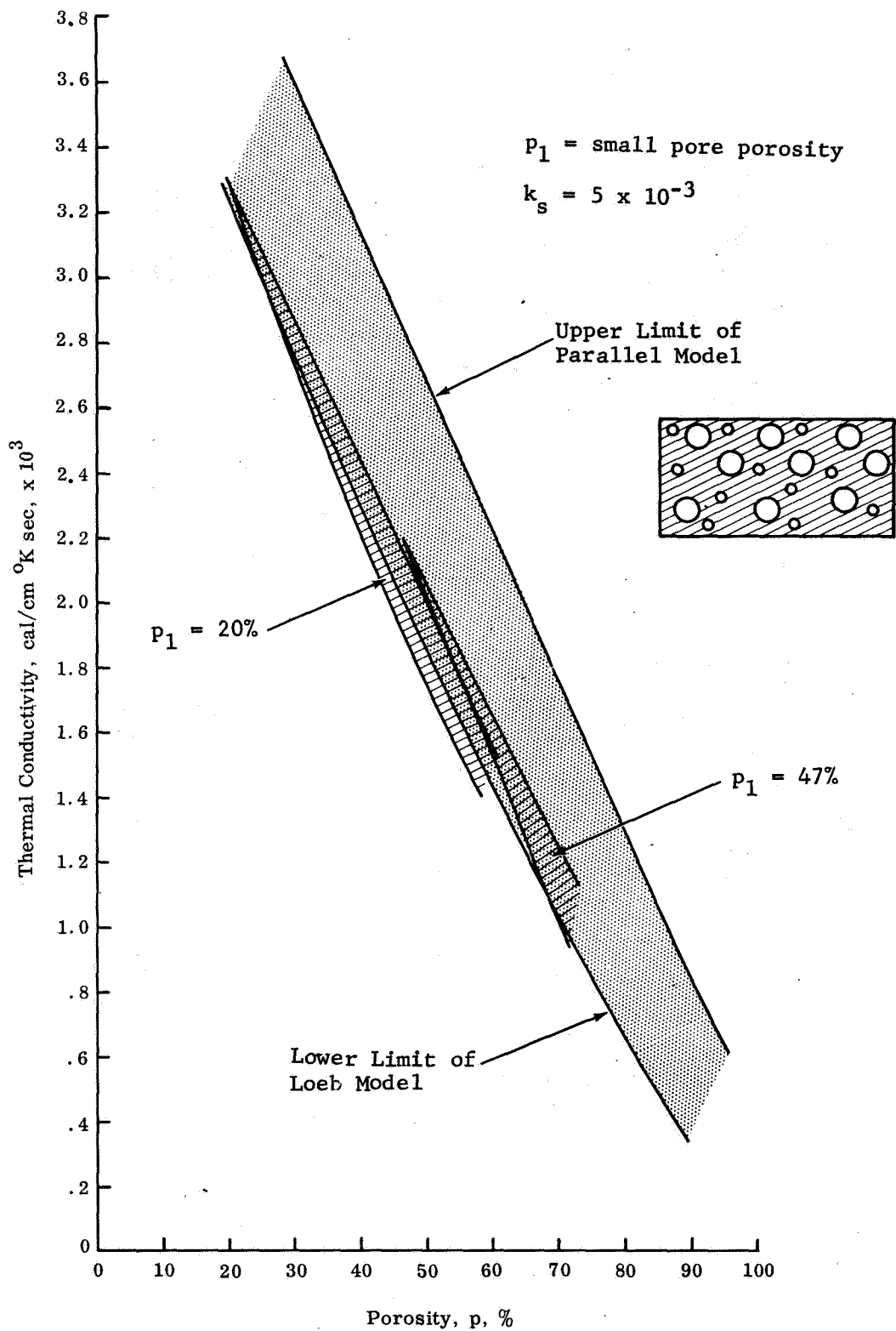


Fig. 10 Thermal Conductivity of Porous Rocks (Cont.)  
 d) Modified Maxwell Model

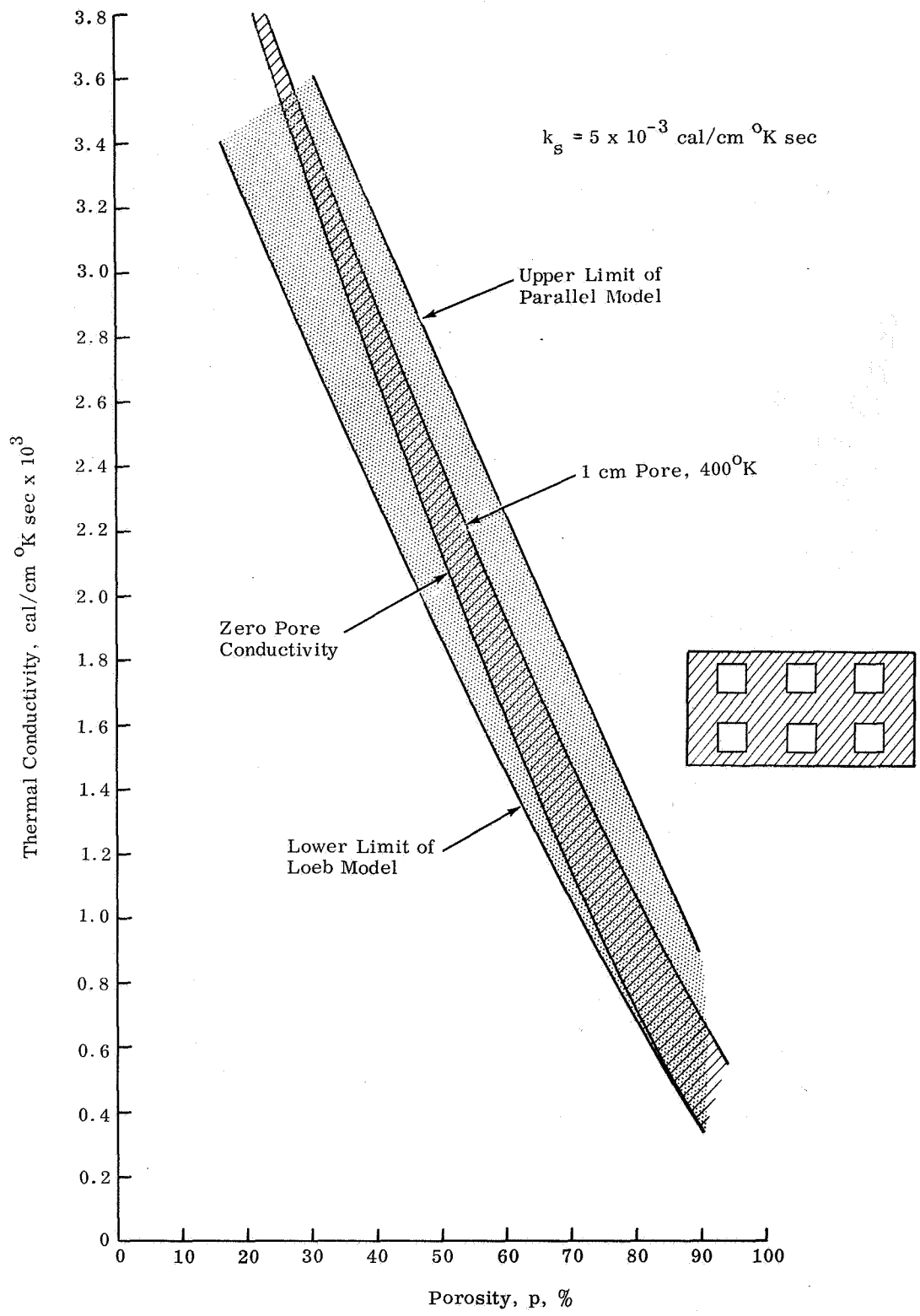


Fig. 10 Thermal Conductivity of Porous Rocks (Cont.)  
 e) Russell Model

$$k_s = 5 \times 10^{-3} \text{ cal/cm } ^\circ\text{K sec}$$

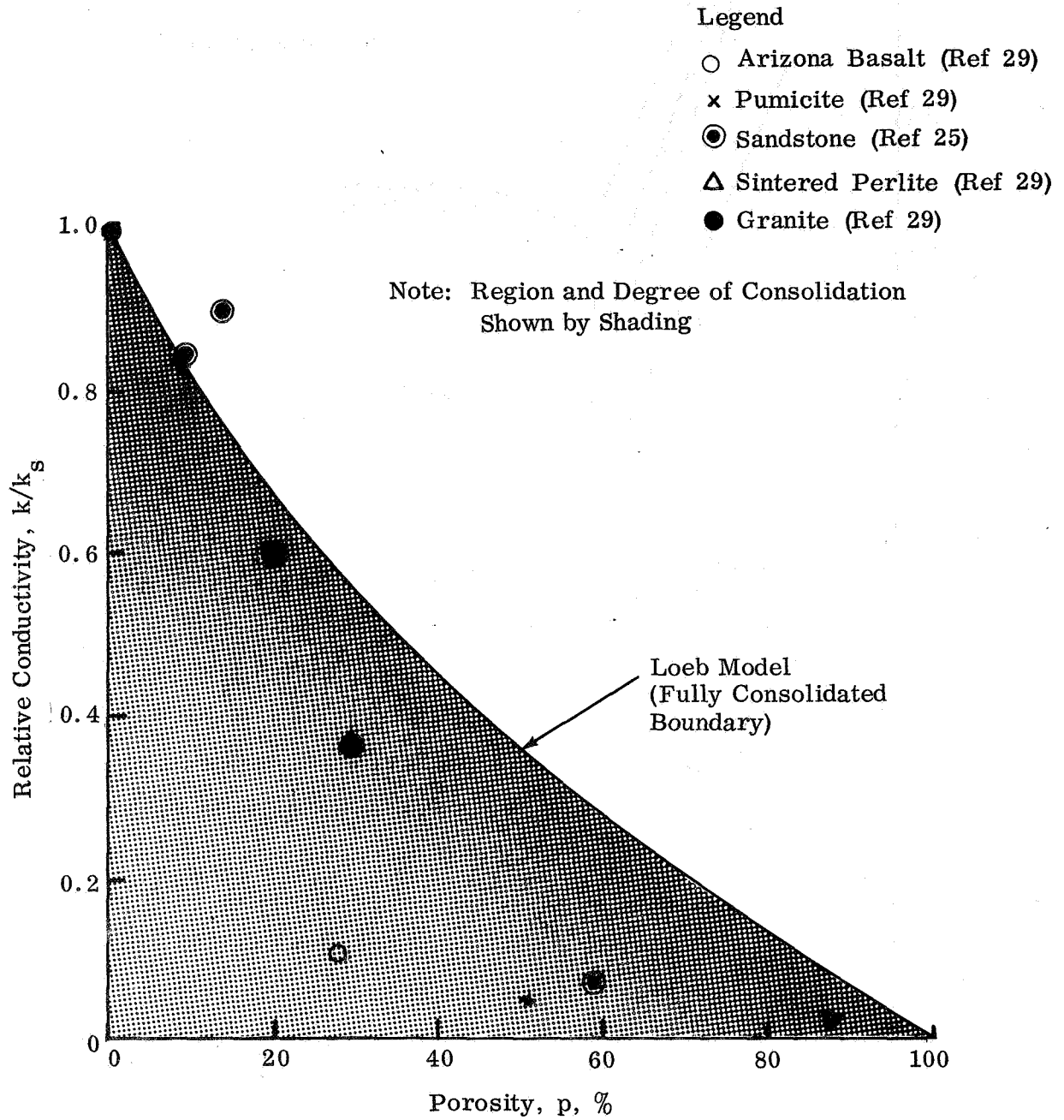


Fig. 11 Comparison of Loeb Model with Experimental Data on Thermal Conductivity of Porous Rocks

## PHASE IB: MECHANICAL PROPERTIES

### DEFINITION OF MODELS AND TERMS

As in the analysis of the thermal properties in Phase IA, the porous models considered in this phase consist of the "particulate" and the "vesicular" varieties shown in Fig. 12. In the former model, discrete particles are mechanically interlocked or bound with relatively weak molecular forces of attraction. In the latter model, the strength is due to solid bridges between particles or elements surrounding concave or convex cavities.

As explained in the next section, two versions of the particulate model have to be considered, namely, those having very dense or very loose packing, as shown in Fig. 12: The densely packed or "cannonball" version of the particulate model is representative of conventional, "engineering" soils commonly encountered on the earth. The properties and behavior of such soils have been widely investigated. The loosely packed or "fluff" version of the particulate model is much less understood, but is of greater interest in lunar studies because of its high porosity.

The terms "densely packed" or "cannonball" as used in this study apply to soils with a porosity of less than 50 percent and which fail predominantly in "lateral shear." The terms "loosely packed" or "fluff" apply to soils with a porosity of greater than 50 percent and which fail predominantly in "local shear." These modes of failure are illustrated in Fig. 13. The arbitrary use of 50 percent porosity as a boundary line between the two modes of failure is justified later in this study.

The term "vesicular" is used in a very broad sense to indicate rocks or sintered materials that contain a significant percentage of pores. These pores may have been created either by gas expansion at the time of rock formation, or left as cavities during the agglomeration and sticking of particles. On the earth, such materials appear as scoriae and welded tuff at places of volcanic activity. There are indications that similar types of porous materials also exist on the moon.

### PROBLEM AREAS

The mechanical analysis of the particulate model is complicated by the fact that no single relationship can adequately describe the strength of this medium at all porosities. It is necessary to treat the underdense and densely packed versions separately

because each exhibits a different mode of failure as shown in Figs. 13a and b. Fluffy soils, unlike conventional soils, fail in a manner similar to dry, uncompacted snow. This failure is characterized by volume reduction and the progressive collapse and compression of the loose aggregate immediately under the applied load.

In our search of the literature of soil mechanics and related fields, we have not come across any theoretical or empirical expressions that account for or predict the failure of highly porous granular media under compressive or shear loads. The solution offered in this report is a preliminary attempt to fill this gap. The results are compared with experimental data recently reported by workers at NASA.

The classic, soil mechanics solution to the problem of soil strength applies to what we call the "cannonball version of the particulate model." This model assumes relatively dense (i.e., incompressible) packing in which failure is characterized by a slight volume increase (called "dilatancy") and bodily movement of the soil mass in the failure zone. As shown in Fig. 13a, this zone generally extends beyond the immediate area where the load is applied. Intergranular friction along the failure plane constitutes the major portion of the resistance against the applied compressive or shear stresses. Most natural terrestrial soils fail predominantly in this manner, as they rarely reach or exceed a porosity of 50 percent. In relating bearing strength with porosity, in this model, we have leaned heavily on available knowledge and data in the literature of soil mechanics.

As in the treatment of the fluff model, a similar attempt is made to solve the strength problem of the vesicular model (i.e., where the solid phase is continuous). This model, like the "fluff," has not been widely explored. However, advantage is taken of available strength data on manufactured porous materials. A "best fit" empirical expression is developed as a preliminary yardstick which may later be refined by actual tests on natural, porous rocks.

In the analyses of bearing strength that follow, the "fluff" is treated first, followed by the "cannonball" and "vesicular" models.

## BEARING STRENGTH OF PARTICULATE MODELS

### The "Fluff" Model

We have defined the "fluff" as the underdense version of the particulate model. In seeking an analytical solution to the bearing strength of this relatively unexplored medium, the following approach is pursued:

- Step 1: Postulate a mode of failure.
- Step 2: Verify or refine, qualitatively, the above postulate by means of an experimental model.
- Step 3: Identify the first order geometrical and force parameters, and relate, quantitatively, the strength of the fluff with these parameters.

#### Step 1: Postulation of a Mode of Failure

To postulate a mode of failure for the underdense version of the particulate model, it is necessary to determine the boundaries of the disturbed zone, the behavior of the particles within and outside this zone, and the nature and magnitude of the forces that are developed before and during failure. This can be best done by comparing the deformational behavior of the well-known dense (incompressible) medium with the postulated behavior of the underdense (compressible) medium as depicted in Fig. 13. The following postulations are made.

Boundaries of the Disturbed Zone — In the fluffy model, the disturbed zone is limited very nearly to the area immediately under the pad. A vertical wall is sheared as the pad penetrates into the soil. The depth of the compressed material under the pad is unknown. In the cannonball model, sinkage can take place only through lateral displacement of a mass of soil away from the pad along a shear surface that is determined by the coefficient of friction of the soil.

Behavior of Soil Within and Outside of Disturbed Zone — As the pad penetrates into the fluffy soil, a "bulb" of compacted material builds up under the pad and increases in thickness as the pad sinks deeper. The rate of the increase in thickness of the bulb with depth and the density profile of the soil within the disturbed zone are not known. In the cannonball model there is, theoretically, no differential movement of particles within the disturbed mass of soil other than along the plane of failure. During failure, when the particles slide over one another, a slight expansion of volume (called dilatancy) occurs.

Failure Criterion — Qualitative load-sinkage curves shown in Fig. 15 indicate that the point of actual failure is not as clearly defined in the fluffy model, in which bearing strength is postulated to be depth dependent, as it is in the cannonball model, which is known to "yield" suddenly when the applied load overcomes the static friction and cohesion along a critical plane. Bearing strength, in this case, is defined as the normal load that can be imposed upon the surface of a soil before the system fails in shear. In the case of the fluffy model, it is not meaningful to speak of bearing strength, as such, without associating this strength with a given depth of sinkage.

Nature and Magnitude of Forces Resisting Penetration — In addition to work done in compressing the fluffy model and expanding the cannonball model, the major forces that resist the penetration of a pad in both models are those of interparticle friction and adhesion. It is very likely however, that the relative contribution of these forces differ in each model. It is reasonable to neglect adhesion in the cannonball model because the particles have a large volume to surface ratio. We may easily assume that friction predominates as a resisting force by virtue of the fact that two relatively rough and unyielding surfaces are rubbing against each other along the plane of failure. While the particles in the cannonball model do undergo elastic and possibly plastic deformation, it is reasonable to assume that in the fluffy model the particles "give" (by rotating and/or translating) before plastic deformation takes place, and that they are rarely in a position to rub against one another and develop frictional forces. Since the particles in this model are inherently very fine (hence susceptible to attractive forces) and a great number of them are contained within a unit area of the failure plane, adhesional forces will play a predominant role. Consequently, an important factor in predicting the bearing strength of fluffy soils is a knowledge of the number of particle bonds that are severed during failure, and the strength of each bond. The latter could depend upon the environment or,



(as would be the case on the moon) upon the ambient vacuum. The number of severed bonds will depend upon the initial and final porosity of the system as well as on the depth of the "bulb" of compacted soil formed under the pad. The experimental model described in the next section was developed and tested in an attempt to verify the postulated model and clarify some of the questions discussed above.

## Step 2: Preliminary Experimental Model

A crude experimental model of the fluffy soil was built in order to observe the movement of soil particles in and around the disturbed zone and to determine the thickness of the "bulb" formed under the pad at various stages of penetration. This was accomplished by using a plexiglass container (4 x 4 inches square and 10 inches high) in which all four sides were scored with black horizontal lines 1/4-inch apart. The container was filled with loosely sifted alternating 1/4-inch red and gray layers of very fine fluffy powders, the interface of the layers roughly corresponding to the horizontal markings, as shown in Fig. 14. An average porosity of 65 percent was estimated for the soil in the container on the basis of weight and volume measurements and an average "real" density of  $2.5 \text{ g/cm}^3$  for the powders used. The gray powder is ground basalt (particle size  $< 37\mu$ ) and the red powder is made up of synthetic "microballoons."

A 1-inch thick perforated cap having 1 x 1/2-inch cutouts at the middle of each side was fitted tightly on top of the container to serve as a guide for 1 x 1/2-inch rectangular wooden bars that were used as plungers. The 1-inch side of the plunger faced the inner side of the container wall as shown in Figs. 14 b, c, and d. The plungers were pushed into the soil by hand at all four sides and photographs were taken at various depths of penetration. No attempt was made to measure depth versus sinkage because the primary object of the experiment was to observe the behavior of the soil during compaction or failure. The four sequential photographs of side No. 3 shown in Fig. 14 are typical of all sides in depicting the soil "profile" during the experiment.

The photographs corroborate some of the points we postulated above and clarify other points that were left in doubt. The following preliminary comments may be made on the basis of visual examination of Figs. 14b, c, and d.

Boundaries of the Disturbed Zones — As postulated, the disturbed zone is limited to the area immediately under the pad. No lateral movement of soil or disturbance of the surrounding surface

(as would be encountered in the well-known cannonball model) is observed. We also notice that the thickness of the disturbed zone increases with depth but not indefinitely as we suspected. According to this experiment (limited to four trials only), the compressed bulb under the pad does not seem to increase in thickness beyond a depth of penetration equal to about three times the width of the pad. The settlement curve in this region is represented in Fig. 15 by line OA. At point A, the bulb appears to reach its maximum thickness, which is about equal to the width of the pad, and then stays constant. Contrary to our postulation, vertical compaction appears to stop beyond this point, and lateral compaction begins to occur instead. There is clear evidence in Fig. 14d that at these depths the compacted bulb acts as a wedge and pushes the tenuous material to the sides and compacts the surrounding quasi-stationary soil. This phenomenon is more clearly depicted in the diagram in Fig. 16 where a vertical line is shown joining the inflection points of the horizontal flow lines and deviating slightly away from the sheared plane down to a certain depth B. The system would probably reach its maximum bearing strength at depth B, as no additional resisting forces are likely to be developed during penetration beyond this point. The increase in penetration resistance due to lateral compaction between levels A and B is qualitatively represented by curve AB on the settlement curve in Fig. 15. Assuming a semi-infinite medium of fluffy soil, the settlement curve indicates a nearly constant bearing strength beyond point B. In a layered model consisting of fluff over hardpan, "bottom" effects will cause the compacted bulb under the pad to fail in lateral shear instead of lateral compaction. Under these conditions, the settlement curve will level off and exhibit a "yield" point similar to the cannonball model as depicted in Figs. 13 and 15.

Behavior of Soil Within and Outside of Disturbed Zone — The photographs in Fig. 14 clearly show the formation of a compacted bulb under the pad as we postulated, but they also reveal an unexpected disturbance of the soil below the compacted bulb, as well as outside of it in the lateral direction, particularly after the bulb reaches its maximum thickness and begins to act as a wedge as mentioned above. We can approximately determine the density profile of the material in these exterior zones from the pattern of the "flow lines." This knowledge could be very useful in estimating the number of particle bonds that are severed during failure along the vertical "shear" plane.

Nature of Forces Resisting Penetration — The downward inclination of the flow lines toward the pad could be invoked as evidence to support our postulations that the material along the vertical

wall fails in tension rather than in shear. The particles at the interface of the quasi-stationary medium and the downward moving bulb appear to pull one another down by realigning themselves until they break away. It is reasonable to state that adhesional rather than frictional forces predominate along this plane by virtue of the fact that at least one of the rubbing soil surfaces is "soft" and yielding, and does not offer sufficient normal resistance for frictional forces to develop. A second component of soil resistance comes into play when the vertically compacted bulb has reached its maximum thickness and begins to compact the soil laterally. We may conclude that the bearing strength of semi-infinite fluffy media (i.e., where there are no "bottom" effects) has two components, one of which is the tensile force needed to sever interparticle bonds at the interface between the disturbed and the quasi-stationary media, and the other component is the force needed to compact the soil laterally. Both of these components build up gradually during sinkage to a certain depth, then they are likely to remain constant. Beyond this depth, contrary to what we postulated, semi-infinite media could exhibit a bearing strength that is nearly independent of depth. This statement would imply that, theoretically, a pad or footing that applies a static pressure less than the terminal bearing strength of the fluff would sink into the medium down to a finite depth and then come to a stop; however, if the applied pressure is beyond the terminal bearing strength, the footing could sink in indefinitely (assuming we neglect friction). Both of these bearing strength components depend upon the initial and final porosity of the system. The former is known or measurable; the latter could be estimated on the basis of experimental models such as the one we described. Unfortunately, testing this particular, improvised model is very laborious, and the obtained data are rather crude. However, improvements can be made if necessary.

### Step 3: Theoretical Analysis

We shall limit the analysis of the bearing strength of fluffy soils to the uppermost region (about a pad width in depth), where only vertical compaction takes place. The region of lateral compaction at lower depths, where the fluff reaches its "terminal" bearing strength, will not be considered in this study.

Assumptions — Consider a circular pad of diameter  $D$ . In penetrating through a depth  $z$  into the fluff, the pad compacts the material from an initial porosity  $p_0$  to a final porosity  $p_f$  and thickness  $t$ , as shown in Fig. 17. In deriving a theoretical expression for the mean bearing strength of the fluff, we make the following simplifying assumptions:

- a) The fluff under and around the compacted plug  $t$  remains undisturbed. This implies that the applied load is transmitted to a bottom layer (at porosity  $p_0$ ) when the uppermost layer is fully compacted down to a final porosity  $p_f$ .
- b) The mean effective bonding force per particle contact is  $q$  expressed in dynes, and the resultant of such force is parallel and opposite to the applied force.  $q$  represents a predominantly adhesive or adhesion-dependent force.
- c) The particle system is homogeneous, that is, the initial porosity  $p_0$  within the total volume is also the void fraction within any cross section.
- d) All the particles are solid spheres of equal diameter  $d$ .
- e) Neutral stresses, due to pore pressure changes during compaction, are negligible. This assumption is valid when the fluff is in a vacuum or when the pad sinkage is very slow.
- f) The maximum load  $F$  that the pad can support at depth  $z$  is equal to  $F_s + F_c$ , where  $F_s$  is the force necessary to "shear" the compacted plug along a vertical plane around the perimeter of the pad, and  $F_c$  is the force necessary to compact each successive layer of fluff under the compacted plug.
- g) Quantitatively,  $F_s$  or  $F_c$  is equal to  $q$ , the bonding force per particle contact, times the total number of particle bonds disrupted.

According to assumption g:

$$F_s = n_s m_s q \pi D t ,$$

where  $n_s$  is the number of particles per unit cross section, and  $m_s$  is the mean number of points of contact per particle on the disrupted side of a cross section. Also,

$$F_c = \left( \frac{n_v m}{2} \right)^{\frac{2}{3}} q \frac{\pi D^2}{4} ,$$

where  $n_v$  is the average number of particles per unit volume, and  $m$  is the mean coordination number, i.e., the average number of points of contact between one particle and its neighbors. In the above equation  $n_v m$  is divided by two because each point of contact is shared by two particles. The exponent  $\frac{2}{3}$  is used to convert the total number of contacts per unit volume to total number of contents per unit cross section by virtue of assumptions a and c.

According to assumption f ,

$$F = n_s m_s q \pi D t + \left( \frac{n_v m}{2} \right)^{\frac{2}{3}} q \frac{\pi D^2}{4} .$$

$$f = \frac{4F}{\pi D^2} = 4 n_s m_s q \frac{t}{D} + \left( \frac{n_v m}{2} \right)^{\frac{2}{3}} q . \quad (13)$$

$$f = f_s + f_c , \quad (14)$$

where

$f$  = bearing strength in  $g/cm^2$ ,

$f_s$  = "shear" component of bearing strength, and

$f_c$  = "compaction" component of bearing strength.

Expressions for  $f_s$  and  $f_c$  will now be derived in terms of soil properties that are readily measurable, such as porosity and grain size.

"Shear" Component of Fluff Bearing Strength — According to Eqs. (13) and (14)

$$f_s = 4 n_s m_s q \frac{t}{D} . \quad (15)$$

The average number of particles per unit section across the actual "shear" plane shown in Fig. 18a:

$$n_s = \frac{4(1 - p_o)}{\pi d_{av}^2} ;$$

in Fig. 18b

$$\frac{\pi d_{av}^2}{4} = \frac{\pi d^2}{6} ;$$

hence,

$$n_s = \frac{6(1 - p_o)}{\pi d^2} .$$

The average number of bonds per particle to the right of "shear" plane in Fig. 18 is

$$m_s = \left[ \frac{\pi d^2}{4} / \pi d^2 \right] m = \frac{m}{4} .$$

Let

$n_o$  = initial number of particles per unit volume in compacted fluff;

$n_f$  = final number of particles per unit volume in compacted fluff;

$v_s = \pi d^3/6$ , the volume of a particle.

Consider, in Fig. 17, a unit horizontal cross section under the pad. According to assumption a) we have

$$(z + t)n_o = tn_f$$

$$t = \frac{n_o}{n_f - n_o} z \quad (16)$$

$$n_o = \frac{1 - p_o}{V_s} \quad (17)$$

$$n_f = \frac{1 - p_f}{V_s} \quad (18)$$

$$t = \frac{1 - p_o}{p_o - p_f} .$$

By replacing the values of  $n_s$ ,  $m_s$ , and  $t$  in Eq. (15),

$$f_s = \frac{6mqz}{\pi Dd^2} \cdot \frac{(1 - p_o)^2}{p_o - p_f} \quad (19)$$

Compaction Component of Fluff Bearing Strength — According to Eqs. (13) and (14)

$$f_c = \left( \frac{n_v m}{2} \right)^{\frac{2}{3}} q \quad (20)$$

In Fig. 17, consider a unit volume of uncompacted fluff such that  $z + t = 1$ . According to assumption a) and Eq. (16),

$$\frac{t}{z} = \frac{n_o}{n_o - n_f}$$

According to the same assumption, we obtain the following relationship for penetrating the pad through thickness  $t$ ,

$$n_v = n_f \frac{t}{z} = \frac{n_f n_o}{n_f - n_o}$$

Replacing  $n_o$  and  $n_f$  by their values in Eqs. (17) and (18) yields

$$n_v = \frac{6(1 - p_o)(1 - p_f)}{\pi d^3 (p_o - p_f)},$$

and replacing  $n_v$  in Eq. (20) yields

$$f_c = \left[ \frac{3(1 - p_o)(1 - p_f) m}{\pi(p_o - p_f)} \right]^{\frac{2}{3}} \frac{q}{d^2} \quad (21)$$

Porosity Dependence of Coordination Number  $m$  — An empirical expression of  $m$  versus  $p_o$  is derived in Fig. 19, based on a straight line fit of five data points in the region of high porosity. This line intersects the abscissa at 100 percent porosity (point 1), where the coordination number is zero, and passes through points 3, 4, and 5, which represent the well-known  $m$  versus  $p_o$  relationship of ordered, stable packings, such as the diamond cubic, single cubic, and the body centered. We can safely ignore the fact that the face centered packing (point 6) does not fall on the straight line. This point is not in the region of porosity that is of interest in this study.

Point 2 in Fig. 19 is based on a computer-derived model developed by Dr. C. H. Li of Grumman (Ref. 40). In this theoretical model the particles are assumed to fall vertically and pack randomly under conditions of infinite surface stickiness. Dr. Li has tried various distributions of particles in the bottom layer, with matrices up to  $20 \times 20$  particles. He reports that all cases result in a porosity of 84 percent (with few percent fluctuation) and an average coordination number very close to 2.0. This point fills the gap in our knowledge of  $m$  between 66 and 100 percent porosities, and justifies the use of the relationship

$$m = 12(1 - p_o) \quad (22)$$

between 30 and 100 percent porosities.

Average Interparticle Bond  $q$  — According to assumption d), the derivation of the mean bonding force between particles during compaction will be based on a tensile, rather than on a frictional, mode of failure. This assumption may be justified by the fact that when two particles are in a position to rub against one another, they are more likely to rotate and translate together (due to the tenuity of the medium) and then be "pulled" away from one another before sufficient resistance could be built to make them react against a frictional force. Whatever shear and frictional forces could develop may be indirectly represented by  $q$ , since these forces are essentially a form of adhesion.

According to thermodynamic theory (Ref. 41) the adhesive force  $q$  between two surfaces of curvature  $\epsilon_1$  and  $\epsilon_2$  is expressed by the formula

$$q = \frac{2\pi}{\epsilon_1 + \epsilon_2} f(e) ,$$



where  $f(e)$  is a material- and environment-dependent energy function. The adhesive force between two spheres of diameter  $d$  will be

$$q = \frac{\pi d}{2} f(e) . \quad (23)$$

In a two phase, solid-gas system, consisting of solids 1 and 2 and an adsorbed interface 3,

$$f(e)_t = \sigma_{13} + \sigma_{23} - \sigma_{12} , \quad (24)$$

where the subscript  $t$  denotes a two phase (i.e., "contaminated") system;  $\sigma_{13}$  and  $\sigma_{23}$  are the interfacial tensions of the solids and the adsorbed phase, and  $\sigma_{12}$  is the interfacial tension of solids 1 and 2. The negative sign in Eq. (24) indicates that surfaces will attract or repel one another depending on whether  $\sigma_{13} + \sigma_{23}$  is greater or smaller than  $\sigma_{12}$ . In two phase systems (such as moist soils) the surfaces will generally attract one another if the adsorbed phase wets the solids.

The case of a monophasic (i.e., "clean") system of particles (likely to exist on the moon) has been investigated in a previous Grumman report (Ref. 42). It was demonstrated on the basis of surface tension theory that

$$f(e)_m \approx 2\sigma_2 ,$$

where the subscript  $m$  denotes a monophasic system. It was concluded that surfaces in such a system necessarily attract one another and that the adhesion is stronger in the absence of an adsorbed interface; that is,

$$f(e)_m > f(e)_t .$$

Soil experiments performed in an ultrahigh vacuum (as discussed below) validate these conclusions.

Theoretical Bearing Strength of Fluffy Soils — In replacing the value of  $m$ , Eq. (22), in Eq. (19), we will let

$$m = 12(1 - p_f) \quad \text{instead of} \quad m = 12(1 - p_o) ,$$

because the number of particle contacts to the right of the shear plane in Fig. 18 is determined by the actual porosity  $p_f$  of the compacted plug of thickness  $t$ . But when replacing the value of  $m$ , in Eq. (21) we will use

$$m = 12(1 - p_o) .$$

Combining Eqs. (13), (19), (21), (22), and (23) we get

$$f = \left\{ 36 \frac{z}{D} \cdot \frac{(1 - p_o)^2 (1 - p_f)}{p_o - p_f} + 8 \left[ \frac{(1 - p_o)^2 (1 - p_f)}{p_o - p_f} \right]^{\frac{2}{3}} \right\} \frac{f(e)}{d} \quad (25)$$

or

$$f = \left( N_s \frac{z}{D} + N_c \right) \frac{f(e)}{d} . \quad (26)$$

Plots of  $N_s$  and  $N_c$  as a function of  $p_o$  are shown in Figs. 20a and 20b, for values of  $p_f$  equal to 0.3, 0.4, and 0.5. We notice that  $N_s$  and  $N_c$  are not very sensitive to changes in  $p_f$ , particularly at high initial porosities.

Equation (26) indicates that the most important soil properties that influence the bearing strength of fluff are initial porosity, surface energy of particles, and particle size. It is interesting to compare Eq. (26) to the well-known Terzaghi formula

$$f = S_g D \rho N_\rho , \quad (27)$$

for the bearing strength of incompressible soils (Ref. 43). In Eq. (27)  $S_g$  is the shape factor of the pad,  $\rho$  is the bulk density of the soil (related to porosity  $p_o$ ), and  $N_\rho$  is an empirical factor that depends upon the angle of internal friction of the

soil. We notice that plate diameter  $D$  does not play as major a role in determining the bearing strength of fluff in Eq. (26), as it does in the case of conventional, incompressible soils, Eq. (27). Plate size affects only one of the two strength components of the fluff and, in contrast to Eq. (27), appears at the denominator because of "perimeter effects."

We also note in Eq. (26) that the fluff bearing strength is depth-dependent. If we arbitrarily select a depth of sinkage equal to one pad diameter, then we may use the formula

$$f = (N_s + N_c) \frac{f(e)}{d} \quad (28)$$

as a convenient expression for predicting or comparing the strength of fluffy soils. The  $z/D = 1$  ratio may also be adopted in future measurements as a reference for comparing data by various investigators. When using Eq. (28) it is important to recall that the soil should fail predominantly in volumetric compression down to a depth equal to at least one pad diameter.

Comparison with Experimental Data — Few sources of experimental data on fluff bearing strength versus porosity or bulk density have come to our attention (Refs. 44 through 47). Data reported by Hanks and McCarty (Ref. 44) are shown in Fig. 21. Various size plates were used, but the measurements were made at about a depth equal to one-half the plate width ( $z/D = \frac{1}{2}$ ). The curve that fits the data points suggests a final porosity  $p_f$  of about 50 percent, because the curve becomes asymptotic around this value. By substituting the above values of  $z/D$  and  $p_f$  in Eq. (25) and by removing the  $f(e)/d$  term by normalizing the theoretical expression at the  $p_o = 53$  percent data point, we can plot the curves for  $f$ ,  $f_s$ , and  $f_c$ , as shown in Fig. 21.

The theoretical curve matches the experimental curve reasonably well, especially when we take into consideration differences in particle shape and size distribution between the assumed model and the test specimens. For instance, mechanical interlocking, being more pronounced between natural, irregular particles than between smooth spherical particles, may account for the slightly higher strength exhibited by the experimental curve. The  $f_s$  and  $f_c$  components of  $f$  are also plotted in Fig. 21 to show their relative contribution to the total strength. The plots show that at this particular  $z/D$  ratio the "shear" component predominates.

The large scatter of the test data near 50 percent porosity may not necessarily be accidental. This is a region of transition or discontinuity, where "local" and "lateral" modes of shear failure combine in varying degrees. The soil in this region is neither sufficiently porous nor sufficiently dense to fail completely by one or the other mode. It reaches its terminal porosity at  $z < D/2$ , then begins to shear laterally, but does not reach its maximum resistance at  $z = D/2$ , where the bearing strength is recorded. Consequently, the curve dips temporarily, until the soil becomes sufficiently dense to fail predominantly in lateral shear at or above  $z = D/2$ . It is to be expected, therefore, that the curve should resume its ascent toward higher strength values at  $p_0 < 50$  percent.

In view of the reasonably good agreement between experimental data and the normalized theoretical function, we may now derive an empirical value for the term  $f(e)/d$ .

According to Eq. (26),

$$\frac{f(e)}{d} = \frac{f}{N_s \frac{z}{D} + N_c}$$

Using the Hanks and McCarty data at  $z/D = \frac{1}{2}$  and  $p_f = 0.5$  we obtain

$$\frac{f(e)}{d} = 0.104 \text{ psi} \quad \text{or} \quad 7200 \text{ dynes/cm}^2$$

By assuming an average particle size of 50 microns, the mean surface tension of the two phase particle system is

$$f(e) = 36 \text{ dynes/cm}$$

This value appears to be reasonable in the light of present theoretical knowledge and experimental data on the adhesion between a spherical and plane surface. Lowe and Lucas (Ref. 48) and Bradley (Ref. 49), in agreement with Deryaguin (Ref. 41), report that the mutual attraction or adhesion between particles varies as the first power of particle size. For a spherical particle of diameter  $d$  resting on a plane surface, the force of attraction  $q$  is expressed as

$$q = Ad \quad (\text{in dynes}),$$

where  $A$  is a material constant and  $d$  is in cm. According to Eq. (23), the adhesion between two spherical particles will be

$$q = \frac{A}{2} d . \quad (29)$$

Lowe and Lucas (Ref. 48) have computed a theoretical value for  $A$  equal to 314 dynes/cm for quartz surfaces. Bradley (Ref. 49) checked this value experimentally under dry and relatively clean conditions and found the constant  $A$  for smooth quartz spheres to be 212. It is reasonable to attribute the discrepancy between the theoretical and measured values of  $A$  to the departure of the test surfaces from an atomically smooth and clean surface.

By equating Eqs. (23) and (29),

$$q = \frac{\pi}{2} df(e) = \frac{A}{2} d ,$$

and by solving for  $f(e)$  we get

$$f(e) = \frac{A}{\pi} .$$

The table below lists the various numerical values of  $f(e)$  in dynes/cm.

TABLE III

Surface Energy Between Two Contacting Spheres

Condition	Surface Energy $A$	dynes/cm $f(e)$	Reference
Theoretical (Ideally clean and smooth spheres)	314	100	Lowe and Lucas (Ref. 48)
Experimental (Polished spheres in air)	212	68	Bradley (Ref. 49)
Experimental ("natural" particles in air)	69	36	Computed from Hanks and McCarty data (Ref. 44) for average $d = 50$ microns

More extensive data on bearing strength versus porosity has recently been published by Jaffe (Ref. 45). These data, taken at about  $z/D = 1$ , agree quite closely with the Hanks and McCarty data, as shown on a semilog plot in Fig. 22. Equation (26) is also plotted in this figure for various values of  $f(e)/d$  and  $z/D$ . Note that the curves are relatively insensitive to changes in  $z/D$  for values between  $\frac{1}{2}$  to 1, particularly at high porosities. The  $f(e)/d$  function that gives the best fit with the test data is  $10^4$  dynes/cm<sup>2</sup>. It is difficult to interpret this figure in terms of the surface energy of the particle system because of the wide range of particle sizes that make up the test specimens. Nevertheless, it is instructive to note that the theoretical curve follows the test data quite closely and that the direction of the scatter is more or less consistent with the change in grain size. The Jaffe data between 80 to 90 percent porosity would have come much closer to the theoretical curve had the particles been of uniform size, as in the theoretical model. Since very fine particles are necessary to achieve high porosities, it would be desirable in future experiments (although laborious and expensive) to use the same, fine particles at all porosities in order to reduce the number of experimental variables, and hence, the apparent scatter of the results.

In the region of discontinuity discussed above (i.e., around 50 percent porosity), the scatter in the Jaffe data is similar to that of Hanks and McCarty. Beyond this region, the Jaffe data exhibit the upward trend we anticipated earlier on the basis of the Hanks and McCarty data. According to these independent tests, 50 percent porosity appears to be a valid boundary between the fluff and cannonball versions of the particulate model, as we originally postulated. This boundary, in terms of bearing strength, appears to be of the order of 10 psi. In Fig. 22, the part of the theoretical curve beyond this boundary is of course fictitious. Its actual shape and trend is explored in the section on the "Cannonball" Model.

#### Effects of the Lunar Environment on Fluffy Soils

The strength or behavior of particulate materials, unlike that of their massive counterparts, depends on the magnitude and relative contribution of surface and body forces within the particle system. These forces are largely environment dependent. The lack of an atmosphere and a reduced gravity field on the moon are likely to affect the behavior of soils, particularly the highly porous variety, in a manner foreign to our experience on earth. Three of these effects, two of which are due to vacuum and the third to low

gravity, have been investigated at Grumman. The experienced changes in soil behavior due to all three simulated lunar conditions have been in the direction of increased strength. The data in Fig. 22 on soil strength versus porosity will now be evaluated in the light of these experiments which are reported in detail in Refs. 42 and 50.

Low Vacuum Effects - The first effect of soil hardening due to vacuum is related to the absence of pore gases. This effect takes place in fluffy soils only, when the porosity of the fluff undergoes a rapid reduction due to the application of a transient load such as may take place during landing or locomotion. Under atmospheric conditions, the strength of the fluff will be less than that suggested by Eq. (26) because the "quickenning" action of compressed pore fluids will tend to pull the particles away from each other. This effect is illustrated in Figs. 23a and 23b, which show results of a drop test in fluff under vacuum and air conditions (Ref. 42). In vacuum (Fig. 23a), the fluff has sufficient strength to support the fallen square plate, but in air (Fig. 23b), the plate disappears from sight, leaving the trace of a square crater. Equation (26) could express the strength of fluff in air (provided the bearing pressure is applied very slowly), but in a vacuum, it could apply to both static and dynamic loadings, provided, of course, that soil inertia effects are negligible.

Ultrahigh Vacuum Effects - The second effect of soil hardening due to vacuum is related to the absence of adsorbed gases. This effect, unlike the former, is "chemical" in nature and involves the action of latent forces of adhesion that come into play with the depletion of interfacial impurities when the vacuum is sufficiently high. As discussed earlier when introducing the energy term  $f(e)$ , surface tension theory predicts stronger adhesion in the absence of an adsorbed phase. Experiments were performed at Grumman, in which basalt, glass, and alumina powders were tumbled continuously in a vacuum in order to clean them of their adsorbed impurities (Ref. 42). Extensive sticking between particles took place when the pressure dropped to the  $10^{-10}$  torr range. The same particles failed to stick under similar conditions when the ambient pressure was not allowed to drop below  $10^{-3}$  torr. The adhesion results shown in Fig. 13 are qualitative, but sufficiently repeatable to verify theoretical predictions, and suggest that the energy term  $f(e)$  in Eq. (26) is environment dependent and likely to be greater under vacuum conditions prevalent on the moon. According to Eq. (26), the interparticle bond in the Hanks and McCarty soil

tests performed in air appears to be of the order of 1 dyne per particle contact. Similar tests could be performed in an ultra-high vacuum. The surface energy  $f(e)$  or mean bonding force could be estimated from the bearing test results by using the method described above. It would be desirable in such a test to use uniform spherical particles to justify the use of the theoretical model in interpreting test results. It would also be of interest to seek a theoretical or experimental correlation between thermal conductivity  $k$  and the surface energy function  $f(e)$ . We have no knowledge whether such a correlation exists at the molecular level.

Gravity Effects - The third and last effect of soil hardening we will discuss is that due to low gravity field. Equation (25) indicates that the bearing capacity of fluff is independent of the gravity field, because no term involving the weight of the soil appears in the expression. However, the bearing capacity of densely packed soils expressed by Eq. (27) is clearly dependent on the gravity field, because it is directly proportional to  $\rho$ , the unit weight of the soil. This conclusion is borne out by soil bearing experiments performed at Grumman under gravity fields ranging from 0.1 g to 3 g's (Ref. 50). Some of the test results, shown in Fig. 25 show that the bearing strength of the densely packed beach sand, representing the cannonball model, is directly proportional to the gravity field, whereas the strength of the loosely sifted fine pumice, representing the fluff model, is nearly independent of it.

These results show that, in a fluff of given porosity, a given weight will sink less under 1/6 g than under 1 g, but in a densely packed soil, sinkage will not be a function of g, because the weight of the object producing the sinkage and the weight of the soil [ $\rho$  in Eq. (27)] resisting the applied load will change by the same amount. Thus, the effect of low gravity is beneficial in fluffy soils where such benefits are most needed.

The beneficial effect of reduced gravity on locomotion in fluffy media is illustrated in Fig. 22 in terms of astronaut footprint pressure under 1 g and 1/6 g. According to the test data in this figure, an astronaut could stand on a 80 percent porous soil under 1/6 g, or a 60 percent porous soil under 1 g, and experience the same sinkage, which (assuming  $z/D = \frac{1}{2}$ ) is about 2 inches. A sixfold reduction in the gravity fields appears to be equivalent to a gain in fluff bearing strength associated with a 20 percent difference in porosity.



## The "Cannonball" Model

We have defined the "cannonball" model as the densely packed version of the particulate model. The "densely packed" material may actually have densities ranging from "loose" to "very dense" (in conventional soil mechanics terms) provided its porosity is below 50 percent.

### Mode of Failure

The choice of a 50 percent porosity as a boundary separating the fluff and cannonball versions of the particulate model can further be validated by the fact that the behavior of the individual particles and the forces generated during failure are different in the respective models. The low number of contact points associated with the underdense state allows a certain freedom of movement of the individual particles; therefore, no appreciable frictional resistance is generated during the relocation of the particles. As the number of contact points increases, less and less freedom of movement remains for the individual particles. At six contacts per particle, the reaction forces generated by an external force are statically determined and the degree of freedom is zero. We notice in Fig. 19 that the six-point-contact packing corresponds to a porosity of 48 percent. In this state any movement of the particle would necessarily develop friction and the mode of failure would be controlled by the frictional resistance; the resulting pattern of shear stress field is a cannonball type of failure. Thus six contacts per particle appears to be the upper limit for the underdense state. This concept is consistent with the number of contact points obtained in systematic packing of spheres, since in the loosest cubic packing, the number of contact points is six.

In the "densely packed state" compression of the material beneath the loading plate is insignificant compared to the compression in the underdense state. Characteristic of the cannonball type of failure is a relatively small sinkage up to the yield load, at which the shear resistance of the material against lateral displacement is overcome. Any load increase beyond this load results in a large sinkage. The pressure-sinkage curve shows a definite break at the yield point, thus allowing the bearing strength to be defined as the pressure at the yield point (see Fig. 15). Thus the bearing strength of a densely packed material is not associated with a specific value of sinkage, but rather with a well pronounced change in the rate of the sinkage.

## Bearing Strength

The development of interparticle friction in densely packed materials results in a mode of failure where the role of shearing stresses is predominant. The bearing strength of densely packed particulate materials, which fail in shear by developing a cannon-ball type of failure, can be computed by the bearing capacity theories which were originally developed for the purpose of determining the ultimate load carrying capacity of strip foundations resting at a certain depth on a soil having both friction and cohesion. For the purpose of this correlation study, the bearing strength of particulate (cohesionless) materials, loaded on the surface by a circular plate, is of interest. For this particular case the classical bearing capacity equation by Terzaghi (Ref. 43) reduces to a single term expressing the bearing capacity resulting from the shearing resistance developed by the weight of the soil. This term noted earlier is

$$f = \rho D S_g N_{\rho} , \quad (27)$$

where

$f$  = bearing strength,

$\rho$  = unit weight of material,

$D$  = diameter of loaded area,

$S_g$  = shape factor for circular areas, and

$N_{\rho}$  = bearing capacity factor for the two dimensional case, that is dependent on the friction angle.

It is noted that in determining bearing capacities for foundations the above term has little significance, since its magnitude is usually minor compared to the other terms (not shown) which express the bearing strength due to lateral surcharge and cohesion. Probably for this reason, the solutions available for the determination of  $N_{\rho}$  in terms of friction angle are only approximately based on a shear stress field. Because of the theoretical difficulties involved, many investigators approximated the three dimensional case of a circular loading area by applying an empirically or semiempirically determined shape factor  $S_g$  to the  $N_{\rho}$  factor which was determined for the two dimensional case. Others attempted to obtain solutions by numerical integrations of the differential equations set up for the problem. The range of the

$S_g N_p$  values obtained by these various approaches is shown in Fig. 26. Of the curves shown, 1 and 2 are numerical solutions of differential equations for the three dimensional case, and 3 through 6 are semiempirically determined shape factors combined with  $N_p$  values derived for the two dimensional case. The appreciable difference between curves 1 and 2 results from different assumptions regarding the circumferential stress in the stress field: curve 1 is based on the circumferential stress being equal to the radial stress; in curve 2 the circumferential stress is equated to the minor principal stress. In this study, curve 4 is used because it agrees reasonably well with experimental results.

#### Relationship Between Internal Friction and Porosity

As shown in the preceding section, the surface bearing strength of densely packed particulate materials can be calculated within reasonably narrow confidence limits from the angle of internal friction of the material. However, the surface bearing strength, in addition to being dependent on the angle of internal friction, is also dependent on the shape and size of the loaded area. Therefore, the bearing strength cannot be considered as a true material property, and, for this reason, it is more appropriate to seek correlation between the angle of internal friction and porosity (both true material properties) than between porosity and bearing strength. Once a correlation has been established between porosity and angle of internal friction the bearing strength for any size and shape of the loaded area and for any porosity may be calculated from Eq. (27).

For the ultimate purpose of correlating thermal properties with the angle of internal friction, from which the bearing strength may be calculated, use is made of the porosity, which is a convenient common correlation parameter. For proper correlation, it is essential that both the thermal properties - porosity correlation and the porosity-internal angle of friction correlation, refer to the same basis. Theoretical relationships between thermal properties and porosity have been developed for models consisting of one size spheres in various arrangements resulting in a variation of porosity. To conform with this model closely, only granular soils with uniform or close to uniform grain size distributions were considered in establishing correlation between porosity and angle of internal friction.

Results of experiments performed by various investigators on uniformly graded, but various size granular materials have been compiled and are graphically shown in Fig. 27. The correlation

between porosity and angle of internal friction is good, considering that the data refer to natural materials which differ in mineral composition, as well as in the size and roundness of individual particles. A study of the test results shown in Fig. 24 and of other data indicates that, in contrast to the underdense state, particle size does not significantly influence the strength properties characterized by the friction angle. The limited spread of the friction angle values shown in Fig. 27 is attributable to the effect of mineral composition and particle shape and also to the method of testing and human evaluation factors.

#### Relationship Between Bearing Strength and Porosity

As discussed in the preceding paragraphs, the bearing strength of the densely packed state, depends on the size and shape of the loaded area. For the purpose of comparison with the underdense state, bearing strengths were computed for 3-inch diameter circular plates by using Eq. (27) and  $N_p$  values according to curve 4 in Fig. 26. The  $N_p$  values were selected on the basis of friction angles which were determined for each porosity from the correlation curve shown in Fig. 27. The results of these computations are shown in Fig. 28.

In addition to the bearing strength values obtained from theoretical calculations and the porosity-friction angle correlation, experimental data on the bearing strength of densely packed particulate materials having various porosities are also available. Although a relatively large number of tests have been made on such materials, only relatively few are adequately documented with respect to porosity and particle size distribution of the particulate material. Because the tests were generally performed with plate diameters other than 3 inches, adjustments were made in the bearing strength for the differences in the diameter on the basis of Eq. (27), which indicates that the bearing strength is proportional to the diameter. The available experimental data, plotted in Fig. 28, show good agreement with the theoretical curve.

For the range of porosities approaching the underdense state, the bearing strength data and computed values show a larger spread than elsewhere. This is a transition zone at both sides of the 50 percent porosity, where the mode of failure is neither distinctly of the cannonball type nor of the compression type. Accordingly, there is some discrepancy between experimental data and computed values that are based on idealized conditions.

## Effect of Lunar Environment on Densely Packed Soils

The correlation between porosity and the angle of internal friction established in the preceding paragraphs is based on experimental data performed on terrestrial materials in a terrestrial environment. The bearing capacity theories, which were used for the calculation of bearing strength from the angle of internal friction, were developed for terrestrial conditions. The effect of the lunar environment on both the material properties and the bearing strength derived therefrom is discussed below.

From the viewpoint of the mechanical properties of densely packed particulate materials, the following three major environmental factors are significant: gravity, temperature, and absence of atmosphere.

Gravity - As was discussed earlier in connection with the fluff, the bearing capacity of densely packed particulate materials is theoretically proportional to gravity. The experimental results are shown in Fig. 25a. Thus, in contrast to the underdense state of particulate materials, where interparticle attraction forces and bearing strength are independent of gravity, in the densely packed state bearing strength is proportional to gravity and no advantage from the low gravity field of the moon is derived.

Temperature - While the temperature range at the surface of the moon is much different from that on the earth, no major effect of the temperature on the mechanical properties of densely packed particulate materials is anticipated. Temperature dependence of the strength of quartz has been reported (Ref. 51) as generally showing an increase of strength with the decrease in temperature. However, no comprehensive investigation of the effect of temperature on the strength of nonmetallic materials has been made, and data on the effect of low temperatures are lacking. It is conceivable that low temperatures would affect the interparticle friction and thereby the strength of a particulate material. Further research is needed to supplement the available data and clarify the effect of temperature on the frictional properties of minerals postulated as constituents of the lunar surface.

Absence of Atmosphere - The absence of atmosphere is expected to influence the bearing strength of densely packed particulate materials through changes in coefficient of interparticle friction.

In the ultrahigh vacuum of the moon all adsorbed surface layers with a vapor pressure higher than that of the vacuum are removed, and new surfaces, created by geological or astrophysical forces, remain clean or can be contaminated only by materials with vapor pressures lower than the exceedingly low pressure of the vacuum of the moon. The interparticle friction in the absence of contaminants may be higher than that experienced under normal conditions on the earth. Metal to soil friction tests performed at Grumman in air and in a moderate vacuum give some evidence to this effect (Ref. 52). Currently, attempts are being made to perform these friction experiments in an ultrahigh vacuum (Ref. 53).

The interparticle friction affects the bulk internal angle of friction of a densely packed particulate material. In principle this has been recognized, but at the moment no satisfactory analytical solution is available that would relate interparticle friction to bulk internal angle of friction with the porosity as parameter.

Existing theories regarding the contribution of the interparticle friction to the bulk shearing resistance of particulate materials are, in one respect or other, imperfect and do not satisfactorily explain the interaction of interparticle friction and particle interlocking. Many attempts to investigate the problem experimentally have not been very illuminating (Refs. 54 and 55). However, the principle that the shearing resistance of a particulate soil has two components, one representing the contribution of the interparticle friction and the other that of the interlocking of the particles, is generally recognized. The effect of interlocking is greatest for the most dense packing and decreases with the increase in porosity. At a certain porosity there is no expansion upon shearing; it may be assumed that the interlocking effect is zero, and the shearing resistance equals the interparticle friction. On this basis the correlation between internal friction and porosity, shown in Fig. 27, is also valid for the effect of interlocking; the friction angle at the highest porosity equals the interparticle friction, and the increase of the internal friction over that in the loosest state is the effect of interlocking.

Indications are that the interparticle friction increases as the surface contaminants are removed in ultrahigh vacuum. The effect of such an increase on the bulk internal friction would depend on the porosity of the particulate material and on the range of the interparticle friction in which the increase takes place. At high porosities, say in the neighborhood of 50 percent, the increase of the bulk material friction would be proportional to the increase of the interparticle friction. At low porosities and in the low range of interparticle friction, say up to about  $f_p = 0.5$ , the

bulk internal friction is relatively insensitive to changes in the interparticle friction. For example at  $p = 40\%$  an increase of the interparticle friction from  $f_r = 0.3$  to  $f_r = 0.4$  would result in an increase of the bulk angle of internal friction from  $\phi = 29^\circ$  to  $\phi = 33^\circ$ , according to Sjaastad's theory. In the range of high interparticle friction, say above  $f_r = 0.5$ , all theories indicate that the bulk internal friction would exponentially increase with an increase of the interparticle friction. According to some theories, the bulk angle of internal friction reaches infinity at a definite value of interparticle friction; this would mean that above this value of interparticle friction the particulate material would behave as solid.

We conclude this discussion by pointing out that the increase in bearing strength of the cannonball model due to clean surface effects in a high lunar vacuum, would be relatively more appreciable at porosities approaching 50 percent than at the lower porosities, where the mechanical-interlocking component predominates over the purely frictional component.

#### Departures of Natural Soils from Theoretical Model

The theoretical model of densely packed particulate material, consisting of uniform spheres in regular packing, is highly idealized. Any departure from this model that natural soils are likely to exhibit may affect the applicability of the correlations for the idealized model established herein. In the following paragraphs the differences between both terrestrial and postulated lunar soils from their idealized models, and the effect of these differences on the validity of the established correlation, are assessed.

Particles of terrestrial soils have a wide range of shapes. The quartz and feldspar particles are usually bulky and become well rounded if transported or moved about in water for a long time. Such particles resemble smooth spheres fairly closely. Departures from the spherical shape and ideal smoothness may be evaluated from Fig. 27 where friction angles of various material soils are shown. The wide scatter of the friction angle-porosity relationship is due to the effect of roundness, surface smoothness, and mineral composition.

Particles consisting of mica and clay minerals are usually flaky and sometimes elongated. Assemblies of such particles behave differently from the idealized model, and the correlations established for spheres do not apply for such materials.

The particle shape of lunar soils, judging from the shape of meteorites and impact ejecta, is likely to be bulky but not rounded. Angularity generally increases the friction angle; therefore, the upper limit of the porosity-friction angle correlation is likely to apply for such materials.

The sizes of terrestrial soils are rarely confined to a uniform range as assumed in our model. Beach sands and "running" sands are the best known examples of soils having almost uniform sizes. The nearly uniform sizes of these soils are the result of some sorting action of flowing water which probably never existed on the moon. Thus, it is more reasonable to assume that the particle sizes of lunar soils follow some probability distribution.

The deviation of natural soils from the uniform sphere model, in respect to the size of the particles, has important, but not yet evaluated, implications regarding the thermomechanical correlations. As far as mechanical properties are concerned, the interlocking effect in an assembly of particles that have a wide range of sizes is more pronounced than in one having uniform sizes. On the other hand, at a given porosity, the relative density of a packing (i.e., the density related to the maximum and minimum densities of a particular particle size distribution) is less in a particulate material with a wide range of sizes than in one with uniform sizes. Further investigations are required to evaluate the effect of these two factors on the mechanical properties. Because particle size distribution affects thermal properties in two ways, via radiative and solid conductivity, it is possible that the correlation established for uniform size spheres will also hold approximately true for materials consisting of a wide range of particle sizes. Further investigations are required to evaluate the degree of the correlation or to establish new correlations for particulate materials with more than one particle size.

#### Semiempirical Strength-Porosity Relationship of Particulate Media

Best-fit curves for the bearing strength versus porosity of "fluff" and "cannonball" type soils are shown in Figs. 22 and 28. The two curves are combined in Fig. 29; for the sake of clarity, the data points are omitted. The composite curve represents the bearing strength of particulate (i.e., nonconsolidated) media over the full range of porosities conceivable for such media. About four orders of magnitude of bearing strength are encompassed by the composite curve, ranging from 0.1 to 100 psi.



The "fluff" and "soils" portions of the curve in Fig. 29 overlap in the 1 to 7 psi region. The resulting discontinuity at about 50 percent porosity should not be surprising, since the material on either side of this line obeys different laws of failure. In the densely packed state (porosity  $\ll$  50%), soil bearing strength is largely a function of plate size and interparticle friction. In the underdense state (porosity  $\gg$  50%), these factors become less and less important and new ones come into play, such as depth of sinkage, surface energy, and particle size.

A much wider scatter of data is generally observed in the region of transition (near 50% porosity) than at very low or very high porosities. The scatter in this region appears to be due to the unpredictable interaction of lateral and local shear movements during failure. The relatively large number of factors that come into play during such complex failures are more difficult to control than when failure is due predominantly to either one or the other mode.

Despite the observed discontinuity and scatter, the over-all composite curve in Fig. 29 could serve as a useful lower boundary for the strength of porous media. The upper boundary (not shown in Fig. 29) would be represented by the bearing strength versus porosity curve of "vesicular" media, which we previously defined as a porous material in which the solid phase is fully continuous. The following sections deal with the mechanical properties of these relatively unexplored media.

## BEARING STRENGTH OF VESICULAR MODEL

### Literature Review on Vesicular Rocks

The mechanical properties of porous rocks, such as scoriaceous lavas, pumiceous rock froths, and related rocks are poorly documented in the literature. Available general information on rock mechanics is largely contained in mining, civil engineering, and geophysical publications. There are many varieties of rock froths all over the world whose mechanical properties are not known. Geologists have rarely concerned themselves with the mechanical properties of porous rocks. Interest in these materials has been largely stimulated by recent investigations of the optical and thermal properties of the lunar surface (Refs. 6 and 7) and the upwelling of molten silicates in a vacuum (Ref. 56).

The following sources were checked for relevant information on the mechanical properties of porous rocks:

1. Bibliography and Index of North American Geology, United States Geological Survey.
2. Geological Society of American Bibliography and Index.
3. Geoscience Abstracts, American Geological Institute.
4. NASA's STAR Publications.
5. Annals of the N.Y. Academy of Sciences.
6. SCIENCE, A.A.A.S. publication.
7. International Journal of Rock Mechanics and Mining Science.
8. Bulletin of the American Geophysical Union.
9. Journal of the Soil Mechanics and Foundation Division, A.S.C.E.
10. ICARUS.

Many other publications were also consulted. The most valuable information sources on engineering properties of rocks in general were found in the International Journal of Rock Mechanics and Mining Science.

The most inclusive known geologic literature is contained in the U.S.G.S.'s Bibliography on North American Geology and in the Bibliography of the Geological Society of America, Exclusive of North America. The 1785-1918 U.S.G.S. Geologic Literature on North America contains many sources on lava, igneous rocks, and volcanoes, but no mention of mechanical properties of rock froths are quoted.

The 1919-1928 U.S.G.S. Bibliography of North American Geology contains sections on engineering geology and mining geology, which were checked, but which contained no reference on mechanical properties of rock froths. The section on igneous and volcanic rocks was extensive, but no information on rock froth mechanics was evident.

The 1929-1939 U.S.G.S. Bibliography of North American Geology contains no significant references on engineering properties of rocks. The 1940-1949 U.S.G.S. Bibliography of North American Geology has extensive sections on lavas and engineering geology, but there is no mention of mechanical properties of rock froths.

The 1950-1959 U.S.G.S. Bibliography of North American Geology reveals nothing of immediate value under sections such as engineering geology and lavas. There is extensive literature on volcanology (Hawaiian volcanoes), but nothing on specific engineering properties of porous lavas. However, there are several quoted references on physical properties of mine rocks, stress data, and other factors on strength and elastic properties of rocks, time dependent deformation and failure of geologic materials, ways of measuring rock pressures, etc.

The 1960 U.S.G.S. Bibliography of North American Geology has a reference on rock mechanics, but nothing on rock froths. The 1961 U.S.G.S. Bibliography of North American Geology contains several references on rock mechanics and physical rock properties. The section on igneous petrology contains no sources of information on vesicular rocks. This last publication became available in 1965. The U.S.G.S. Bibliographies for the years 1962-1965 are not yet published.

Another important bibliography, which is exclusive of North America, is that published by the Geological Society of America (G.S.A.). Here too the respective sections on engineering geology, igneous geology, and lavas were carefully examined and checked. Like the U.S.G.S. Bibliography, it contains references dealing with the mechanical and engineering properties of rocks. However, there is nothing significant on specific strength properties of rock froths.

Some timely and useful information on rock mechanical properties was noted in the International Journal of Rock Mechanics and Mining Science, Colorado School of Mines Quarterly, Engineering Mining Journal, and Mechanics, which is sponsored by the Penn State University Mineral Industries Experimental Station. Most of the references contained in these publications deal with the mechanical properties of rocks in general.

Rock mechanics is a new science, and the chapter on the mechanics of porous rocks is yet to be written. What follows is a brief stress analysis of rigid-porous media and a preliminary compilation of useful strength versus porosity data on such manufactured porous materials as ceramics, porous plastics, cellular concrete, etc.

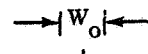

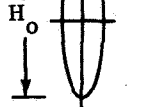
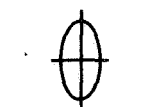
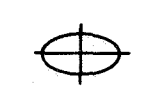

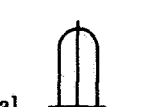
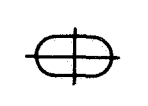

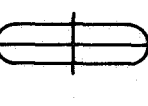
## Stresses in Porous Media

In general, the mechanical properties of porous materials are the result of a combination effect of the mechanical properties of the constituent solid material and the intricate internal stress pattern ensuing from the pore geometry. Regarding the strength properties, the most significant effect of the pores is 1) that their surface must be free of normal and shear stresses and, therefore, only stress patterns compatible with this condition can exist within the material; and 2) that they reduce the effective cross-sectional area. A recent preliminary evaluation of these effects, made at Grumman, is reported in Ref. 57. This study showed that the strength of porous materials possessing a systematic arrangement of spherical holes rapidly decreases with the increase in porosity.





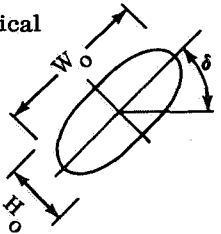
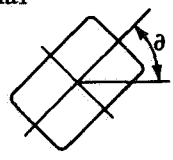
Pore geometry, however, is likely to be far more intricate in most natural vesicular rocks than the idealized arrangements shown in Fig. 30. Unfortunately, beyond visual descriptions and over-all porosity percentages there is very little information available on the pore geometry and the distribution of pore sizes in terrestrial vesicular rocks. These factors affect the internal stress distribution, and hence the strength of the porous system. A three dimensional analytical solution for the stress concentration around holes is available only for the case of a single spherical cavity in a uniform stress field, while numerous investigations, including photoelastic analyses, have been made in connection with the effect of holes on the stress distribution in two dimensional plates and also in connection with the problem of stress distribution around tunnel and underground openings having various cross sections. Although internal stresses that are developed during compression in porous rocks are essentially three dimensional, a qualitative assessment of the effect of pores on the internal stress distribution may be made on the basis of two dimensional cases. Table IV summarizes the stress concentration factors for various shapes of openings as obtained from Ref. 58. From this tabulation the following conclusions may be drawn.

An opening in a uniform stress field with an axis that is codirectional with the stress field results in a stress concentration of the same sign and about 1.5 to 9 times the applied stress and of the opposite sign about equaling the magnitude of the applied stress. Openings with the axis inclined to the direction of the uniform applied stress field result in higher stress concentration factors for stresses of the same sign. Stress concentrations of the opposite sign are in the same range as for openings with codirectional axis.

Stress Concentrat

Single Opening:		Maximum Normal Stress		Ratio of Stress Conc
Three Dim: Spherical		+	-	
		1.93-2.17	0.21-1.0	2.17-9.0
Circular		3.0	1.0	3.0
Elliptical	 $\frac{W_o}{H_o} = 0.25$	1.5	1.0	1.5
	 $\frac{W_o}{H_o} = 0.5$	2.0	1.0	2.0
	 $\frac{W_o}{H_o} = 2.0$	5.0	1.0	5.0
	 $\frac{W_o}{H_o} = 4.0$	9.0	1.0	9.0
Ovaloidal	 $\frac{W_o}{H_o} = 0.25$	1.5	0.9	1.7
	 $\frac{W_o}{H_o} = 0.5$	1.6	0.85	1.9
	 $\frac{W_o}{H_o} = 2.0$	3.4	0.85	4.0
	 $\frac{W_o}{H_o} = 4.0$	4.8	0.85	5.6

Factors Around Openings

			Max Normal Stress		Ratio of Stress Conc	
			+	-		
Rectangular, Rounded Corners		$\frac{W_o}{H_o} = 0.25$	1.5	1.0	1.5	
		$\frac{W_o}{H_o} = 0.5$	1.5	1.0	1.5	
		$\frac{W_o}{H_o} = 2.0$	2.5	0.8	3.12	
		$\frac{W_o}{H_o} = 4.0$	3.0	0.8	3.75	
Single Inclined Opening			Max Normal Stress		Ratio of Stress Conc	
Elliptical		$\frac{W_o}{H_o}$	+	-		
		2 @ delta = 0	5.0	@ delta = 45°	1.1	4.55
		3 @ delta = 0	7.0	@ delta = 45°	1.3	5.4
		4 @ delta = 0	9.0	@ delta = 45°	1.5	6.0
Rectangular		$\frac{W_o}{H_o}$				
		1 @ delta = 45°	4.7	@ delta = 67.5	1.3	3.6
		2 @ delta = 45°	1.6	@ delta = 45°	5.7	3.5
		3 @ delta = 45	1.8	@ delta = 45°	6.5	3.6
4 @ delta = 45	2.0	@ delta = 45°	7.1	3.5		
Multiple Openings			Max Normal Stress			
Row of Circular Openings			+	-		
			3.26	0.6	5.4	

The increase of the concentration of stresses around a row of circular openings is small compared with that around a single opening. The stress concentration factor increases from 3 to 3.26 for stresses of the same sign. For a row of circular holes spaced with centers at two diameters, the average stress in between the holes is twice that of a single hole in an infinite mass. Thus, the average stress between holes increases much more rapidly than the maximum stress occurring at the place of critical concentration. The concentration of stresses with the sign opposite to that of the applied stresses is less in the case of a row of holes than when only a single hole is present. Thus adjacent holes appear to relieve the concentration of stresses of the opposite sign.

In the derivation of the above concentration factors it is assumed that the holes are located in an infinite uniform stress field. Because of this assumption, the above stress concentration factors do not lend themselves readily for correlation with porosity. The most important conclusion that can be derived from the above analyses of the strength properties of porous rocks is that holes invariably produce boundary stresses of a sign opposite to that of the applied stress. Because of the development of stress concentrations of both signs, the bulk strength properties of porous rocks may either depend on the compressive or the tensile strength of the nonporous rock material. Since the tensile strength of rocks is generally many times less than their compressive strength, the tensile strength of the nonporous material is likely to govern both the bulk compressive and the tensile strengths of porous rocks. Concerning the bulk compressive strength, the most critical situation occurs when a hole or a hole pattern is located in a zone where compressive stresses are already concentrated due to another system of holes. Such porosity patterns, known as primary and secondary porosities, are frequently observed in terrestrial volcanic rocks. The hole sizes in the two patterns may differ by an order of magnitude. For example, measurements of pore sizes in pumice made by Prado laboratories by the mercury intrusion method (Ref. 59) indicate that 47 percent of the pore volume is in the  $200\mu$  to  $50\mu$  range and 30 percent in the  $0.5\mu$  to  $0.1\mu$  range. A schematic presentation of these effects is shown in Fig. 31.

### Mechanical Properties of Manufactured Porous Materials

In view of the scarcity of information available on the mechanical properties of highly porous natural rocks and the difficulties of analytically determining these properties on the basis of pore

geometry, it is of interest to examine the reported, mechanical properties of manufactured highly porous materials with particular respect to the strength-porosity relationship.

### Porous Ceramics

Recent developments in the field of ceramics resulted in increasing attention to porous ceramic products and in systematic studies of the porosity-strength relationship for these materials. Unfortunately, these studies do not include the range of very high porosities which is of primary interest with respect to the postulated lunar vesicular rocks. Since in the present correlation study only those aspects of the mechanical properties of ceramics are of interest which have a bearing on the porosity-strength correlation, details of these investigations are not repeated here. A brief summary of the pertinent findings is given below.

Results of experiments performed on porous alumina, zirconia, and other ceramic materials indicate that the strength-porosity relationship may be fairly well represented by a straight line on a semilog plot in the porosity range of about 10 to 60 percent. When experiments were carried out with porosities larger than about 60 percent, the strength showed a sharper drop with porosity than the straight line would indicate. Figure 32 shows these results together with strengths of other porous materials in relation to their porosity.

Duckworth, Ryshkewitch (Refs. 60 and 61), and others expressed the semilogarithmic straight line relationship in the form

$$f = f_0 e^{-bp} \quad (30)$$

where

$f$  = strength of porous material,

$f_0$  = strength of nonporous material,

$b$  = parameter, and

$p$  = porosity.

This empirical relationship does not satisfy the condition of zero strength at 100 percent porosity, therefore, its extrapolation for a porosity range beyond that for which it was established is not



justified. It is noted here, that the term  $f_0$  designates a theoretical strength of the nonporous material which is obtained as the intercept of the straight line at zero porosity. This is not necessarily the same as the strength of an ideally nonporous material, because at low porosities the straight line relationship may not hold due to the effect of the pores on fracture initiation.

Hasselmann (Ref. 62) proposes that another type of relationship (developed to express the porosity dependence of elastic moduli) be also used to express the strength-porosity relationship. The proposed relationship is as follows:

$$f = f_0 \left[ 1 + \frac{Ap}{1 - (A + 1)p} \right], \quad (31)$$

where

$p$  = porosity and

$A$  = experimentally determined parameter.

Knudsen (Ref. 63) is in favor of using a relationship originally proposed by Bal'shin to express the variation of strength of ceramics with changing porosity. This equation is of the form

$$f = f_0 (1 - p)^m, \quad (32)$$

where  $m$  = empirical constant. A discussion of the applicability of these equations to the strength of porous rocks is given below together with the evaluation of porosity-strength relationships of other materials.

### Rigid Plastic Foams

Rigid plastic foams include a large variety of types having a wide range of physical properties. Investigations of the strength properties of rigid urethane foams have been carried out for a wide range of porosities and are, therefore, of particular interest. The strength of rigid urethane foams is influenced by many factors, such as catalyst, type of mixing and base materials, foaming system, etc. It was found, however, that the influence of these factors on the strength is only slight if they do not change the density of the rigid foam (Ref. 64).

The density-strength relationship indicated by the experimental results is a narrow, straight band on a double logarithmic plot. The centerline of this band corresponds to a relationship of the type

$$f = f_0(1 - p)^m,$$

the same as proposed by Knudsen for ceramic materials. For rigid urethane foams the  $m$ -parameter which fits the experimental results best is found to be 1.416. The band is plotted in semi-logarithmic scale in Fig. 32 for comparison with ceramic and other materials. For porosities of up to about 60 percent, the above exponential type of relationship fits a straight line in the semi-logarithmic plot fairly close. This is in accordance with Knudsen who pointed out that in the low porosity range experimental results fit either type of relationship fairly well, and that by proper selection of parameters the two equations can be made almost identical in the low porosity range.

#### Cellular Concrete

Cellular concretes are produced by mixing gas generating agents with the other ingredients of concrete and expanding the mixture to a desired volume prior to the setting of the cement. The expanded concrete is then cured either by conventional moist curing methods or in an autoclave at a high temperature. The resulting concrete has a homogeneous cell structure and a density varying from 10 to 100 lbs/cu ft.

Strength properties of cellular concretes are of particular interest to the manufacturers since their products are used as building blocks or other structural elements. A compilation of strength test results from a variety of sources was made by Valore (Ref. 65). The results of tests on moist, cured, cellular pure cement and cement-sand concrete are shown in Fig. 33. The data are from various sources and were obtained on various size specimens and by different testing methods. Despite these differences, the overriding effect of the porosity on the strength of these cellular concretes is remarkable.

In the referenced study no attempt was made to express the strength-porosity relationship for cellular concretes in an analytical form. The general trend of this relationship is similar to that found for other materials as can be seen from Fig. 32.

The test results may be fairly closely fitted on the log-log plot by a straight line (Fig. 33). This yields a value of 2.6 for  $m$  in Eq. (32) for pure cement and 3.4 for cement-sand cellular concretes.

#### Other Porous Materials

The data available on the strength of other porous materials are also plotted in Fig. 32. For some materials, such as pumice block and foamglass, strength data for only one porosity value were obtainable.

#### Empirical Strength-Porosity Relationship of Vesicular Media

In order to compare and evaluate the various forms of porosity-strength relationships proposed by various investigators, Fig. 34 has been prepared. Curve 1 of this figure shows the relationship proposed by Ryshkevitch, Duckworth, and others for ceramic materials. The parameter "b" was taken as 7, which was found to fit experimental data on porous alumina. Curve 2 shows the relationship proposed by Hasselman, with  $A = -4$ , which was found to fit data on the elastic moduli of alumina. Since close linear correlation exists between the elastic moduli and strength of the porous materials, the same parameter was used to illustrate the strength-porosity relationship. Curve 3 shows the strength-porosity relationship established for rigid urethane foams. The area reduction factors obtained analytically (Ref. 57) for cubic and rhombic arrangement of spheres are also shown (curves 4 and 5).

The proposed relationships equally indicate that porosity reduces the strength of the materials in excess of the proportion by which the average cross section is reduced by the porosity. For a systematic arrangement of spherical holes, the minimum area in critical cross sections shows a similar relationship with porosity as the semiempirical relationships proposed to represent the strength-porosity relationship.

In the study of lunar surface materials, the high porosity range is of interest. While the various relationships illustrated in Fig. 34 could be made to fit experimental data quite closely in the lower porosity range by suitable selection of the free parameter, the fit will not be as good at high porosities.

This point is illustrated in Fig. 35 which shows the porosity-strength relationships in the high porosity range for the three expressions indicated in Fig. 34. The parameters of these expressions were normalized for the condition that at  $p = 50$  percent,

the strength is 20 percent of the nonporous strength. Figure 35 shows clearly that curve 1 does not meet the condition of zero strength at 100 percent porosity. Also, the other two curves differ appreciably from curve 1 and from each other.

It appears that curve 3, expressed by

$$f = f_0(1 - p)^m,$$

is a better choice. This expression was found valid for rigid urethane foams for porosities encompassing practically the whole range from 0 to 100 percent. As Fig. 35 shows, its use in the high porosity range is conservative when the  $m$ -parameter is established on the basis of strength data in the medium porosity range. For vesicular rocks, the  $m$ -parameter would have to be determined empirically. A literature search for information on the strength of vesicular rocks showed that there are not sufficient data available for even a tentative determination of the  $m$ -parameter.

If we adopt the above expression as the most valid, we may assign a value of 20,000 psi as a reasonable figure for the strength  $f_0$  of the nonporous natural rock. This figure is based on data compiled in Table V. As to the parameter  $m$ , a value higher than 1.434 (established for rigid-urethane foams) would appear justified. The value for  $m$  that gives a best fit to the test data compiled in Fig. 32 is 2.6. Therefore, the expression

$$f = 20,000 (1 - p)^{2.6} \quad (33)$$

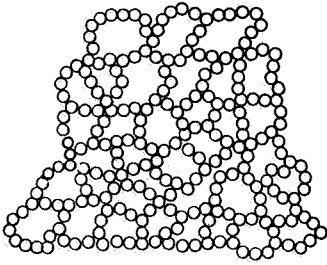
is tentatively proposed as an empirical formula for the strength of vesicular rocks. An experimental program involving a sufficient number of strength tests on vesicular rocks having various porosities is needed to establish the  $f_0$  and  $m$  parameters with a reasonable degree of confidence.

TABLE V

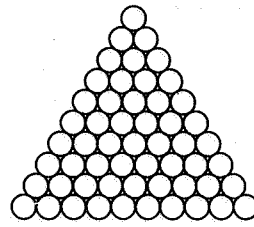
Physical Properties of Rocks

Compiled by Lawrence C. Wood (Ref. 66)

Rock Type	Average Crushing Strength lbs/in <sup>2</sup>	Range of Strength lbs/in <sup>2</sup>	Tensile Strength lbs/in <sup>2</sup>	Shearing Strength lbs/in <sup>2</sup>
Granite	21,030	5260 - 53900	427 - 711	2135 - 4266
Syenite	27,850	14220 - 48900		
Diorite	27,850	13660 - 36980		
Gabbro, Diabase, etc.	25,600	6540 - 66800		
Gneiss	22,190	11520 - 46500		
Quartzite	28,730	3693 - 45500	427 - 1282	1422 - 4266
Marble	14,500	4405 - 37220	427 - 1282	
Sandstone		1563 - 35800	142 - 427	1422 - 2844
Limestone		853 - 51150	427 - 853	2135 - 3555
Slate	21,020	8530 - 44500	3555	
Serpentine	17,490	8960 - 17490	853 - 1563	2560 - 4840
Tuff	4,405	1422 - 7390		
Basalt	35,580	28440 - 49750		711 - 2135
Felsite	34,820	28440 - 41200		

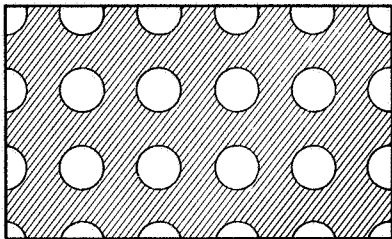


a) Fluff  
(porosity >50%)

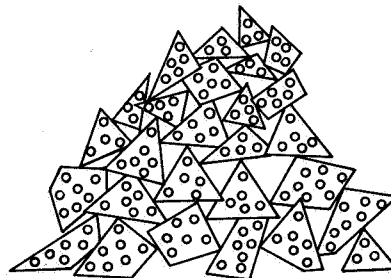


b) Cannon Ball  
(porosity <50%)

Particulate Models

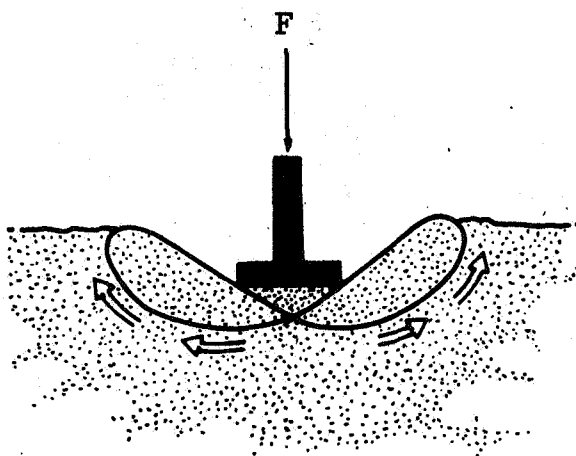


Vesicular  
(any porosity)

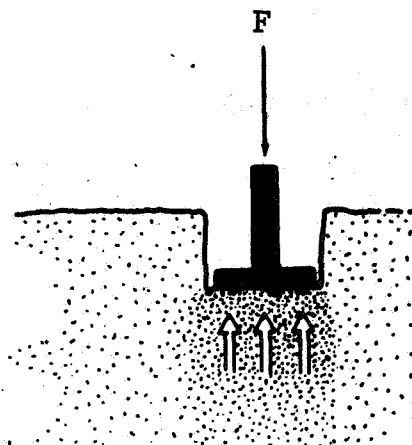


Hybrid  
(any porosity)  
(Ref Phase IV)

Fig. 12 Major Postulated Lunar Surface Model

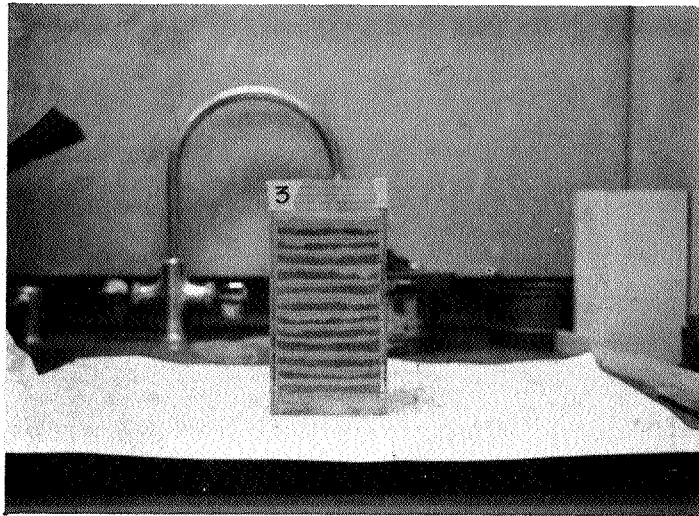


(a) "Cannonball" Model  
Lateral Shear Failure

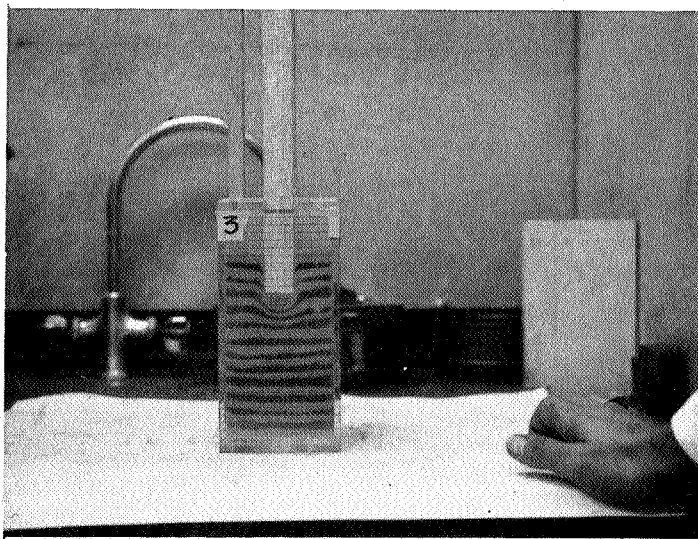


(b) "Fluff" Model  
Local Shear Failure

Fig. 13 Modes of Failure in Particulate Media



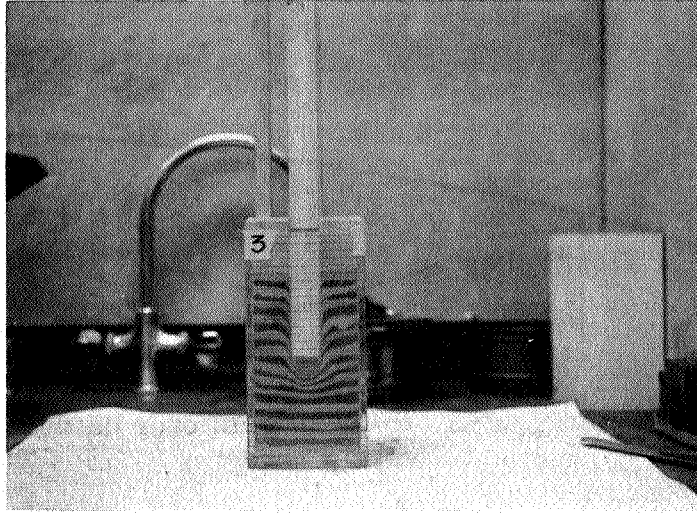
a) Undisturbed Soil



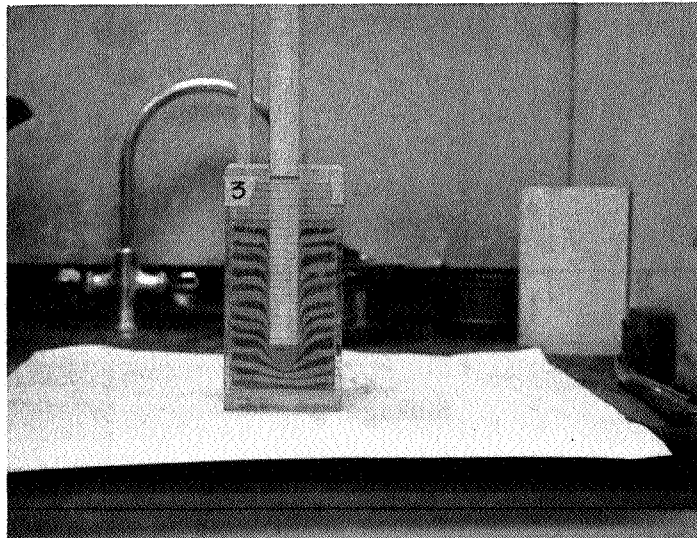
b) Penetration =  $1\frac{1}{2}$ " , Depth of Compressed Bulb  $\approx \frac{3}{4}$ "

Fig. 14 Failure Patterns in Fluff Model  
(Sheet 1 of 2)





c) Penetration = 3", Depth of Compressed Bulb  $\approx$  1"



d) Penetration =  $4\frac{1}{2}$ ", Depth of Compressed Bulb  $\approx$  1"

Fig. 14 (Cont.) Failure Patterns in Fluff Model  
(Sheet 2 of 2)

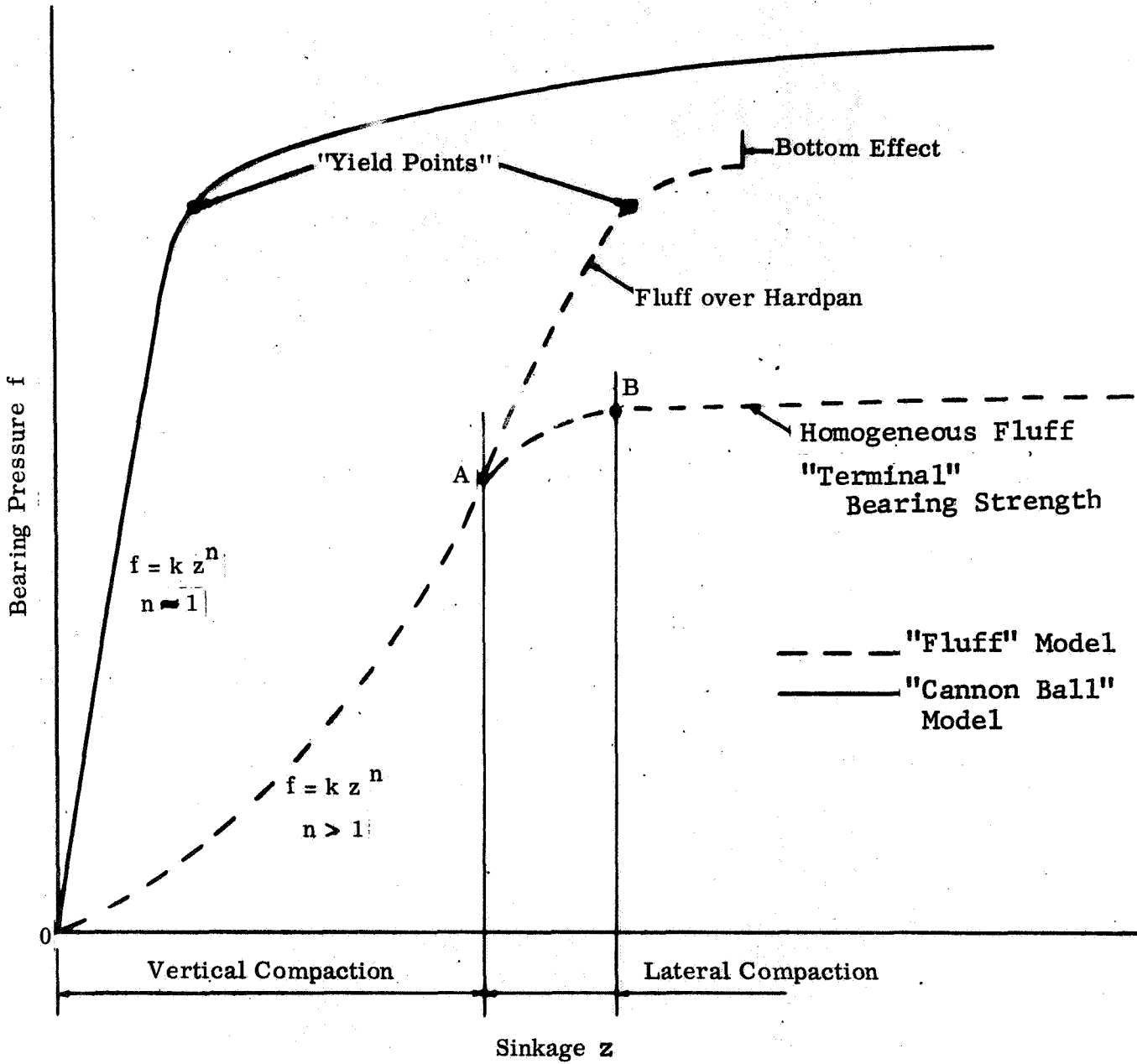


Fig. 15 Settlement Curves in Particulate Media

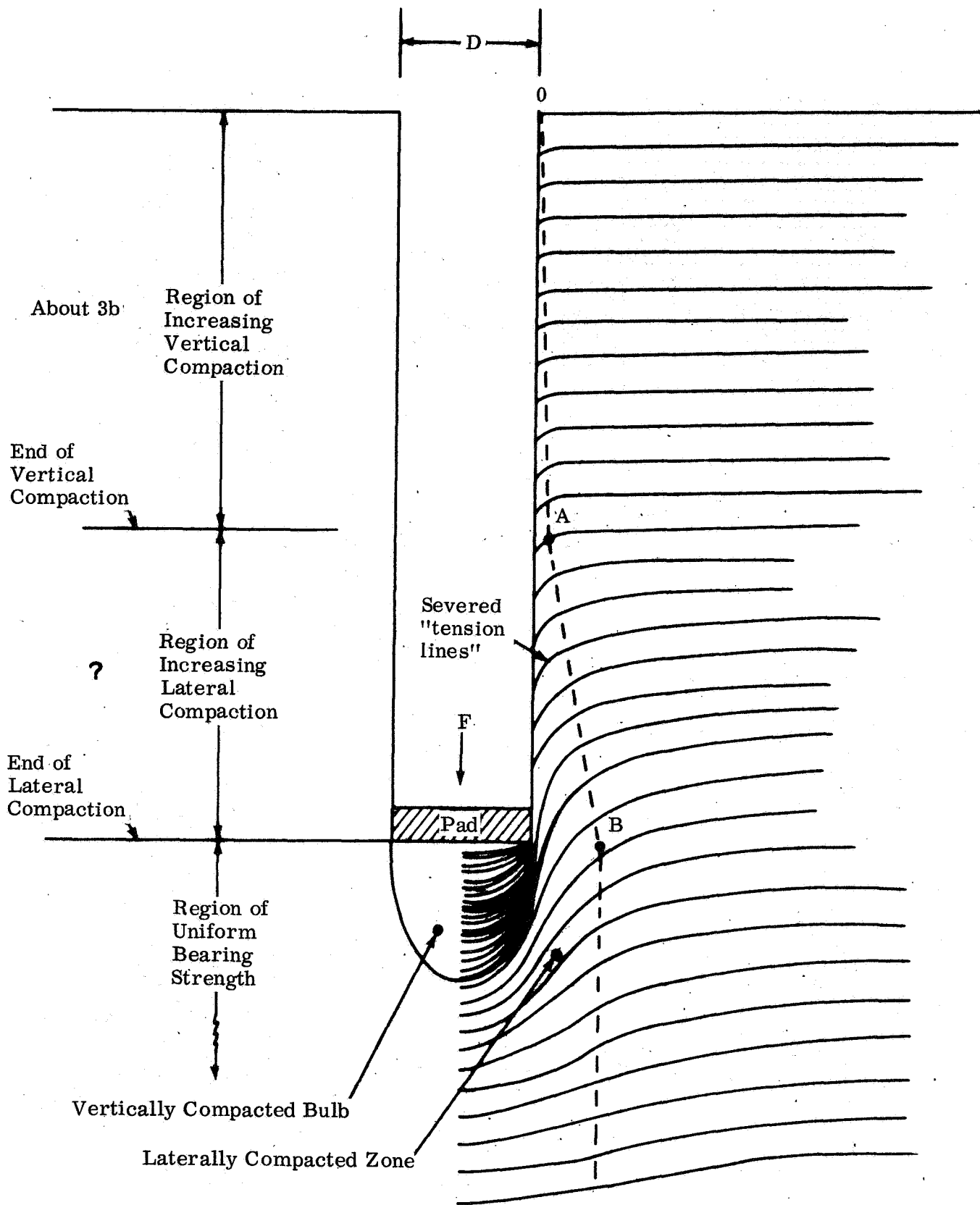


Fig. 16 Postulated Failure Mode in Semi-Infinite Fluffy Medium

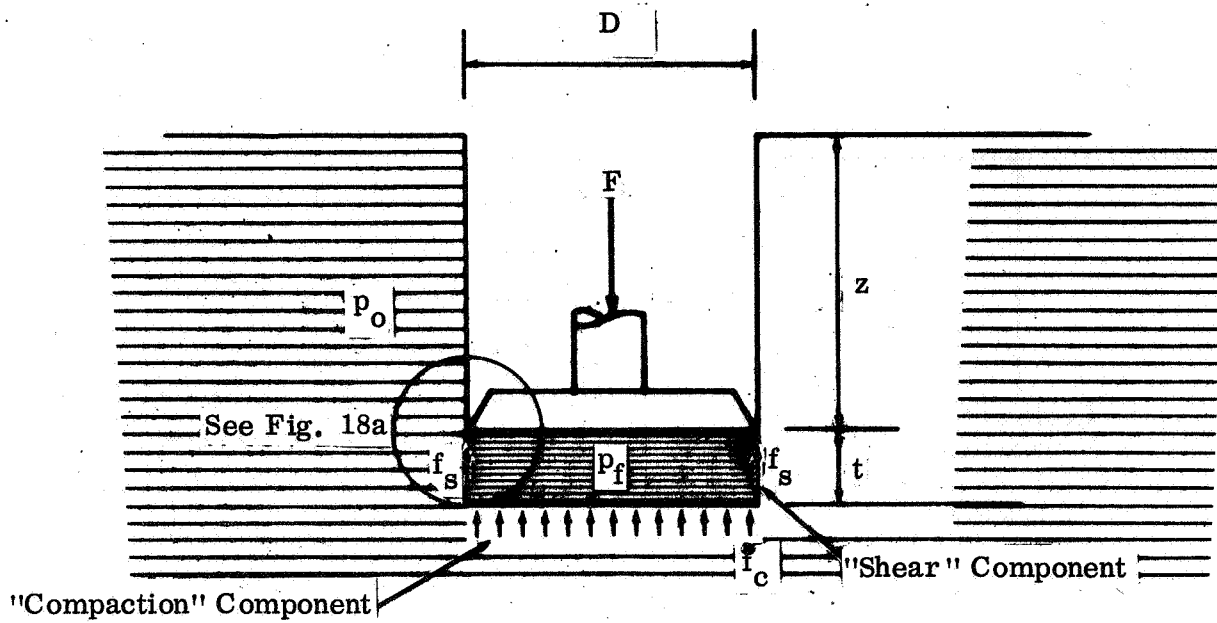


Fig. 17 Compaction in Fluffy Soil

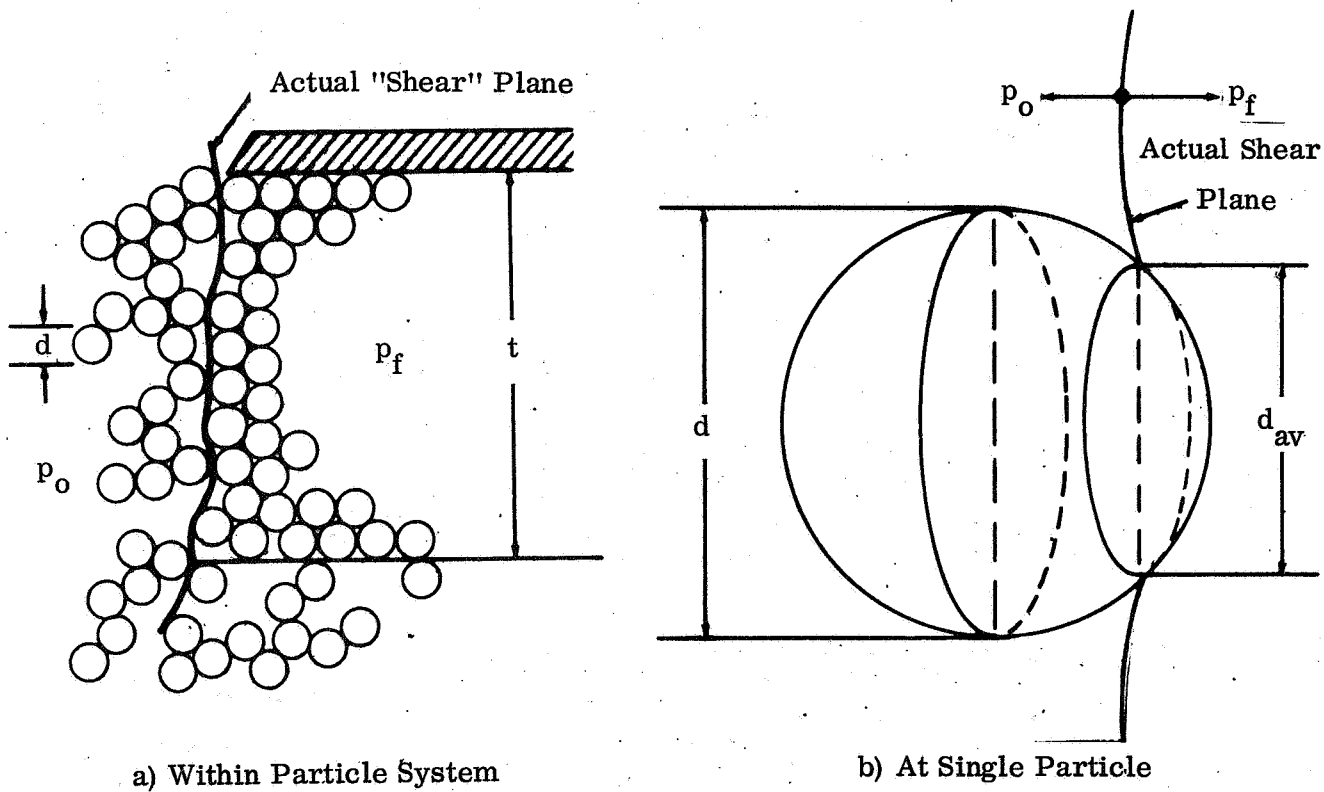


Fig. 18 Interface Between Undisturbed and Compacted Fluffs

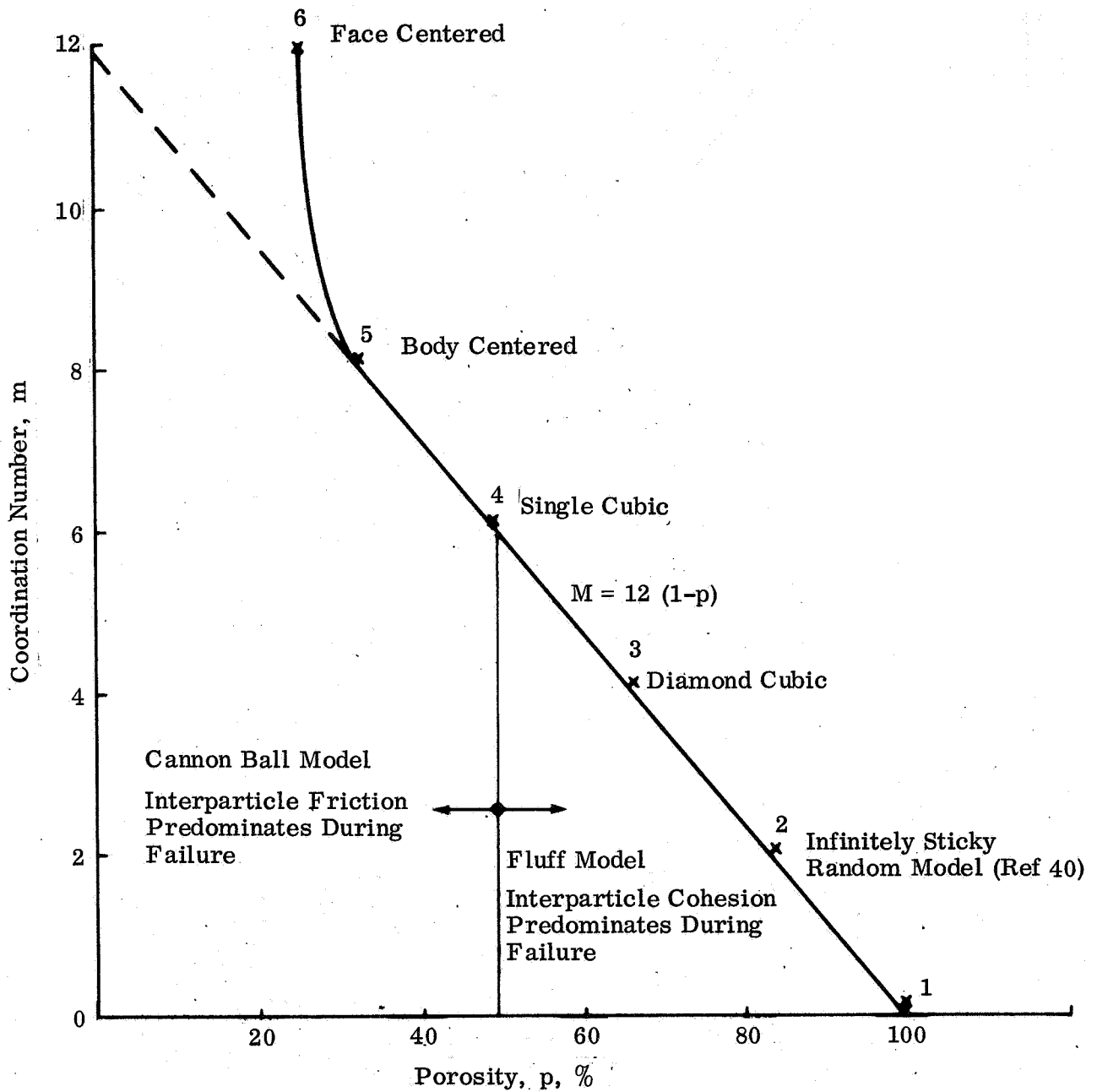


Fig. 19 Relationship Between Coordination Number  $m$  and Porosity  $p$

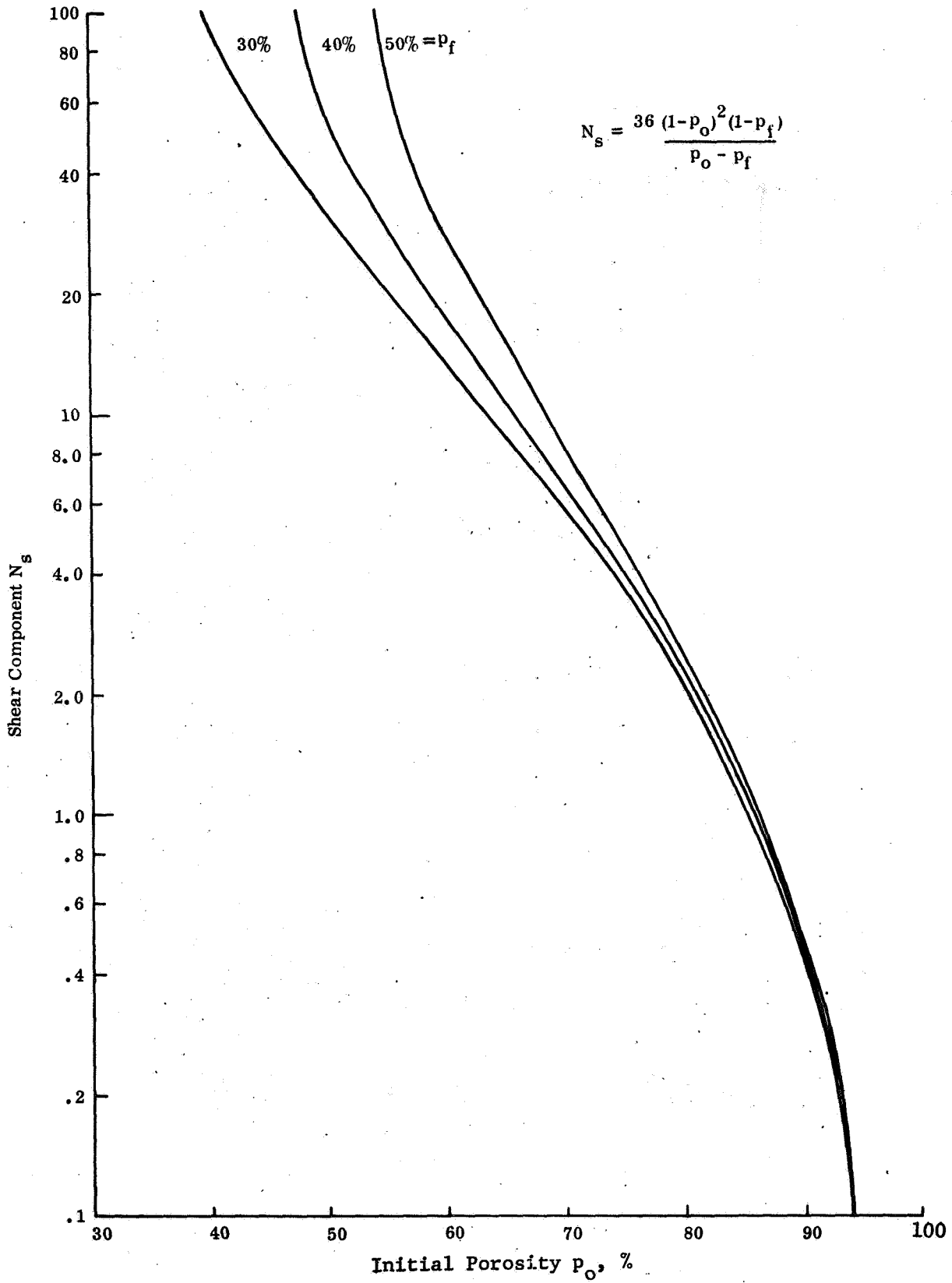


Fig. 20a Relationship Between Initial Porosity  $p_o$  and Bearing Capacity Factors, Shear Component  $N_s$

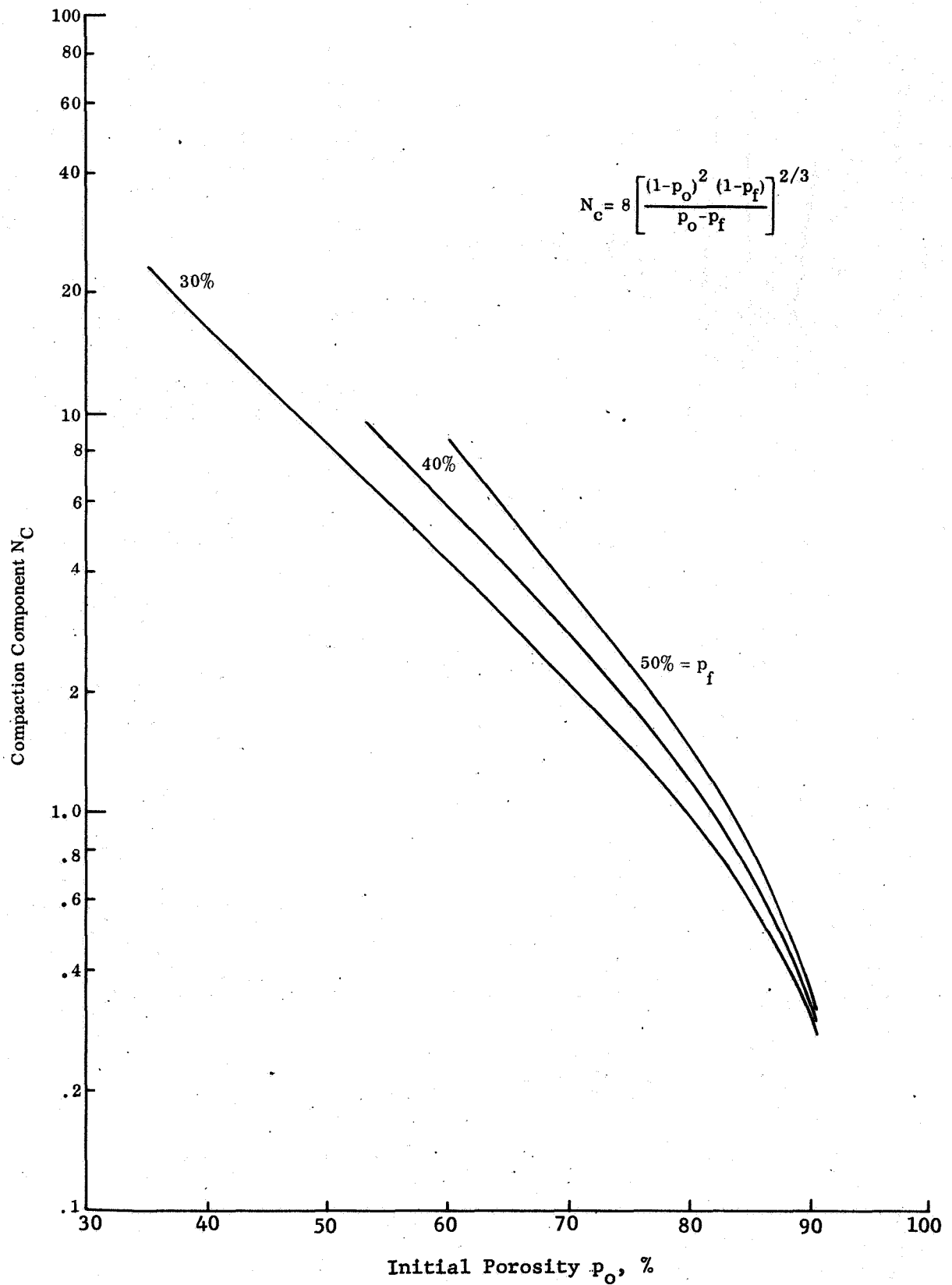


Fig. 20b Relationship Between Initial Porosity  $p_o$  and Bearing Capacity Factors, Compaction Component  $N_c$

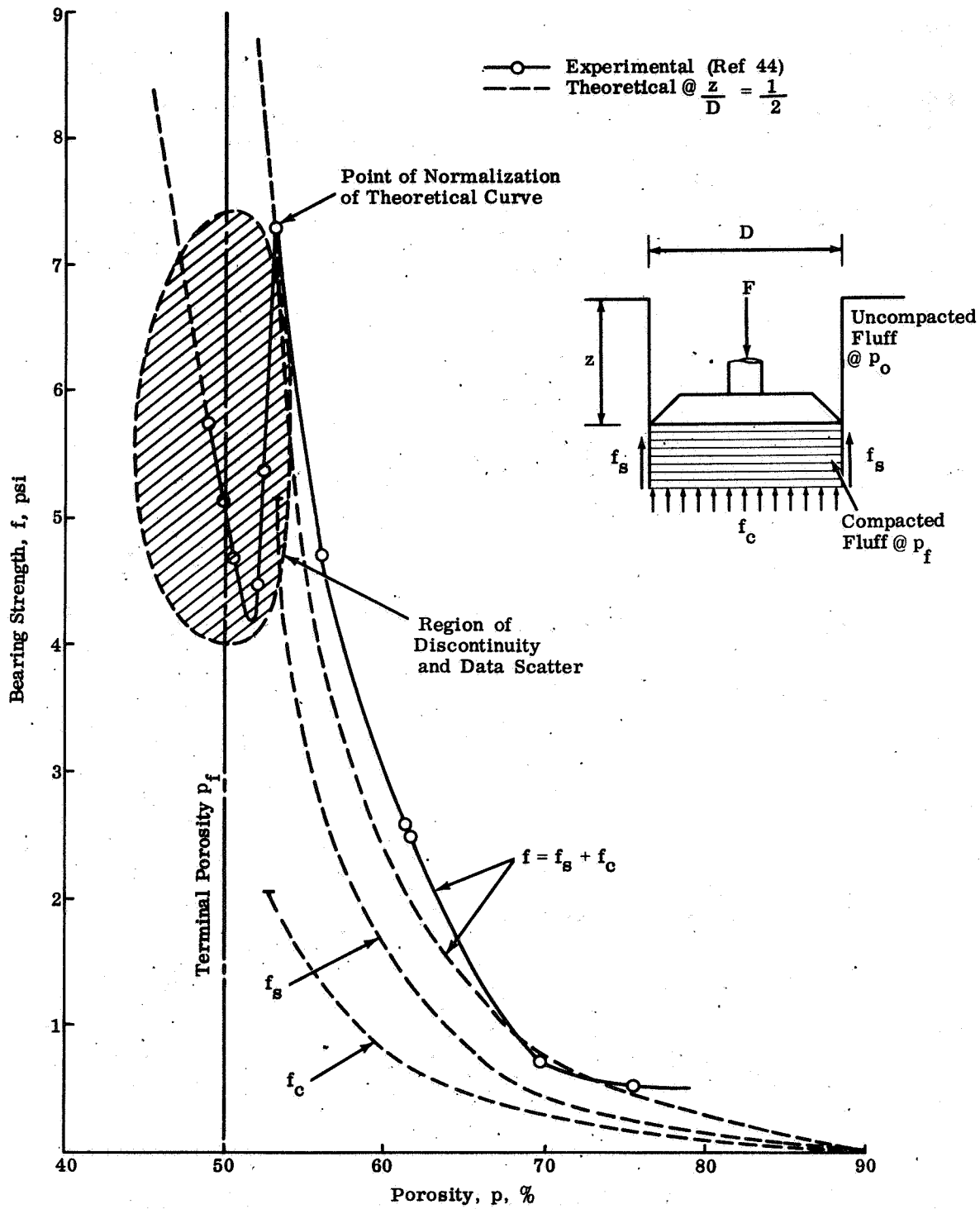
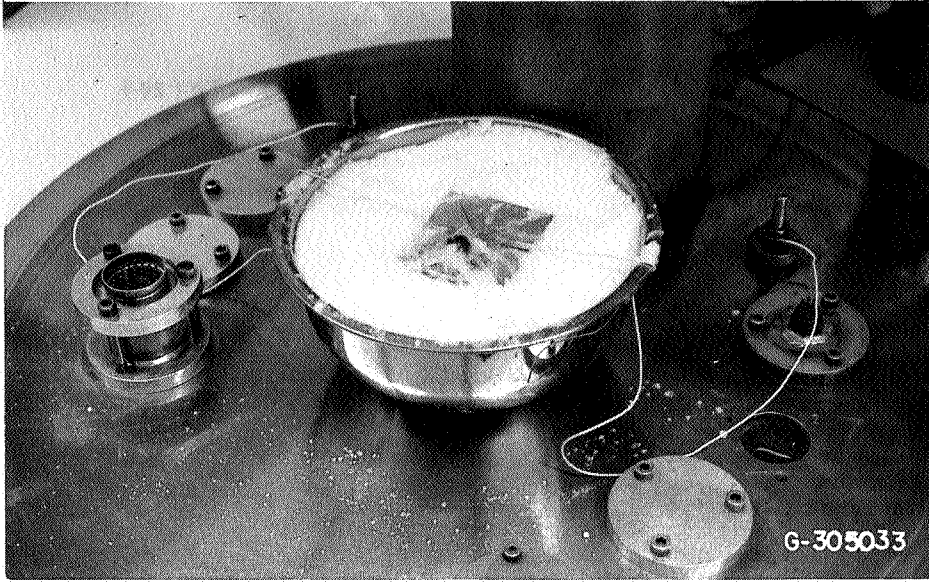


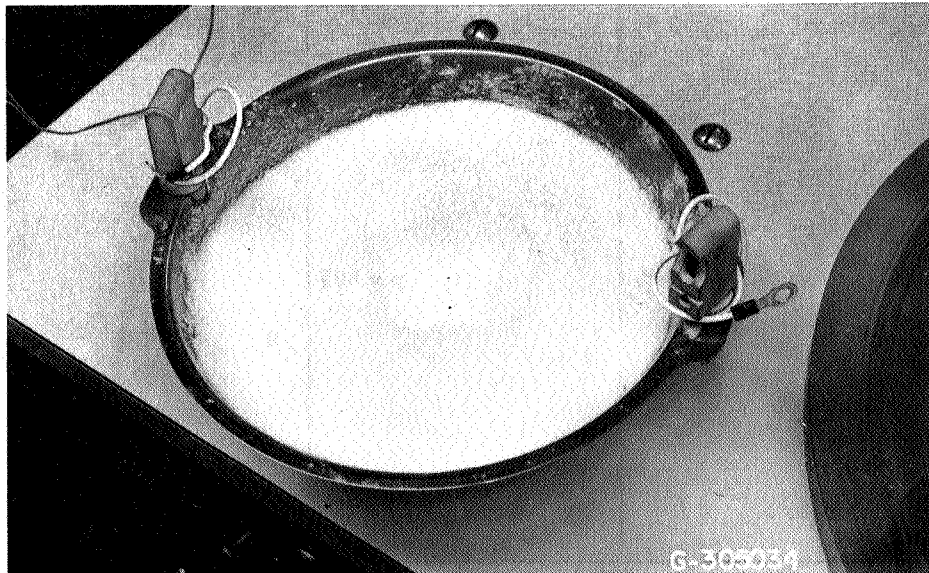
Fig. 21 Bearing Strength of Fluff versus Porosity (Ref. 44)







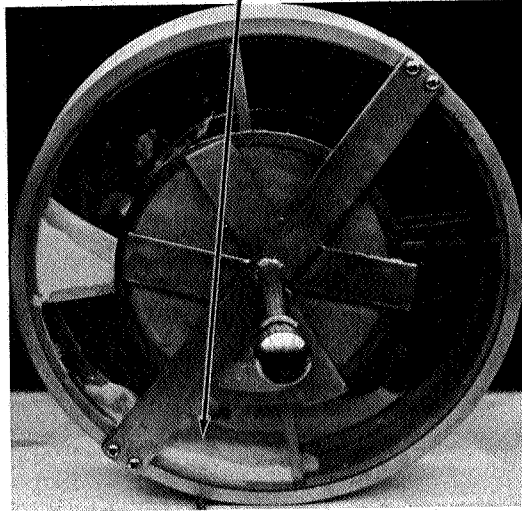
(a) In Vacuum



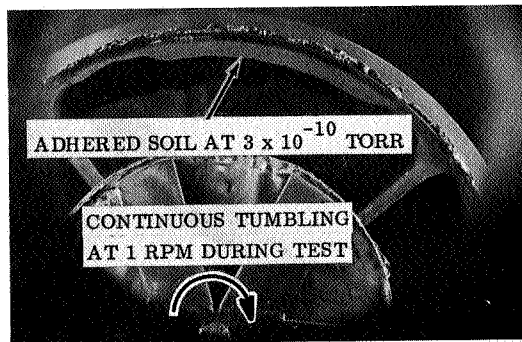
(b) In Air

Fig. 23 Drop Test in Fluff (Ref. 42)

LOOSE SOIL (100 MICRON PARTICLES)

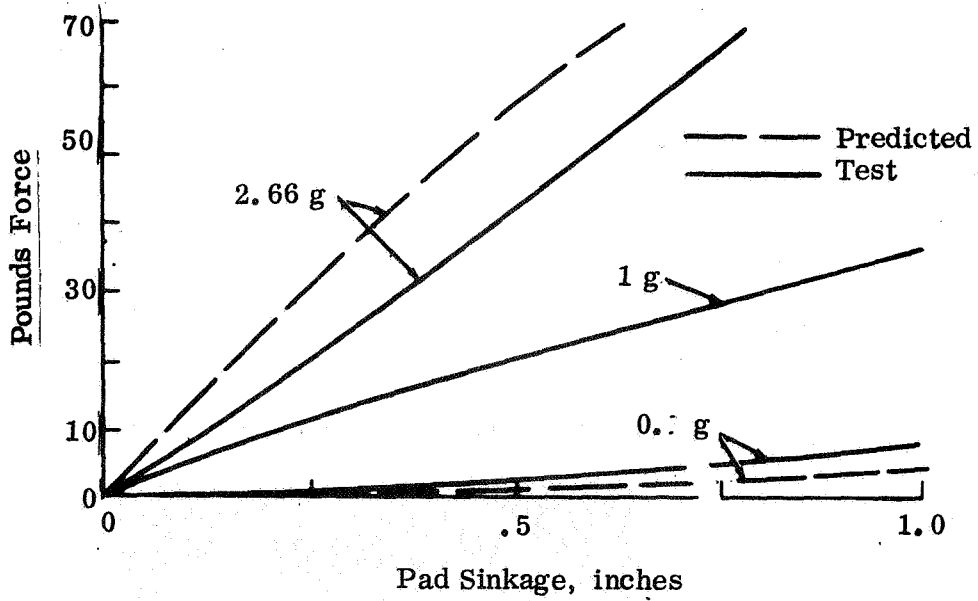


(a) BEFORE VACUUM EXPOSURE

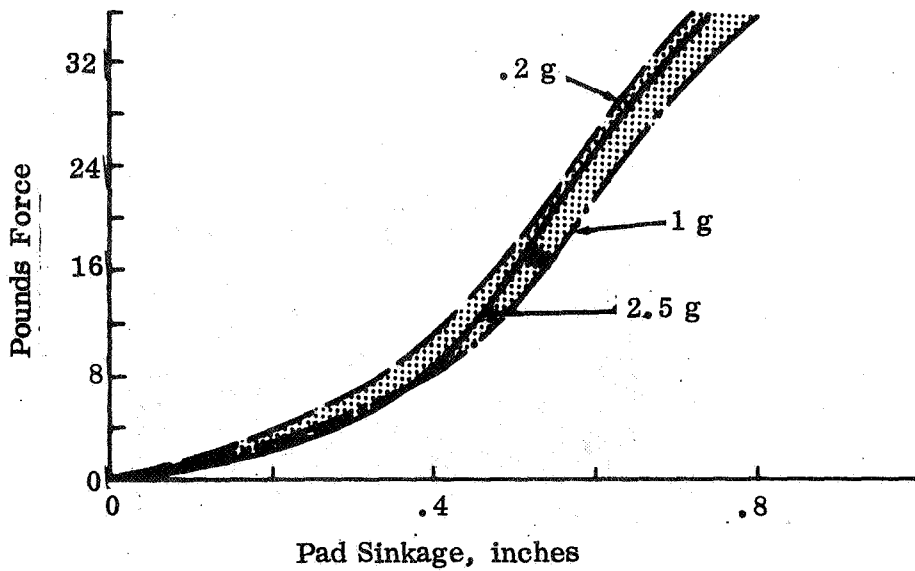


(b) AFTER VACUUM EXPOSURE ( $10^{-10}$  TORR)

Fig. 24 Soil Adhesion in Ultra High Vacuum (Ref. 42)



a) Cannonball Model (Coarse Beach Sand)



b) Fluff Model (Loosely Sifted Pumice)

Fig. 25 Soil Bearing Strength Under Varying Gravity Fields (Ref. 50)

- 1 Mizuno - Theoretical for Circular Footing (Ref 67)
- 2 Berezancev - Theoretical for Circular Footing (Ref 68)
- 3 Terzaghi -  $0.6 N_\gamma$  (For Strip Footing) (Ref 69)
- 4 DeBeer-Ladanyi -  $0.6 N_\gamma$  (For Strip Footing) (Ref 70)
- 5 Brinch Hansen -  $\left[1 - \frac{1}{2} (0.2 + \tan^6 \phi)\right] N_\gamma$   
(For Strip Footing) (Ref 71)
- 6 Meyerhof -  $\left[1 + 0.1 \tan^2 \left(\frac{\pi}{4} + \frac{\phi}{2}\right)\right] N_\gamma$   
(For Strip Footing) (Ref 72)

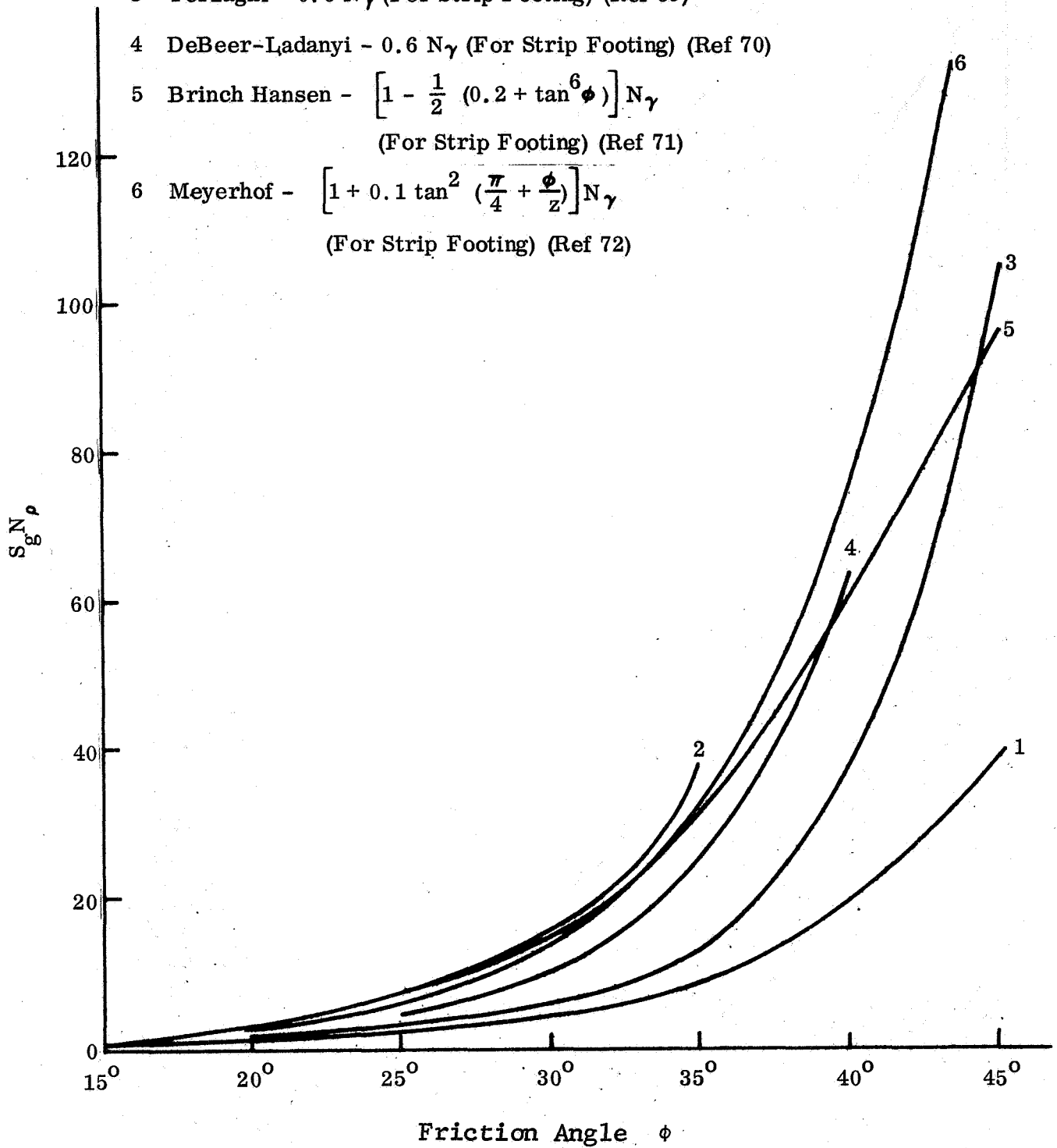
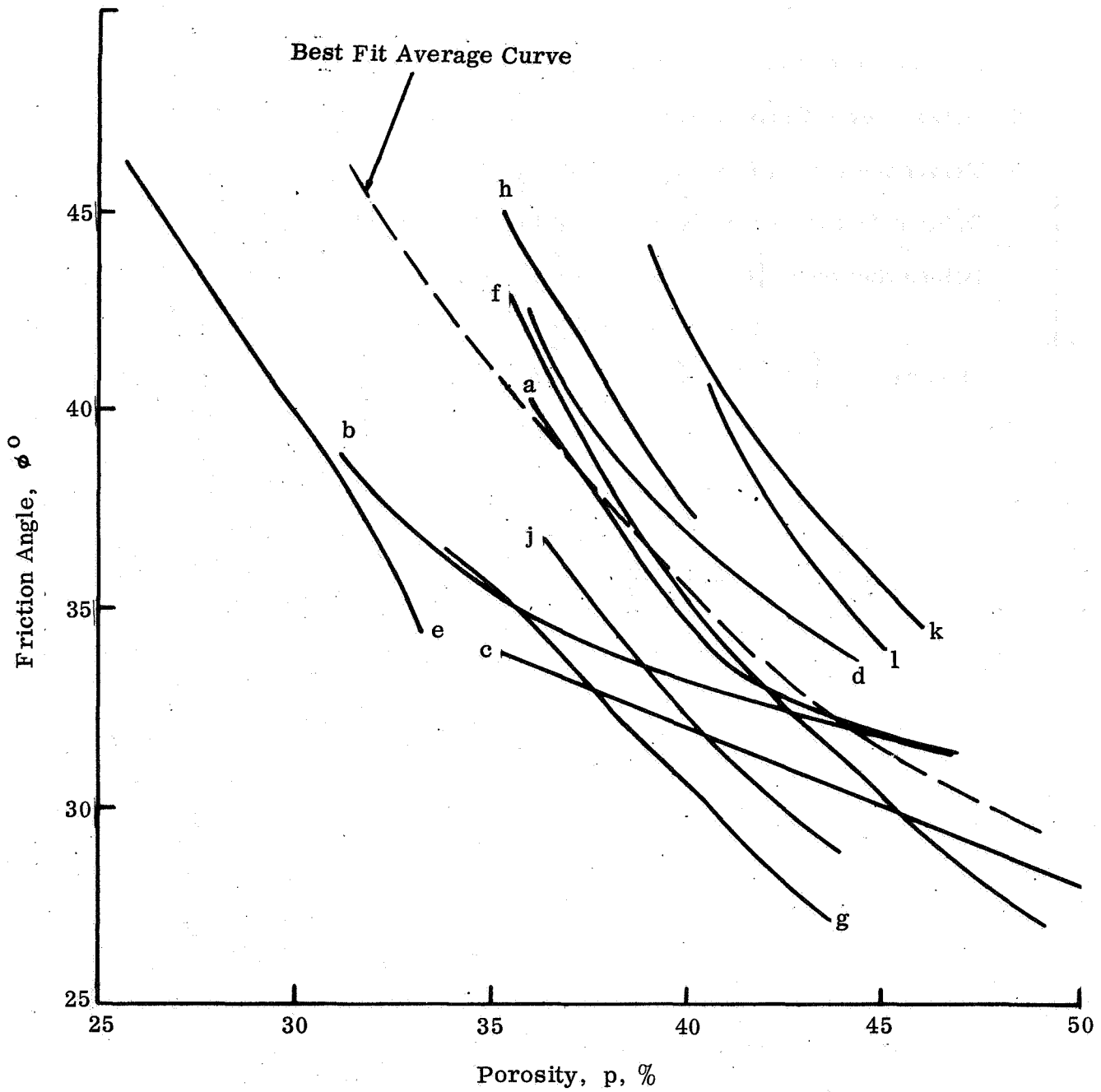


Fig. 26 Theoretical  $S_g N_\rho$  Values



- a) Bishop, Ref 73   b) Tschebofarioff, Ref 74   c) Kezdi, Ref 75   d) Brohms-Jamal, Ref 76  
 e) Chen, Ref 77   f) Keisel, Ref 77   g) Bureau of Reclamation, Ref 78   h) Meyerhof, Ref 79  
 j) Hansen, Ref 80   k) Bishop-Eldin, Ref 81   l) Kjellman-Jakobson, Ref 82

Fig. 27 Empirical Correlation of Frictional Angle and Porosity

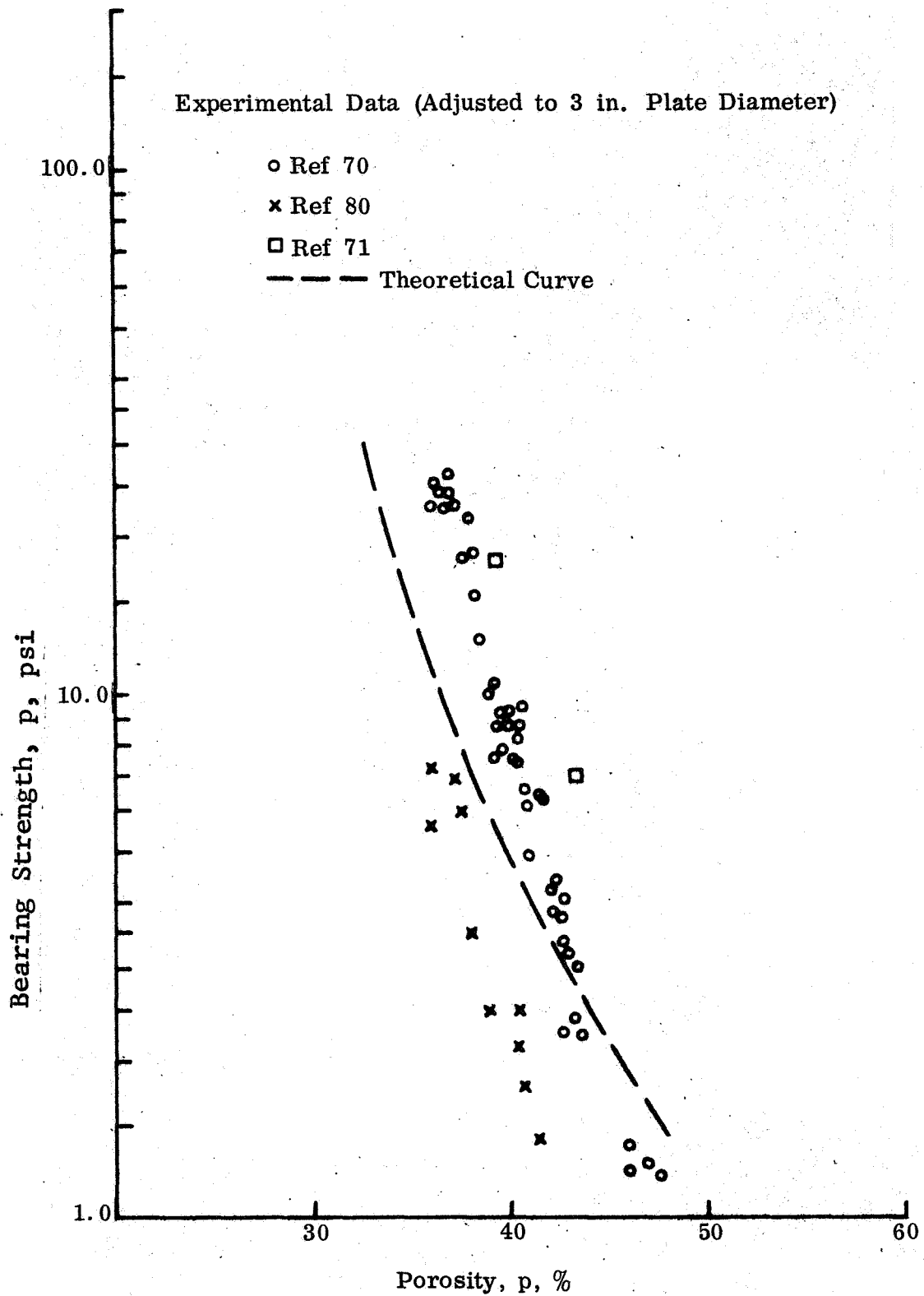


Fig. 28 Best-Fit of Theoretical Functions of Bearing Strength of "Cannonball" Model with Experimental Data

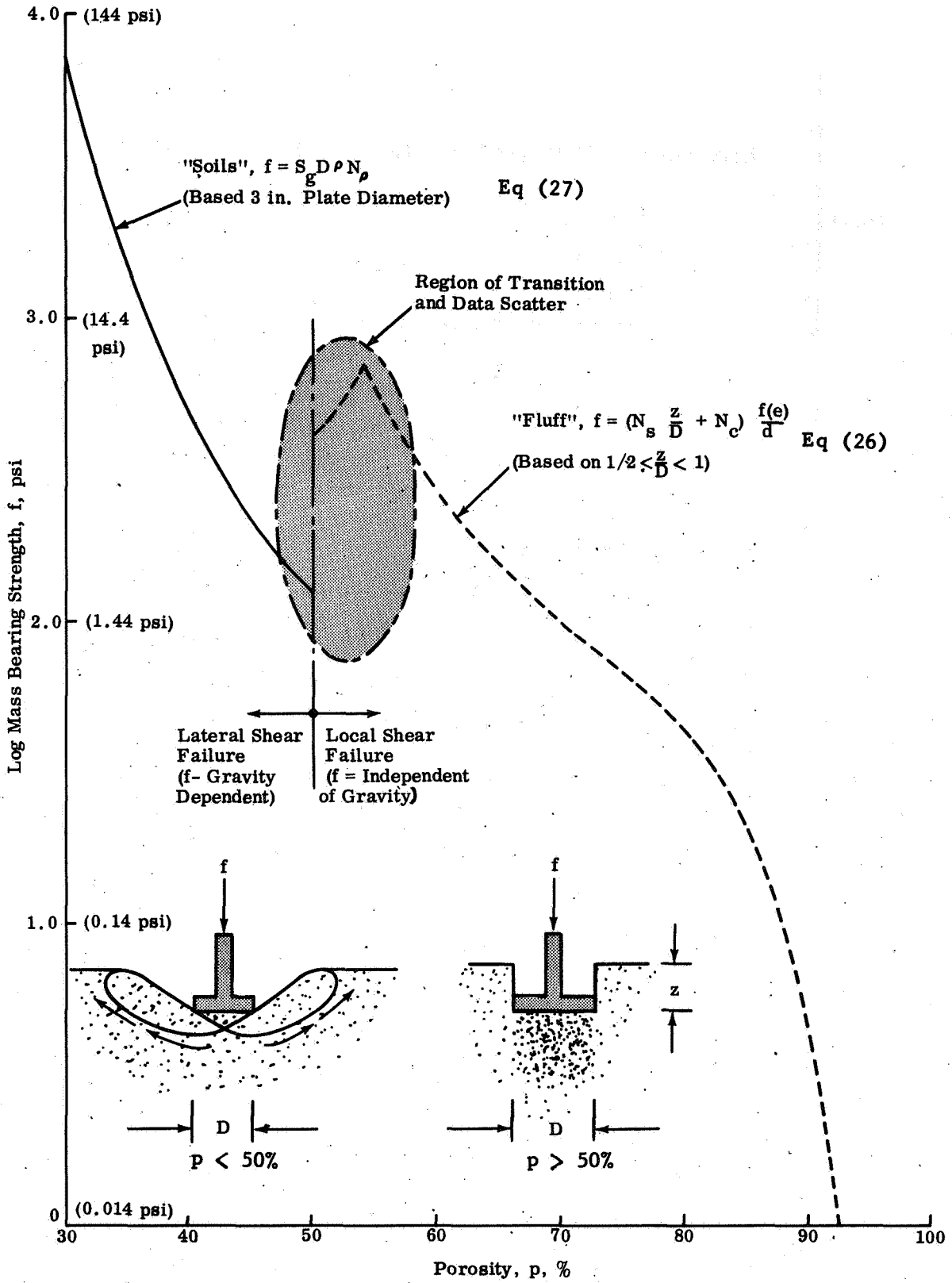


Fig. 29 Bearing Strength of Particulate Media versus Porosity (Ref. Figs 22 and 28)



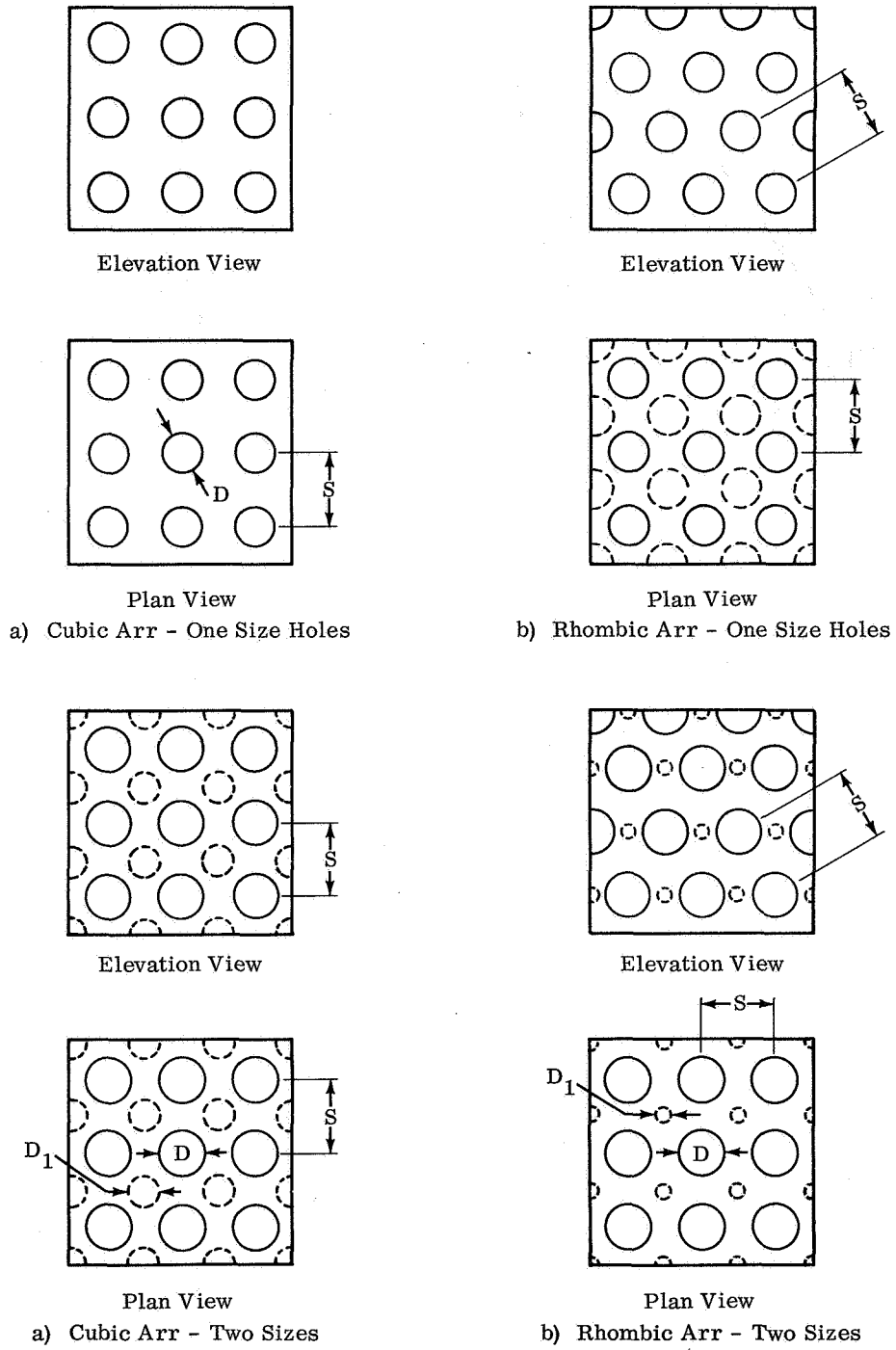


Fig. 30 Systematic Arrangement of Spherical Holes in Vesicular Media

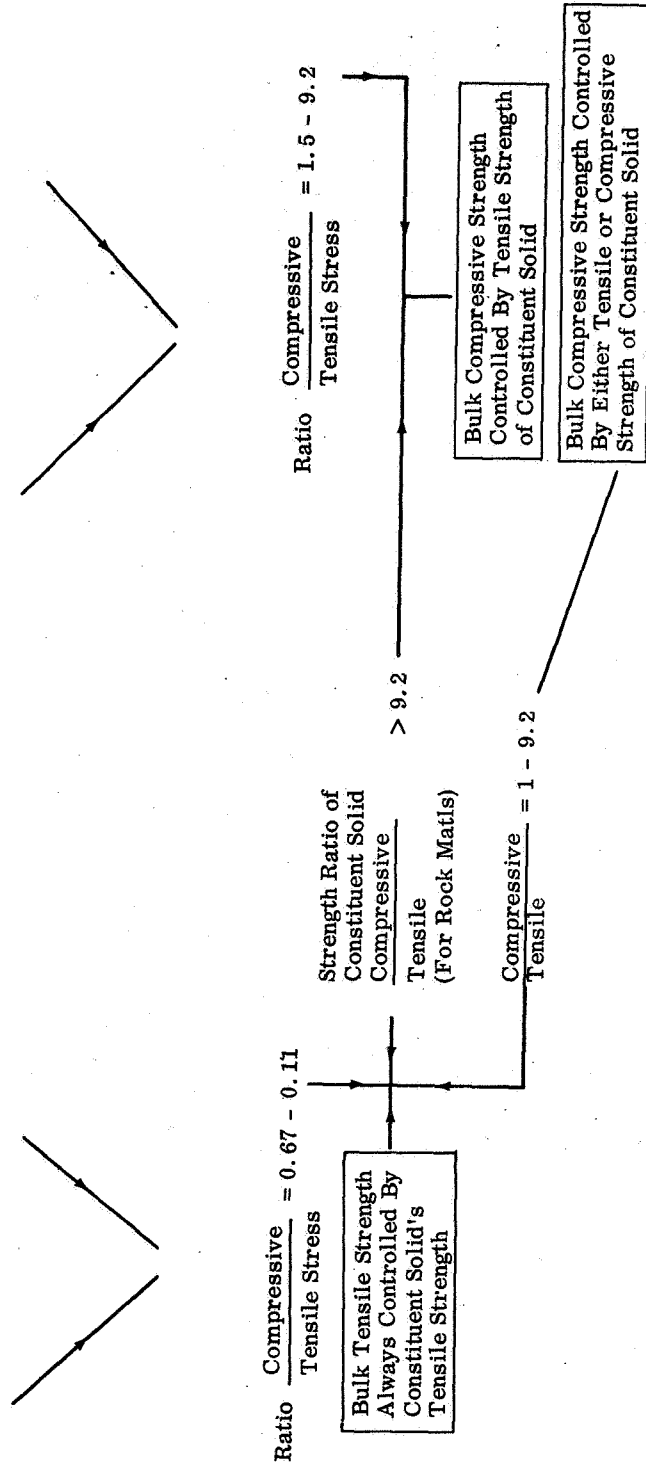
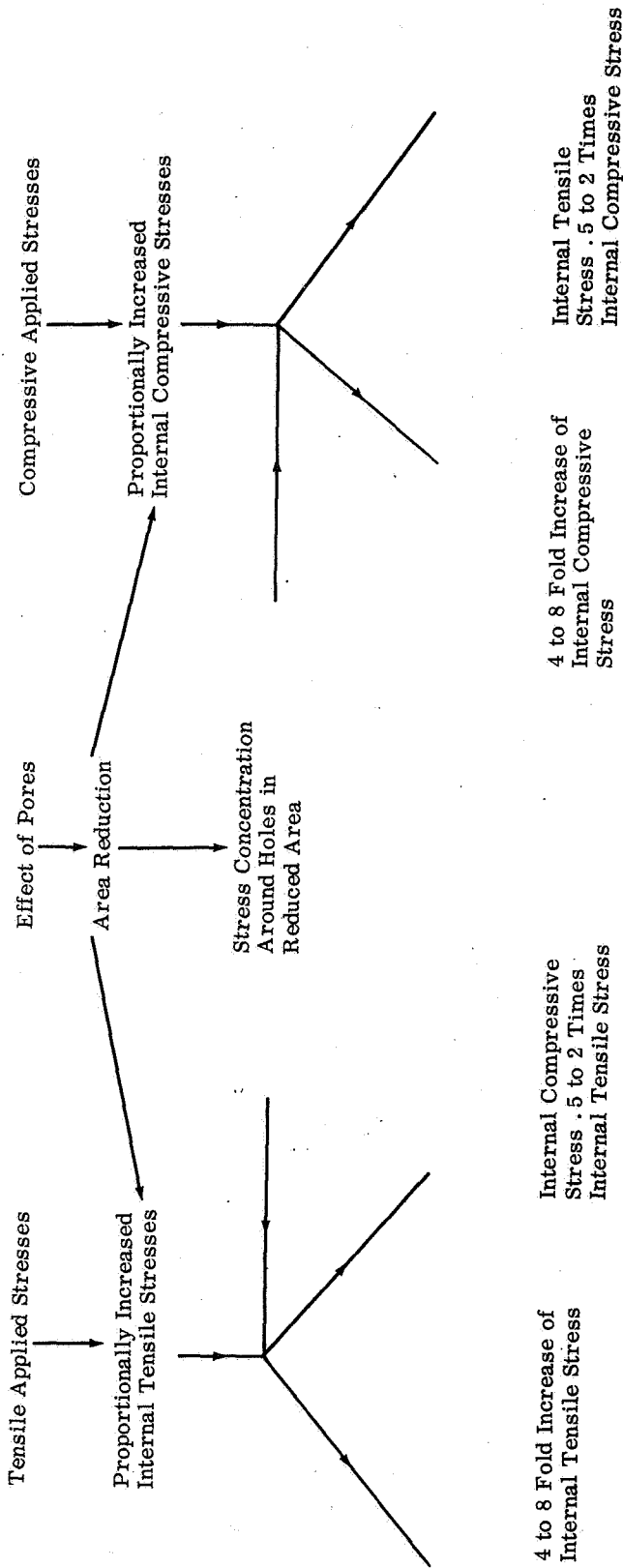
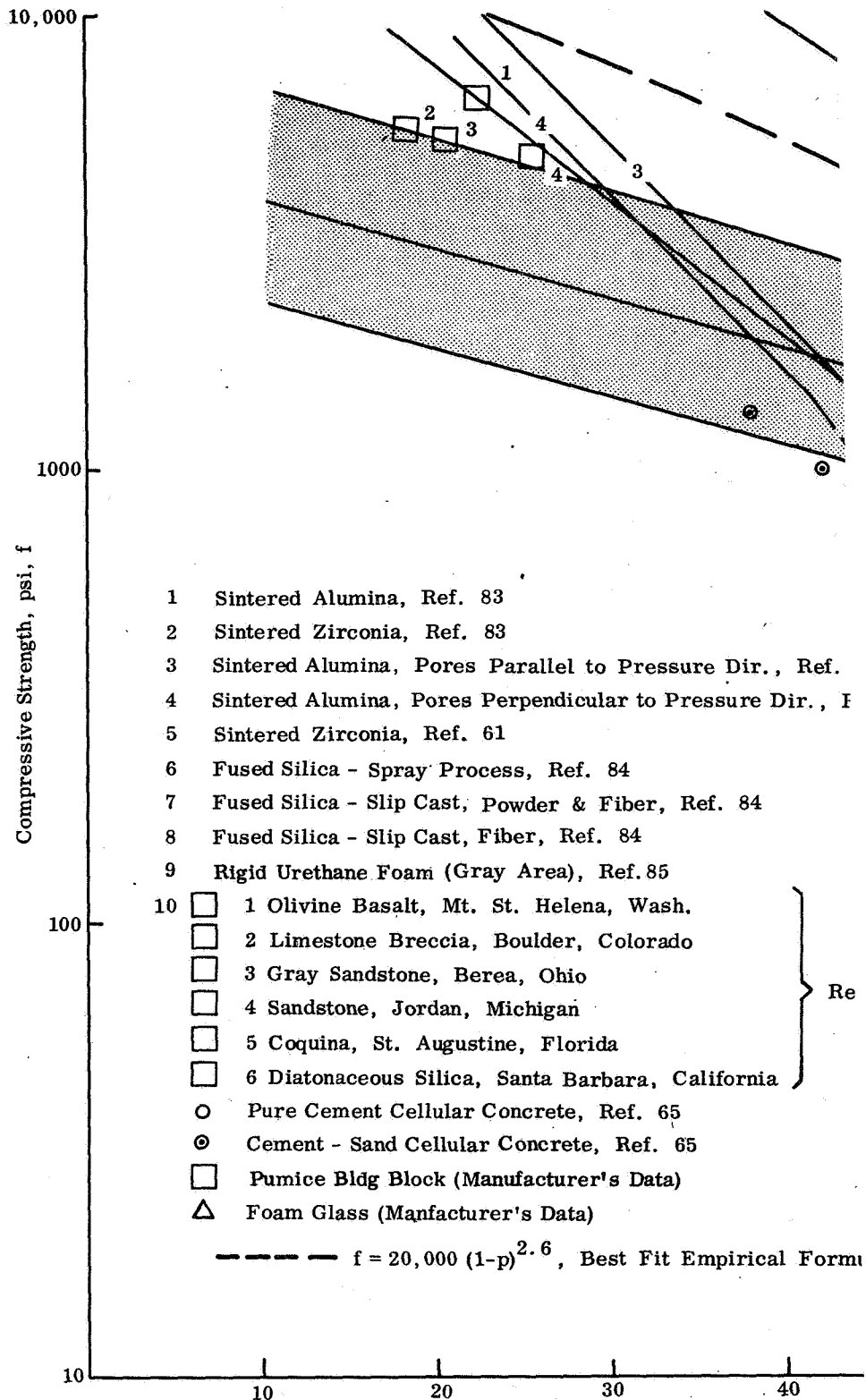


Fig. 31 Stress Distribution in Vesicular Media



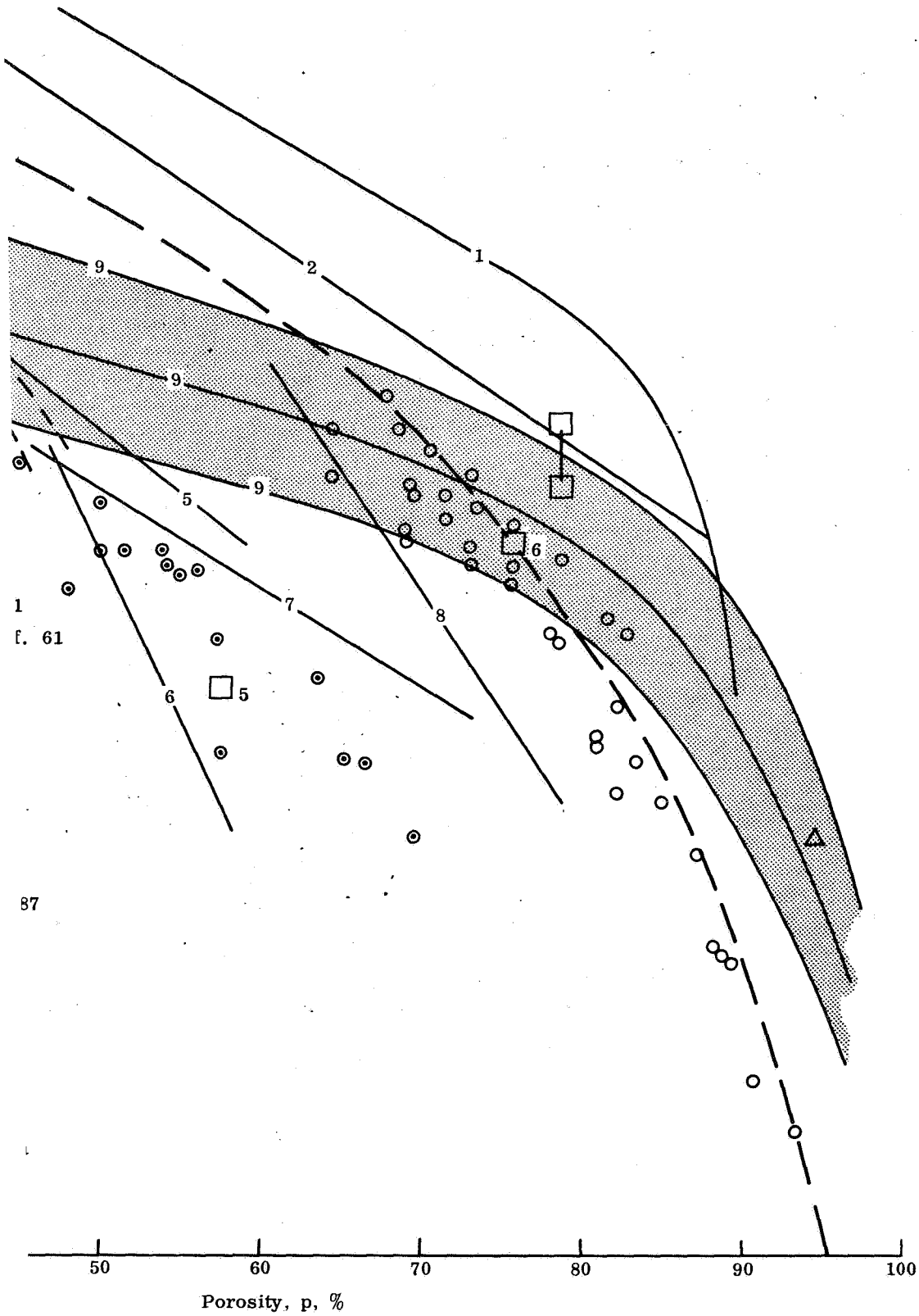


Fig. 32 Reported Strength-Porosity Data on Vesicular Media and Best-Fit Curve for Porous Rocks

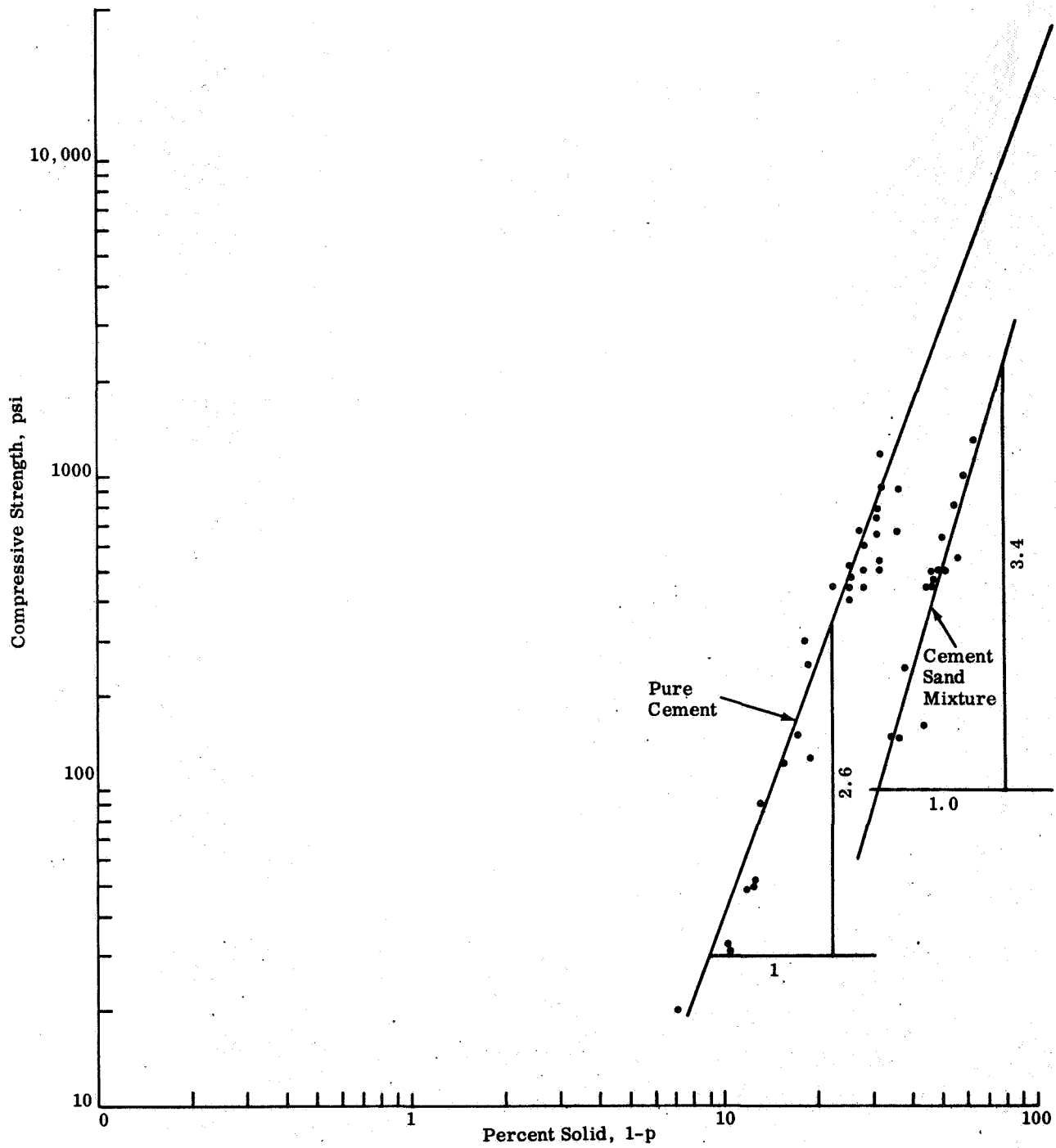
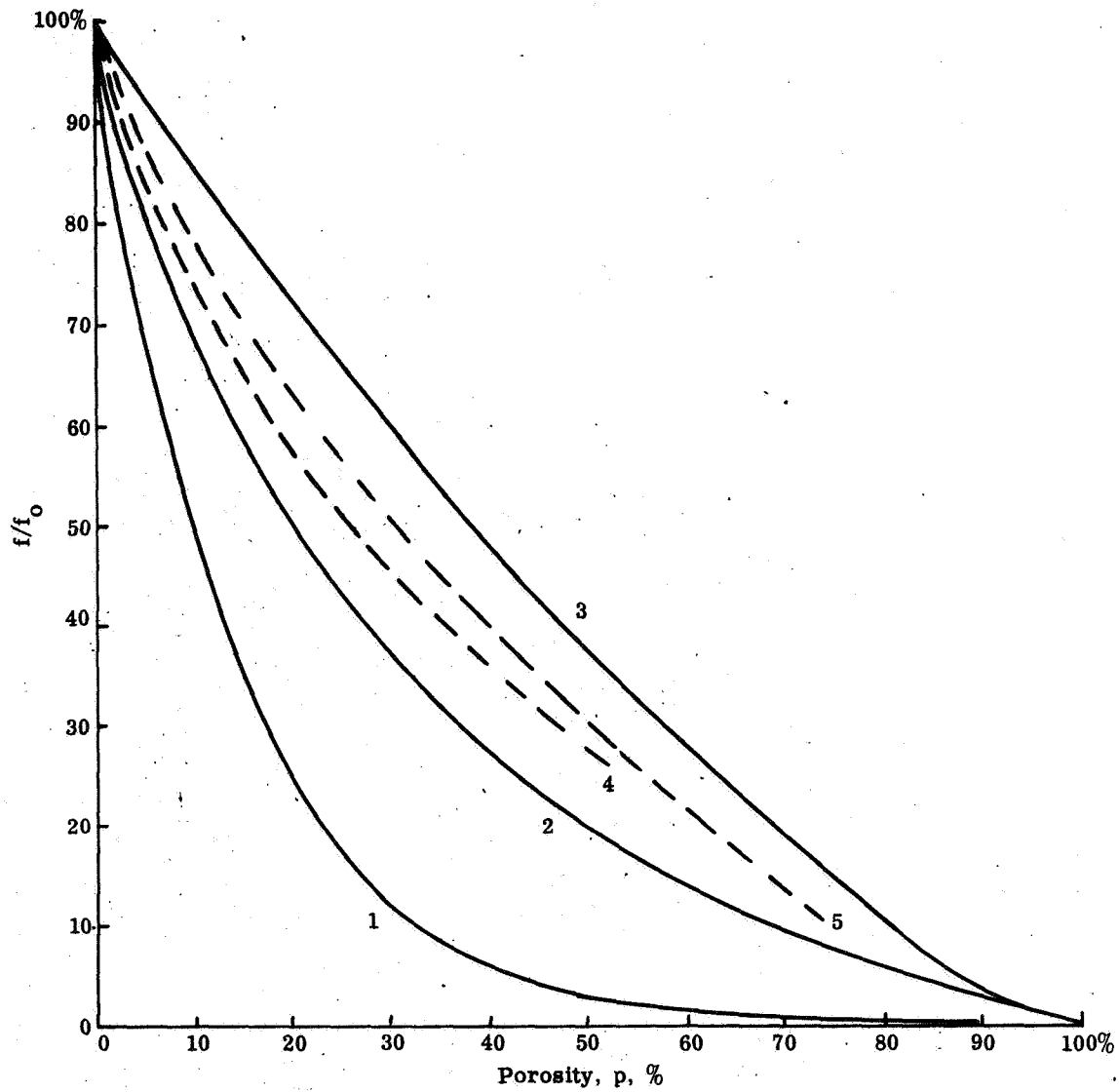


Fig. 33 Strength-Porosity Relationship for Cellular Concrete (Ref. 65)



- 1  $f = f_0 e^{-bp}$   $b = 7.0$  Ref (60)
- 2  $f = f_0 \left[ 1 + \frac{AP}{1 - (A + 1)p} \right]$   $A = -4.0$  Ref (62)
- 3  $f = f_0 (1 - p)^m$   $m = 1.416$  Ref (63)
- 4 Area Reduction - Cubic Arrangement of One Size Spherical Holes Ref (87)
- 5 Area Reduction - Rhombic Arrangement of One Size Spherical Holes Ref (87)

Fig. 34 Comparison of Proposed Strength-Porosity Relationships

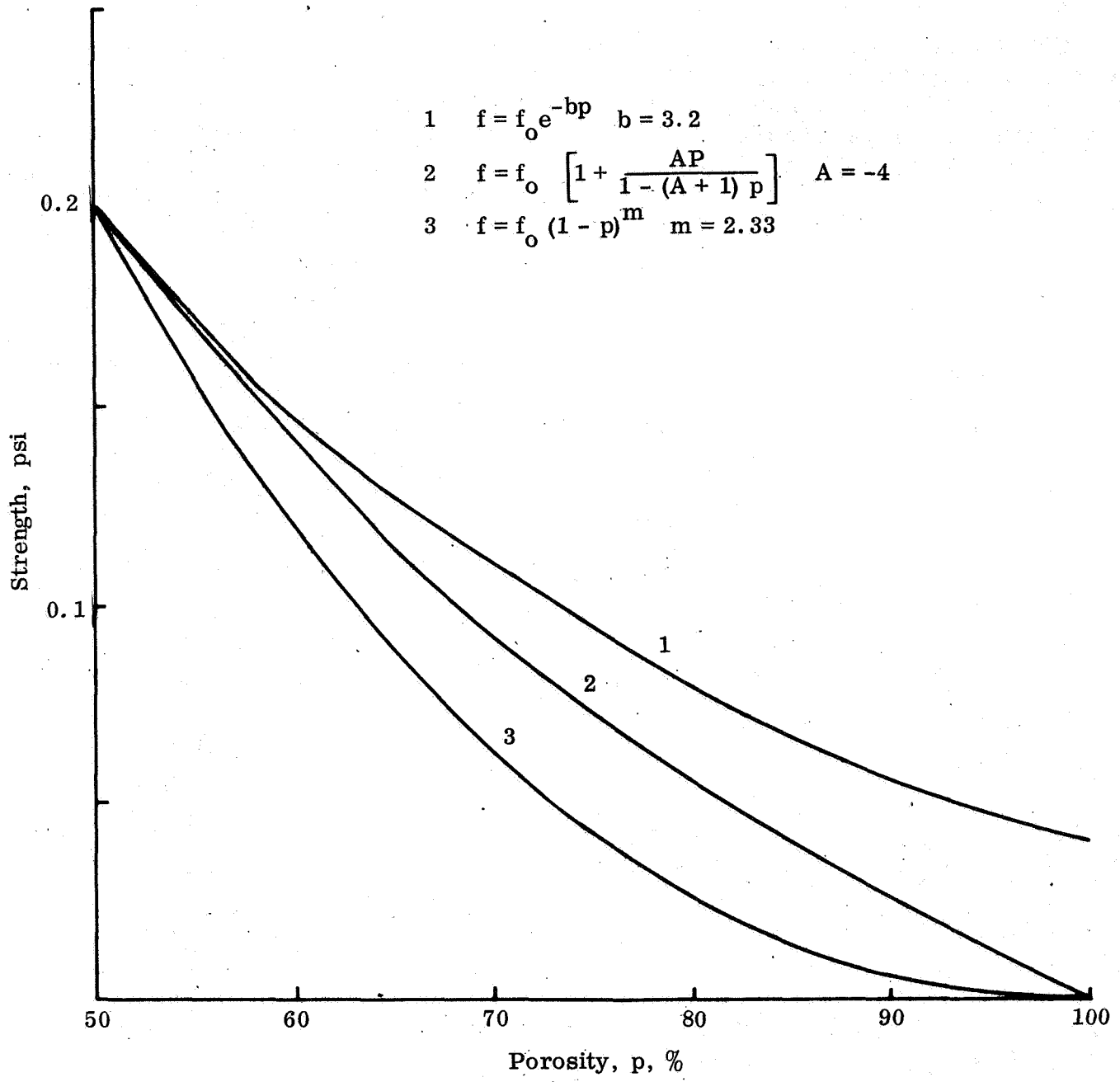


Fig. 35 Strength-Porosity Relationship in the High Porosity Range

## PHASE II: THERMOPHYSICAL ANALYSIS OF THE LUNAR SURFACE

### PURPOSE

The purpose of this analysis is to determine whether the nighttime temperatures of the lunar surface adequately define the postulated models and, if they do, to use the midnight temperature of a particular area of the moon as an index of the bearing strength of that area.

### BACKGROUND

Thermal radiation from lunar surface areas in the infrared region of the electromagnetic spectrum has been measured by numerous investigators (Refs. 88, 89, and 90). This has been done for both lunations and eclipses with the results being presented as effective surface temperature variations as a function of time. Figures 36 and 37 give typical lunation and eclipse temperature variation curves based on radiation measurements in the 8 to  $14\mu$  region. To derive thermal properties from the observed temperature variations, a physical model of the lunar surface must be assumed. The simplest model assumed has been one that considers the surface to be a homogeneous semi-infinite solid with temperature and depth independent thermal properties, and a blackbody radiator. With this model only one thermal parameter  $(k\rho c)^{-\frac{1}{2}}$ , the thermal inertia, is required to determine the temperature variation of the surface for a given solar heating input. The best fits to lunation and eclipse data using this model have given values of  $(k\rho c)^{-\frac{1}{2}}$  ranging from 500 to 1000 (in cal-cgs units). Recent lunation data in the infrared region (Ref. 88), in addition to microwave emission data (Ref. 91), indicate, however, that the homogeneous model cannot give a good fit to the data for any value of  $(k\rho c)^{-\frac{1}{2}}$ . To resolve this lack of correlation of the homogeneous model and resolve some of the inconsistencies in the various data, it is desirable to analyze more detailed models of the lunar surface. In addition, only by determining the full extent of various models that can adequately describe the thermal behavior will knowledge of the full range of possible thermophysical properties be ascertained.



## THERMAL PROPERTIES

This section discusses the following thermal properties that are relevant to the interpretation of the lunar thermal emission:

1. emissivity,
2. albedo or reflectivity,
3. thermal conductivity, and
4. specific heat.

### Emissivity

In general the emissivity will depend on both direction and wavelength. In the wavelength region of importance for lunar thermal emission, an average directional emissivity can be defined by

$$\bar{\epsilon}(\theta, T) = \frac{\int_8^{14} R(\theta, \lambda, T) d\lambda}{\int_8^{14} B(\lambda, T) d\lambda} ,$$

where  $R$  is the real surface radiance at angle  $\theta$  from the normal,  $B$  the blackbody radiance, and  $\lambda$  is the wavelength in microns. The above assumes that the surface is impermeable to radiation and that the surface temperature can characterize the radiation. Because a surface radiates in all directions, it is necessary to know the total hemispherical emittance  $\bar{\epsilon}$  which is defined by

$$\bar{\epsilon} = 2 \int_0^{\pi/2} \bar{\epsilon}(\theta) \cos \theta \sin \theta d\theta ,$$

where  $\bar{\epsilon}(\theta)$  is the directional emissivity at angle  $\theta$  to the normal over the 8 to 14 $\mu$  wavelength band. To analyze the lunar thermal data rigorously both the hemispherical emissivity and the directional emissivity must be known as a function of the viewing angle of the area considered. Unfortunately, these properties of the lunar surface or of terrestrial analogs are not well known. This topic is further discussed in Phase IV in connection with experiments that could improve our knowledge in this area.

Emissivity measurements of the lunar surface were performed by Markov and Khokhlova (Ref. 92). They measured the reflected radiation at 3.6 $\mu$  during the penumbral phase of an eclipse. By assuming a gray body (emissivity independent of wavelength), they established an emissivity of 0.62 for the 8 to 14 $\mu$  range for the continents and 0.83 for the seas. Their assumption of a gray body is justified by their observation of approximately equal brightness temperatures at 3.6 $\mu$  and 8 to 14 $\mu$  wavelengths.

In view of the above, it appears desirable to discard the assumption of blackbody behavior made by previous investigators. The mathematical model developed therefore includes emissivity as a variable parameter.

#### Albedo or Reflectivity

The lunar surface temperature will depend on the amount of incident energy that is absorbed. The energy absorbed in turn will depend on the angle of incidence of the solar radiation and the total albedo defined as the fraction of incident radiation on a surface reflected into the hemisphere. Because the albedo for a surface is wavelength dependent, an average albedo weighted according to the energy distribution in the solar spectrum must be used. The variation of total albedo with angle of incidence is a complex function of the material and geometric properties of the surface. Until recently, this variation of total albedo with angle of incidence has received little attention. A recent study of Polgar and Howell (Ref. 93) obtained variations of 20 percent in absorptivity of conical cavities as the angle of solar incidence was varied. The possible existence of a lunar surface structure of many cavities make this study particularly relevant. Coulson (Ref. 94) obtained total albedo variations for terrestrial materials from 55 percent to 85 percent depending on the angle of incidence. However, we continue to use a constant albedo until lunar data on the variation of albedo with incident angle becomes available.

## Thermal Conductivity

As shown in Phase IA, the thermal conductivity of lunar surface materials may be highly dependent on temperature, especially if they are of particulate form; therefore, the mathematical model describing the heat conduction of the lunar surface includes a thermal conductivity which is a function of temperature.

A temperature dependent thermal conductivity was first used by Wesselink (Ref. 95) who assumed a purely radiative component and arrived at a 0.3 mm upper limit to the grain size of the lunar soil. Muncey (Ref. 96), in an attempt to reconcile lunation and eclipse temperature measurements, assumed a linear variation of the thermal properties with temperature. He concluded that a dust layer overlaying a material of a  $\gamma$  of 400 could satisfy both lunation and eclipse data.

The most recent and detailed studies of the effects of temperature dependent thermal properties are those of Ingrao et al. (Ref. 97) and Linsky (Ref. 98). They considered models of conductivity with a solid and radiative component, as well as models with linear temperature dependence. They were able to obtain reasonable fits to Murray and Wildey's lunation data and to their own eclipse data on Tycho by using both types of temperature dependent models. They concluded that it is not possible to uniquely decide which model applies to the lunar surface regions studied.

Linsky used temperature dependent models to match a minimum nighttime temperature of 90°K. In addition, two of his models gave good agreement with radio brightness temperatures as a function of wavelength.

All of the above studies were similar, in that they aimed at "tailoring" models that gave best agreement with specific lunar temperature data. Because Low's recent measurements (Ref. 99) indicate possible wide ranges in lunar surface thermal behavior, it appears that the above studies are only valid for those particular locations where the temperature data were obtained. Our objective in this study is not limited to matching specific lunar data. We are more concerned with the behavior of lunation temperatures as a function of parameters that affect thermal conductivity and bearing strength. Consequently, our expressions of thermal conductivity, used in the solution of heat conduction of the lunar surface, are dependent not only on temperature, but also on particle size and porosity.

## Specific Heat

Previous investigators have considered the specific heat of the lunar surface material to be invariant with temperature. An exception is Muncey (Ref. 96) who considered a linear variation of specific heat with temperature. Experimental data (Refs. 100 and 26) for specific heats of rocks and minerals indicate a  $T^{\frac{1}{3}}$  variation with temperature. In the temperature range of 100 to 400°K, this variation is not as significant as the variation of thermal conductivity and therefore will be neglected.

## MATHEMATICAL MODEL

The surface is considered as the boundary of a semi-infinite solid. Because the depths involved are quite small in comparison with the radius, the curvature of the surface is neglected. In addition, roughness is neglected. The only spatial coordinate, therefore, is depth below the surface ( $x$ ). The thermal properties are assumed to be temperature dependent. The equation for heat conduction in the solid for the above assumptions is

$$\rho c(T) \frac{\partial T}{\partial t} = \frac{\partial}{\partial x} k(T) \frac{\partial T}{\partial x} , \quad (34)$$

where the thermal conductivity  $k(T)$  and specific heat  $c(T)$  are functions of temperature. At the surface, heat is lost by thermal radiation to space. It is assumed that all the absorption of solar radiation occurs at the surface. Therefore, the thermal energy balance for the surface is

$$\sigma \bar{\epsilon} T^4 = A(t) + k(T) \frac{\partial T}{\partial x} , \quad (35)$$

where  $\sigma$  is the Stefan-Boltzman constant,  $\bar{\epsilon}$  is the total hemispherical emittance, and  $A(t)$  is the time dependent heat absorption rate. The second term on the right represents the heat flux across the surface. The absorption rate will depend on the angle of incidence of the solar heat flux. For an area on the surface with latitude  $\beta$  and longitude  $\delta$ , the absorption rate is given by

$$A(t) = A_0 (1 - R) \cos \beta \cos \left( \delta + \frac{2\pi t}{P} \right) , \quad (36)$$

where  $A_0$  is the solar constant ( $2.0 \frac{\text{cal}}{\text{cm}^2 \text{min}}$ ),  $R$  is the total hemispherical albedo, and  $P$  is the lunation period.

For the model in which the lunar surface consists of a multi-layer structure (vertical inhomogeneity) each with independent thermal properties, the basic heat conduction equation is used for each layer. The boundary condition at the interface between two layers is given by

$$k_i \frac{\partial T_i}{\partial x} = k_{i+1} \frac{\partial T_{i+1}}{\partial x} .$$

For an eclipse, the absorption rate from the sun is written as  $A(t)f(t)$ , where  $f(t)$  is approximated as a linearly decreasing function during the penumbral phase and vanishes at the beginning of the umbral phase.

The area of the surface under consideration may consist of two or more distinct regions (horizontal inhomogeneity) with different thermal properties, e.g., islands of bare rock surrounded by a sea of dust. The radiation emitted over the 8 to 14 $\mu$  wavelength range is then equal to the quantity  $q$  defined by

$$q = \sigma \sum_i f_i \int_8^{14} \epsilon_i(\lambda) B(\lambda, T_i) d\lambda ,$$

where

$$B(\lambda, T) = \frac{c_1}{\lambda^5} \left( \frac{1}{\exp\left(\frac{c_2}{\lambda T}\right) - 1} \right) ;$$

the area  $i$  is represented by temperature  $T_i$ , emissivity  $\epsilon_i$ , and fraction  $f_i$  of total area. The effective blackbody temperature of the area is then obtained from

$$\int_8^{14} B(\lambda, T_{BB}) d\lambda = q .$$

For the case of variable surface emissivity, the effective blackbody temperature is calculated from

$$\int_8^{14} B(\lambda, T_{BB}) d\lambda = \int_8^{14} \epsilon(\lambda) B(\lambda, T) d\lambda .$$

where  $T$  is surface temperature. In all cases it is the effective blackbody temperature that is compared with the observed data. This is done to be consistent with the published values of temperature which were obtained by converting radiance measurements to effective blackbody temperatures.

A finite difference technique is used to solve the partial differential equations. Because of the temperature dependence of thermal properties, the heat conduction equation is nonlinear. In addition, the radiation boundary condition equation is nonlinear. To allow for these nonlinearities a modification of a method first suggested by Jaeger (Ref. 102) is used.

Differentiating the r.h.s. of Eq. (34) we obtain

$$\rho c \frac{\partial T}{\partial t} = \frac{dk}{dT} \left( \frac{\partial T}{\partial x} \right)^2 + k \frac{\partial^2 T}{\partial x^2} .$$

The first term on the right illustrates the nonlinearity. By replacing the derivatives in the above equation by the finite difference approximations, using  $m$  to designate a space node of width  $\Delta$  and  $n$  to designate a time interval of width  $\tau$ ,

$$\frac{\partial^2 T}{\partial x^2} = \frac{T_{m+1}^n - 2T_m^n + T_{m-1}^n}{\Delta^2}$$

$$\frac{\partial T}{\partial t} = \frac{1}{\tau} (T_m^{n+1} - T_m^n),$$

and

$$\frac{\partial T}{\partial x} = \frac{1}{2\Delta} (T_{m+1}^n - T_{m-1}^n),$$

and solving for  $T_m^{n+1}$ , we obtain

$$T_m^{n+1} = T_m^n + \frac{\alpha\tau}{4\Delta^2 k} \frac{dk}{dT} \left[ (T_m^n)^2 - 2T_{m+1}^n T_{m-1}^n + (T_{m-1}^n)^2 \right] + \frac{\alpha\tau}{2\Delta} (T_{m+1}^n - 2T_m^n + T_{m-1}^n).$$

The normal Schmidt stability criteria of  $\alpha\tau/\Delta^2 = \frac{1}{2}$  has been found to lead to oscillations for the nonlinear case. A value of  $\alpha\tau/\Delta^2 = \frac{1}{4}$  has therefore been used, thereby leading to a nonoscillatory solution. Substituting  $\frac{1}{4}$  for  $\alpha\tau/\Delta^2$  in the above equation yields

$$T_m^{n+1} = \frac{1}{4} (T_{m+1}^n + 2T_m^n + T_{m-1}^n) + \frac{1}{16k} \frac{dk}{dT} \left[ (T_{m+1}^n)^2 - 2T_{m+1}^n T_{m-1}^n + (T_{m-1}^n)^2 \right].$$

The finite difference form of the boundary equation is

$$\bar{\epsilon}\sigma (T_0^n)^4 - A(t) + 2\bar{\epsilon}\sigma (T_0^n)^3 (T_0^{n+1} - T_0^n) = \frac{k}{2\Delta} (T_1^n - T_{-1}^n) .$$

The above equation is derived by assuming an average radiation heat flux in the interval  $t, t + \tau$  at time  $t$  rather than the instantaneous value. The average radiated heat flux is given by

$$\bar{\epsilon}\sigma \left[ T^4 + \frac{\tau}{2} \frac{d}{dt} (T^4) \right] = \bar{\epsilon}\sigma \left[ (T^4) + 2\tau T^3 \right] .$$

The Planck distribution integral  $\int_0^{14} B(\lambda, T) d\lambda$  was evaluated from computed tables (Ref. 103) as a function of temperature, and stored in the computer memory for use in solving the equations in which it appears.

#### CASE STUDIES OF THE LUNAR SURFACE FOR LUNATION COOLING

The computer program based on the above equations has been used to study the thermal behavior during a lunation for six cases as described in Table VI.

TABLE VI

Cases Studied for Lunation Cooling

Case No.	Material	Temperature Dependence	Variables	Figs.
1	Homogeneous	no	$\gamma = (k\rho c)^{-\frac{1}{2}}$	38
2	Homogeneous	no	Latitude	40
3	Two-layer	no	$\gamma$ and thickness of layers	41-44
4	Homogeneous	no	Emissivity	45
5	Homogeneous-Particulate	yes	Porosity, grain size	46-48
6	Homogeneous-Vesicular	no	Porosity, pore size	49-50



Case 1 essentially represents existing solutions in the literature. Plots of lunation temperature for given values of  $(k\rho c)^{-\frac{1}{2}}$  or  $\gamma$  are shown in Fig. 38. The results check reasonably well with those of Krotikov and Shchuko (Ref. 5) shown in Fig. 39. This model has also been analyzed for eclipse cooling and checked with Jaeger's solution, which is based on similar assumptions (Ref. 102). Although these results are not shown, the agreement is equally good. For this report, the study of eclipse temperatures has been abandoned in favor of lunation temperatures because the latter, as explained in a subsequent section, are more pertinent to the problem of correlating thermal and mechanical properties.

The rest of the cases listed in Table VI are selected to show how lunation temperatures "behave" under given inputs. These inputs may consist of changes in geometrical or material properties (some of these are listed in Table VI as "variables") or they may consist of a mathematical refinement such as inserting a temperature dependent function of thermal conductivity into the program. Our studies in Phase I have indicated that this particular refinement is warranted only for Case 5 (the particulate model) where radiative conduction, which is strongly temperature dependent, can be of the same order as, or greater than, the solid conduction. The remaining sections in this phase discuss the results obtained with Cases 2 to 6.

#### EFFECTS OF LATITUDE AND ROUGHNESS ON LUNATION TEMPERATURES

Case 2 illustrates the effect of latitude on lunation temperatures (shown in Fig. 40) for lunar latitudes of  $0^\circ$ ,  $30^\circ$ ,  $60^\circ$ , and  $75^\circ$ . A homogeneous, temperature independent model is assumed with a gamma of 1000.

As indicated by the family of curves in Fig. 40, the daytime temperature is quite sensitive to the latitude coordinate, whereas the nighttime temperature is not. As a case in point, the high noon temperature decreases by  $111^\circ\text{K}$  in going from the equator to the  $75^\circ$  parallel, while the corresponding midnight temperature decrease is only  $10^\circ\text{K}$ .

The effects of surface irregularities were not taken into account in this study. Qualitative estimates of the effects of roughness can be made, based on the results obtained for a smooth surface, by considering the following.

A rough surface can be considered as being composed of planes with random orientations. At a given phase, the solar radiation will be incident at different angles on these slopes. The average temperature obtained by a radiation measurement will be a weighted average of the individual temperatures of the various planes. The inferred temperature deduced from earth based observations should be higher than that of a smooth surface at that latitude. This is due to the fact that the viewing angle gives more weight to those slopes whose normals are oriented toward the same direction as the incident solar radiation. This effect should be significant during the daytime when the temperature is quite sensitive to the orientation of the incident radiation as shown by Fig. 40. Daytime temperature measurements could therefore serve as a method of estimating surface roughness by determining its enhancement over the predicted value, based on a smooth surface, for the particular latitude. The effect of variations in thermal properties should be small as discussed in Phase IA.

During the lunar nighttime the effect of roughness will be small as inferred by the small variation of temperature with latitude. This emphasizes the significance of nighttime temperature as an index of material rather than surface geometric properties. This point is further discussed below.

Roughness effects on eclipse and lunation temperatures are important, but far too complex to be dealt with in this study. The potential usefulness of the lunar emission data in the infrared has not been fully appreciated as a source of information on the roughness of the lunar surface. Such data may be used to verify or complement the roughness inferred from photometric, polarimetric, radar, and other sources. To attempt this work it is first necessary to know the directional variation of emission from the lunar surface. These data are essentially the infrared counterpart of the lunar photometric data at optical wavelength. Only limited data has been reported (Ref. 104) on this effect.

#### IMPORTANCE OF LUNAR NIGHTTIME TEMPERATURE DATA

The solution of Case 1 (Fig. 38) indicates that the nighttime temperature is a sensitive index to the thermal inertia parameter  $\gamma$ . During insolation, the surface temperature is in near equilibrium, thus large variations in  $\gamma$  do not significantly affect the surface temperature. During the lunar nighttime however, the surface temperature is determined almost exclusively by the thermal parameters of the lunar material. During the penumbral and umbral phases of an eclipse, the temperature cooling curves

will sensitively depend on the thermal parameters also. However, there are other parameters that will also affect the cooling behavior such as roughness, infrared transparency, and heat sources, all of which are discussed below.

Bastin (Ref. 105) suggests that lunar roughness on a centimeter scale could account for anomalously high temperatures (hot spots) that were uncovered by Saari and Shorthill (Ref. 106) during eclipse cooling. Using a simple roughness model, he calculates an increase of  $40^{\circ}\text{K}$  in surface temperature as compared to that of a smooth surface under identical cooling conditions. During the lunar nighttime, the considerably greater cooling times available would require a roughness scale of the order of decimeters to account for hot spots. Radar data indicate a smooth surface at this scale. Roughness can probably be ruled out as a factor in explaining hot spots during the lunar night unless radar data for a hot spot region show anomalously high return. Another possible explanation, offered by Buettner (Ref. 100), to account for eclipse hot spots is that of infrared transparency. During eclipse cooling, there is a large temperature gradient occurring within the first centimeter of the lunar material. Partial transparency of infrared radiation of the material in the 8 to  $14\mu$  range would give misleadingly high surface temperature readings as inferred by radiation sensors. During the lunar night, however, the effect of transparency is not nearly as significant since the temperature gradient is considerably more shallow.

Regarding a third possibility — whether the observed "hot spots" are due to internal heat sources — it is not clear at this time whether temperature measurements during a lunation could confirm or disprove this hypothesis, which is certainly interesting and deserving of more attention.

The apparently less ambiguous use of nighttime temperatures for determining  $\gamma$ , coupled with the better detectors available to measure low temperatures at high resolution, present a cogent argument for increasing the meager data presently available. We hope that our analysis will lend further justification for initiating new lunar measurements.

#### AVAILABLE LUNAR NIGHTTIME TEMPERATURE DATA

Pettit and Nicholson (Ref. 90) made the first determination of lunar nighttime temperatures and obtained a value of  $120 \pm 5^{\circ}\text{K}$  for the midnight temperature by using a vacuum thermocouple. By

using more recent atmospheric transmission data, a correction of the midnight temperature to  $108^{\circ}\text{K}$  was made (Ref. 106). Sinton (Ref. 89) determined a midnight temperature of  $122 \pm 3^{\circ}\text{K}$  for two areas near the limb. Murray and Wildey (Ref. 88) and Saari and Shorthill (Ref. 106) measured nighttime temperatures from which extrapolated midnight temperatures of  $106^{\circ}\text{K}$  and  $99^{\circ}\text{K}$  were obtained. These temperatures can perhaps best be described as upper limits to the midnight temperature. Low (Ref. 99), using a very sensitive bolometer, was able to obtain measurements of midnight temperatures ranging from less than  $70^{\circ}\text{K}$  to over  $150^{\circ}\text{K}$ .

#### NIGHTTIME TEMPERATURES FOR TWO-LAYER MODELS

The two-layer model was first used by Piddington and Minnett (Ref. 110) to explain their microwave temperature measurements. Since then this model has been used by several investigators (Jaeger, Ref. 102; Sinton, Ref. 89) to match successfully lunar eclipse cooling curves. Because of the short cooling time during an eclipse, temperature changes occur within the upper centimeter of surface material. Hence, the interpretation of eclipse data in terms of a two-layer model would converge to the homogeneous model for upper layer thicknesses exceeding a few millimeters.

The object of this study is not necessarily to "match" actual lunar data, which at best is meager at this time, but to determine the effect of varying upper layer thicknesses on lunation temperatures as a function of the thermal parameters of both layers. The usefulness of this study, which to our knowledge has not been previously made, resides in the fact that the lunar midnight temperature, by virtue of its greater penetration depth, is a sensitive index of the material properties of the uppermost layer of the moon to as much as 15 centimeters. In addition, this index enables one to eliminate various other explanations that have been offered to account for the recently observed thermal anomalies discussed above.

The two-layer model consists of an upper layer of "soft" insulating material supported by an underlayer of "harder," more conductive material. The following combinations of  $\gamma$  values ( $\gamma = (\kappa\rho c)^{-\frac{1}{2}}$ ) were studied (a higher  $\gamma$  value corresponds to a more highly insulating or "softer" material):

<u>Upper Layer <math>\gamma_0</math></u>	<u>Lower Layer <math>\gamma_1</math></u>
1250	250
1250	20
1000	250
1000	20
750	250
750	20

Figure 41 is a typical plot of lunation temperature as obtained from the IBM 7094 CALCOMP plotter. Temperature is plotted versus lunation time. A lunation time of 0 or 1.0 corresponds to high noon of the lunar day, and a lunation time of 0.5 corresponds to midnight. All the curves are for upper and lower layer  $\gamma$  values of 1000 and 250, respectively. The lunar night is in the region between 0.25 and 0.75. As seen from Fig. 41, there is very little difference in the temperature curves during solar insolation for different upper layer thicknesses. During the lunar nighttime ( $0.25 \leq t \leq 0.75$ ) however, the lunation curves show appreciable differences. The thinner the upper layer, the hotter the surface temperature tends to be. This can be explained in the following manner: the thicker the insulating layer, the more effective it is as a barrier to heat flow. The surface temperature reaches a balance that is controlled by the heat flow radiating from it and the heat flow coming from the interior. As the insulating layer becomes thicker, it effectively prevents more heat from flowing from the interior to the surface, consequently the surface cools more rapidly. An exception to this occurs at the beginning of lunar night. There is a crossing over between the two lowermost curves. Initially the temperature of the thicker layer is higher, but it then decreases below the temperature of the thinner layer at a lunation time of 0.325. The crossover is caused by the fact that the thermal energy content of the thicker layer is higher at the inception of nighttime. As the influence of this initial condition diminishes with time, the presence of the lower layer becomes dominant, thereby resulting in a lower rate of cooling for the surface with a thinner insulating layer.

In Fig. 41, we can readily see that there is very little variation between the various curves of the two-layer models, other than in the nighttime region. We may, therefore, use the midnight temperature as a convenient parameter that characterizes a lunation curve. Figures 42 and 43 are plots of midnight temperature versus upper layer thickness. Figure 42 is for a lower layer  $\gamma$  value of 250 with each curve representing a different upper layer  $\gamma$  value. The curves converge to a midnight temperature of 138°K,

which represents the results for a homogeneous model with the lower layer  $\gamma$  value of 250. The curves become asymptotic at midnight temperatures ranging from about 90 to 102°K, with upper layer  $\gamma$ 's ranging from 1250 to 750. This asymptotic behavior is due to the attenuation of the thermal heat wave as it progresses through the material. This effectively makes the surface temperature independent of the nature of material below a certain depth. The two-layer model, therefore, converges to the homogeneous model when the upper layer becomes sufficiently thick.

The limitations of midnight temperatures for the determination of a unique two-layer model is readily apparent. For a given midnight temperature, there is a range of  $\gamma$  values and upper layer thicknesses that are possible. This is illustrated in Fig. 44, where the  $\gamma$  of the upper layer is plotted against the thickness of this layer for a midnight temperature of 110°K. Each curve represents a different lower layer  $\gamma$  value. The curves are asymptotic to a  $\gamma$  value of 580, which corresponds to the homogeneous model.

Although the curves in Figs. 41 through 44 speak for themselves, it is interesting to point out that the inability of the midnight temperature to discriminate between the effects of the  $\gamma_0$  and  $z_0$  parameters of the two-layer model is not a serious limitation. This is because, as the results point out, these two parameters (related to the hardness and depth of the uppermost layer) vary in a "compensating" manner as far as the suitability of the layer for engineering operations on the moon is concerned. We notice in Fig. 44, that for a given midnight temperature, high  $\gamma$  values (representing "soft" materials) are associated with shallow layers of the orders of a few centimeters, overlying a much harder material. Conversely, thermally homogeneous layers, that could range in depth from a few centimeters to infinity, have to be associated with relatively hard materials ( $\gamma_0 = 500$ ) to satisfy a midnight temperature of 110°K.

It is conceivable, however, that a layer on the lunar surface would be both deep and soft if its midnight temperature is appreciably lower than 110°K. The possibility, as revealed by our analysis, that soft and deep layers of the lunar surface could correspond to a midnight temperature of 70°K, plus the probability, as revealed by Low's recent lunar measurements, that such areas could exist on the moon, lend a great deal of scientific importance and engineering urgency for performing additional analyses and high-resolution lunar measurements of the nighttime temperatures of specific areas of the lunar surface.

## NIGHTTIME TEMPERATURES FOR A HOMOGENEOUS MODEL AS FUNCTIONS OF $\gamma$ AND EMISSIVITY

The thermal inertia constant  $\gamma$ , or the midnight temperature  $T_m$ , of a given area of the moon may be used as an index of the hardness of that area if it is assumed that the thermal conductivity of that area does not vary with temperature. Low  $\gamma$  or high  $T_m$  values would be indicative of relatively high bearing strength; conversely, high  $\gamma$  and low  $T_m$  values would be indicative of a low bearing strength. Naturally,  $T_m$  is a more convenient index than  $\gamma$ , because it is directly measured or related to the energy emitted at a given lunar phase, whereas  $\gamma$  has to be estimated from the over-all lunation data, and is subject to a greater number of assumptions.

In view of present familiarity with  $\gamma$  as a thermophysical parameter, and the newness of  $T_m$  as a substitute for  $\gamma$ , we have extended the solution of the homogeneous, temperature independent model in order to present a  $\gamma$  versus  $T_m$  relationship at various emissivities and for midnight temperatures ranging from 50 to 200°K. Recent measurements by Low (Ref. 99) indicate nighttime temperatures of this order.

Figure 45 shows the lunar midnight temperature as a function of the thermal inertia parameter  $\gamma$  for emissivities of 0.8, 0.9, and 1.0. As discussed in the Mathematical Model Section, the results are presented in terms of an equivalent blackbody surface temperature. The calculations of surface temperatures, however, are made using the indicated emissivities.

For a given value of  $\gamma$ , the surface temperature is greater for lower emissivities. This results from the less rapid cooling of the surface during the nighttime for lower emissivities. It can be shown that the nighttime temperature is inversely related to the product of  $\gamma$  and  $\epsilon$ . This means that only the product of  $\gamma$  and  $\epsilon$  can be estimated from a nighttime temperature measurement. Because the emissivity of most materials is in the range 0.8 to 1.0, the inferred value of  $\gamma$  should be in error by not more than 10 percent if a value of 0.9 is used for the emissivity.

The 70°K to 150°K nighttime temperatures reported by Low correspond roughly to materials ranging in hardness from the consistency of "fluff" to that of porous rock. According to Fig. 45, these temperatures correspond roughly to  $\gamma$  values of 5000 and 140, respectively. The thermal and mechanical properties of these materials are analyzed in Phase I and correlated in Phase III.

## NIGHTTIME TEMPERATURES FOR A PARTICULATE MODEL WITH TEMPERATURE DEPENDENT THERMAL CONDUCTIVITY

This section deals with Case 5 where we examine the dependence of lunation temperatures on particle size and porosity for the thermal conductivity model derived in Phase IA. This is done in two ways: by examining the equations of heat conduction with the derived thermal conductivity expression, and by obtaining computer solutions for lunation temperatures for various values of the parameters.

In contrast to Cases 1 to 4, where the thermal conductivity is independent of temperature, the temperature variations of the lunar surface can no longer be evaluated in terms of the thermal inertia constant  $\gamma$ . The use of the midnight temperature ( $T_m$ ) as an index of material hardness was not necessary in Cases 1 to 4, however, in Case 5 it is.

The dependence of  $\gamma$  on temperature is shown by Fig. 8 for a porosity of 70 percent and various particle sizes. It is seen that  $\gamma$  decreases with increasing temperature for all particle sizes shown. This is due to the inverse dependence of  $\gamma$  on a thermal conductivity, which has a radiative component that increases with temperature. Hence, it is apparent that  $\gamma$  is not as useful a parameter in characterizing the thermal behavior of a material whose thermal properties vary with temperature as for the constant thermal properties case. For example, a  $\gamma$  of 1000 could correspond to a particulate material with a number of porosities and particle sizes exhibiting quite different lunation temperature variations. In order to uniquely characterize the cooling behavior of the surface temperature of a material, it is not its  $\gamma$ , but rather a knowledge of the dependence of its thermal properties on temperature that is of importance.

The thermal conductivity of the particulate model is of the form

$$k = C_1(1 - p)z^{\frac{1}{3}} + \frac{C_2dT^3}{1 - p},$$

where the constants  $C_1$  and  $C_2$  are functions of the material properties;  $z$  is the layer thickness,  $d$  the particle size,  $T$  the temperature, and  $p$  the porosity. For purposes of this study, we assume that the lunar surface is composed of basalt or a basalt-like material for which the constants  $C_1$  and  $C_2$  can be calculated. (Recent Luna 10 measurements of the radioactivity of the lunar surface seem to indicate levels consistent with that of basalt.)

The layer thickness requires further discussion. The model we developed for powders predicts that the thermal conductivity is a function of depth. This is due to the dependence of contact



area on the weight of material above the contact region. In order to simplify the problem of calculating the lunar surface temperatures, we developed a computer program that can separately incorporate a temperature dependent thermal conductivity and a depth dependent conductivity, but cannot include both variations simultaneously. Because the thermal conductivity depends on the cube of temperature and only on the 1/3 power of depth, the assumption was made that an average effective depth corresponding to 20 cm should be used in the computer program as a first approximation. In future studies, it would be desirable to revise the computer program to include temperature and depth variation of thermal conductivity simultaneously.

For certain limiting cases we can gain some insight into the dependence of porosity on lunation temperatures by examining the equation of heat conduction and the boundary condition equation. For the case of a temperature dependent thermal conductivity, the heat conduction equation is

$$\rho c \frac{dT}{dt} = \frac{\partial}{\partial x} k(T) \frac{\partial T}{\partial x} .$$

We substitute in the equation of heat conduction the following expressions for the density and thermal conductivity:

$$\rho = \rho_0(1 - p)$$

$$k(T) = c_1(1 - p) + \frac{c_2 T^3}{1 - p} ,$$

where  $\rho_0$  is the density of the solid material,  $c_1$  and  $c_2$  are material constants, and  $p$  is the porosity. The resulting equation is

$$\rho_0 c(1 - p) \frac{\partial T}{\partial t} = \frac{\partial}{\partial x} \left[ \left( c_1(1 - p) + \frac{c_2 T^3}{1 - p} \right) \frac{\partial T}{\partial x} \right] . \quad (37)$$

The radiation boundary condition is given by

$$\sigma \epsilon T^4 = A(t) + \left[ c_1(1 - p) + \frac{c_2 T^3}{1 - p} \right] \frac{\partial T}{\partial x} . \quad (38)$$

The effect of porosity ( $p$ ) can be determined for two limiting cases. The first case occurs when the radiation term of the thermal conductivity is much larger than the contact conduction term, i.e.,

$$\frac{c_2 T^3}{1-p} \gg c_1(1-p) .$$

This would be true for combinations of large particles, high temperatures, and high porosities. By neglecting the contact conduction term and making the transformation

$$y = (1-p)x ,$$

the equation of heat conduction becomes

$$\frac{\partial T}{\partial t} = \frac{c_2 T^3}{\rho_0 C} \left( \frac{\partial T}{\partial x} \right)^2 + \frac{3c_2 T^2}{\rho_0 C} \left( \frac{\partial T}{\partial x} \right)^2$$

and the boundary condition transforms to

$$\sigma \epsilon T^4 = A(t) + c_2 T^3 \frac{\partial T}{\partial y} .$$

The coefficients of the above equations are seen to be independent of porosity. This indicates that surface temperature variation will not depend on porosity. Porosity only acts in the radiation dominant case as a scale factor in establishing the variation of temperature with depth. One can therefore conclude that, for this case, no information can be obtained about the porosity from measurements of surface temperature alone.

The second case considered occurs when the radiation term of the thermal conductivity can be neglected when compared with the contact conduction term. This approximation is applicable for conditions of small particle size and low temperature. By substituting the transformation

$$z = \left( \frac{\rho_0 C}{k_0} \right)^{\frac{1}{2}} x$$

into Eqs. (37) and (38) and neglecting the radiation term we obtain

$$\frac{\partial T}{\partial t} = \frac{\partial^2 T}{\partial z^2}$$

$$\sigma \epsilon T^4 = A(t) + (c_1 \rho_0 C)^{\frac{1}{2}} (1 - p) \frac{\partial T}{\partial z} .$$

The solution to the above equations at the boundary depends on the parameter  $(c_1 \rho_0 C)^{\frac{1}{2}} (1 - p)$ . This parameter is simply the reciprocal of the thermal inertia constant which shows a dependence on the porosity as given by

$$\gamma \sim \frac{1}{1 - p} .$$

This result is due to the dependence of both density and thermal conductivity on the solid fraction for the case where radiation can be neglected. The general case, where radiation and contact conduction must both be considered, does not lend itself readily to examination of porosity effects without obtaining solutions to heat transport equations.

Computer solutions to the equations were obtained for the combined case of radiation and conduction for various values of porosity and particle size. Typical results are shown in Fig. 46, where the surface temperature variation during a lunation is given for different combinations of particle size and porosity. The curves show a similar behavior to the temperature independent case, Fig. 41. The lunar mid-night temperature (lunation fraction = 0.5) can again be conveniently used to describe lunation behavior.

### Discussion of Results

Figures 47 and 48 present the midnight temperature of a particulate model of the lunar surface as functions of particle size and porosity. The two extreme cases, radiation dominance and contact conduction dominance, can be examined in terms of the effect of these variables on midnight temperatures  $T_m$ . The radiation dominant case corresponds to large particles, where  $T_m$  is high and nearly independent of porosity. In contrast, the conduction dominant case corresponds to small particles, where  $T_m$  is low but strongly dependent on porosity. According to these figures,

a high lunar midnight temperature would imply a material composed of large particles (mm to cm), but of uncertain porosity. However, low midnight temperatures appear to be less ambiguous to interpret; high porosities and small particles (of the order of microns) seems to be necessary to account for them. The correlation of these nighttime temperatures with bearing strength is discussed in Phase III.

#### NIGHTTIME TEMPERATURES FOR A VESICULAR MODEL

This section deals with the thermal behavior of a vesicular lunar surface in which the solid phase is fully continuous. The analysis of this case is relatively simple because the thermal conductivity of this material, unlike that of powders discussed in Phase IA, is nearly independent of temperature. Therefore, the standard solution for Case 1, where  $\gamma$  is the characteristic parameter, can be used for this case.

By using the temperature independent relationship developed for the Loeb model in Phase IA, the  $\gamma$  versus porosity relationship is derived and shown as curve 1 in Fig. 49. It should be stressed that this curve represents the limiting case, where the solid phase in the porous material is fully continuous. The data points plotted in this figure do not fall on curve 1, primarily due to only partial consolidation in the solid phase. Curve 1 is therefore a lower limit for  $\gamma$  values at a given porosity.

For the temperature independent case,  $\gamma$  uniquely determines the midnight temperature at a given emissivity. By using the relationship in Fig. 45 (for  $\epsilon = 0.9$ ), the midnight temperature versus porosity of a vesicular lunar surface is derived and shown in Fig. 50. The curve in this figure represents again the limiting case of full consolidation. The intermediate, partially consolidated cases, as represented by the data points, fall into the shaded area. Figure 50 indicates that a given lunar midnight temperature could correspond to a wide range of porosities depending upon the degree of consolidation of the material. This uncertainty could be somewhat reduced by using porosities that are compatible with lunar data obtained at shorter and longer wavelengths. For instance, investigations at Grumman show that the average photometric properties of the lunar surface are best reproduced at porosities of 70 percent and higher. Radar investigations suggest lower porosities (Ref. 107) below a depth of a few centimeters. These average porosities are represented by a cross-hatched vertical column in Fig. 50. Upper values of lunar midnight temperatures, corresponding to these porosities, range from 160 to 180°K. It is of interest to recall that the highest lunar nighttime temperature recently reported by Low is 150°K.

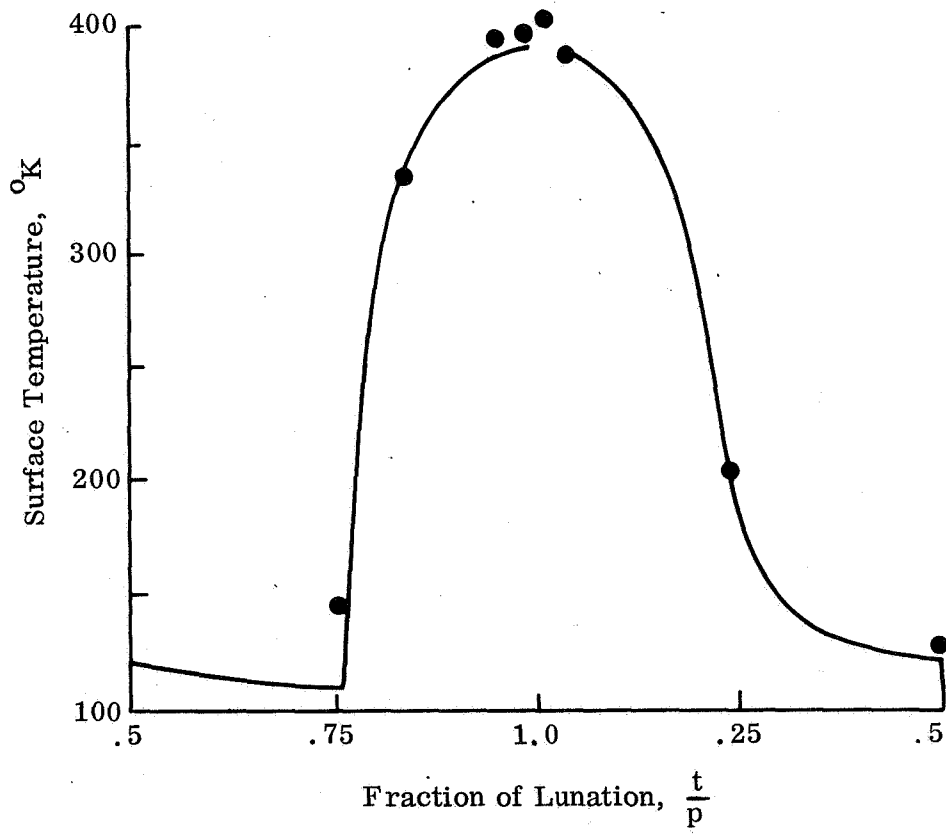


Fig. 36 Lunation Temperature Data Taken From Sinton (Ref. 89)

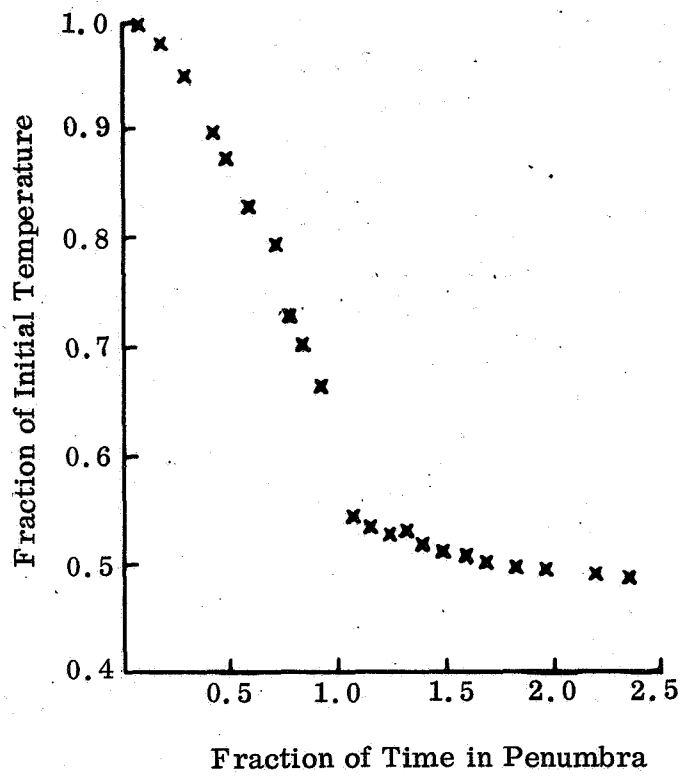
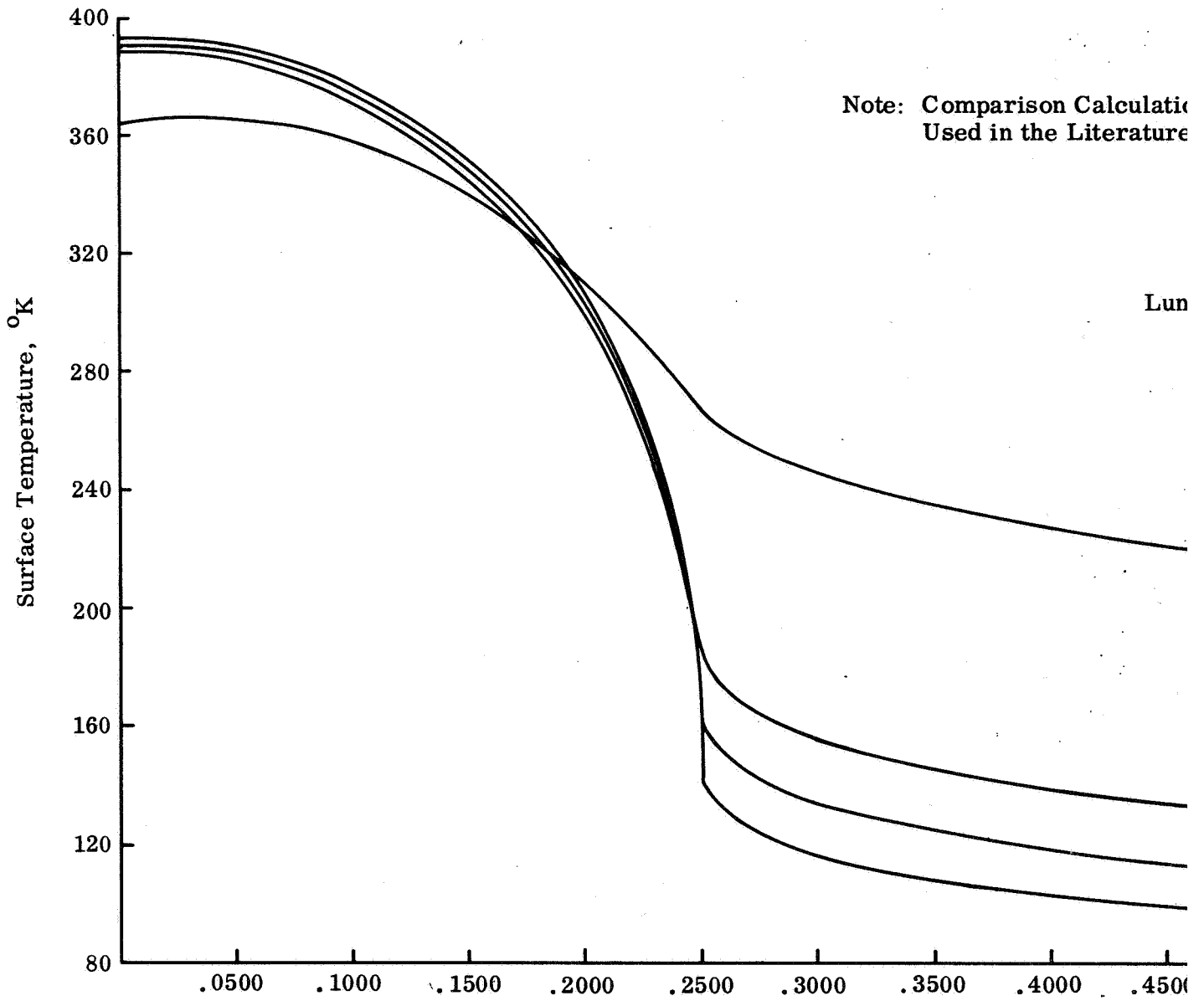


Fig. 37 Eclipse Temperature Data Taken From Pettit (Ref. 90)



Based on Assumption Previously  
(ref Fig. 39)

Surface Temp

$\gamma = 20$

.250

500

1000

Duration Time

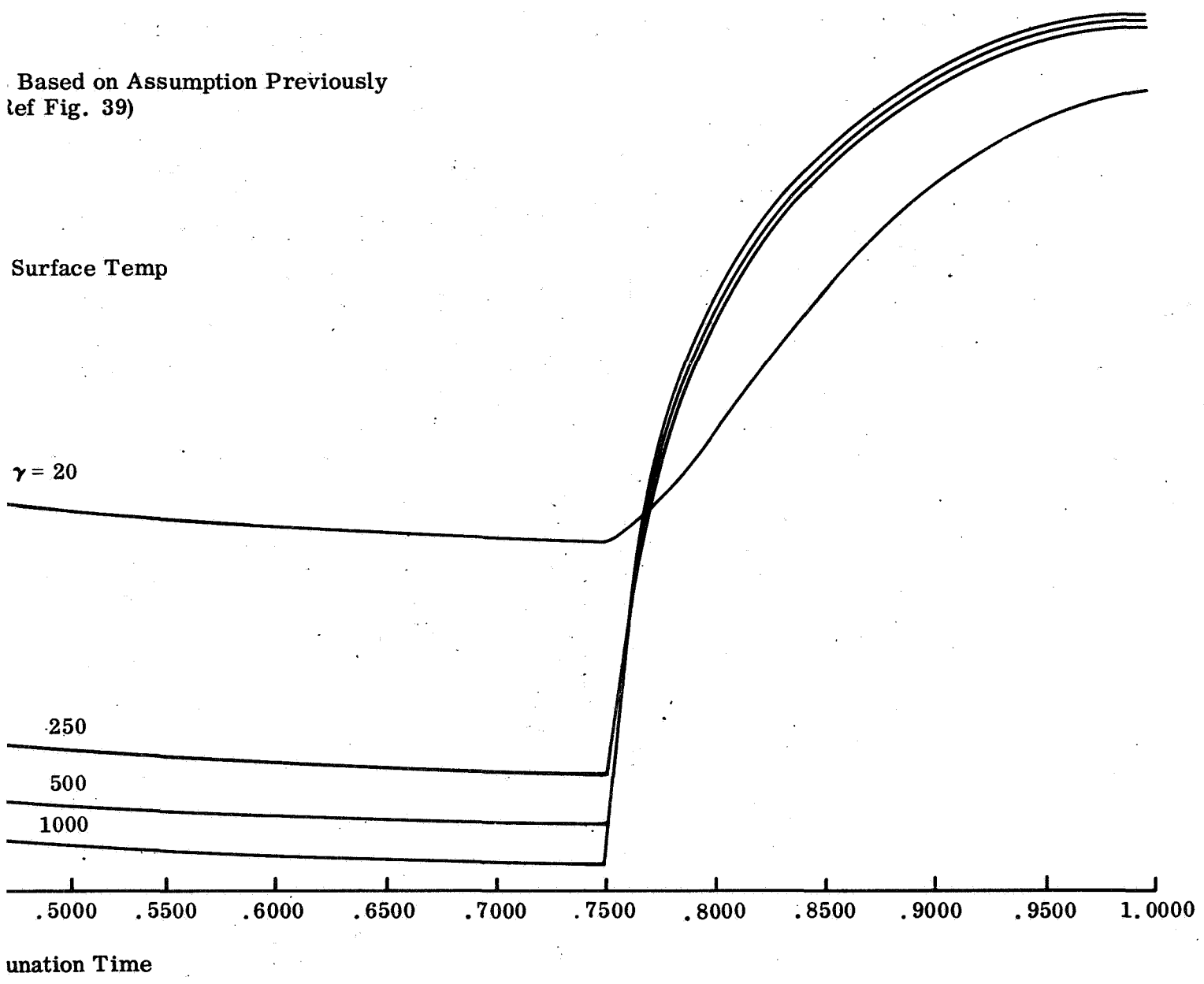


Fig. 38 IBM 7094 Calculated Luration Temperatures for Various Values of  $\gamma = (k\rho c)^{-1/2}$



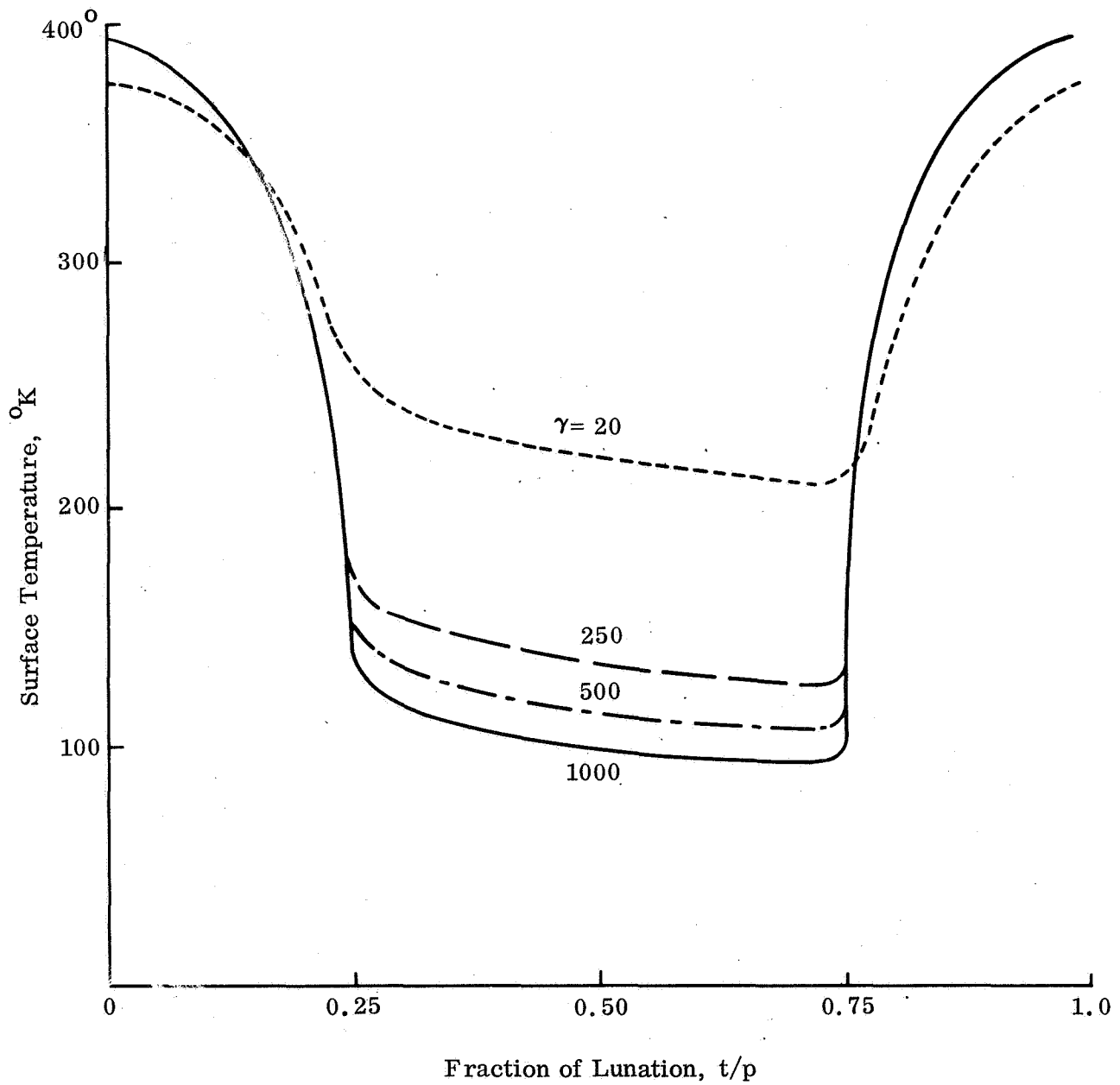
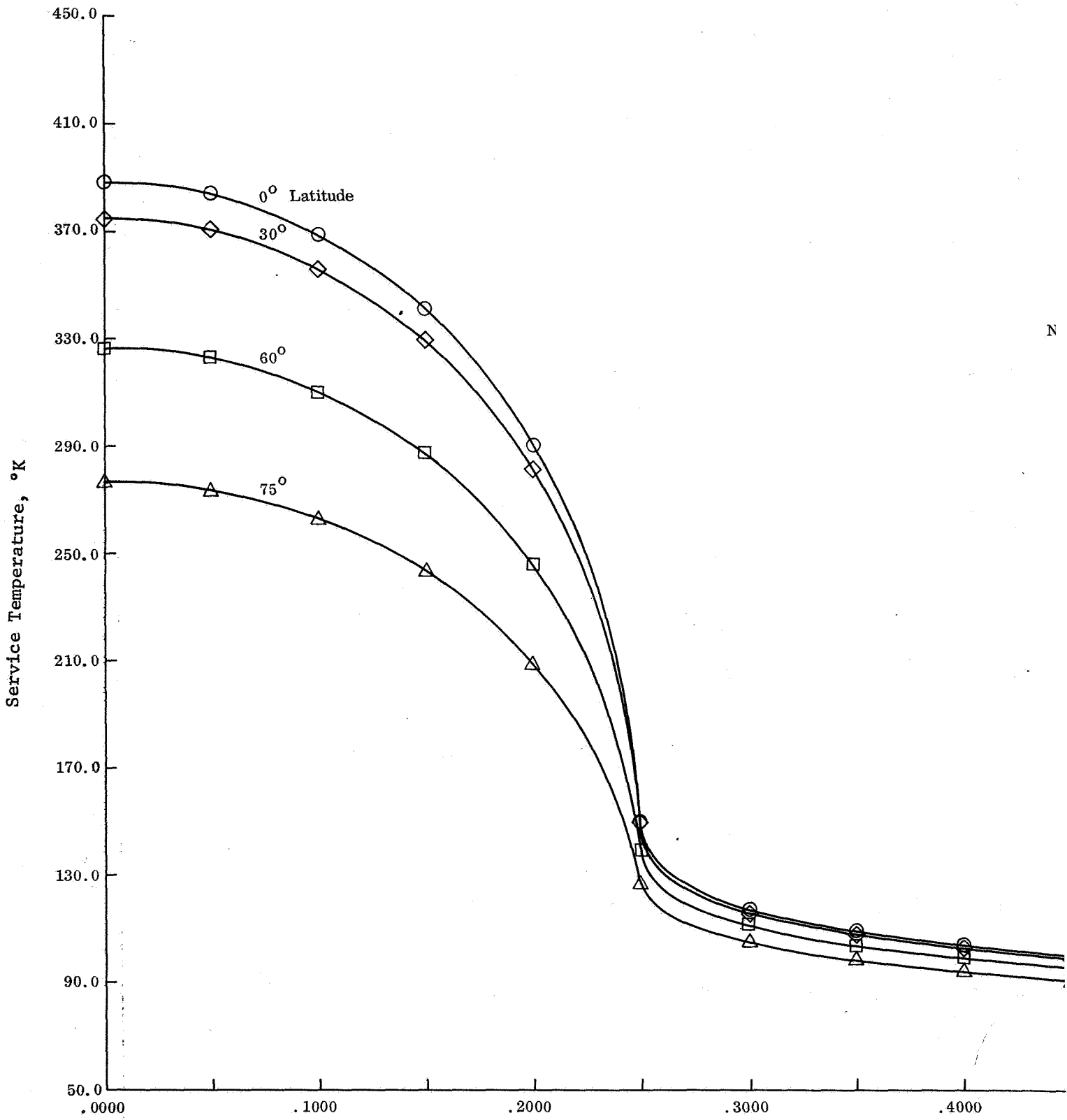


Fig. 39 Calculated Luration Temperatures for Various Values of  $\gamma$  from Krotikov, V. D. and Shchuko, (1963) (Ref. 5)



us Temperature  
t Model  
 $\tau = 1000$

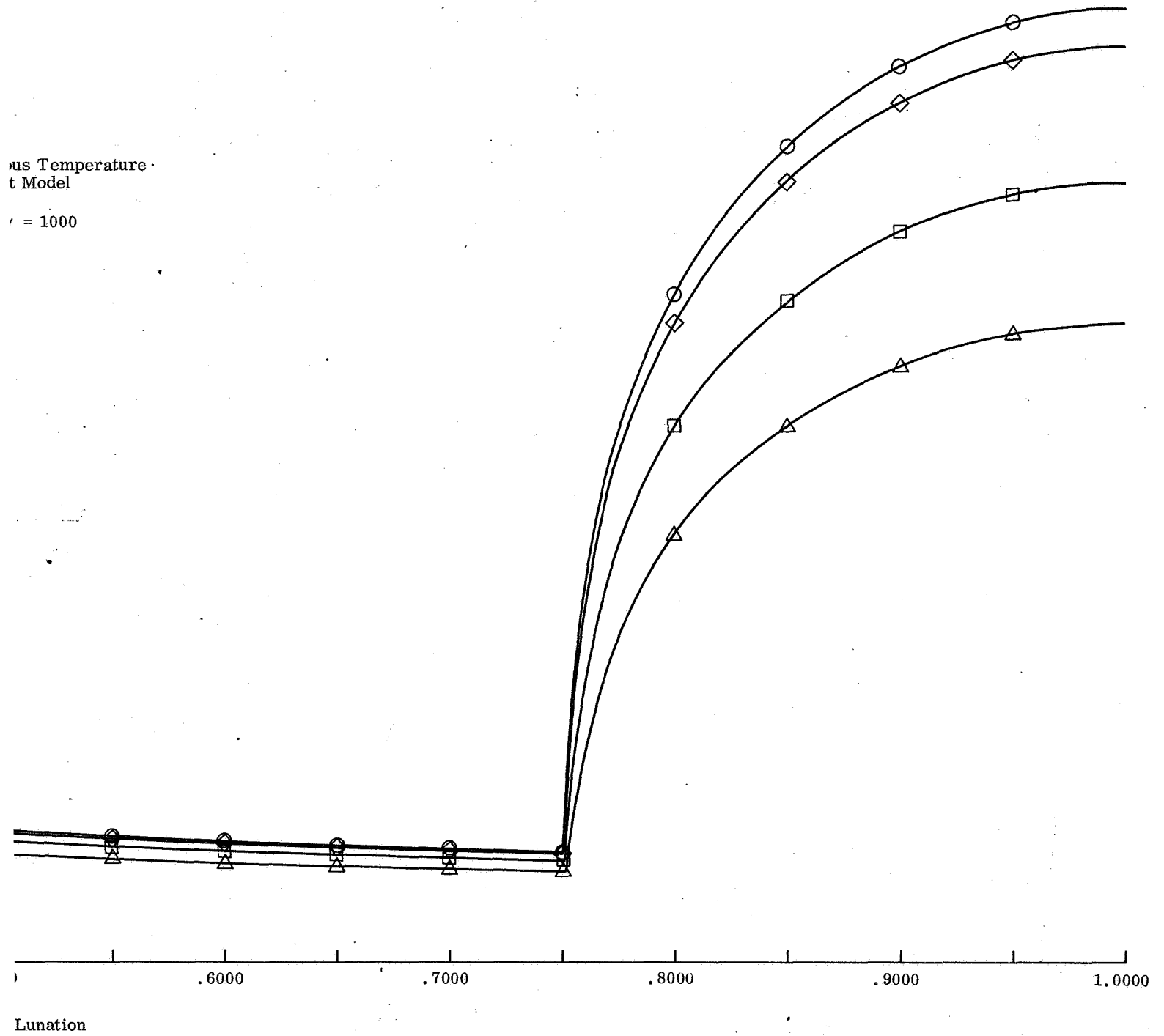


Fig. 40 Effect of Latitude on Lunation Temperatures

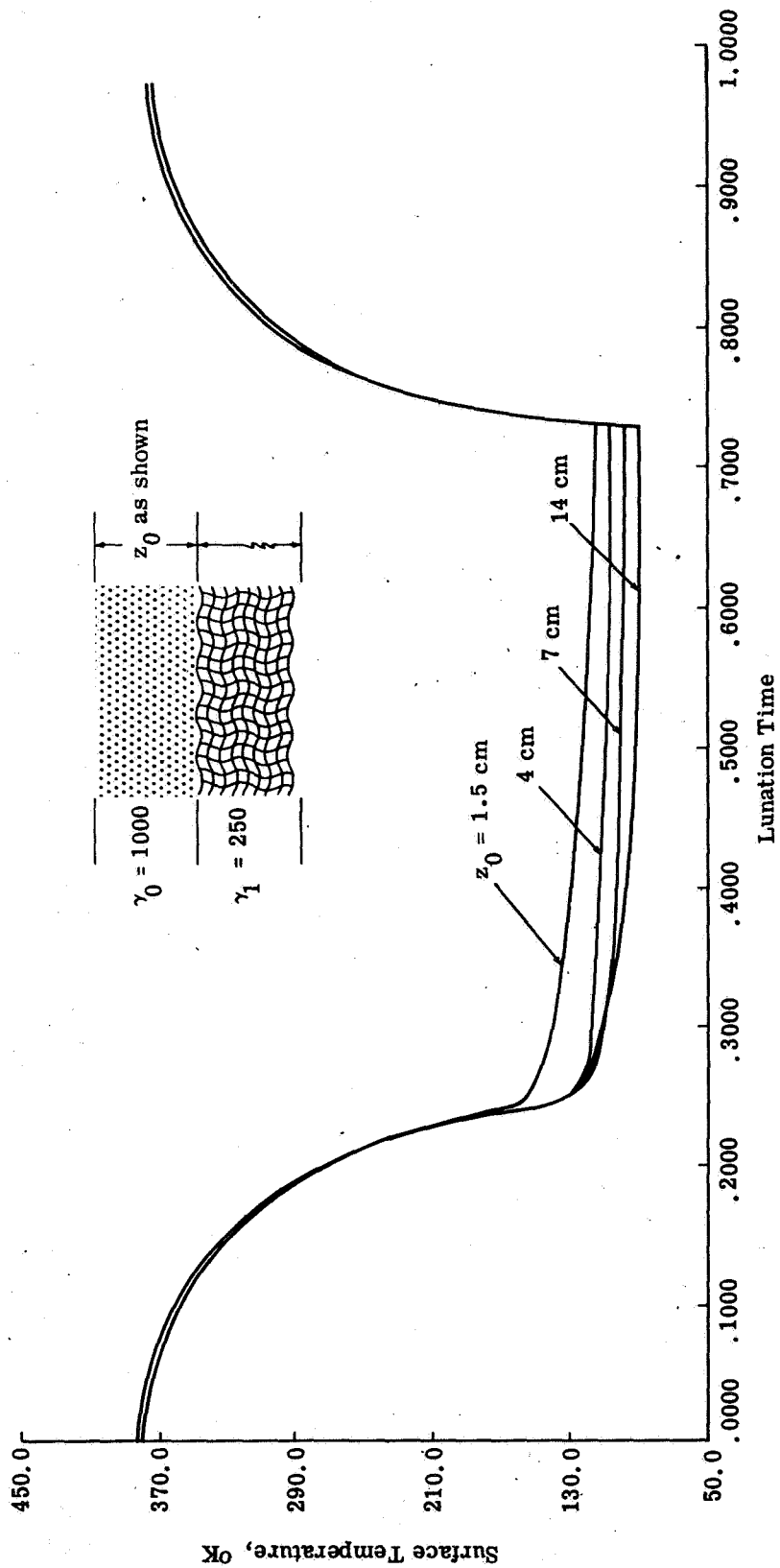


Fig. 41 Lunation Temperatures of Moon for Two-Layer Model

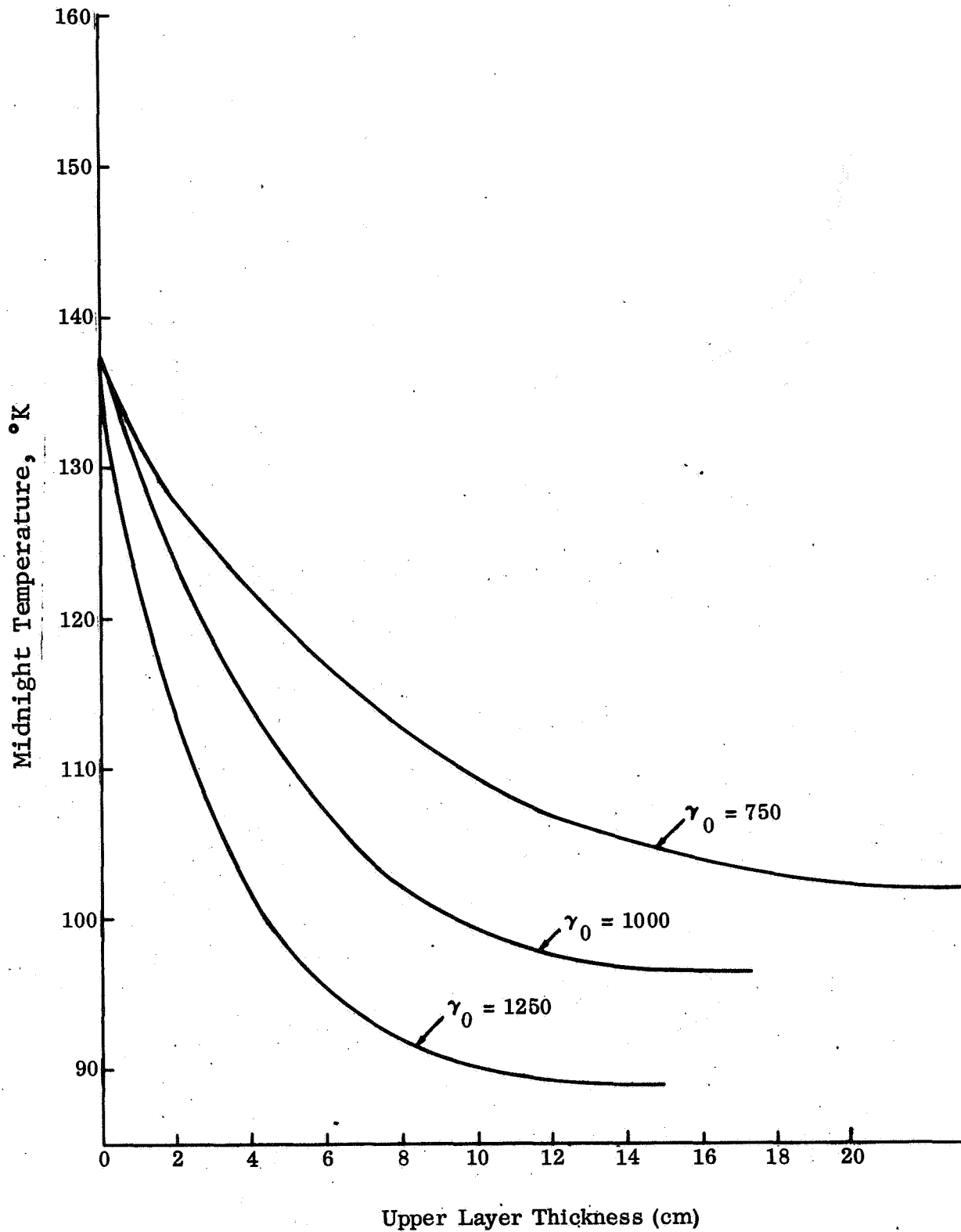


Fig. 42 Lunar Midnight Temperatures versus Upper Layer Thickness for Lower Layer  $\gamma_1 = 250$  and Upper Layer  $\gamma_0$  as Shown

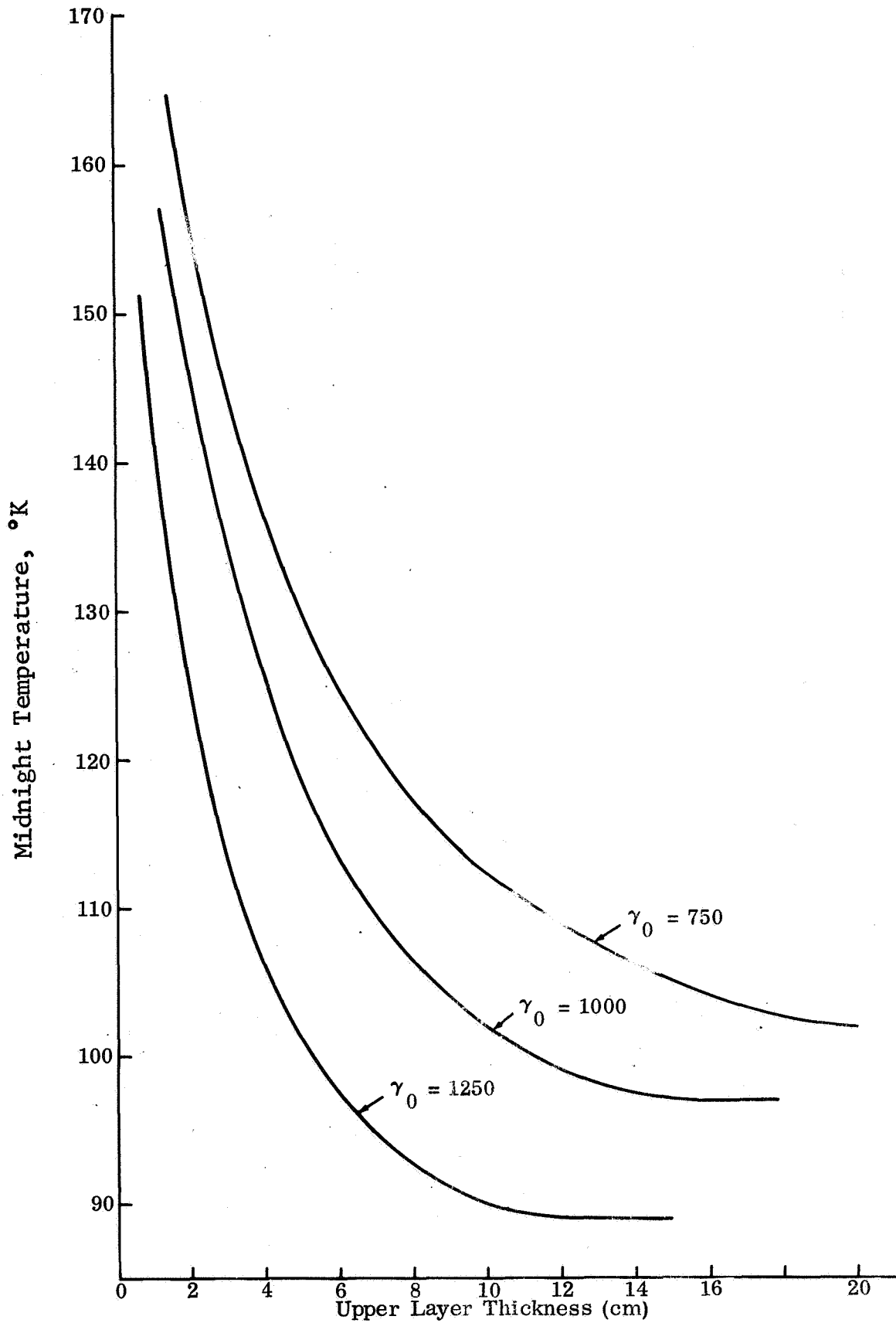


Fig. 43 Lunar Midnight Temperatures versus Upper Layer Thickness for Lower Layer  $\gamma_1 = 20$  and Upper Layer  $\gamma_0$  as Shown

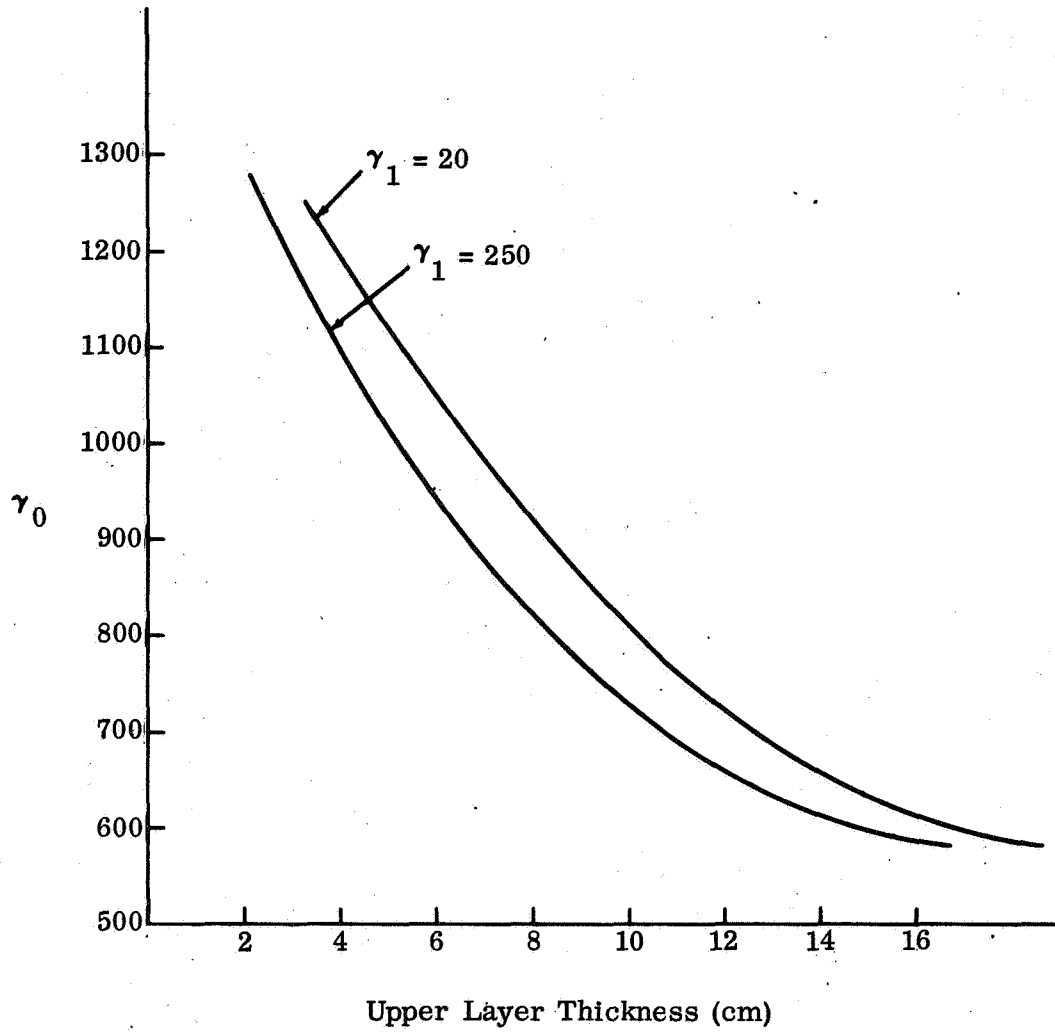


Fig. 44  $\gamma_0$  versus Thickness of Upper Layer for Midnight Temperature of  $110^\circ\text{K}$  Lower Layer  $\gamma_1$  as Shown

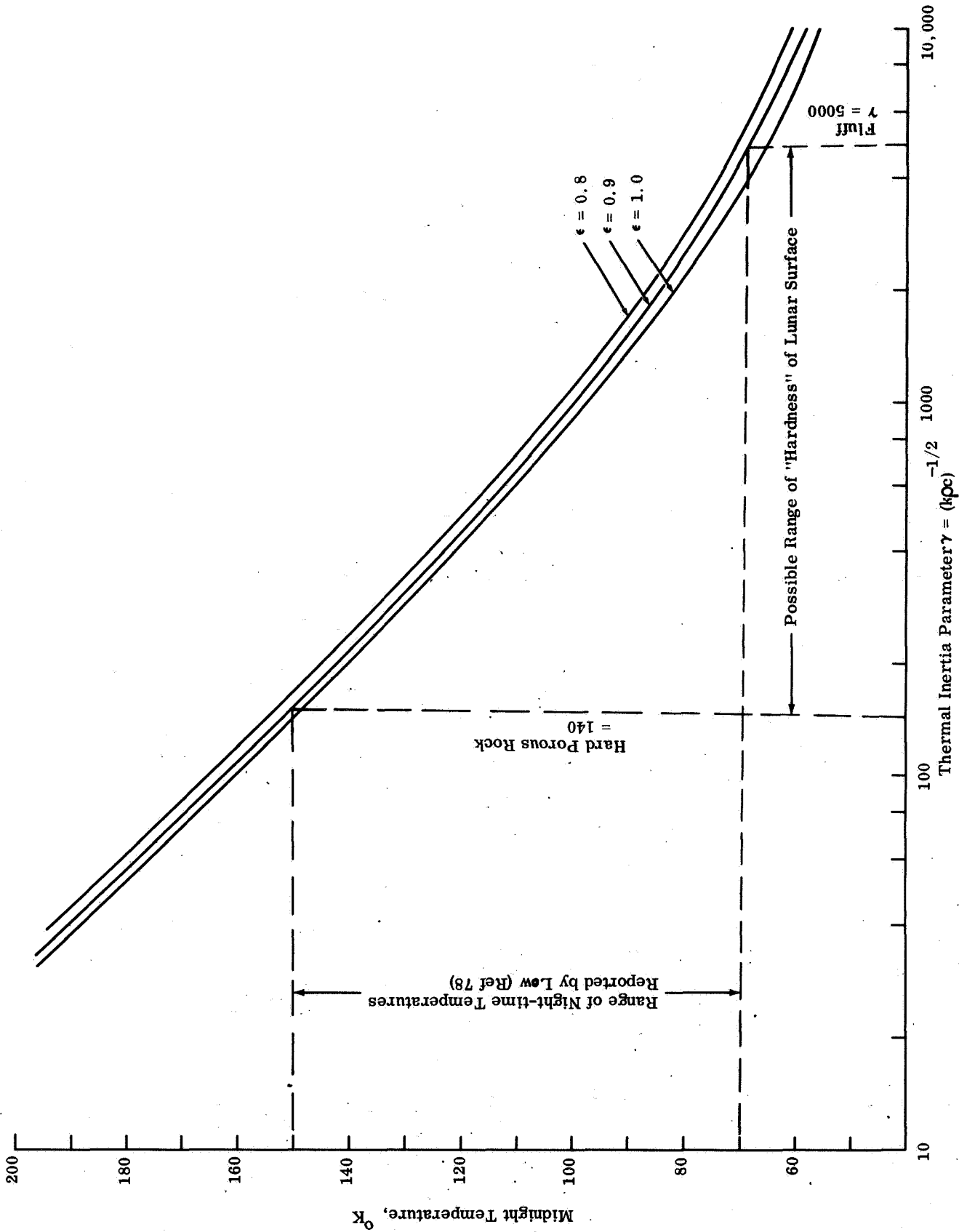
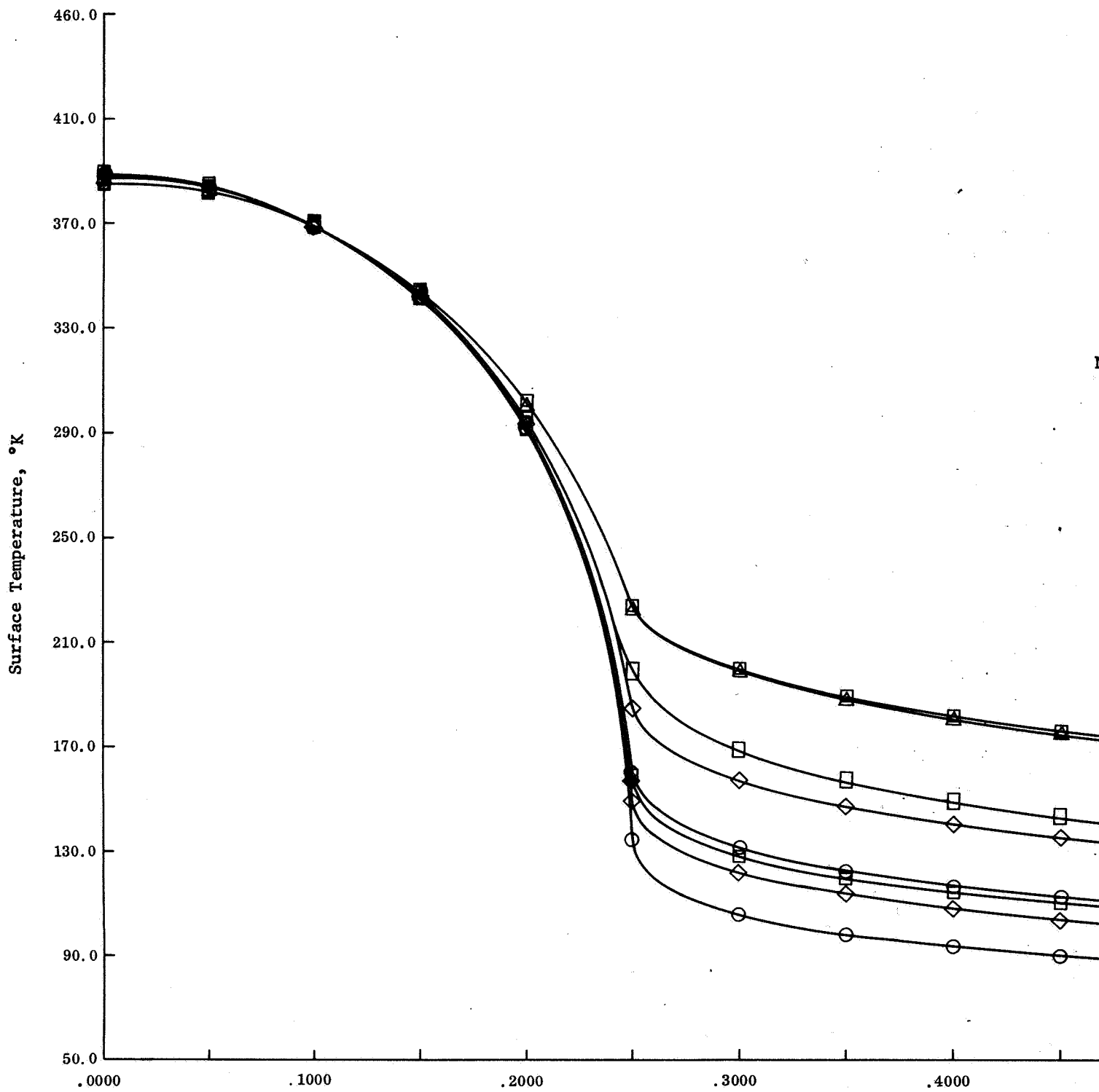


Fig. 45 Lunar Midnight Temperature versus  $\gamma$  and at Various Emissivities  
 Note: Homogeneous, Temperature Independent Model





Fr

141-1

e: Homogeneous, Temperature  
Dependent, Particulate Model

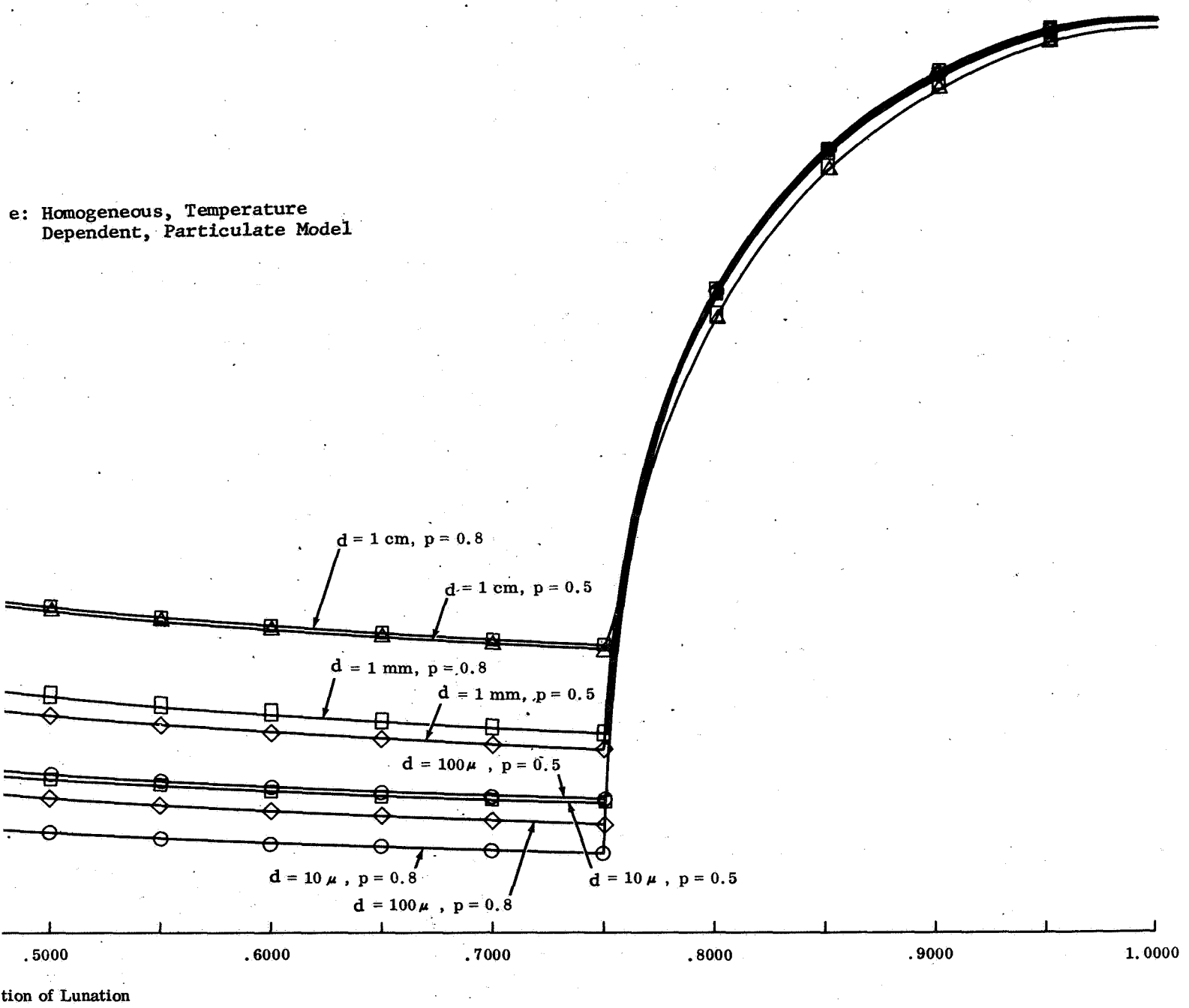


Fig. 46 Family of Lunation Curves at Various  
Porosities and Particles Sizes

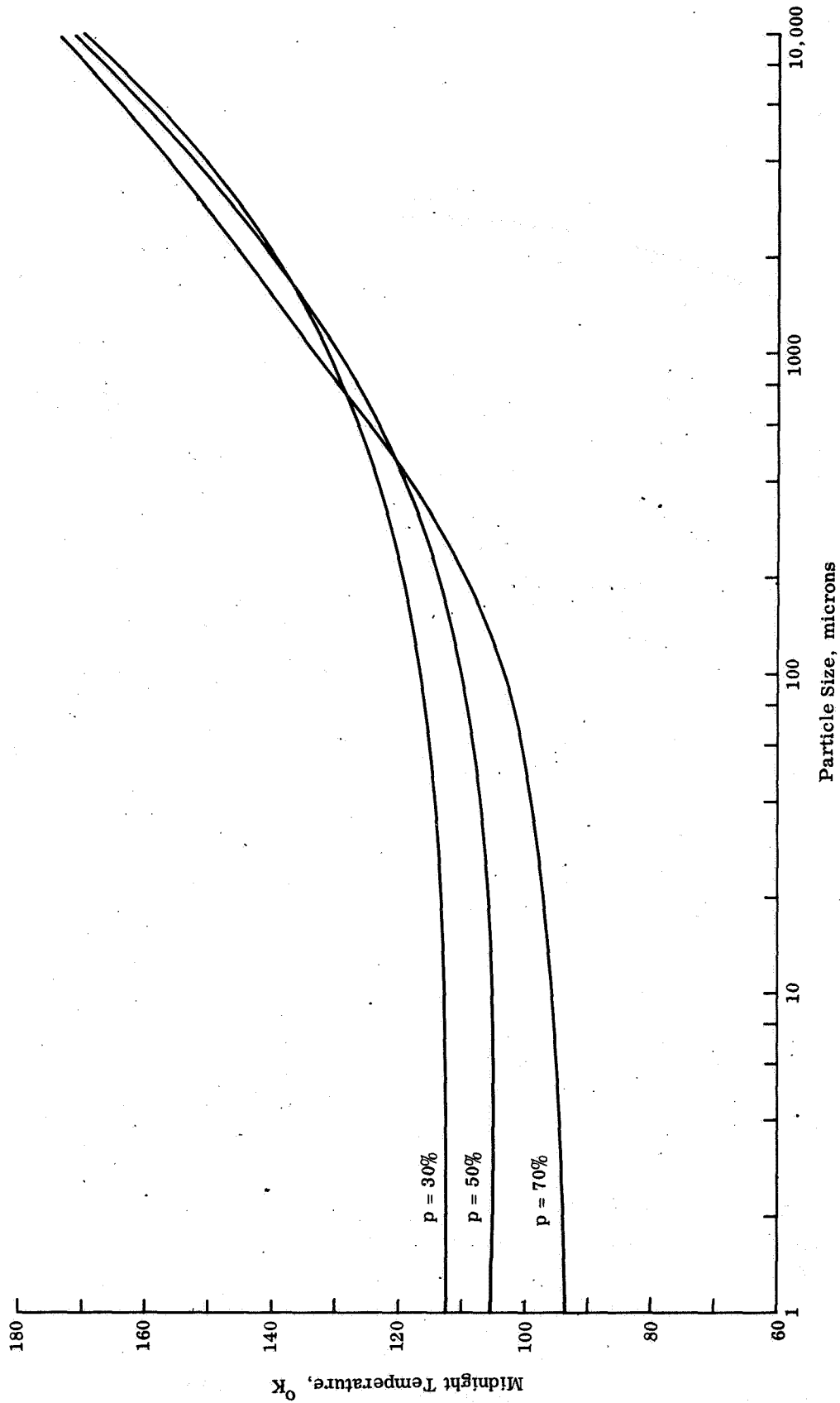


Fig. 47 Lunar Midnight Temperature versus Particle Size at Various Porosities  
 Note: Homogeneous Temperature Dependent Particulate Model

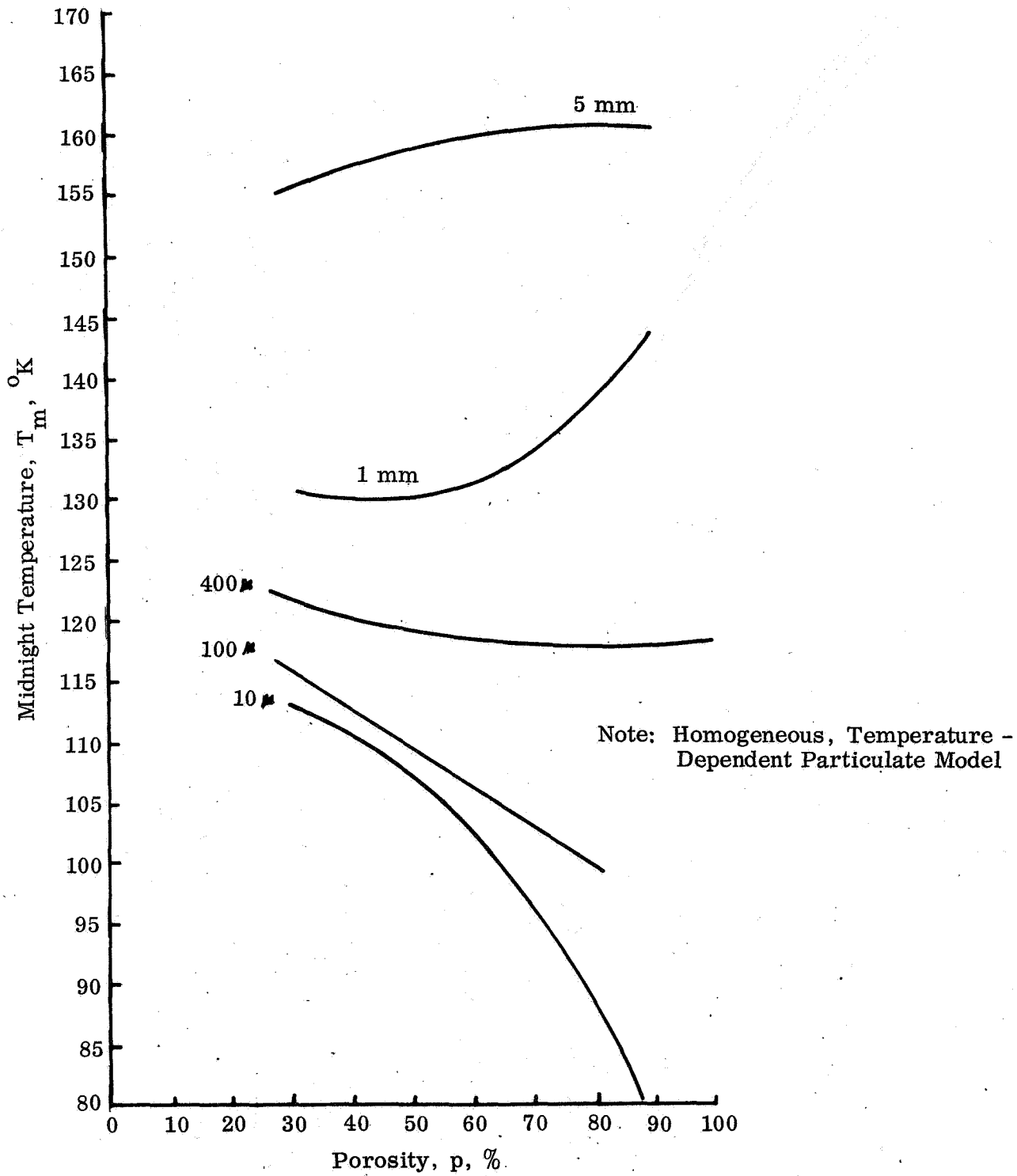


Fig. 48 Midnight Temperatures versus Porosity at Various Particle Sizes

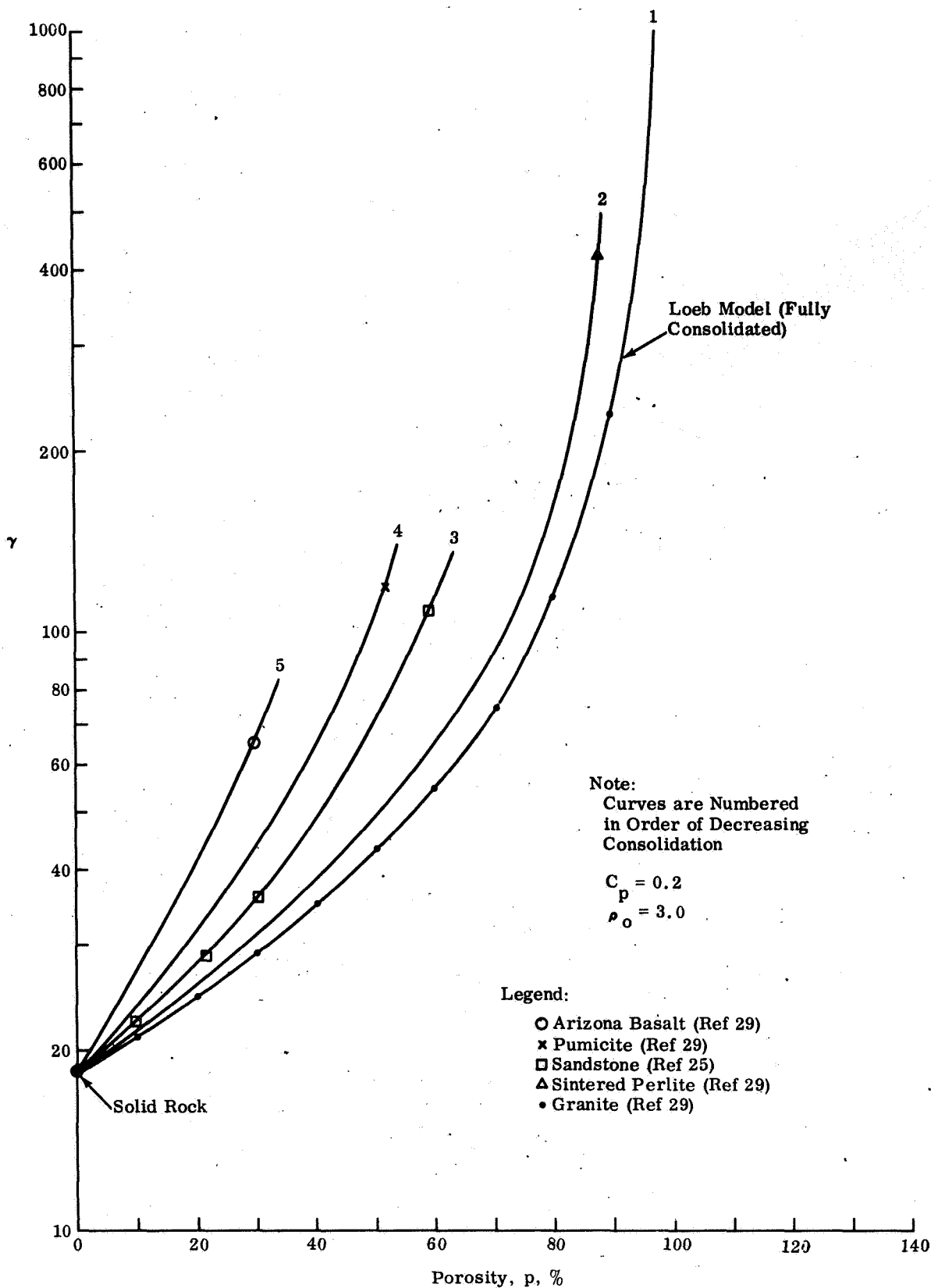


Fig. 49  $\gamma$  versus Porosity for a Vesicular Model

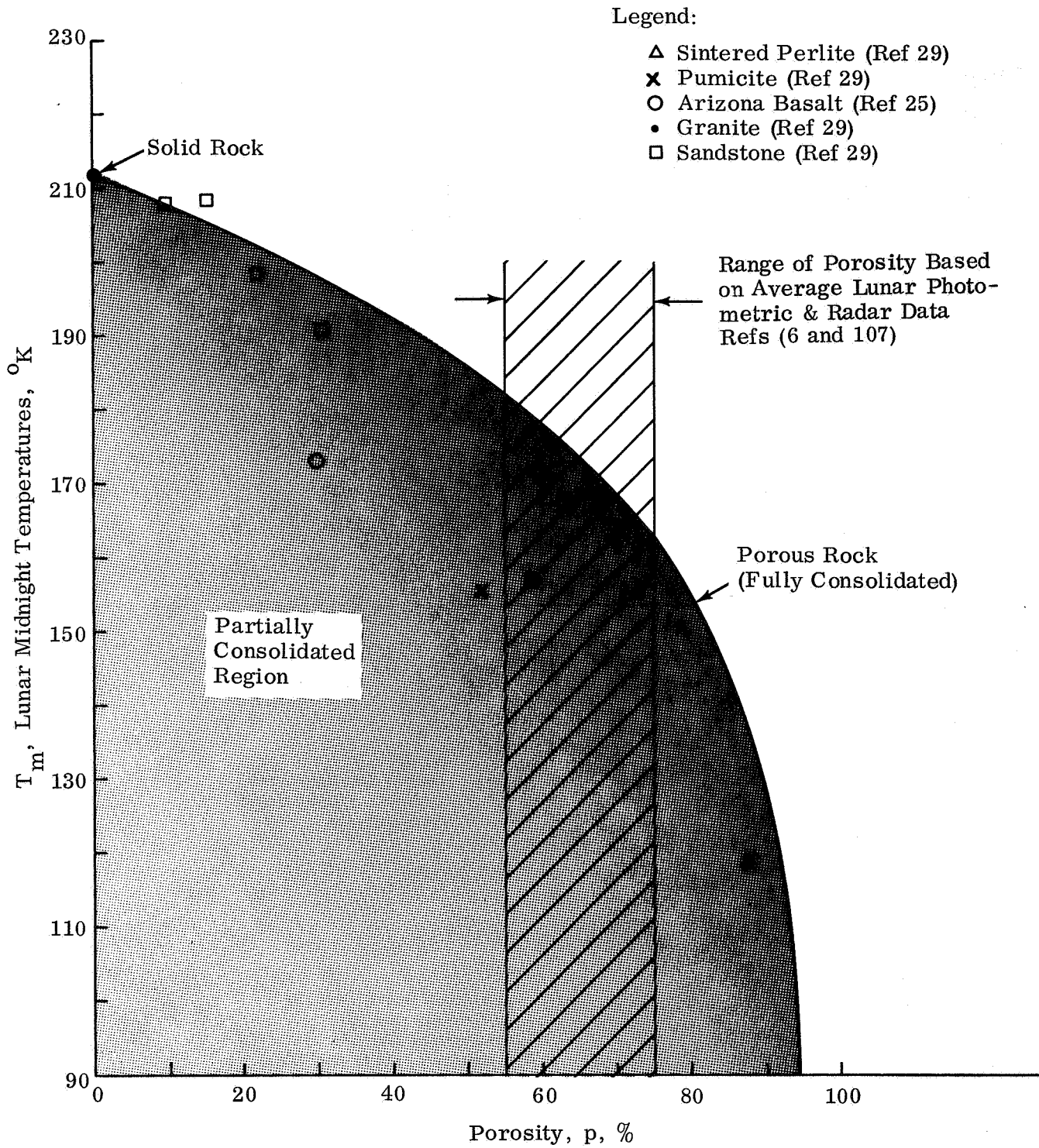


Fig. 50 Lunar Midnight Temperature versus Porosity for a Vesicular Model

### PHASE III: CORRELATION OF THERMAL AND MECHANICAL PROPERTIES OF THE LUNAR SURFACE

The main objective of the study is fulfilled in this phase of the report. This is accomplished in three steps. In step one, bearing strength versus porosity data on all porous media analyzed in Phase IB are abstracted in a single figure (Fig. 51); these media include fluff, soils, and porous rocks. Similarly, in step two, lunar midnight temperature versus porosity data, on the same materials as analyzed in Phases IA and II, are abstracted in another figure (Fig. 52). In step three, the data in Figs. 51 and 52 are cross-plotted (Fig. 53) in terms of lunar midnight temperature versus bearing strength. Surveyor 1 data are evaluated in the light of the results.

#### REDEFINITION OF SOME TERMS

The term "mechanical properties" has been used throughout this study to mean primarily bearing or crushing strength. However, the term "thermal properties," as applied to the moon, needs re-defining. It was first used in this study, as has generally been the practice in the literature, to imply the thermal inertia constant  $\gamma$  of the lunar surface. Later in this study, for reasons of necessity or convenience discussed in Phase II, it became more meaningful to imply the nighttime temperature of the lunar surface. The midnight temperature  $T_m$  was selected as a convenient index. Specifically then, by "correlation of the thermal and mechanical properties of extraterrestrial materials" we mean a correlation between midnight temperatures and bearing strength of the lunar surface.

In order to determine whether such a correlation is possible, three key properties of porous media were singled out (namely, porosity, degree of consolidation, and grain or pore size), and their relationship with bearing strength and lunar midnight temperatures were established in Phases I and II, respectively. The above key properties will now be used as links to correlate lunar midnight temperature with bearing strength.

The analyses in Phases I and II were made for the complete conceivable range of porosity and grain (or pore) size, but only the limiting cases of the "degree of consolidation" were considered; i.e., those two conditions where the solid phase is either fully discontinuous or fully continuous. These conditions have been

labeled particulate and vesicular representing soils and porous rocks, respectively, as illustrated in Fig. 12. Unfortunately, the intermediate conditions of partial consolidation, which most commonly occur in nature, are not as amenable to analysis as the limiting cases. However, it will be shown that this analytical difficulty does not seriously hamper the final correlation except in some cases which may best be resolved by actual experiments.

#### BEARING STRENGTH OF POROUS MEDIA (Fig. 51)

A new perspective on the bearing strength of porous media is gained by taking the individual curves of fluff, soils, and porous rock in Figs. 29 and 32 and plotting them on one set of coordinates as shown in Fig. 51. Notice that what we called vesicular and particulate media are in effect the upper and lower strength envelopes of a vast "gray" area consisting of partially consolidated materials. Such materials may encompass the full gamut of porosities and a bearing strength of about six orders of magnitude (from  $10^{-2}$  to  $10^4$  psi).

The boundary curves determine minimum and maximum strengths that are possible at a given porosity, or minimum and maximum porosities that are possible at a given strength. For instance at 70 percent porosity, a material could have a bearing strength of 1 psi or 1000 psi, depending whether it is fluff or fully consolidated porous rock. Conversely, at a given bearing strength, say 10 psi, porosities may range from 35 to 99 percent depending again upon the degree of consolidation.

Figure 51 shows that soils that obey the principles of conventional soil mechanics encompass a relatively narrow range of bearing strength and porosity. The porosity range (26 to 50 percent) is generally lower than those estimated for the outermost few centimeters of the lunar surface, but the range of bearing strength (1 to 100 psi) may well encompass values that are typical for most of the lunar surface, as attested by the Surveyor 1 data (see discussion of these data below). Unfortunately, this range of bearing strength is the most ambiguous to interpret in terms of porosity or degree of consolidation. Note that in Fig. 51, this range is common not only to densely packed soils, but also to highly porous consolidated materials. The outer regions above 100 psi and below 1 psi, are easiest to interpret since they are predominated by porous rocks and fluffs, respectively.



## MIDNIGHT TEMPERATURES OF PARTICULATE AND VESICULAR LUNAR SURFACES (Fig. 52)

The heat conduction of the lunar surface during a lunation is solved in Phase II for models of the lunar surface consisting of particulate (unconsolidated) and vesicular (fully consolidated) materials. The results, expressed in terms of lunar midnight temperature  $T_m$  versus porosity  $p$ , are summarized in Fig. 52. Particulate materials, unlike porous rocks, show a grain or pore size dependence because of the dominance of the radiative component of heat conduction (see Phase IA).

Remember that the results shown in Fig. 52 are based on two major assumptions, namely, that the material is homogeneous both in the vertical and horizontal directions and that surface roughness and internal heat sources have been neglected. In the absence of these effects, thermal conductivity (hence  $T_m$ ), is primarily a function of three physical parameters, namely: porosity, degree of consolidation, and grain or pore size. In the radiation-dominant case, porosity is not an important parameter, but grain size is.

Materials termed fluff, soils, and partially or fully consolidated porous rocks occupy distinct areas in Fig. 52. The boundaries of these areas are reasonably well defined by the above three parameters. Fluffs, for instance, occupy the lower right corner of Fig. 52, describing a region where fine submillimeter particles intersect the high porosity region ( $p \gg 50\%$ ). The upper boundary of the fluff region is arbitrarily set at about 1 mm. It is reasoned that particles larger than 1 mm cannot maintain porosities above 50 percent without interparticle bonds stronger than those provided by van der Waals forces of attraction. For porosities above 50 percent, and particles larger than 1 mm, it is necessary to postulate some cold welding or partial consolidation between the solid elements. For this reason the area above  $T_m = 130^\circ\text{K}$ , which corresponds to large particles, is shaded and labeled as the partially consolidated region. As we move to the right along a horizontal line across this region, both the degree of consolidation and the porosity of the material increase. Thus, a given lunar midnight temperature could denote a uniform bearing strength, regardless of porosity, because a decrease in strength due to an increase in porosity is compensated by a corresponding increase in interparticle bond. This concept is discussed in greater detail in the next section.

At the lower end of the temperature scale, the partially consolidated region merges into soils or fluff, depending upon porosity, but at the upper end it is delimited by the solid, porous

rock curve which represents the fully consolidated state (i.e., solid phase fully continuous) at a porosity that is the maximum possible for a given  $T_m$ . Lunar "hot spots" generally exhibit nighttime temperatures above  $130^\circ\text{K}$ . According to Fig. 52, these temperatures correspond either to a densely packed aggregate of solid, cohesionless, gravel-size particles or to porous, partially consolidated aggregates or rocks (at  $p \gg 50\%$ ).

If we postulate a porosity of 70 to 80 percent for the uppermost few centimeters of the lunar surface on the basis of the lunar photometric data (Ref. 6), then it is reasonable to associate midnight temperatures of thermally enhanced areas with underdense, partially consolidated materials.

#### CORRELATION OF LUNAR MIDNIGHT TEMPERATURE AND BEARING STRENGTH (Fig. 53)

Porosity and particle size are parameters common to both Figs. 51 and 52. The ordinates of these figures, lunar midnight temperature  $T_m$  and bearing strength  $f$  are cross plotted in Fig. 53 by using the common parameters as links. The correlation between  $T_m$  and  $f$  appears quite good particularly at "anomalous," very low and very high temperatures. Except for some ambiguities discussed below, there is a definite trend of increasing midnight temperatures with increasing bearing strength. Low midnight temperatures ( $T_m < 100^\circ\text{K}$ ) correlate with fluff ( $f \ll 1$  psi); high midnight temperatures ( $T_m > 130^\circ\text{K}$ ) correlate with porous rocks ( $f \gg 70$  psi). The terms high, low, or intermediate are relative to the range of temperatures shown in Fig. 53.

The intermediate temperatures (between 100 and  $130^\circ\text{K}$ ) are of special interest because most available data on lunar nighttime temperatures fall into this range. Unfortunately these temperatures, unlike those that are higher or lower, are difficult to correlate with bearing strength because they correspond to a region of transition between particulate and vesicular materials. Figure 53 shows that all three materials, fluff, soils, and porous rock, occupy this region in varying degrees. It does not appear possible to predict whether intermediate temperatures are indicative of consolidated, unconsolidated, or partially consolidated materials. All that is possible to infer from these temperatures is that the bearing strength of the material could be anywhere between 1 and 70 psi, depending mostly upon its grain size and porosity. This range of bearing strength is not very wide but it is critical because it encompasses minimum allowable bearing strength values that would be specified for most lunar surface operations.

Knowledge of the grain size, porosity, or degrees of consolidation of the lunar surface appears to be needed most at intermediate temperatures in order to complete the correlation. We will discuss these effects successively, and then illustrate the application of this knowledge in interpreting Surveyor 1 data.

#### Grain or Pore Size Effects in Correlating $T_m$ and $f$

A brief reference to the previous phases of this study would explain why grain size interferes with the correlation at lunar midnight temperatures below 130°K. We established in Phase I that the bearing strength of soils is nearly independent of grain size, but their thermal conductivity (hence  $T_m$ ) is not. We further established that the grain size dependence of thermal conductivity is due entirely to the radiative component, which is temperature dependent. Consequently, 1 mm soil particles would exhibit a higher temperature during a cooling phase than 10 $\mu$  particles. Figure 53 shows that this effect is less pronounced in fluffs (1 to 100 $\mu$ ) because the relative contribution of radiative heat transfer lessens with particle size and temperature.

The correlation of high midnight temperatures with porous rocks is not obscured by grain or pore size effects (despite the high temperatures) largely because radiative conduction is negligible; solid conduction, the predominant component in this case, is approximately independent of pore size and temperature (see Phase IA).

#### Effects of Porosity and Degree of Consolidation in Correlating $T_m$ and $f$

Another reason why the correlation at high lunar midnight temperatures is the least ambiguous is because it appears to be independent of both porosity and degree of consolidation. None of these key factors appears in Fig. 53. It is obvious why porosity is eliminated when plotting this curve, but it is not immediately clear why the "region of consolidation," represented by the shaded area in Figs. 51 and 52, is "compressed" into the solid curve in Fig. 53. The reason is largely because the porosity and degree of consolidation are mutually compensating properties as far as their effect on thermal conductivity and bearing strength is concerned. This point warrants further clarification.

In Figs. 51 and 52, imagine a horizontal line intersecting the solid, porous rock curve at a porosity of about 85 percent. This porosity corresponds to a bearing strength of about 140 psi

and a  $T_m$  of 148°K. Remember that this porosity is only an upper limit; a limit where the solid phase is fully continuous. Conceivably, there could be a large number of partially consolidated areas on the moon that could exhibit the same midnight temperature provided their porosity is less than 85 percent. Theoretically all these areas should have the same bearing strength if their departure from the limiting 85 percent porosity is compensated by a proportional increase in the number of microcracks or poorly welded junctions in the solid phase. Actually, as we move toward the left along a horizontal line in Figs. 51 and 52, the drop in porosity is more apparent than real. All specimens of porous rock that fall on this line have effectively the same porosity as the limiting case (85 percent); i.e., the amount of solid material per unit area that is effective thermally and mechanically stays constant. What actually increases at lower porosities is the amount of unconsolidated material, which merely occupies space and remains ineffective in transferring heat or stress. These concepts are illustrated in Fig. 54 which shows schematic cross sections of porous rocks at various stages of consolidation and porosity. All these specimens have the same bearing strength  $f$  and thermal conductivity  $k$  or  $T_m$ . We show how their "effective porosity," "apparent porosity," and degree of consolidation should vary in order to satisfy the condition of constant  $f$  and constant  $T_m$ . By our definition, "effective" and "apparent" porosity are the same only when the solid phase is fully continuous or 100 percent consolidated. According to this definition, the abscissa in Figs. 51 and 52 would be "apparent porosity," and the solid, "porous rock" curves would be the locus of effective porosities.

Most natural rocks on earth, and very likely on the moon, are not fully consolidated, as they are rarely free of genetic or environment induced flaws. It is neither possible nor does it appear necessary to determine the number and location of these flaws, or the extent to which they reduce thermal conductivity and bearing strength. The real index for both of these properties is neither "apparent porosity" nor degree of consolidation, but "effective porosity," which, in theory at least, is defined by the solid curves in Figs. 51, 52, and 53 (assuming that radiative heat transfer is negligible). It is not surprising, therefore, that both "apparent porosity" and "degree of consolidation" have eliminated themselves out of the correlation in plotting Fig. 53. The solid line in this figure is theoretically valid not only for the "limiting case" of full consolidation, but also for the more common cases of partial consolidation.

It follows from the above discussion that with no prior knowledge of porosity, pore size, or degree of consolidation, lunar "hot spots" which exhibit midnight temperatures above 130°K could be directly correlated with bearing strength. However, this conclusion must remain tentative until substantiated by experiments. Measurements of thermal conductivity (in vacuo) and bearing strength should be made on natural porous rocks or sintered ceramics at various stages of consolidation. Thermal conductivity values could be converted to equivalent lunar midnight temperatures according to the analysis in Phase II. A direct plot of  $T_m$  versus  $f$  values thus obtained should show to what extent their correlation is independent of porosity and degree of consolidation. The theoretical curve in Fig. 53 seems to be intuitively reasonable. In actuality, this curve is more likely to be a "band" whose boundaries may best be determined by experiments.

\*\*\*\*\*

A flow chart of the key equations and figures leading to the final correlation is shown in Fig. 55.

#### THERMAL AND MECHANICAL PROPERTIES OF SURVEYOR 1 LANDING SITE

It is of interest to examine briefly whether the measured or estimated thermal and mechanical properties of the Surveyor 1 landing site, as reported in Ref. 108, are reasonable and mutually consistent.

In Fig. 53, we show a cross hatched vertical column at 5 to 10 psi, the measured dynamic bearing strength of the Surveyor site. We will assume for the purpose of this study that this is also the static bearing strength. Since no on-site or earth-based measurement of the nighttime temperature of this particular area exists, we have no way of determining the ordinate of this data point in Fig. 53. However, an estimated  $\gamma$  value of 800, based on eclipse measurements, is given in Ref. 108. This value of  $\gamma$  intersects the cross hatched column in Fig. 53 at a point slightly below the correlation curve. Actually, the fit of this data is likely to be even better than shown in Fig. 53, because the  $\gamma$  of 800 is based on eclipse isotherms, whereas the correlation curve

is based on lunation temperatures. It is well known that  $\gamma$  values are generally lower for lunation cooling than for eclipse cooling. Therefore, the reported bearing strength and thermal properties of the Surveyor site are reasonable and consistent.

Concerning the mechanical properties, the following preliminary estimate on the soil parameters of the Surveyor site is given in Ref. 108: cohesion is between 0.02 to 0.05 psi; the friction angle is between  $30^\circ$  and  $40^\circ$ , and the bulk density is  $1.5 \text{ g/cm}^3$ .

According to Fig. 51, these values (for terrestrial soils) are nearly consistent with the measured bearing strength of 5 to 10 psi on the moon, if we neglect differences in earth and moon gravity fields (a questionable assumption for a soil having a friction angle of  $30^\circ$  to  $40^\circ$  and a bulk density of  $1.5 \text{ g/cm}^3$ , see Fig. 25). A close examination reveals that the suggested value of bulk density is not consistent with a 5 to 10 psi soil on earth, and does not account for the predominantly compressive mode of soil failure evidenced by published photographs. In addition, the suggested value of cohesion appears to be too weak to account for the apparent absence of loose dust as suggested by the results of a jet impingement test and the cleanliness of spacecraft radiative surfaces as inferred from the temperature of these surfaces. These inconsistencies are discussed in greater detail in Ref. 109, where it is concluded that a bulk density of about  $1 \text{ g/cm}^3$  accounts better for the observations and measurements. The proposed revision suggests an underdense, partially consolidated material approximated on earth by snow or semiwelded tuffs. The cohesion appears to be of the order of a few psi rather than a fraction of a psi. The friction angle is probably negligible. These estimates could be verified or improved by additional analysis of the Surveyor data (Ref. 109). The principles of conventional soil mechanics do not readily apply to the study of the revised, "underdense" material because such materials undergo a different mode of failure. Their thermal and mechanical properties are largely unexplored. Some of the experiments which could improve our knowledge in these areas are discussed in the next phase of this report.

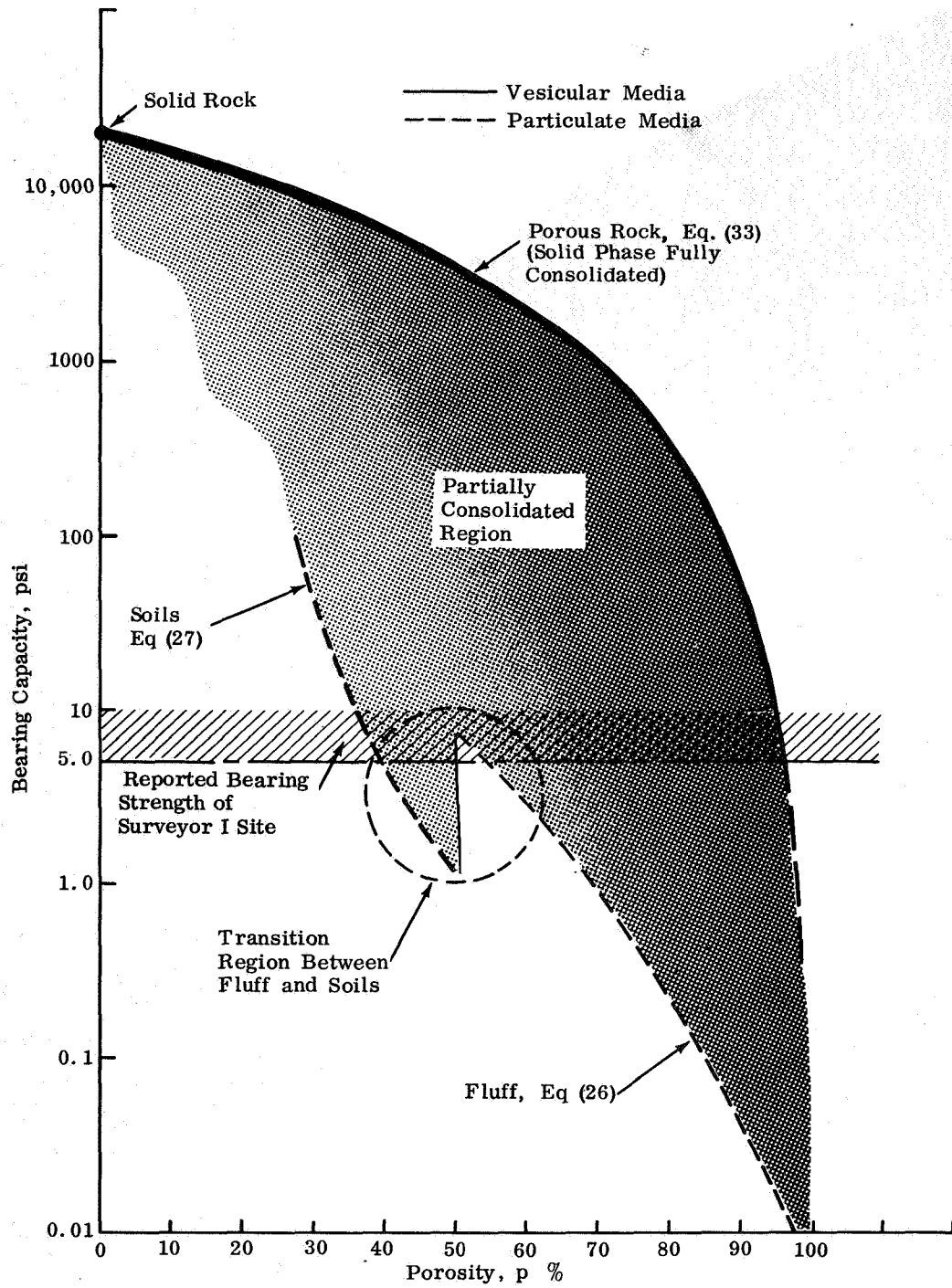


Fig. 51 Summary, Strength-Porosity Relationship of Porous Media

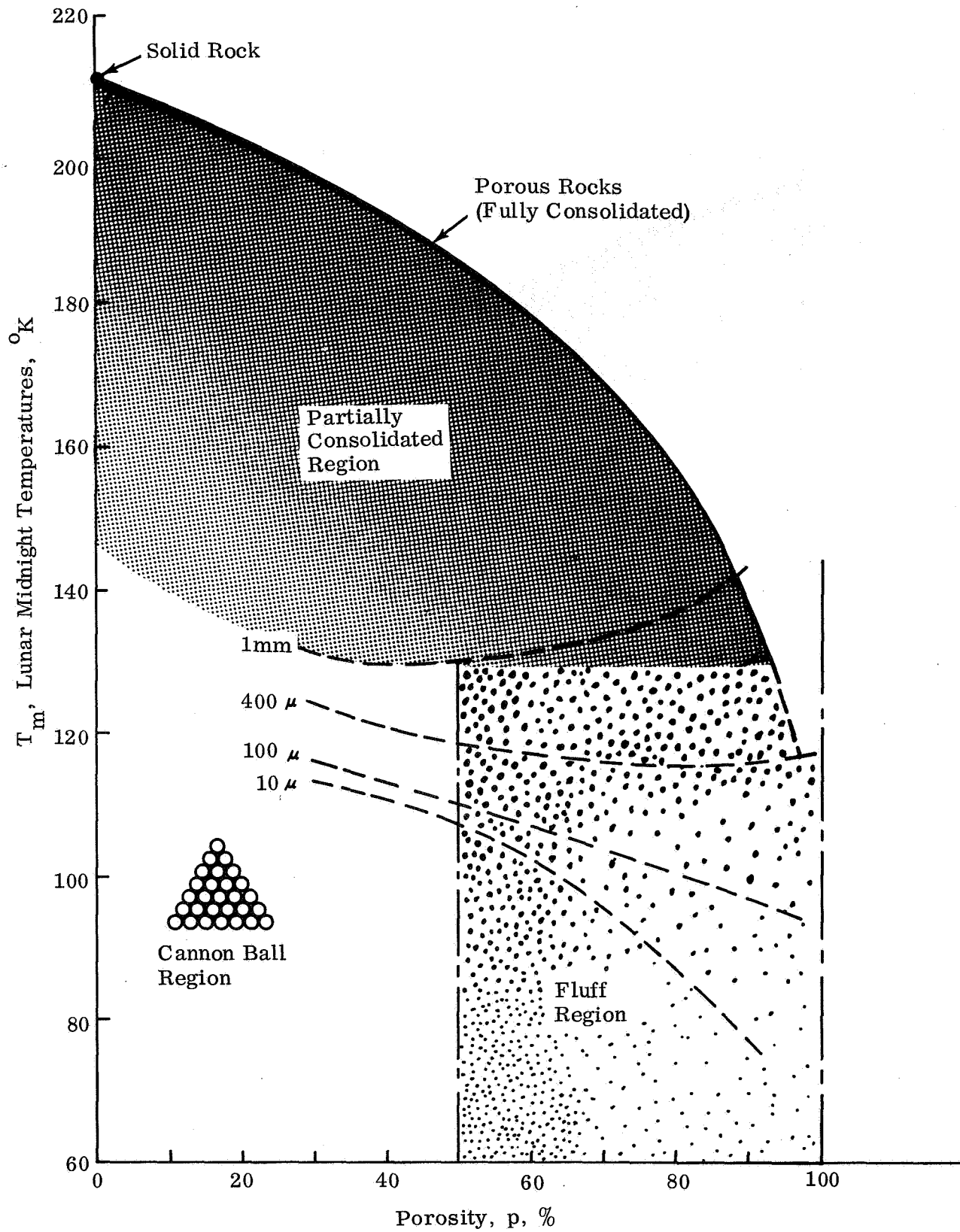


Fig. 52 Summary, Lunar Midnight Temperatures versus Porosity



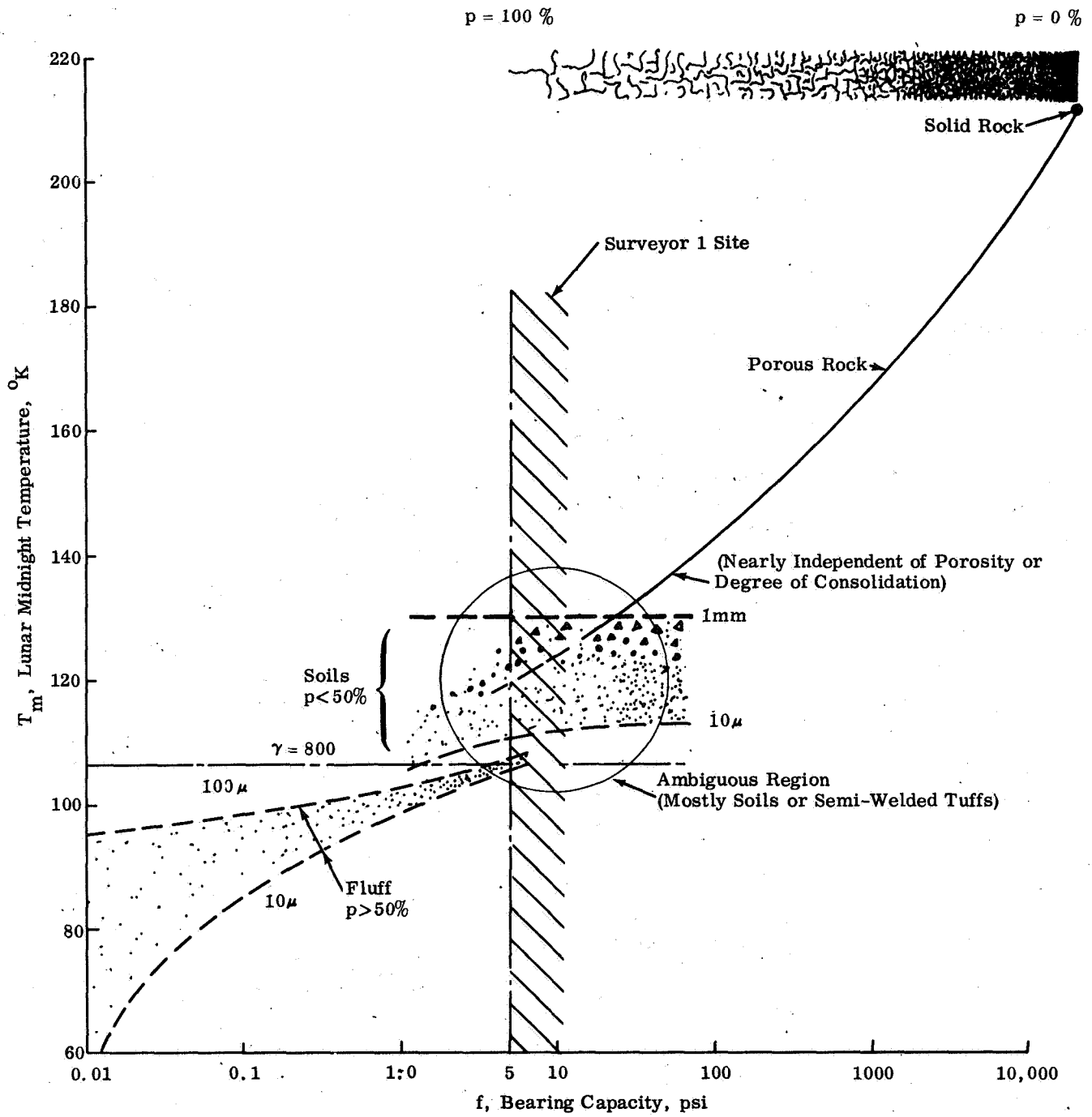
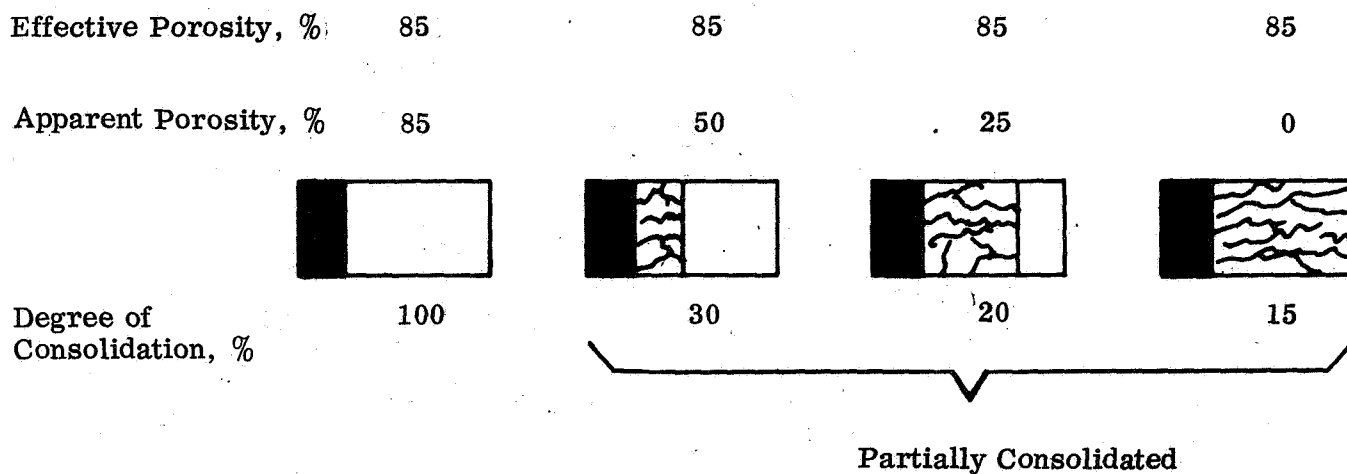


Fig. 53 Correlation of Lunar Midnight Temperature and Bearing Strength



Legend



Solid, Fully Continuous, Thermally and Mechanically Effective

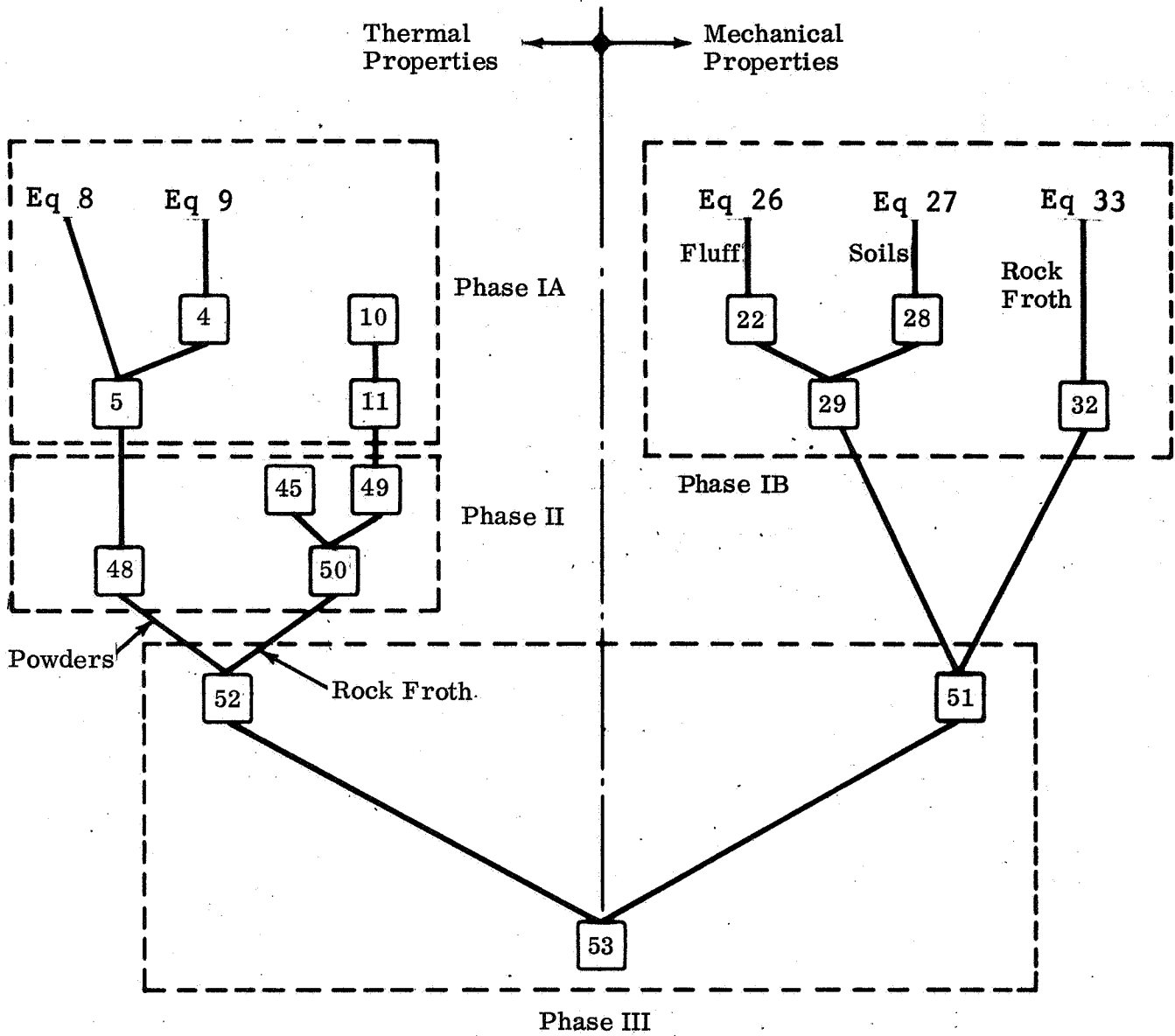


Solid, Fully Discontinuous Due to Microcracks, Thermally and Mechanically Ineffective



Void

Fig. 54 Schematic Cross Sections of Porous Rocks at  $T_m = 148^\circ\text{K}$  and  $f = 140$  psi (Ref. Figs. 51 and 52)



Note: Figure Numbers are Shown in Boxes

Fig. 55 Flow Chart of Key Equations and Figures Leading to the Correlation

## PHASE IV: RECOMMENDED PROGRAMS IN LUNAR THERMOPHYSICS

This phase discusses various areas of further investigation in lunar thermophysics including theoretical analyses, laboratory experiments, and direct lunar observations. Their major purpose is to substantiate and/or complement the results and conclusions of this study.

### THEORETICAL ANALYSES

There is little justification for pursuing analytical studies of thermal and mechanical properties of powders and porous rocks beyond the point reached in Phase I without substantiating our theoretical expressions with test data. In view of the scarcity of available test data, the most important recommendation that can be made for future work pertaining to Phase IA or IB is to implement an experimental program for measuring the thermal conductivity and bearing strength of powders and porous rocks under conditions suggested by theory. This program is discussed below in the Laboratory Experiments Section.

There are, however, a number of useful theoretical topics related to Phase II, that fall outside the scope of this report. We recall that this report has concerned itself only with the correlation of the thermal and mechanical properties of an idealized, smooth, homogeneous model of the lunar surface. Effects of internal heat sources, surface roughness, vertical layering, and horizontal inhomogeneities on the nighttime temperatures were not considered, but deserve to be studied. (Only a limited number of the vertically layered models are analyzed in this report.) These effects may complicate, but not necessarily obscure the correlation. An additional refinement that could be introduced into the computer program is a simultaneous dependence of thermal conductivity on both temperature and depth.

Obviously, lunar data at infrared wavelengths do not lead to a model of the lunar surface or of layers beneath the surface that is unique in terms of porosity, grain size, and degree of consolidation, particularly at "intermediate" midnight temperatures. It is conceivable, however, that thermal emission from beneath the surface at microwave frequencies could complement the infrared data and lead to a less ambiguous model. A new set of relationships could be developed in terms of the electrical, thermal, and mechanical properties of the material. As similar laboratory data on lunar

analog become available, these relationships could help narrow the wide range of physical parameters, which complicate the correlation of thermal and mechanical properties at infrared wavelengths.

To summarize, future areas of theoretical investigations that look the most promising in the light of this study are as follows:

- Analytical refinements of present lunar model based on infrared data. These refinements include the study of lunation temperatures for a model of the lunar surface in which a) thermal conductivity is both temperature and depth dependent, and b) vertical or horizontal inhomogeneities exist.
- Analysis of surface roughness effects on thermal enhancement as a function of scale of roughness and time of cooling (i.e., eclipse or lunation).
- Analysis of thermal emission of the moon at microwave frequencies in conjunction with analysis in this report based on infrared data.

## LABORATORY EXPERIMENTS

Experiments that appear desirable may be divided into two groups. Experiments in the first group are designed to improve the analytical correlation which is based on a homogeneous model. In the second group, experiments are designed to study effects of inhomogeneities and surface roughness. The inhomogeneities include vertical layering and horizontal discontinuities such as islands of rock froth surrounded by less conductive materials. These effects have not been considered in this report. They could be studied analytically and/or experimentally. Some of these experiments are discussed in this phase; a survey and evaluation of various techniques and systems for the measurement of thermal properties are presented in a supplementary report (Ref. 111).

### Group I Experiments (To Improve the Analytical Correlation)

Experiments in this area are designed either to verify the key assumptions on which the thermal and mechanical analyses are based or to complement the analytical results with experimental data in certain areas that defy analysis.

The correlation studies presented in this report are based on available information on the strength and thermal conductivity of terrestrial materials, and estimates regarding the effect of the lunar environment on the strength of these materials. These studies have also revealed that there are certain areas where, on the basis of present knowledge, empirical or theoretical relationships can only be established with a limited degree of confidence, but with additional experimental data, the confidence limits could be improved.

#### Particulate (Unconsolidated) Materials

The purpose of testing these materials is to verify the temperature, porosity, and grain size dependence of thermal conductivity, as suggested by our mathematical model in Phase IA. Grain size and temperature dependence, in particular, seem to be a major source of ambiguity in correlating lunar midnight temperatures below 130°K. The thermal conductivity of various silicate powders should be measured as a function of temperature, grain size, and porosity. Available thermal and mechanical data are not sufficient to indicate that the mathematical model (consisting of monosize spherical particles) is a true representation of a natural sample. In both thermal and mechanical experiments, effects of nonuniformity in particle shape and size distribution should be studied to confirm the approximate validity of the analytical correlations and establish adjustment factors, if necessary. Certainly more bearing strength data on fluffs would be useful, particularly with regard to the effect of ultrahigh vacuum on interparticle bond. It must be recognized, however, that these experiments, like the thermal measurements, are delicate and laborious.

#### Vesicular Materials

The purpose of testing these materials is to verify the thermal and mechanical models used in Phase I. The thermal conductivity of consolidated materials, unlike that of powders, is almost independent of temperature and pore size. Thermal conductivity of various silicate rocks or ceramics should be measured as a function of, at least, temperature, pore size, porosity, and degree of consolidation. The physical parameters may be better controlled when using manufactured specimens. Available thermal data are not sufficient to indicate that the mathematical models, discussed in Phase I, are true representations of natural or manufactured specimens.

Remember that the porosity-strength relationship established for the vesicular model, in Phase IB, was based mostly on experimental results obtained with manufactured materials. It is recommended that this relationship be verified, and that experimental

constants are established for highly porous natural rocks, such as pumice, scoria, and cinders.

Another purpose of testing these materials is to verify the final analytical results which indicate that the correlation between thermal conductivity (or lunar midnight temperature) and bearing strength is nearly independent of porosity and degree of consolidation (see Phase III).

#### Transition Region Between Particulate and Vesicular Materials

We single out the transition region between soils and porous rocks because it corresponds to lunar nighttime temperature and bearing strength values typical for most of the observed lunar surface. Surveyor 1 appears to have landed on such an area (see Phase III). Certainly more thermophysical data are needed for materials that occupy this region. These include densely packed soil, very porous rocks ( $p > 75\%$ ), preferably of a low degree of consolidation, and "hybrid" materials discussed in the next section.

#### "Hybrid" Materials

There is another likely lunar surface model that should be introduced at this point for possible future study. This model would consist of large, centimeter-size, microporous particles. It may be termed a "hybrid" model since, strictly speaking, it is neither particulate nor vesicular, but a cross between the two. It would have a higher porosity than its particulate or vesicular counterparts because its porosity would be the sum of the voids within, as well as between, the particles. Mechanically, the hybrid model could behave like the cannonball model, and hence, may be as strong, if not stronger (because of mechanical interlocking), despite the fact that its porosity may approach that of fluff. The individual microporous particles would conduct heat as the vesicular model, but the over-all particle system could have a lower conductivity than its particulate or vesicular counterparts because of its inherent high porosity, and the consequent reduction of the solid component of thermal conductivity.

This model was not originally considered. However, in the light of our studies, it appears to be sufficiently unique (thermally and mechanically) and realistic in lunar terms to deserve further attention. Coarse volcanic cinders, shown in Fig. 56a and b, are the closest natural representation of this model. Experiments at Grumman show that these materials reproduce the photometric and polarimetric properties of the moon better than most

natural specimens that have come to our attention (Refs. 6 and 7). Close-up photographs of the moon taken by Luna 9 and Surveyor 1 suggest a material similar in texture to coarse volcanic cinders or a bed of porous vesicular material littered with broken porous rocks. The thermal properties of such a "hybrid" material remain largely unknown and should be investigated. Similarly, there is practically no experimental information on the mechanical properties. The strength of a hybrid model may be different from that of the particulate model, inasmuch as the individual grains may be subject to crushing at the points of contact. Manufactured or natural lightweight aggregates of various types would be easily available and serve as a good representation of the hybrid model. A testing program would include both studies of the mode of failure, (which is expected to differ from the densely packed version of the particulate model), and the strength characteristics as a function of particle size and total porosity.

#### Group II Experiments (To Study Roughness, Directionality, and Heterogeneity Effects on Remote Sensing of Thermal Emission)

The correlation discussed in Phase III and the experiments discussed in Group I of this phase are limited to relatively smooth and homogeneous models. Roughness and directional effects could cause thermal enhancement during a cooling phase, and complicate the correlation depending upon the scale of roughness and the lengths of the cooling phase.

An important laboratory effort, which has not been fully appreciated, is the simulation of eclipse and lunation cooling. There are several reasons why the thermal relationship of the sun-moon-earth system should be simulated. These reasons are related to roughness and the directional and inhomogeneity effects as explained below.

Lunar infrared emission data, collected during an insolation, could be a valuable source of information on the roughness of the lunar surface. Such data may be used to verify or complement the roughness inferred from photometric, polarimetric, radar, and other sources. These data are essentially the infrared thermal counterpart of the lunar photometric data at optical wavelengths. Their simulation and analysis would be a logical extension of our photometric and polarimetric work at Grumman (Refs. 6 and 7).

To analyze the lunar thermal data rigorously, both the hemispherical emissivity and directional emissivity must be known as a function of the viewing angle of the area considered. The hemispherical emissivity is required for the analytical model that



describes the thermal behavior (see Phase II). The directional emissivity is needed to translate the radiance measurements to equivalent surface temperatures. We know of no measurement of directional emissivity of simulated lunar surfaces. If the lunar surface were a smooth dielectric, emissivity would be a pronounced function of angle of observation, and would fall to very low values at high obliquity in accordance with Fresnel's equations. Any theoretical pattern such as this would be modified heavily by surface roughness. Recently published data, based on the observations of Shorthill and Saari, indicate pronounced directionality of emission with respect to the observer (Ref. 110). Temperature measurements aboard the Surveyor 1 spacecraft on the moon indicate similar effects (data not yet published, private communication with Dr. Jaffe of JPL). It therefore appears desirable to obtain directional emissivity data experimentally from lunar analogs. Finally, simulation of eclipse or lunation cooling is more expedient than analysis for determining the effect of complex "inhomogeneities" (vertical or horizontal) on temperature changes. By means of such a simulation, one could directly estimate the thermal inertia constant  $(k\rho c)^{-\frac{1}{2}}$  rather than measure  $k$ ,  $\rho$ , and  $c$  in separate experiments, as has been the practice to date.

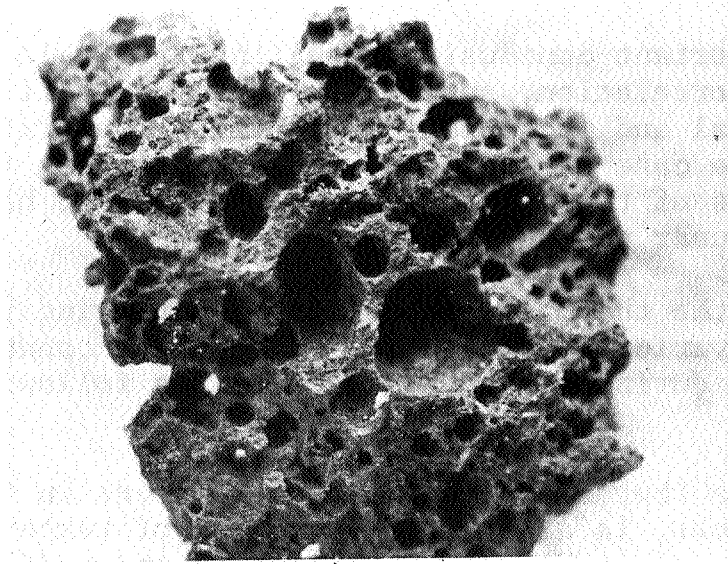
#### EARTH-BASED OBSERVATIONS

Our current analysis indicates that the nighttime portion of the lunation temperature curve is a sensitive index of the thermal conductivity, and hence, the bearing strength of the cooling material. Current data on lunar nighttime temperatures are neither extensive nor precise. Consequently, of immediate need is "mapping" of lunar nighttime emission at infrared wavelengths, preferably at a 20-micron window. In addition, it would be very desirable to measure the thermal emission of the same areas during an eclipse and at high noon for both infrared and radio wavelengths in order to narrow the number of possible interpretations of the data. Eclipse temperatures resulting from a shorter cooling transient give a better indication of roughness effects on thermal enhancement. Similarly, high noon or subsolar temperatures could reveal whether internal heat sources contribute to thermal enhancement observed at night. For instance, if a given area of the moon exhibits an anomalously high temperature during an eclipse but not during the night, it is reasonable to attribute the thermal enhancement to roughness effects. On the other hand if an area is thermally enhanced at night but not at high noon, then it is reasonable to rule out internal heat sources as contributing factors and associate the "hot spot" with a thermally more conductive, hence, mechanically stronger material. As to measurements of radio-emission

at longer millimeter waves, they are necessary to determine the inhomogeneity of the layers with depth. It is also advisable to use wavelengths in the decimeter range. However, because of degradation of resolving power, such measurements can be made from satellites placed around the moon.

Recent, preliminary, ground-based measurements by F. Low of the University of Arizona, at 18 arc seconds resolution, have revealed pre-dawn, cold limb temperatures ranging from 70°K to 150°K with a typical value of 90°K (Ref. 99). According to our analyses, these temperatures correspond to five orders of magnitude of bearing strength ranging from 0.01 psi to 1000 psi. At this state of our knowledge of the moon it appears hazardous to select a lunar landing site that has a nighttime temperature below 100°K.

More extensive and precise ground-based observations of the dark moon should begin as soon as possible, preferably at relatively low resolution, at first, followed by observations at higher resolution of those areas that merit further investigation. Resolutions of 10 arc seconds are possible with 5-foot telescopes. These measurements are by no means easy to make in view of the very low temperatures involved. However, it is hoped that this study has provided sufficient theoretical justification for initiating such an observational program. Remote sensing of the moon could complement, in many respects, the mission of unmanned probes. It provides the opportunity for repetitive and synoptic coverage of large areas not readily accessible by other means. The correlation of ground-based measurements with on-site Surveyor type data opens up the possibility of increasing the usefulness of these probes by converting their landing sites to "calibrated bench marks." This concept is discussed in greater detail in Ref. 109 in connection with the evaluation of Surveyor 1 data.



Single Particle (Magnif. 25x)



Fig. 56 Hawaiian Volcanic Cinders  
("Hybrid" Model)

## CONCLUSIONS

The most important conclusion resulting from this study is that there is a correlation, subject to certain qualifications, between the thermal and mechanical properties of extraterrestrial materials. In the case of the moon, this correlation is best expressed in terms of the nighttime temperatures and bearing strength of the lunar surface.

Analyses of the thermal conductivity and bearing strength of porous media and various case studies of the heat conduction of the lunar surface during a lunation lead to the following results and conclusions:

The effective thermal conductivity of powders in vacuo, unlike that of porous rocks, is a sensitive function of temperature and grain size due largely to the predominance of the radiative component of heat transfer. This finding, which remains to be verified by experiments, has necessitated separate, temperature-dependent and temperature-independent solutions of the lunation thermal cycle. The solutions indicate that thermal inertia constant  $\gamma$ , as such, does not characterize uniquely the temperature variations of the lunar surface in the temperature-dependent case but the nighttime temperatures do. It is found that the midnight temperature  $T_m$ , can be used in all cases as a convenient index of mechanical properties.

Mechanical analyses, corroborated by available test data, indicate that silicate minerals, ranging from tenuous fluff to solid rock, encompass a bearing strength of about 6 orders of magnitude ( $10^{-2}$  to  $10^4$  psi). This spectrum of bearing strength correlates, theoretically, with a lunar midnight temperature variation of about  $150^\circ\text{K}$  ranging from  $60^\circ\text{K}$  to  $210^\circ\text{K}$ . With the exception of some local ambiguities, there is a definite trend of increasing bearing strength with increasing nighttime temperature. Low  $T_m$  values correlate with soft, loose powders; high  $T_m$  values correlate with hard, porous rocks.

The correlation is ambiguous at intermediate lunar midnight temperatures ( $100^\circ\text{K} < T_m < 130^\circ\text{K}$ ). These temperatures correspond to a "transition region" where the bearing strength of consolidated and unconsolidated media overlap. The porosity and degree of consolidation of lunar areas that exhibit these temperatures are theoretically difficult to predict. These areas could be covered either with densely packed, cohesionless soils or highly porous consolidated

conglomerates. If the material is soils, the correlation is further complicated by the fact that its bearing strength could be anywhere between 1 and 70 psi depending mostly on its particle size and porosity. The main reason for this ambiguity is attributed to the fact that the bearing strength of soils is very sensitive to changes of porosity but relatively insensitive to changes of particle size, whereas the thermal conductivity of soils appears to be more sensitive to changes of particle size than of porosity, when the radiative component predominates. Laboratory measurements of thermal conductivity and bearing strength as a function of particle size and porosity and analysis of lunar thermal emission at longer, millimeter wavelengths could possibly reduce the ambiguity.

Particle size effects complicate but do not obscure the correlation at midnight temperatures below  $100^{\circ}\text{K}$ . Such temperatures are exhibited only by very porous, unconsolidated materials like loose dust. At this state of our knowledge it would be prudent to locate these areas on the moon and avoid them.

The ambiguity due to particle size (resulting from radiative effects) is most pronounced at intermediate midnight temperatures which, unfortunately, are the ones most frequently observed on the lunar surface. The bearing strength of the Surveyor 1 landing site correlates with these temperatures which may be considered as the average for the lunar surface.

The correlation is least ambiguous at anomalous, midnight temperatures above  $130^{\circ}\text{K}$ . These temperatures indicate a relatively hard and dust-free surface. It seems advisable at this time to limit the choice of potential lunar landing sites to those areas that exhibit midnight temperatures above  $130^{\circ}\text{K}$ . It is clear that surface roughness effects and internal heat sources, not considered in this study, could interfere with the correlation. If these effects do exist, it seems theoretically possible to disentangle their contribution to the nighttime thermal emission by additional lunar observation during an eclipse and at normal solar incidence.

Recently observed (Ref. 99) high resolution lunar nighttime temperature data, ranging from 70 to  $150^{\circ}\text{K}$  suggest that the surface of the moon is not as homogeneous on a Km-scale as it appears to be at much larger scale, and that localized areas widely differing in hardness from the consistency of fluff to that of porous rock appear to exist on the moon and are amenable to earth-based detection and analysis.

High resolution, synoptic data on lunar nighttime temperatures could complement on-site lunar probe data in selecting safe lunar landing sites and pave the way to a more effective, long range exploration of the moon. However, much remains to be learned about the engineering and geologic implication of lunar thermal anomalies.

## RECOMMENDATIONS

An equally important conclusion reached in this study is the specific type of thermal data on the moon and on laboratory specimens that are urgently needed. Among the most important of these are the following:

- Theoretical Analyses: 1) Effects of surface roughness (i.e., directional effects) and internal heat sources on thermal enhancement at infrared wavelengths. 2) Extensions of analyses in this report to microwave frequencies.
- Laboratory Experiments: Measurements of thermal conductivity and bearing strength of porous media (i.e., fluff, soils, natural or manufactured porous-solids, "hybrid" materials, etc.) in the light of theoretical analyses made in this report and past experience. (See Phase I and Appendices A and B). Thermal conductivity measurements in vacuo, to be useful, should be made as a function of porosity, grain size, and temperature.
- Lunar Observations: "Mapping" of nighttime infrared thermal emission of the moon preferably through a 20 micron window.

These and other areas are discussed in greater detail in Phase IV of this report.

## REFERENCES

1. Halajian, J. D., and Reichman, T., Correlation of Mechanical and Thermal Properties of Extraterrestrial Materials, First Progress Report, Contract NAS 8-20084, Grumman Research Department, September 1965.
2. Halajian, J. D., and Reichman, T., Correlation of Mechanical and Thermal Properties of Extraterrestrial Materials, Second Progress Report, Contract NAS 8-20084, Grumman Research Department Memorandum RM-309, February 1966.
3. Halajian, J. D., and Reichman, T., Correlation of Mechanical and Thermal Properties of Extraterrestrial Materials, Third Progress Report, Contract NAS 8-20084, Grumman Research Department Memorandum RM-331, June 1966.
4. Jaeger, T. C., "The Surface Temperatures of the Moon," Austr. J. Phys., Vol. 6, 1953, p. 10.
5. Krotikov, V. D., and Shchuko, O. B., "Heat Balance of the Lunar Surface During a Lunation," Soviet Astronomy, Vol. 7, 1963, p. 228.
6. Halajian, J. D., Photometric Measurements of Simulated Lunar Surface, Final Report, Contract NAS 9-3182, Grumman Research Department Reports RE-219, July 1965 and RE-245, April 1966.
7. Egan, W. G., Smith, L. L., and McCoyd, G. E., Polarimetric Measurements of Simulated Lunar Surfaces, Final Report, Contract NAS 9-4942, Grumman Research Department Report RE-250, May 1966.
8. Krotikov, V. D., and Troitskii, V. S., "Radio Emission and Nature of the Moon," Soviet Physics, Vol. 6, 1963, p. 841.
9. Godbee, H. W., and Ziegler, W. T., "Thermal Conductivities of  $MgO$ ,  $Al_2O_3$ , and  $ZrO_2$  Powders to  $850^\circ C$ . II. Theoretical," J. of Applied Phys., Vol. 37, 1966, p. 56.
10. Everett, A., Glaser, P. E., and Wechsler, A. E., Thermal Conductivity of Powders, Summary Report on Contract No. NAS 8-1587, 27 March 1961-27 April 1962.



11. Gorrington, R. L., and Churchill, S. W., "Thermal Conductivity of Heterogeneous Materials," Chem. Eng. Progress, Vol. 57, No. 7, July 1961, p. 53.
12. Riemann, G. M. H. W., Die Partiellen Differential Gleichungen der Mathematischen Physik, Band 1, 1914, p. 474.
13. Fenech, H., and Rohsenow, W. M., "Prediction of Thermal Conductance of Metallic Surfaces in Contact," ASME J. of Heat Transfer, Vol. 85, February 1963, p. 15.
14. Clausing, A. M., and Chao, B. T., "Thermal Contact Resistance in a Vacuum Environment," Paper No. 64-HT-16 presented at AIChE-ASME Heat Transfer Conference, Cleveland, Ohio, August 9-12, 1964.
15. Kragelsky, V., and Demkin, N. B., "Contact Area of Rough Surfaces," Wear, Vol. 3, 1960, p. 170.
16. Dallavalle, J. M., Micromeritics - The Technology of Fine Powders, 2nd Ed., Pitman Publishing Corporation, 1948.
17. Jones, F. L., The Physics of Electrical Contacts, Oxford At The Clarendon Press, 1957.
18. Love, T. J., An Investigation of Radiant Heat Transfer in Absorbing, Emitting, and Scattering Media, ARL 63-3, Wright-Patterson Air Force Base, Ohio, 1963.
19. Wesselinck, A. J., "Heat Conductivity and the Nature of the Lunar Surface," Material Bull., Astronomical Institute of Netherlands, Vol. 10, 1948, p. 351.
20. Laubitz, M. J., "Thermal Conductivity of Powders," Can. J. Phys., Vol. 37, 1959, p. 798.
21. Schotte, W., "Thermal Conductivity of Packed Beds," A.I.Ch.E. Jour., Vol. 6, 1960, p. 63.
22. Clark, S., "Absorption Spectra of Some Silicates in the Visible and Near Infrared," American Mineralogist, Vol. 142, 1957, p. 732.
23. Gehrels, T., "A Model of the Lunar Surface," Icarus, Vol. 3, 1964, p. 491.

24. Hamaker, H. C., Radiation and Heat Conduction in Light Scattering Material, Philips Research Report, Vol. 2, 1947, p. 55.
25. Woodside, W., and Messmer, J. H., "Thermal Conductivity of Powders Media II: Consolidated Rocks," J. of Applied Phys., Vol. 32, No. 9, September 1961, p. 1705.
26. Bernett, E. C., Wood, H. L., Jaffe, L. D., and Martens, H. E., Thermal Properties of a Simulated Lunar Material in Air and in Vacuum, Jet Propulsion Laboratory Technical Report No. 32-368, November 25, 1962.
27. Glaser, P. E., (ed.), Studies of the Physical Characteristics of Probable Lunar Surface Materials: Part II, Office of Aerospace Research Report, November 1964, p. 68.
28. Salisbury, J. W., and Glaser, P. E., Studies of the Physical Characteristics of Probable Lunar Surface Materials: Part I, Office of Aerospace Research Report, January 1964, pp. 116, 152, 154, 149, 158.
29. Wechsler, A. E., and Glaser, P. E., "Pressure Effect on Postulated Lunar Materials, Icarus, Vol. 4, 1965, pp. 342, 348, 349.
30. Ruh, E., "Improved Method of Measuring Thermal Conductivity of Dense Ceramics," J. of the Am. Ceramic Soc., Vol. 37, No. 5, May 1954, p. 326.
31. Loeb, A. L., "A Theory of Thermal Conductivity of Porous Materials," J. Am. Ceramic Soc., Vol. 37, 1954, p. 96.
32. Maxwell, J. C., Electricity and Magnetism, Dover Publishing Co., 3rd Ed., Vol. I, 1891, p. 440.
33. Runge, I., Z. Tech., Physik, Vol. 6, 1925, p. 61.
34. Russell, H. W., "Principles of Heat Flow in Porous Insulators," J. Am. Ceramic Soc., Vol. 18, 1935, p. 1.
35. Tsao, G. T., "Thermal Conductivity of Two Phase Materials," Ind. & Eng. Chem., Vol. 53, 1961, p. 393.
36. Woodside, W., "Calculation of the Thermal Conductivity of Porous Media," Can. J. Physics, Vol. 36, 1958, p. 815.

37. Wechsler, A. E. et al., Thermal Conductivity of Non-Metallic Materials, Summary Report, Contract No. NAS 8-1567, 27 April 1963.
38. Woodside, W., and Messmer, J. H., "Thermal Conductivity of Porous Media I: Unconsolidated Sands," J. Ap. Phys., Vol. 32, 1961, p. 1688.
39. Francl, J., and Kingery, W. D., "Experiemntal Investigation of Effect of Porosity on Thermal Conductivity," J. Am. Ceramic Soc., Vol. 37, 1954, p. 99.
40. Li, C. H., "Random Packing of Sticky Spheres," Grumman Research Department, Private Communication, May 1966.
41. Deryaguin, B. V., J. of Phys. Chem., No. 6, 1935, p. 1306; Colloidal J., No. 69, 1934, p. 155, and No. 5, 1961.
42. Halajian, J. D., Soil Behavior in a Low and Ultrahigh Vacuum, Grumman Research Department Report RE-197J, ASME paper 64-WA/AV-14, December 1964.
43. Terzaghi, K., and Peck, R. B., Soil Mechanics in Engineering Practice, John Wiley and Sons, Inc., N. Y., 1948.
44. Hanks, R., and McCarty, J. L., Investigation of the Use of Penetrometers to Determine the Capability of Dust Materials to Support Bearing Loads, NASA Langley Research Center Report TN-D3200, January 1966.
45. Jaffe, L. D., "Bearing Strength of 'Fairy Castle' Structures," J. Aerophys. Res., Vol. 70, No. 24, December 1965.
46. Hubbard, J. H., Gall, E. S., and Keller, D. J., "The Development of a Lunar Soil Simulant," Dept. of the Army, Ohio River Division Laboratory Corps of Engineers, April 1966.
47. Hapke, B., "Packing Properties of Fine Powders and the Depth of the Lunar Dust Layer," J. Geophys. Res., Vol. 68, 1963, pp. 4545-4570.
48. Lowe, H. J., and Lucas, D. H., "Static Electrification," Brit. J. Appl. Phys. Suppl., No. 2, 1953, p. S40.
49. Bradley, R. S., Phil. Mag., Vol. 13, 1932, p. 853; Trans. Faraday Soc., Vol. 32, 1936, p. 1088.

50. Halajian, J. D., Gravity Effects on Soil Behavior, Grumman Report No. ADR04-04-63.1, May 1963.
51. Westbrook, J. H., "Temperature Dependence of Strength and Brittleness of Some Quartz Structures," J. Am. Cer. Soc., Vol. 41, No. II, November 1958.
52. Penn, S. H., Determination of the Coefficient of Friction Between Metals and Nonmetallic Solids at Ultrahigh Vacuum, Grumman Research Department Report RE-205, Final Report on Contract No. NAS 8-5415, March 1965.
53. Mohr, G., Determination of the Coefficient of Friction Between Metals and Nonmetals at Ultrahigh Vacuum, Grumman Research Department Progress Reports 0284-1 to 24, 1965-66.
54. Hill, L. R., Shear Strength of Randomly Packed Granular Media in Vacuum, Research Report, Department of Civil Engineering, Princeton University, N. J., 1965.
55. Horn, H. M., "An Investigation of the Frictional Characteristics of Minerals," Ph.D. Thesis, University of Illinois, 1961.
56. Halajian, J. D., The Case of a Cohesive Lunar Surface Model, Grumman Report ADR04-04-62.2; Annals of the New York Academy of Sciences, Vol. 123, Art. 2, July 1965, pp. 671-710.
57. Karafiath, L. L., Preliminary Analysis of the Mechanical Properties of Postulated Lunar Vericular Rocks, Grumman Research Department Memorandum RM-328, June 1966.
58. Obert, L., Durall, W. I., Merrill, R. H., "Design of Underground Openings in Competent Rock," Bulletin 587, U. S. Bureau of Mines.
59. "Pore Spectia of Rocks," Communication of Prado Laboratories, Cleveland, Ohio.
60. Duckworth, W., "Discussion of Ryshkewitch Paper," J. Am. Cer. Soc., Vol. 36, No. 2, February 1953.
61. Ryshkewitch, E., "Compression Strength of Porous Sintered Alumina and Zirronics," J. Am. Cer. Soc., Vol. 36, No. 2, February 1953.

62. Hasselman, D. P. H., "On the Porosity Dependence on the Elastic Moduli of Polycrystalline Refractory Materials," J. Am. Cer. Soc., Vol. 45, No. 9, 1962.
63. Knudsen, F. P., "Dependence of Mechanical Strength of Brittle Polycrystalline Specimens on Porosity and Grain Size," J. Am. Cer. Soc., Vol. 42, No. 8, 1950.
64. Bender, R. J., Handbook of Foamed Plastics, Lake Publishing Co., 1965.
65. Valore, R. C., "Cellular Concretes Processes," J. Am. Concr. Inst., Vol. 50, 1954.
66. Wood, L. C., "Physical Properties of Rocks," American Geological Institute, Data Sheet No. 24, Geotimes, Vol. 5, No. 7, 1961.
67. Mizuno, T., "On the Bearing Power of Soil Under a Uniformly Distributed Circular Load," Proceedings: 3rd Int. Conf. Soil Mech. and Found. Eng., Vol. 1, 1953.
68. Berezancev, V. G., "Axialsymmetric Problem of the Ultimate Load in Granular Materials," (in Russian) Gostechizdat, 1952.
69. Teizaghi, K., Theoretical Soil Mechanics, New York, Wiley, 1943.
70. de Beer, E. E., and Ladany, B., "Etude Experimentale de la Capacite Portante du Sable Sous des Fondations Circulaires Etablies en Surface," Proc. 5th Int. Conf. Soil Mech. and Found. Eng., Vol. 1, 1961.
71. Hvorslev, M. J., "The Basic Sinkage Equations and Bearing Capacity Theories," Unpublished report, U. S. Army Engineer Waterways Experiment Station, Wicksburg, Miss., 1963.
72. Meyerhof, G. G., "Some Recent Research on the Bearing Capacity of Foundations," Can. Geotechnical J., Vol. 1, No. 1.
73. Scott, R. I., Principles of Soil Mechanics, Addison-Wesley Reading, Mass., 1963.
74. Tschebotarioff, G. P., Soil Mechanics, Foundations and Earth Structures, McGraw-Hill, New York, 1951.
75. Kezdi, A., "Talajmechanika," Tankonyvkiado, Budapest, 1952.

76. Broms, B. B., and Tamal, A. K., "Analysis of the Triaxial Test-Cohesionless Soils," Proc. 6th Int. Conf. on Soil Mech. and Found. Eng., Vol. 1, 1965.
77. Caquot, A., and Kerisel, J., Traite de Mecanique des Sols, 3rd Ed., Paris, Gauthier-Vittars, 1956.
78. Earth Manual, 1st Ed., U. S. Bureau of Reclamation, Denver, Colorado, 1960.
79. Meyerhof, G. G., "An Investigation of the Bearing Capacity of Shallow Footings on Dry Land," Proc. 2nd Int. Conf. on Soil Mech. and Found. Eng., Vol. 5, 1948.
80. Hansen, B., "The Bearing Capacity of Sand, Tested by Loading Circular Plates," Proc. 5th Int. Conf. Soil Mech. and Found. Eng., Vol. 1, 1961.
81. Bishop, A. W., and Eldin, A. K. G., "The Effect of Stress History on the Relation Between Phase and Porosity in Sand," Proc. 3rd Int. Conf. Soil Mech. and Found. Eng., Vol. 1, 1953.
82. Kjellman, W., and Jakobson, B., "Some Relations Between Stress and Strain in Coarse Strained Materials," Proc. Royal Swedish Geotechn. Institute, Stockholm, 1955.
83. Trostel, L. J., Jr., "Strength and Structure of Refractories as a Function of Pore Content," J. of the Am. Ceramic Soc., Vol. 45, No. 11, November 1962.
84. Sznonn, R. E., Harris, G. M., and Vasilos, T., "Effect of Porosity on Mechanical, Thermal and Dielectric Properties of Fused Silica," Ceramic Bulletin, Vol. 44, No. 5, 1965.
85. Bender, R. J., Handbook of Foamed Plastics, Lake Publishing Company, 1965.
86. Griffith, J. H., Physical Properties of Typical American Rocks, Iowa State College Eng. Exp. Sta. Bulletin, No. 131, 1937.
87. Karafiath, L. L., Preliminary Analysis of the Mechanical Properties of Postulated Lunar Vesicular Rocks, Grumman Research Department Memorandum RM-328, June 1966.
88. Murray, B. C., and Wildey, R. L., "The Surface Temperature Variations During the Lunar Nighttime," Astrophys. J., Vol. 139, 1964, p. 734.

89. Sinton, W., Physics and Astronomy of the Moon, Academic Press, 1962.
90. Pettit, E., and Nicholson, S. B., "Lunar Radiation and Temperature," Astrophys. J., Vol. 71, 1930, p. 102.
91. Piddington, J. H., and Minnett, H. C., "Microwave Thermal Radiations From the Moon," Austr. J. of Sci. Research, Vol. A2, 1949, p. 63.
92. Markov, M. N., and Khokhlova, V. L., "Coefficients of Emission in the IR Region of Spectrum," Soviet Physics, Vol. 9, 1965, p. 621.
93. Polgar, L. G., and Howell, J. R., "The Directional Radiation Characteristics of Conical Cavities and Their Relation to Linear Phenomena," AIAA Paper, No. 65-669, 1965.
94. Coulson, K. L., University of California, private communication, 1965.
95. Wesselinck, A. J., "Heat Conductivity of Powders," Can. J. Phys., Vol. 37, 1959, p. 798.
96. Muncey, R. W., "Properties of the Lunar Surface as Revealed by Thermal Radiation," Aust. J. Phys., Vol. 16, 1962, p. 24.
97. Ingrao, H. C., Young, A. T., and Linsky, J., A Critical Analysis of Lunar Temperature Measurements in the Infrared, Harvard College Observatory, NsG 64-60, Scientific Report No. 6, 1965.
98. Linsky, J. L., Models of the Lunar Surface Including Temperature-Dependent Thermal Properties, Harvard College Observatory, NsG 64-60, Scientific Report No. 8, 1966.
99. Low, F., "Lunar Nighttime Temperature Measured at 20 Micross," Astrophys. J., Vol. 142, 1965, p. 806.
100. Buettner, K. J. K., "The Moon's First Decimeter," Rand Corporation RM-3262-JPL, 1962.
101. Jura, G., and Pitzer, K. S., "The Specific Heat of Small Particles at Low Temperatures," J. Phys. Chem., Vol. 74, 1962, p. 6030.
102. Jaeger, J. C., "Conduction of Heat in a Solid With a Power Law of Heat Transfer at its Surface," Proc. Cambr. Phil. Soc., Vol. 46, 1950, p. 634.

103. Lowan, A. N., and Blanch, G., "Tables of Planck's Radiation Functions," J. Opt. Soc. America, Vol. 30, 1940, p. 70.
104. Geophysics Laboratory Review, Boeing Scientific Research Laboratories, July-December 1965.
105. Bastin, J. A., "Lunar Hot Spots," Nature, Vol. 207, 1965, p. 1381.
106. Saari, J. M., and Shorthill, R. W., "The Surface Temperature of the Antisolar Point of the Moon," Icarus, Vol. 3, 1964, p. 161.
107. Evans, T. V., and Hagfors, T., On the Interpretation of Radar Reflections from the Moon, Massachusetts Institute of Technology, Lincoln Laboratories, 1964.
108. Surveyor Scientific Evaluation and Analysis Team, Surveyor 1: A Preliminary Report, Scientific and Technical Information Division, NASA SP-126, Washington, D.C.; also in Science, Vol. 152, No. 3730, June 24, 1966.
109. Halajian, J. D., "Mechanical, Optical, Thermal and Electrical Properties of Surveyor 1 Landing Site," Grumman Report AS-424-4, Nov. 1966.
110. Harrison, J. K., Brightness Temperatures of the Moon as a Function of Angle of Observation, Internal Note, R-RP-INT-66-4, NASA Marshall Space Flight Center, Huntsville, Alabama, August 10, 1966.
111. Winston, S., Reichman, J., and Halajian, J. D., "Review and Evaluation of Thermal Measurements of Lunar Analogs," Grumman Research Department Memorandum RM-352, February 1967.